

SEPARATION OF LINE EMISSION FROM STAR FORMATION, SHOCKS, AND AGN IONISATION IN GALAXIES

Joshua Joseph D'Agostino

A THESIS SUBMITTED FOR THE DEGREE OF
DOCTOR OF PHILOSOPHY
OF THE AUSTRALIAN NATIONAL UNIVERSITY



**Australian
National
University**

Research School of Astronomy & Astrophysics

Resubmitted 11th November 2019

Disclaimer

I hereby declare that the work in this thesis is that of the candidate alone, except where indicated below or in the text of the thesis. The work was undertaken between February 2016 and July 2019 at the Australian National University, Canberra. It has not been submitted in whole or in part for any other degree at this or any other university.

A handwritten signature in black ink, appearing to read 'J. D'Agostino', with a large circular flourish at the end.

Joshua Joseph D'Agostino

11th November 2019

To Anna...

Acknowledgements

Over the past few years, I have been provided with the support of many, which ultimately led me to complete a PhD. This is no easy feat, and as such I am eternally grateful to so many people, for without you all it would not have been possible.

Formally, I would like to start by acknowledging the financial support of the Australian Government Research Training Program (RTP) Scholarship, the ANU Supplementary Scholarship, and the Joan Duffield Research Award (2017-18). Such funding has allowed me to complete my work and live comfortably during my time in Canberra.

To my supervisors, Lisa and Brent. In some ways, I feel a little guilty accepting the plaudits for my publications and methods, because I know none of that would have been possible without the guidance of you two. I have no doubt that the wisdom and methodology that I have received and learned from you over the past few years will stay with me for the remainder of my career. Thank you both immensely.

My time at Mt Stromlo certainly would not have been as eventful if it wasn't for the friends I've made along the way. I'd like to give some special shoutouts to my travel buddy Henry, my officemate Ayan, and others such as the GEARS3D group and the Carnegie crew in California (Barry, Jeff, and Mark) who offered help and advice when I asked. Special mentions to both Brad Tucker and Dougal Mackey are in order, because without their organisation of the 2014 Winter School and 2014/15 Summer Research Scholarship program, respectively, who knows whether or not I would have made it to ANU for a PhD. I am grateful to the both of you for giving me my first experiences of the RSAA and Canberra as a whole.

My time in Canberra has not just been about work. Rather, some of my fondest memories over the past few years have come outside of work. Moving to Canberra was my first experience of moving out of home, so to my first ever housemates, Daniel and James, thank you for accompanying me during that steep learning curve in my life. To my sporting friends, particularly my football teammates at ANUFC, and the boys whom I accompanied to the Eastern Uni Games in 2017 (Champions!), not only did you all provide me with a much-needed distraction outside of work, but the genuine friendships I made with you all is something I will always remember. Good luck in the NPL2!

There is a group of people though who deserve their own separate and special mention: my futsal friends. You were the group with whom I felt the most comfortable and had the most fun. Having moved over to Canberra on my own, I really felt a sense of belonging with you guys, and I know with you I have made friendships which I will cherish forever. I look forward to our next meeting, whether that's in your backyard or mine.

And lastly, to my dear family, and girlfriend Anna. Through the support of all kinds from a young age, you encouraged me to follow my dreams. I dedicate this to you all more than anyone else. There have been extremely trying and testing times for me, having moved here by myself, but I would tell myself to grit my teeth in the knowledge it would all be worth it in the end. I know it has been. I can't wait to be back where I belong. They say, "home is where the heart is," and my heart has always been in Adelaide.

I can't wait to be home.

Abstract

The processes of star formation and the accretion from an active galactic nucleus (AGN) are known to be linked, and together they drive the evolution of their host galaxy. Yet the exact nature of the link between the two processes remains uncertain. The advent of integral field spectroscopy has advanced the study of star formation-AGN mixing, through spatially-resolved spectra showing the mixing across a galaxy. This thesis builds upon the previous work of star formation-AGN mixing, and also considers the contribution from a third ionising source, shocks, subsequently.

The first part of this thesis concerns photoionisation modelling. Specifically, we study the systematic effects and uncertainties present in photoionisation models on the BPT diagram, as a result of using various examples and values of model parameters. On average, we show that differences in the input physics of differing model codes account for a ~ 0.1 dex in $[\text{O III}]/\text{H}\beta$ and $[\text{N II}]/\text{H}\alpha$ ratios.

The second part of this thesis applies photoionisation models to the study of star formation-AGN mixing, in order to calculate the relative contributions of star formation and AGN ionisation to line emission in IFU data. The application of photoionisation models to this study allows the relative contribution of each ionisation source to be calculated using theory, rather than by empirical means. Data used during this work is from the TYPHOON/PrISM survey. We also rebin the data to lower resolutions to study the effects of spatial resolution on star formation-AGN mixing. Results show that lowering the resolution will overestimate the contribution from the AGN. Low-surface-brightness features, such as shocks or diffuse ionised gas (DIG), also appear at lower resolutions as the data is rebinned.

In the third part of the thesis, we consider the inclusion of shocks in star-formation-AGN mixing, leading to the study of star formation-shock-AGN mixing. Conventional methods used to calculate the relative contribution of star formation and AGN to line emission, such as the BPT diagram, prove ineffective in separating line emission from shocks and AGN. We display a new three-dimensional diagnostic diagram, which aids in the simultaneous separation of line emission from all three ionising sources. This new diagram retains emission-line ratio information used in the BPT diagram, while adding distance and velocity dispersion values for each spaxel in the IFU datacube. To demonstrate this diagram, we use the high spatial and spectral resolution data of the Siding Spring Southen Seyfert Spectroscopic Snapshot Survey (S7). Specifically, we use the prototypical Seyfert galaxy NGC 1068 as a test case. Our results show that data on the 3D diagram displays two distinct mixing sequences of spaxels, which we show to be a star formation-AGN sequence, and star formation-shock sequence. Significant scatter is present towards the AGN and shock regions of their relevant sequences, indicating mixing between the emission from shocks and AGN also.

In the fourth part of the thesis, we further the results of the previous section by calculating the relative contribution of line emission from star formation, shocks, and AGN in each spaxel of the galaxy NGC 1068 from the S7. When compared to simply star formation-AGN mixing, the results suggest that the shocked emission mixes primarily with the AGN emission. Hence, not accounting for shocks in the decomposition will greatly overestimate the true contribution of photoionisation from the AGN. The results also show that if $\text{H}\alpha$ is

to be used as a star formation rate indicator, then separation of the line emission between as many sources as possible should be performed to provide accurate results. The fifth and final part of the thesis provides a brief overview on possible future work in the field.

Contents

List of Figures	xi
List of Tables	xxiii
List of Publications	xxv
1 Introduction	1
1.1 The Interstellar Medium	1
1.1.1 Sources of Ionisation in the ISM	2
1.2 Optical Spectroscopy and Integral Field Units	7
1.2.1 Integral Field Spectroscopy	7
1.2.2 Emission-Line Diagnostics	8
1.3 Photoionisation Modelling	11
1.4 Thesis Overview	12
2 H II Region Modelling	17
2.1 Introduction	18
2.2 Sample Description	21
2.3 MAPPINGS V	21
2.4 Stellar Radiation Field	22
2.4.1 SPS Codes	22
2.4.2 SFH and Age	24
2.4.3 Initial Mass Function	25
2.4.4 Stellar Tracks and Metallicities	25
2.4.5 Stellar Atmospheres	26
2.5 Photoionisation Models	27
2.5.1 Abundance Sets	27
2.5.2 Depletion Factors	27
2.5.3 Model Geometry	29
2.5.4 Pressure and Density	29
2.5.5 Ionisation Parameter	30
2.5.6 Boundedness	30
2.5.7 Fiducial Model	31
2.6 Model Comparisons	32
2.6.1 Ionising Radiation Field	32
2.6.2 BPT Diagrams	45
2.7 Discussion	59
2.7.1 Spread of SDSS galaxies	59
2.7.2 Further Ionising Processes	61
2.8 Conclusions	61

3	Star Formation-AGN Mixing with the TYPHOON/PrISM Survey	65
3.1	Introduction	66
3.2	Sample Selection	68
3.2.1	NGC 1365	68
3.2.2	NGC 1068	68
3.3	Observations and Data Reduction	69
3.3.1	Observations	69
3.3.2	Data Reduction	70
3.4	Photoionisation Model Grids	75
3.4.1	Starburst Model Grid	75
3.4.2	AGN Model Grid	76
3.5	The Starburst-AGN Mixing Sequence	78
3.5.1	Use of Photoionisation Grids	78
3.5.2	Starburst Basis Line	79
3.5.3	Nuclear Column	81
3.5.4	Relative AGN Fractions	81
3.6	Investigating the Effect of Spatial Resolution	88
3.6.1	Effect of Resolution on the AGN Fraction	88
3.6.2	Effect of Resolution on Low Surface Brightness Features	89
3.7	Conclusions	101
3.8	Appendix: Power-Law Spectral Index	102
4	The Three-Dimensional Diagnostic Diagram	107
4.1	Introduction	108
4.2	Data Selection	108
4.3	Issues with Current Diagnostics	109
4.4	The 3D Diagnostic Diagram	110
4.5	Results	112
4.6	Summary and Future Work	114
5	Separating Line Emission from Star Formation, Shocks, and AGN Ionisation in NGC 1068	119
5.1	Introduction	120
5.2	Siding Spring Southern Seyfert Spectroscopic Snapshot Survey (S7)	121
5.3	NGC 1068	122
5.4	Photoionisation Models	123
5.5	Separating Line Emission from Star Formation, Shocks, and AGN	123
5.5.1	The Need for a New Diagnostic	123
5.5.2	The 3D Diagnostic Diagram	124
5.5.3	Defining the Star Formation, Shock, and AGN Extrema	126
5.5.4	Calculating the Star Formation-Shock-AGN Fraction	130
5.6	Comparison with Other Data	138
5.7	Conclusions and Future Work	142
6	Future Work	145
6.1	The Effect of Resolution on the Star Formation-Shock-AGN Fraction	145

6.1.1	Spatial Resolution	146
6.1.2	Spectral Resolution	154
6.2	Future Directions	165
7	Conclusions	167
7.1	H II Region Modelling	167
7.2	Star Formation-AGN Mixing with TYPHOON/PrISM	168
7.3	The Three-Dimensional Diagnostic Diagram	168
7.4	Separating Line Emission from Star Formation, Shocks, and AGN Ionisation	169
7.5	The Effect of Resolution on the Star Formation-Shock-AGN Fraction, and Future Directions	169
	Bibliography	171

List of Figures

1.1	Schematic diagram from Beckmann & Shrader (2012), showing how the unified model of AGN can be interpreted as many different AGN types, dependent on viewing angle.	3
1.2	The Horsehead Nebula, an H II region in the Orion Molecular Cloud Complex, in the constellation of Orion. Image taken from Astronomy Picture of the Day (APOD).	5
1.3	Figure 1 from Ho (2008), showing the spectra of several different galaxy types. Certain strong emission lines are labelled.	8
1.4	A spiral galaxy with an integral field unit from the MaNGA survey (Bundy et al. 2015) superimposed. Each circle represents a single fibre on the IFU.	9
1.5	Illustration of a datacube, showing the two spatial dimensions providing the image, and a third wavelength dimension. Credit: ESO/MUSE consortium/R. Bacon/L. Cal[Pleaseinsertintopreamble]ada. https://www.eso.org/public/images/eso1407a/	10
1.6	Emission-line diagnostics of Baldwin et al. (1981) and Veilleux & Osterbrock (1987), taken from Kewley et al. (2006). Data points are a subset of the Sloan Digital Sky Survey (SDSS) Data Release 4 (Adelman-McCarthy et al. 2006, see Kewley et al. 2006 for full details).	10
1.7	BPT diagram and corresponding map of NGC 7130, from Davies et al. (2014a). The colour-coding between the two panels is identical. Spaxels found towards the edge of the galaxy are shown with low [O III]/H β and [N II]/H α ratios, and spaxels found towards the centre have high emission-line ratios.	11
2.1	Example of a photoionisation grid used by many in the astrophysics community in recent years, overlaid on the distribution of galaxies from SDSS DR7 (Abazajian et al. 2009).	20
2.2	Model grid computed with the SLUG SPS code, using the SB99 combination atmosphere and Geneva HIGH tracks, assuming a continuous SFH at 5 Myr, truncated at 99% hydrogen recombination. The model is annotated showing directions of increasing metallicity Z and ionisation parameter $\log(q(N))$. Five metallicities are used in the model grids: $Z = 0.001, 0.004, 0.008, 0.020,$ and 0.040 . The values of the ionisation parameter used in the model grids range between $\log(q(N)/(\text{cm s}^{-1})) = 6.5$ and 8.5 inclusive, in 0.25 dex increments. The annotations shown on this figure are identical for all models on subsequent figures, unless otherwise stated.	29
2.3	SB99 spectrum of a 5 Myr cluster undergoing constant star formation at $1 M_{\odot} \text{ yr}^{-1}$, treating all stars as pure blackbodies. This is the spectrum to which all spectra in Section 2.6.1 are first normalised.	32

- 2.4 SLUG spectra for an instantaneous SFH cluster of mass $10^6 M_\odot$ for ages 0 – 6 Myr in steps of 0.5 Myr. f_λ/f_0 is the input spectrum normalised to the blackbody spectrum shown in Figure 2.3. All spectra are at a metallicity of $Z = 0.020$. The red vertical lines represent the ionisation potentials of important ISM species; from left to right: H^0 , S^+ , N^+ , O^+ , C^{2+} , He^+ 33
- 2.5 Input spectra (flux in units $\text{erg sec}^{-1} \text{\AA}^{-1}$ vs. energy) of the Geneva HIGH tracks (grey) and the Padova tracks with thermally pulsing AGB stars (blue). f_λ represents the individual input spectra, and f_0 is the blackbody spectrum shown in Figure 2.3. Solid lines are for continuous SFH clusters undergoing star formation at a rate of $1M_\odot \text{ yr}^{-1}$. Dashed lines are for instantaneous SFH clusters of mass $10^6 M_\odot$. The continuous SFH spectra shown at 0 Myr (10 kyr) are for clusters undergoing star formation at a rate of $100M_\odot \text{ yr}^{-1}$, ensuring that the continuous SFH cluster has a mass of $10^6 M_\odot$ for direct comparison to the instantaneous SFH clusters. Each column shows a different cluster age; from left to right: 0 Myr (10 kyr), 3 Myr, 5 Myr. Each row shows a different metallicity; from top to bottom: $Z = 0.004$, $Z = 0.008$, $Z = 0.020$. The red vertical lines represent the ionisation potentials of important ISM species; from left to right: H^0 , S^+ , N^+ , O^+ , C^{2+} , He^+ 35
- 2.6 Input spectra (flux in units $\text{erg sec}^{-1} \text{\AA}^{-1}$ vs. energy) of each of the four SLUG atmospheres for each metallicity value used in the grids. f_λ represents the individual input spectra, and f_0 is the blackbody spectrum shown in Figure 2.3. The atmospheres used in each plot are Kurucz, Kurucz + Hillier (K + H), Kurucz + Pauldrach (K + P), and Kurucz + Hillier + Pauldrach (K + H + P). The left panels show both continuous SFH (solid lines) and instantaneous SFH (dashed lines) clusters of mass $10^6 M_\odot$ at ages of 0 Myr (10 kyr). The right panels show continuous SFH clusters at 5 Myr and instantaneous SFH clusters of mass $10^6 M_\odot$ at 4.5 Myr. The age of 4.5 Myr for the instantaneous SFH cluster was chosen to coincide with maximum W-R activity shown in Figure 2.4. The red vertical lines represent the ionisation potentials of important ISM species; from left to right: H^0 , S^+ , N^+ , O^+ , C^{2+} , He^+ 37
- 2.7 Relative difference between spectra of an instantaneous SFH $10^6 M_\odot$ cluster computed with SB99 and SLUG. The relative difference is shown at ages of 0 Myr (10 Kyr) to 6 Myr inclusive, in increments of 1 Myr. Instantaneous SFH cluster spectra produced with SLUG for each age are shown in panel (h). f_λ in (h) represents the individual input spectra, and f_0 is the blackbody spectrum shown in Figure 2.3. The blue dashed line represents a relative difference of 0. The red vertical lines represent the ionisation potentials of important ISM species; from left to right: H^0 , S^+ , N^+ , O^+ , C^{2+} , He^+ 38
- 2.8 Relative difference between the spectra of SB99 and SLUG for a continuous SFH cluster at $Z = 0.020$ and at an age of 5 Myr. The red vertical lines represent the ionisation potentials of important ISM species; from left to right: H^0 , S^+ , N^+ , O^+ , C^{2+} , He^+ 38
- 2.9 Relative difference between SB99 and SLUG in the number of H^0 -, He^0 - and He^+ -ionising photons vs. Z . All model parameters and input are equal to those in Figure 2.8. 39

2.10	Spectra for instantaneous SFH clusters of age 5 Myr at masses of $10^4 M_{\odot}$ (solid) and $10^6 M_{\odot}$ (dashed), produced with SB99 and SLUG. All spectra are at a metallicity of $Z = 0.020$. f_{λ} represents the individual input spectra, and f_0 is the blackbody spectrum shown in Figure 2.3. The red vertical lines represent the ionisation potentials of important ISM species; from left to right: H^0 , S^+ , N^+ , O^+ , C^{2+} , He^+	40
2.11	Relative difference between spectra of an instantaneous SFH $10^6 M_{\odot}$ cluster computed with BPASS and SLUG. The relative difference is shown at ages of 1 – 6 Myr inclusive, in increments of 1 Myr. Instantaneous SFH binary cluster spectra produced with BPASS for each age are shown in panel (g). f_{λ} in panel (g) represents the individual input spectra, and f_0 is the blackbody spectrum shown in Figure 2.3. The red vertical lines represent the ionisation potentials of important ISM species; from left to right: H^0 , S^+ , N^+ , O^+ , C^{2+} , He^+	41
2.12	Relative difference between the spectra of BPASS and SLUG for a continuous SFH cluster at $Z = 0.020$ and at an age of 5 Myr. The red vertical lines represent the ionisation potentials of important ISM species; from left to right: H^0 , S^+ , N^+ , O^+ , C^{2+} , He^+	42
2.13	Relative difference between the spectra of BPASS and SLUG for a continuous SFH cluster at $Z = 0.020$ and at ages for which the stellar spectrum has reached equilibrium (5 Myr for SLUG, and 10 Myr for BPASS, seen in Figure 2.14a). The red vertical lines represent the ionisation potentials of important ISM species; from left to right: H^0 , S^+ , N^+ , O^+ , C^{2+} , He^+	42
2.14	Spectra of clusters produced with BPASS assuming a continuous and instantaneous SFH in panels (a) and (b), respectively. f_{λ} represents the individual input spectra, and f_0 is the blackbody spectrum shown in Figure 2.3. The red vertical lines represent the ionisation potentials of important ISM species; from left to right: H^0 , S^+ , N^+ , O^+ , C^{2+} , He^+	44
2.15	The $\log(q(N)/(cm s^{-1})) = 7.25$ branch shown at varying ages for continuous SFH clusters in panels (a) and (b), and an instantaneous SFH cluster of mass $10^6 M_{\odot}$ in panel (c). Panel (a) is a continuous SFH cluster using the Geneva HIGH stellar tracks, while panel (b) uses the Padova TP-AGB tracks. Ages for the continuous SFH cluster extend from 0 Myr (10 kyr) to 10 Myr in 0.5 Myr increments. Ages for the instantaneous SFH cluster range from 0 Myr (10 kyr) to 6 Myr in 0.5 Myr increments.	46
2.16	(a) Model grids produced using both the Geneva HIGH tracks and the Padova TP-AGB tracks for a continuous SFH population at age 5 Myr. (b) Model grids produced using different stellar atmospheres for a continuous SFH population at 5 Myr. The atmospheres included in the models are Kurucz, Kurucz + Hillier (K + H), Kurucz + Pauldrach (K + P), and Kurucz + Hillier + Pauldrach (K + H + P). (c) Model grids produced using SLUG and SB99. All parameters associated with these grids are fiducial.	49

2.17	Instantaneous SFH grids of ages 5 Myr produced by SLUG and SB99, for cluster masses of $10^4 M_\odot$ (solid) and $10^6 M_\odot$ (dashed). The stochastic sampling of the IMF demonstrated by SLUG produces spectra of different shapes for clusters at 10^4 and $10^6 M_\odot$, leading to differences in the emission-line ratios. The lack of stochastic IMF sampling shown by SB99 leads to identically shaped ionising spectra for the $10^4 M_\odot$ and $10^6 M_\odot$ clusters, as shown in Figure 2.10.	50
2.18	(a) Model grids produced using BPASS and SB99, both assuming a continuous SFH at an age of 5 Myr. (b) Model grids produced using BPASS and SB99, using SLUG and BPASS continuous SFH input spectra at ages for which the respective stellar cluster reaches equilibrium. All remaining parameters associated with these grids are fiducial.	51
2.19	Model grids of varying pressure for a continuous SFH population at age 5 Myr, from $P/k = 8 \times 10^3$ ($\log(P/k) \sim 4$) to $P/k = 8 \times 10^7 \text{ cm}^{-3} \text{ K}$ ($\log(P/k) \sim 8$), in increments of 1 dex.	52
2.20	Grids of the three highest pressures (red $\Rightarrow P/k = 8 \times 10^5$, orange $\Rightarrow P/k = 8 \times 10^6$, blue $\Rightarrow P/k = 8 \times 10^7$) from Fig. 2.19 plotted with the SDSS DR7 sample. The models show that the SDSS star-forming galaxies are well described by models with pressure $\sim 8 \times 10^5 \text{ cm}^{-3} \text{ K}$. All parameters are fiducial.	53
2.21	Ion fractions of species within the H II region as a function of distance from the ionising source. The corresponding optical depth is also shown. Solid lines show neutral (I) species, dashed lines show singly ionised (II) species, and dot-dashed lines show doubly ionised (III) species. Parameters for this plot are $\log(q) = 6.5$ and $Z = 0.004$. This particular model has been truncated with 1% of H II remaining. All other parameters are fiducial.	53
2.22	Cumulative growth of the BPT emission lines and emission-line ratios as a function of distance through the nebula, normalised to their maximum value, for $\log(q) = 6.5, 7.5$, and 8.5 in panels (a), (b), and (c), respectively. The normalised temperature and density distribution throughout the nebula are also shown. The metallicity for all plots is set to $Z = 0.004$. All other parameters are identical to Figure 2.21.	54
2.23	(a) Model grids computed with varying H II ionisation bounds, given as percentages. The percentage given is the fraction of H II that has undergone recombination to H I. (b) Model grids computed with varying optical depths at the threshold of hydrogen. The optical depth values used are identical to those used by Nicholls et al. (2014).	56

2.24	Density-bounded ($\tau = 1$) grid (red) with pressure $P/k \sim 8 \times 10^7 \text{ cm}^{-3} \text{ K}$, corresponding to an initial electron density $n = 10,000 \text{ cm}^{-3}$ under the assumption of an initial electron temperature of 8000K, shown over the top of the SIGRID sample and grid taken from Nicholls et al. (2014) (multicoloured). The yellow points show the SIGRID sample from Nicholls et al. (2014) , the black points show the low-metallicity DR7 SDSS subset from Izotov et al. (2012) , and the red points show the DR3 SDSS subset from Izotov et al. (2006) . Metallicity values Z are in units of $12 + \log(\text{O}/\text{H})$. Ionisation parameter values are consistent with those used in this paper. All other parameters are fiducial. The density-bounded model better fits the data and helps explain the off-grid data points in Nicholls et al. (2014) . The very high value of $\log(P/k) \sim 8$ is likely to be unphysical and arises as a result of an X-ray deficit in the model ionising spectra.	57
2.25	Isobaric models with pressure values of $P/k = 8 \times 10^7 \text{ cm}^{-3} \text{ K}$, assuming a density-bounded regime for the blue grid and radiation-bounded regime for the red grid. The density-bounded model is truncated at an optical depth of $\tau = 1$, and the radiation-bounded model is truncated at 99% of hydrogen recombination. The very high value of $\log(P/k) \sim 8$ is likely to be unphysical and arises as a result of an X-ray deficit in the model ionising spectra.	58
2.26	Model grids computed using the photoionisation modelling codes <code>MAPPINGS</code> and <code>CLOUDY</code> . All parameters associated with these grids are fiducial.	59
3.1	Colour composite (BVR) and $H\alpha$ maps for NGC 1365 and NGC 1068 from the TYPHOON datacubes. For both images (and all hereafter), north is vertically upwards, and east to the left.	71
3.2	$[\text{O III}]$ distribution maps for NGC 1365 and NGC 1068.	72
3.3	$[\text{N II}]/H\alpha$ and $[\text{O III}]/H\beta$ distribution maps for NGC 1365 and NGC 1068. Contours of $[\text{O III}]$ with a signal-to-noise ratio greater than 3 are included on the $[\text{O III}]/H\beta$ maps. The $[\text{O III}]$ contours are shown for the inner 7 kpc of NGC 1365, ranging from $\log([\text{O III}]) = 1.5$ (light green) to $\log([\text{O III}]) = 0.5$ (deep blue) $10^{-17} \text{ erg s}^{-1} \text{ cm}^{-2} \text{ arcsec}^{-2}$ in increments of 0.5 dex. For NGC 1068, contours for the whole map are shown, ranging from $\log([\text{O III}]) = 5.6$ (light green) to $\log([\text{O III}]) = 1.6$ (deep blue) $10^{-17} \text{ erg s}^{-1} \text{ cm}^{-2} \text{ arcsec}^{-2}$ in increments of 0.8 dex.	73
3.4	The fitting correction applied to the NGC 1068 datacube for NaN spaxels at the centre. Figure shows corrections to the $H\beta$, $[\text{O III}]$, $[\text{O I}]$, $[\text{N II}]$, and $H\alpha$ emission lines. The one-component gaussian fits are shown in red, whilst the two-component fits are shown in blue.	74
3.5	Figure showing the fit to the $[\text{O III}]\lambda 4959$, used to fit the $[\text{O III}]\lambda\lambda 4959, 5007$ when the signal-to-noise in the $H\beta$ profile is too low to provide reliable fit parameters. The one-component gaussian fits are shown in red, whilst the two-component fits are shown in blue.	74
3.6	Figure showing location of H II regions in NGC 1365 in (a) and NGC 1068 in (b). These H II regions were identified using <code>HIIFIND</code> , developed by Thilker et al. (2000)	77

3.7	Figure showing range of electron density across both NGC 1365 in (a) and NGC 1068 in (b).	77
3.8	The BPT diagram of NGC 1365, with each spaxel coloured according to radius from the centre of the galaxy. The black dashed curve is the Kauffmann et al. (2003) empirical maximum starburst line, and the black solid line is the Kewley et al. (2001) theoretical maximum starburst line. The H II region grid is shown in red, and the AGN grid is shown in blue. The solid green grid lines on both grids represent the metallicity at the centre of the galaxy, and the dashed green grid line on the H II region grid represents the metallicity at the edge of the galaxy. Both metallicity values are stated in Table 3.1. . . .	80
3.9	The basis points exhibited on the photoionisation grids, with the location of each constrained using the metallicity measurements of NGC 1365. The starburst basis points SB1, SB2, and SB3 define the starburst basis line, while the basis points SB2, SB3, AGN1, and AGN2 together define the nuclear column. . . .	80
3.10	The AGN fraction for NGC 1365, using the old calculation by Davies et al. (2014a,b) . The method from Davies et al. (2014a,b) gives AGN fractions of up to ~50% for some spaxels below the Kauffmann line – a well-known empirical line which signifies the upper limits of pure star formation.	81
3.11	AGN fraction [O III]/H β vs [N II]/H α diagram for NGC 1365.	82
3.12	The BPT diagram for NGC 1365 showing the fractional contribution of AGN excited gas to the H α line using our new calculation method. This figure also overlays the original Kauffmann et al. (2003) and Kewley et al. (2001) AGN diagnostic lines (black lines, Figure 3.8), the new basis points and mixing curves based on our model grids (pink points and lines, Figure 3.9 and Section 3.5), and the resulting starburst-AGN mixing sequence (green curves). . . .	82
3.13	Map of NGC 1365 (a), with spaxels coloured to the [O III]/H β vs [N II]/H α AGN fraction. The nucleus of NGC 1365 is shown in (b), overlaid with an image from Alonso-Herrero et al. (2012) showing star-forming clusters identified by Galliano et al. (2005) (red stars, M2, ..., M8), the H α hotspot L4 from Alloin et al. (1981) and Kristen et al. (1997) , and light-green contours showing the 70 μ m flux distribution from Herschel PACS (square-root flux scaling, flux density of 85.5 Jy in the inner 15 arcseconds; Alonso-Herrero et al. 2012). The contours are in a square-root intensity scale, with flux of 70 μ m mid-IR emission.	84
3.14	AGN fraction [O III]/H β vs [N II]/H α diagram for NGC 1068.	85
3.15	AGN fraction [O III]/H β vs [N II]/H α diagram, without grids for clarity. Green dashed lines indicate 20%, 40%, 60%, and 80% AGN.	86
3.16	Map of NGC 1068 (a), with spaxels coloured to the [O III]/H β vs [N II]/H α AGN fraction. The nucleus of NGC 1068 is shown in (b). The [O III]/(H α + [N II]) contours from Pogge (1988) are shown on NGC 1068 in (a) and (b) in white. . . .	86
3.17	The percentage of spaxels in the BPTs of both NGC 1365 and NGC 1068 with AGN fractions of greater than 50% as a function of spatial resolution. The four markers indicate (in order): native resolution (169pc and 121pc for NGC 1365 and NGC 1068 respectively), 330pc, 500pc, and 1000pc (1kpc).	91

3.18	The AGN fractions and BPT diagrams coloured by radius for NGC 1365, after rebinning to lower spatial resolutions. Errors for the spaxels on the BPT diagrams are the same as those on the AGN fraction plots.	92
3.19	The [O III]/H β vs [N II]/H α AGN fraction map for NGC 1365, after rebinning to lower spatial resolutions.	93
3.20	Images from Figure 3.19 with a zoom on the nuclear region of NGC 1365 . .	94
3.21	The AGN fractions and BPT diagrams coloured by radius for NGC 1068, after rebinning to lower spatial resolutions. Errors for the spaxels on the BPT diagrams are the same as those on the AGN fraction plots.	95
3.22	The [O III]/H β vs [N II]/H α AGN fraction map for NGC 1068, after rebinning to lower spatial resolutions.	96
3.23	Images from Figure 3.22 with a zoom on the nuclear region of NGC 1068 . .	97
3.24	The velocity dispersion maps for NGC 1365, after rebinning to lower resolutions.	98
3.25	Outflows in [O III]/H β (a) and [N II]/H α (b) seen in the nucleus of NGC 1365 from Veilleux et al. (2003) , coinciding with regions of high velocity dispersion. The [O III]/H β values in (a) range from 0 at the lightest to 3 at the darkest. The [N II]/H α values in (b) range from 0 at the lightest to 1.5 at the darkest.	99
3.26	The velocity dispersion maps for NGC 1068, after rebinning to lower resolutions.	100
3.27	NGC 1365, showing $n = 1000 \text{ cm}^{-3}$ AGN model grids computed with power-law spectral indices of $\alpha = -1.4$ and -1.7	103
3.28	NGC 1068, showing $n = 10000 \text{ cm}^{-3}$ AGN model grids computed with power-law spectral indices of $\alpha = -1.4$ and -1.7	104
4.1	BPT diagram of NGC 1068, coloured by the maximum velocity dispersion in each spaxel.	109
4.2	3D diagnostic diagram of NGC 1068, showing two distinct mixing sequences of spaxels. The velocity dispersion value is the velocity dispersion of the individual components. Each individual-component velocity dispersion is combined with the total flux ('zeroth' component), and the radius value for the spaxel to form a data point. The purple-to-yellow sequence is referred to as the 'first' sequence, and the deep blue-to-yellow sequence is referred to as the 'second' sequence. Grey spaxels are those which are not definitively in either sequence. The first sequence shows mixing between emission from star formation and AGN, and the second sequence shows the mixing between the star formation and shocks. Significant scatter appears between the two sequences, indicating mixing also between the AGN and shocked emission. The three panels below the 3D diagram show the projection in the radius-velocity dispersion plane, radius-ELR function plane, and velocity dispersion-ELR function plane. The separation into two sequences is seen more clearly when studying all three planes.	111
4.3	BPT diagram of NGC 1068, coloured by the ELR function value from Equation 5.1 in each spaxel. The black, solid line is the Kewley et al. (2001) demarcation line, and the black, dashed line is the Kauffmann et al. (2003) demarcation line.	112

4.4	Maps of NGC 1068, showing the distribution of the first sequence of spaxels in (a), the second sequence in (b), and the velocity dispersion in (c). Spaxel colours for (a) and (b) are identical to Figure 4.2. 0.25-7.5 keV <i>Chandra</i> X-ray contours from Young et al. (2001) are also shown on (a).	113
4.5	BPT diagrams showing the spread of spaxels in the first sequence on the left, and second sequence on the right. Spaxel colours are identical to Figure 4.2. The black, solid line is the Kewley et al. (2001) demarcation line, and the black, dashed line is the Kauffmann et al. (2003) demarcation line.	114
5.1	Maps of NGC 1068 showing the distribution and amplitude of each individual velocity component in the data. Dashed lines represent grid lines of constant right ascension and declination.	126
5.2	3D diagnostic diagram showing data from NGC 1068. Red spaxels are spaxels using the first-component fits to the velocity dispersion, blue spaxels are the second-component fits, and green spaxels are the third-component fits. First-, second-, and third-component velocity components in each spaxel, if present, all use the total flux ('zeroth' component) and the distance measurement for the individual spaxel. The ELR function is given in Equation 5.1. Bottom panels show the 2D projections in the distance- σ , ELR function-distance, and ELR function- σ planes. Grey lines in each of the three panels represent the errors associated with each dimension. Errors are omitted from the 3D diagram for clarity.	127
5.3	Maps of the line-of-sight velocity (v_{LOS}) and the velocity dispersion (σ) for NGC 1068 in the S7 field-of-view ($38 \times 25 \text{ arcsec}^2$). The left-hand panels show the maps obtained from the data directly. The right-hand panels show the maps of the model produced using $^{\text{3D}}\text{BAROLO}$. The centre of the galaxy is marked with an 'X' in all panels.	128
5.4	[O III]/H β map in (a) and distance map in (b) for NGC 1068. The distance in each spaxel is calculated by first identifying peaks in the [O III]/H β distribution. Peaks are identified in (a) by red crosses. Dashed lines represent grid lines of constant right ascension and declination.	129
5.5	BPT diagram of NGC 1068 with spaxels coloured to the ELR function in Equation 5.1. The red grid is the H II region model grid, and the blue grid is the NLR model grid, both described in Section 5.4. The green dashed line on the H II region grid is a constructed line of constant metallicity for the outer regions of the galaxy, within the S7 field-of-view. The solid green line on the NLR model is the constructed line of constant metallicity for the centre of the galaxy. Both metallicity values are found in Table 5.1. The light blue points are the basis points used to calculate the star formation and AGN/shock extrema for the 3D diagnostic diagram. Light green points represent the mean value of each pair of light blue basis points, and define the 100% star formation and AGN/shock ELR function values, also found in Table 5.1. The dashed black line is the Kauffmann et al. (2003) demarcation line, and the solid black line is the Kewley et al. (2001) demarcation line.	129

- 5.6 3D diagnostic diagram, showing the ratio of AGN in each spaxel of NGC 1068. Light green points represent the basis points for the ELR function. Bottom panels show the 2D projections in the distance- σ and ELR function- σ planes. Grey lines in the two panels represent the errors associated with each dimension. Errors are omitted from the 3D diagram for clarity. 132
- 5.7 3D diagnostic diagram, showing the ratio of shocks in each spaxel of NGC 1068. Light green points represent the basis points for the ELR function. Bottom panels show the 2D projections in the distance- σ and ELR function- σ planes. Grey lines in the two panels represent the errors associated with each dimension. Errors are omitted from the 3D diagram for clarity. 133
- 5.8 3D diagnostic diagram, showing the ratio of star formation in each spaxel of NGC 1068. Light green points represent the basis points for the ELR function. Bottom panels show the 2D projections in the distance- σ and ELR function- σ planes. Grey lines in the two panels represent the errors associated with each dimension. Errors are omitted from the 3D diagram for clarity. 134
- 5.9 Maps of NGC 1068 showing the distribution of the AGN, shock, and star formation fractions seen in Figures 5.6, 5.7, and 5.8, respectively. In the event that a spaxel contains more than one velocity component, the final ratio is weighted by the the contribution of each component to the total $[\text{O III}]\lambda 5007$ flux. Dashed lines represent grid lines of constant right ascension and declination. 135
- 5.10 BPT diagrams showing data from NGC 1068, colour-coded to the AGN, shock, and star formation fractions in each spaxel. The red grid is the H II region model grid, and the blue grid is the NLR model grid, both described in Section 5.4. The green dashed line on the H II region grid is a constructed line of constant metallicity for the outer regions of the galaxy, within the S7 field-of-view. The solid green line on the NLR model is the constructed line of constant metallicity for the centre of the galaxy. Both metallicity values are found in Table 5.1. The dashed black line is the [Kauffmann et al. \(2003\)](#) demarcation line, and the solid black line is the [Kewley et al. \(2001\)](#) demarcation line. 136
- 5.11 Maps and BPT diagrams of NGC 1068, assuming a star formation-AGN mixing regime on top, and our new star formation-shock-AGN regime below. The spaxels in the bottom BPT diagram and map are coloured by shock + AGN fraction, seen separately in Figures 5.9 and 5.10. The red grid on the BPT diagrams is the H II region model grid, and the blue grid is the NLR model grid, both described in Section 5.4. The green dashed line on the H II region grid is a constructed line of constant metallicity for the outer regions of the galaxy, within the S7 field-of-view. The solid green line on the NLR model is the constructed line of constant metallicity for the centre of the galaxy. Both metallicity values are found in Table 5.1. The light blue points are the basis points used to calculate the AGN fraction in each spaxel (see [D’Agostino et al. 2018](#)). The dashed black line is the [Kauffmann et al. \(2003\)](#) demarcation line, and the solid black line is the [Kewley et al. \(2001\)](#) demarcation line. 138

- 5.12 Maps of NGC 1068 showing the [O III] λ 5007 luminosity attributable to AGN in the left panel, and the 0.25-7.5 keV X-ray photon map from Young et al. (2001) on the right. Contours of each map are shown in the adjacent panel. Dashed lines represent grid lines of constant right ascension and declination. 139
- 5.13 Maps of NGC 1068 showing the [O III] λ 5007 luminosity attributable to shocks in the left panel, and the 3mm radio continuum map from García-Burillo et al. (2017) on the right. Contours of each map are shown in the adjacent panel. Dashed lines represent grid lines of constant right ascension and declination. 140
- 5.14 Maps of NGC 1068 showing the H α luminosity attributable to star formation in the left panel, and the star formation ratio map from Figure 5.9 on the right. Identical contours of the CO(3-2) flux from García-Burillo et al. (2014) are shown on both maps. Dashed lines represent grid lines of constant right ascension and declination. 140
- 5.15 He II/H β distribution map for NGC 1068. The He II/H β ratio in each spaxel has been normalised to the maximum value (He II/H $\beta_{\text{max}} \sim 0.49$). The He II/H β emission is seen to form a clean one-sided cone. Dashed lines represent grid lines of constant right ascension and declination. 141
- 5.16 Distribution of the temperature-sensitive [O III] λ 4363/[O III] λ 5007 line ratio in NGC 1068. Only spaxels with significant detection of both the [O III] λ 4363 and [O III] λ 5007 emission lines are shown (signal-to-noise > 3). Significant spaxels are seen to align with spaxels containing high shock + AGN fractions in Figure 5.9. Dashed lines represent grid lines of constant right ascension and declination. 141
- 6.1 3D diagnostic diagram, showing the ratio of AGN in each spaxel of the 2'' (~159 pc) resolution datacube for NGC 1068. Light green points represent the basis points for the ELR function. Bottom panels show the 2D projections in the distance- σ and ELR function- σ planes. Grey lines in the two panels represent the errors associated with each dimension. Errors are omitted from the 3D diagram for clarity. 147
- 6.2 3D diagnostic diagram, showing the ratio of shocks in each spaxel of the 2'' (~159 pc) resolution datacube for NGC 1068. Light green points represent the basis points for the ELR function. Bottom panels show the 2D projections in the distance- σ and ELR function- σ planes. Grey lines in the two panels represent the errors associated with each dimension. Errors are omitted from the 3D diagram for clarity. 148
- 6.3 3D diagnostic diagram, showing the ratio of star formation in each spaxel of the 2'' (~159 pc) resolution datacube for NGC 1068. Light green points represent the basis points for the ELR function. Bottom panels show the 2D projections in the distance- σ and ELR function- σ planes. Grey lines in the two panels represent the errors associated with each dimension. Errors are omitted from the 3D diagram for clarity. 149

- 6.4 3D diagnostic diagram, showing the ratio of AGN in each spaxel of the 3'' (~245 pc) resolution datacube for NGC 1068. Light green points represent the basis points for the ELR function. Bottom panels show the 2D projections in the distance- σ and ELR function- σ planes. Grey lines in the two panels represent the errors associated with each dimension. Errors are omitted from the 3D diagram for clarity. 150
- 6.5 3D diagnostic diagram, showing the ratio of shocks in each spaxel of the 3'' (~245 pc) resolution datacube for NGC 1068. Light green points represent the basis points for the ELR function. Bottom panels show the 2D projections in the distance- σ and ELR function- σ planes. Grey lines in the two panels represent the errors associated with each dimension. Errors are omitted from the 3D diagram for clarity. 151
- 6.6 3D diagnostic diagram, showing the ratio of star formation in each spaxel of the 3'' (~245 pc) resolution datacube for NGC 1068. Light green points represent the basis points for the ELR function. Bottom panels show the 2D projections in the distance- σ and ELR function- σ planes. Grey lines in the two panels represent the errors associated with each dimension. Errors are omitted from the 3D diagram for clarity. 152
- 6.7 Maps of NGC 1068 showing the distribution of AGN, shock, and star formation fractions. Top row shows the native resolution (1'', ~81 pc) maps, middle row shows the 2'' (~159 pc) resolution maps, and bottom row shows the 3'' (~245 pc) resolution maps. Dashed lines represent grid lines of constant right ascension and declination. 153
- 6.8 3D diagnostic diagram, showing the ratio of AGN in each spaxel of the $R \sim 2000$ resolution datacube for NGC 1068. Light green points represent the basis points for the ELR function. Bottom panels show the 2D projections in the distance- σ and ELR function- σ planes. Grey lines in the two panels represent the errors associated with each dimension. Errors are omitted from the 3D diagram for clarity. 157
- 6.9 3D diagnostic diagram, showing the ratio of shocks in each spaxel of the $R \sim 2000$ resolution datacube for NGC 1068. Light green points represent the basis points for the ELR function. Bottom panels show the 2D projections in the distance- σ and ELR function- σ planes. Grey lines in the two panels represent the errors associated with each dimension. Errors are omitted from the 3D diagram for clarity. 158
- 6.10 3D diagnostic diagram, showing the ratio of star formation in each spaxel of the $R \sim 2000$ resolution datacube for NGC 1068. Light green points represent the basis points for the ELR function. Bottom panels show the 2D projections in the distance- σ and ELR function- σ planes. Grey lines in the two panels represent the errors associated with each dimension. Errors are omitted from the 3D diagram for clarity. 159

- 6.11 3D diagnostic diagram, showing the ratio of AGN in each spaxel of the $R \sim 800$ resolution datacube for NGC 1068. Light green points represent the basis points for the ELR function. Bottom panels show the 2D projections in the distance- σ and ELR function- σ planes. Grey lines in the two panels represent the errors associated with each dimension. Errors are omitted from the 3D diagram for clarity. 160
- 6.12 3D diagnostic diagram, showing the ratio of shocks in each spaxel of the $R \sim 800$ resolution datacube for NGC 1068. Light green points represent the basis points for the ELR function. Bottom panels show the 2D projections in the distance- σ and ELR function- σ planes. Grey lines in the two panels represent the errors associated with each dimension. Errors are omitted from the 3D diagram for clarity. 161
- 6.13 3D diagnostic diagram, showing the ratio of star formation in each spaxel of the $R \sim 800$ resolution datacube for NGC 1068. Light green points represent the basis points for the ELR function. Bottom panels show the 2D projections in the distance- σ and ELR function- σ planes. Grey lines in the two panels represent the errors associated with each dimension. Errors are omitted from the 3D diagram for clarity. 162
- 6.14 Maps of NGC 1068 showing the distribution of AGN, shock, and star formation fractions. Top row shows the native resolution ($R \sim 7000$) maps, middle row shows the $R \sim 2000$ resolution maps, and bottom row shows the $R \sim 800$ resolution maps. Dashed lines represent grid lines of constant right ascension and declination. 163
- 6.15 3D diagram of the $R = 2000$ datacube for NGC 1068. The colour of each spaxel is defined by its component number. Red spaxels are first components, blue spaxels are second components, and green spaxels are third components. 164
- 6.16 3D diagram of the $R = 800$ datacube for NGC 1068. The colour of each spaxel is defined by its component number. Red spaxels are first components, blue spaxels are second components, and green spaxels are third components. . . 164

List of Tables

2.1	Various stellar radiation field models used throughout this paper, with references.	22
2.2	Solar abundance reference set from Anders & Grevesse (1989) , and depletion values using the method from Jenkins (2014) for each element with a logarithmic base depletion of iron of -1.50.	28
3.1	Derived quantities for NGC 1365 and NGC 1068 for use on the BPT diagram.	78
3.2	(i) The percentage of spaxels showing emission from low surface brightness features. Spaxels showing emission from low surface brightness features are defined as being below the nuclear column. (ii) The radius of equal starburst and AGN domination (AGN fraction = 50%) for varying resolutions for both NGC 1365 and NGC 1068. Values are calculated as averages of distances for spaxels with AGN fractions between 45% and 55%. The errors on these values represent the standard deviation of these sets of distances.	90
3.3	AGN fractions for several strong emission lines at varying resolutions for both NGC 1365 and NGC 1068 within the TYPHOON field-of-view. Percentage indicates fraction of luminosity attributable to AGN activity for each line.	91
5.1	Metallicity gradient and 100% emission line ratio values for NGC 1068. Solar metallicity (Z_{\odot}) is set to $12 + \log(\text{O}/\text{H}) = 8.93$ (Anders & Grevesse 1989).	130
5.2	Star formation, shock, and AGN fractions for various strong emission lines in NGC 1068 within the S7 field-of-view. Errors on the star formation, shock, and AGN fractions account for differences in final emission line weighting, uncertainties in photoionisation models, and uncertainties in the fits from LZIFU. Displayed also are the star formation and AGN fractions using the method from D'Agostino et al. (2018) , assuming only star formation-AGN mixing. The errors associated with the star formation-AGN mixing fractions are the result of a 0.1 dex uncertainty in the photoionisation models, and the errors from LZIFU.	131
6.1	Star formation, shock, and AGN fractions for various strong emission lines in NGC 1068 within the S7 field-of-view, for various spatial resolutions. Errors on the star formation, shock, and AGN fractions is assumed to be $\sim 10\%$, similar to the fractions shown in Table 5.2.	154
6.2	Target spectral resolutions R , corresponding standard deviations at the target resolution σ_f , and standard deviations used for the convolution with the native S7 datacube σ_c for the new smoothed datacubes.	155

6.3 Star formation, shock, and AGN fractions for various strong emission lines in NGC 1068 within the S7 field-of-view, for various spectral resolutions. Errors on the star formation, shock, and AGN fractions is assumed to be ~10%, similar to the fractions shown in Table 5.2. 156

List of Publications

As first author

D'Agostino J. J., Poetrodjojo H., Ho I.-T., Groves B., Kewley L., Madore B. F., Rich J., Seibert M., 2018, *Starburst-AGN mixing: TYPHOON observations of NGC 1365, NGC 1068, and the effect of spatial resolution on the AGN fraction*, MNRAS, 479, 4907 (Chapter 3)

D'Agostino, J. J., Kewley, L. J., Groves, B. A., Medling, A., Dopita, M. A., Thomas, A. D., 2019, *A new diagnostic to separate line emission from star formation, shocks, and AGNs simultaneously in IFU data*, MNRAS, 485, L38 (Chapter 4)

D'Agostino, J. J., Kewley, L. J., Groves, B., Byler, N., Sutherland, R. S., Nicholls, D., Leitherer, C., Stanway, E. R., 2019, *Comparison of Theoretical Starburst Photoionisation Models for Optical Diagnostics*, ApJ, 878, 2 (Chapter 2)

D'Agostino, J. J., Kewley, L. J., Groves, B. A., Medling, A. M., Di Teodoro, E., Dopita, M. A., Thomas, A. D., Sutherland, R. S., García-Burillo, S., 2019, *Separating Line Emission from Star Formation, Shocks, and AGN Ionisation in NGC 1068*, MNRAS, 487, 4153 (Chapter 5)

As co-author

Ho, I.; Seibert, M., Meidt, S. E.; Kudritzki, R., Kobayashi, C., Groves, B. A., Kewley, L. J., Madore, B. F., Rich, J. A., Schinnerer, E., **D'Agostino, J. J.**, Poetrodjojo, H., 2017, *The Chemical Evolution Carousel of Spiral Galaxies: Azimuthal Variations of Oxygen Abundance in NGC1365*, ApJ, 846, 39

Poetrodjojo, H., **D'Agostino, J. J.**, Groves, B., Kewley, L., Ho, I., Rich, J., Madore, B. F., Seibert, M., 2019, *The Effects of Diffuse Ionized Gas and Spatial Resolution on Metallicity Gradients: TYPHOON Two-Dimensional Spectrophotometry of M83*, MNRAS, 487, 79

CHAPTER 1

Introduction

Optimism is the faith that leads to achievement. Nothing can be done without hope and confidence.

– Helen Keller

1.1. The Interstellar Medium

Galaxies are primarily comprised of stars. Bound together by gravity, the stars orbit a common centre of mass. The shape that the orbiting stars produce can vary from galaxy to galaxy – some galaxies, like our own Milky Way, are spiral in shape. Others can be elliptical, like an elongated ball. Some do not fit the criteria for any shape, and as such are named ‘irregular’. No matter the shape of the galaxy, one certainty remains amongst all: galaxies are systems of stars.

However, this notion that stars are the fundamental building blocks to galaxies is incomplete. It suggests that stars are to galaxies as atoms are to matter; that nothing more exists beyond the stars, and the planets they may harbour. The truth though, is that many processes occur within the space between the stars in a galaxy: the interstellar medium.

The interstellar medium (ISM) is a very diffuse area of the cosmos, reaching densities as low as $\sim 10^{-4}$ particles per cubic centimetre. At its most dense, coinciding with low temperatures of ~ 10 K, the density may increase to 10^6 particles per cubic centimetre (Ferrière 2001). Compared to the density of air at room temperature, which is roughly 10^{20} particles per cubic centimetre, the sparsity of interstellar space becomes apparent. Nevertheless, this sparse region of space contains many different types of matter. From gas (molecules, atoms) to plasmas (ions, electrons), tiny solid dust particles, and even cosmic rays, the ISM is anything but empty (Ferrière 2001).

As indicated by the presence of plasmas in the ISM, ionisation of the interstellar gas indeed occurs. In fact, the interstellar gas is typically separated into five different categories,

dependent on its temperature and composition: molecular, cold atomic, warm atomic, warm ionised, and hot ionised. Different mechanisms within a galaxy will ionise and excite the interstellar gas to varying degrees, resulting in the five different categories. The following sections detail the several sources of ionisation (and subsequent line emission) relevant to this thesis.

1.1.1. Sources of Ionisation in the ISM

Active Galactic Nuclei

An active galactic nucleus (AGN) is a compact region at the centre of a galaxy, with a very high luminosity. In some cases, this heightened luminosity of the central region can rival the luminosity of starlight from the entire galaxy. Such a high luminosity makes AGN visible at extremely high redshifts (current maximum: $z \sim 7.1$; [Mortlock et al. 2011](#)). The host galaxy of an AGN is referred to as an ‘active galaxy’. The accepted theory for the formation of an AGN is accretion onto the supermassive black hole (SMBH) at the centre of the galaxy. Such accretion can result in radiation across the entire electromagnetic spectrum, by several methods:

- The accretion disk: the process of accretion results in matter orbiting the SMBH, converting the gravitational potential energy of the matter into kinetic energy. The friction between the matter in the accretion disk further converts this kinetic energy into thermal energy, thus heating up the disk (e.g. [Shakura & Sunyaev 1973](#)). The accretion-disk temperature of typical AGN is in the range of $10^4 - 10^5$ K, leading to a spectrum which peaks at optical-ultraviolet (UV) wavelengths. Furthermore, hot material around the accretion disk forms a corona, which can inverse-Compton scatter photons up to X-ray energies (e.g. [Cao 2009](#), and references therein).
- Relativistic jets: some AGN produce twin beams of highly-collimated ionised matter, known as jets. These jets appear perpendicular to the disk of the galaxy, and contain material which has been accelerated to velocities close to the speed of light. The extent of the jets can be anywhere between several thousands to millions of parsecs in length (e.g. [Biretta et al. 1999](#); [Kundt 2014](#)). The mechanism behind jet production in active galaxies remains uncertain. Models of an electrically-neutral composition of nuclei, electrons, and positrons has been proposed (e.g. [Georganopoulos et al. 2005](#)), while other models favour an electron-positron plasma composition (e.g. [Hirotani et al. 2000](#)). At their largest extents, jets are seen to coincide with the radio lobes of radio galaxies (e.g. [Dennett-Thorpe et al. 1999](#)).

AGN can be subdivided into categories, such as radio galaxies with extended radio lobes and jets, Seyfert galaxies ([Seyfert 1943](#), mainly types 1 and 2, also referred to as ‘Type I AGN’ and ‘Type II AGN’ respectively, although this has been further expanded into Seyfert 1.2, 1.5, 1.8, and 1.9, e.g. [Osterbrock 1981](#)), low-ionisation nuclear emission-line regions (LINERS; [Heckman 1980](#)), and quasars. Though there appear to be many different variations of AGN, the many types are now considered to be part of the ‘unified model’ of AGN (e.g. [Antonucci 1993](#); [Urry & Padovani 1995](#)). The unified model explains the differing

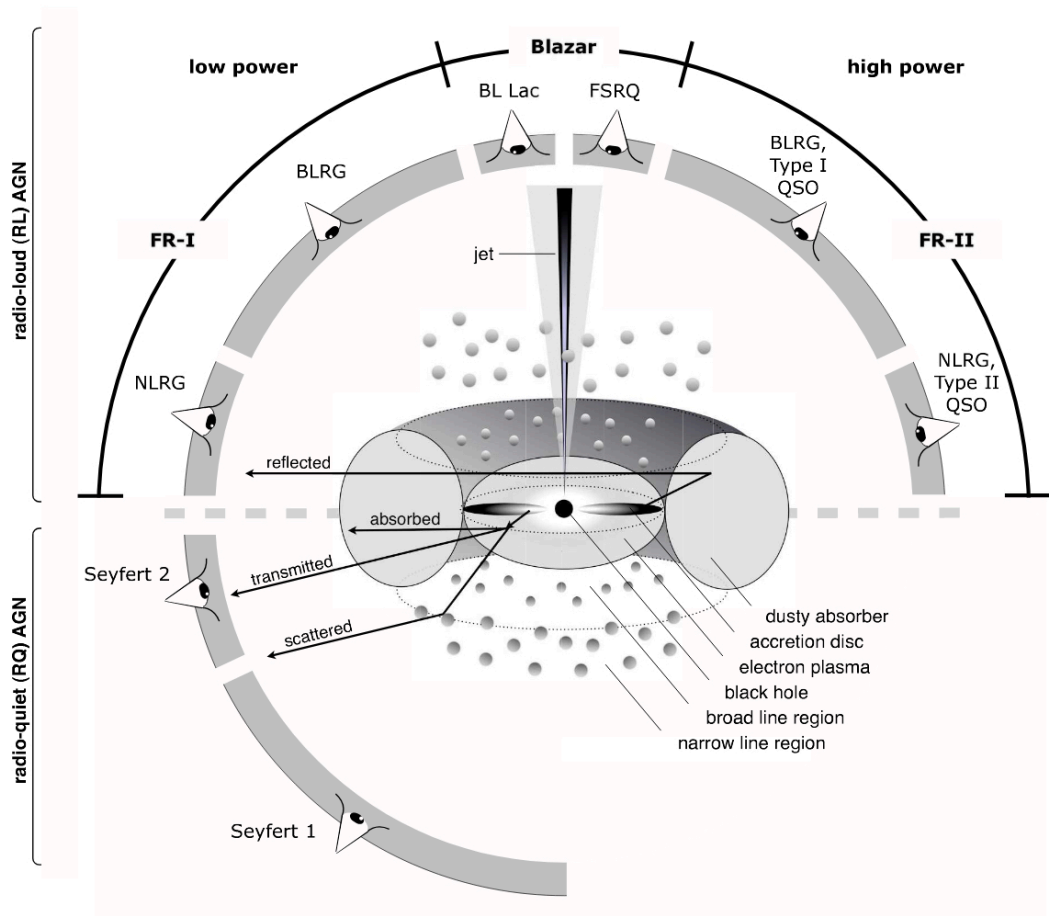


Figure 1.1 Schematic diagram from Beckmann & Shrader (2012), showing how the unified model of AGN can be interpreted as many different AGN types, dependent on viewing angle.

types of AGN as a consequence of the viewing angle, resulting in different properties being observed. This is illustrated in Figure 1.1, which shows an example of the unified model.

The main components of the unified model are as follows:

- An accretion disk, surrounding the SMBH.
- The broad-line region (BLR). This region appears very close to the SMBH, up to radii of 1 pc. The densities in the BLR are very high, surpassing $n_e = 10^9 \text{ cm}^{-3}$ (Peterson 2006). The velocities of the gas clouds in the BLR are extremely high (1000 - 20,000 kms^{-1} ; e.g. Netzer 2015), which gives rise to the extreme Doppler broadening of the emission lines. The high densities in the BLR suppress the emission of forbidden lines (or ‘collisionally-excited’ lines) through collisional de-excitation (e.g. Osterbrock & Ferland 2006).
- The narrow-line region (NLR). This region contains lower-velocity gas clouds, and extends from the end of the BLR up to kiloparsecs from the nucleus. In the event that the NLR extent is large, it will appear as ‘ionisation cones’ extending from the galaxy (e.g. Storchi Bergmann 2015). The density in the NLR is far less than the BLR, with densities typically on the order of $10^3 < n_e < 10^4 \text{ cm}^{-3}$, but can be as high as 10^6 cm^{-3} (e.g. Netzer 1990; Peterson 2006). The lack of a broad component to

the emission lines implies a much lower velocity, typically $\lesssim 500 \text{ km s}^{-1}$ (e.g. [Peterson 2006](#)).

- A dusty torus surrounding the nucleus. The torus provides a link between Seyfert 1 (Sy 1) and Seyfert 2 (Sy 2) galaxies. The two types of Seyfert galaxies are defined by their spectra. Sy 1 galaxies show emission lines with both broad and narrow components. The broad and narrow components are from the BLR and NLR respectively. Sy 2 galaxies only produce emission lines with a narrow component, with no BLR evident. However, spectropolarimetry techniques have shown polarised spectra from Sy 2 galaxies which display broad emission lines (e.g. [Miller & Goodrich 1990](#)). The leading theory following this discovery is that Sy 2 galaxies have a BLR which is obscured from view by the dusty torus, thus combining Sy 1 and Sy 2 galaxies into a single model.

H II Regions

A star cluster is formed in a coalescing giant molecular cloud. The gas clouds tend to be composed of molecular hydrogen – the most abundant element in the universe by far. If the resulting stellar cluster contains stars that are both sufficiently large and hot (in this case, referring to spectral class O and B stars), they will produce enough extreme-ultraviolet (EUV) radiation to firstly dissociate the molecular hydrogen bonds, and then ionise the surrounding atomic hydrogen gas. The consequence of this is what is known as an ‘H II region’ (where the Roman numeral II denotes a singly-ionised species, i.e. H^+).

H II regions produce some of the most stunning pictures in astronomy, and are not to be confused with planetary nebulae (which are the product of stellar death, rather than birth). One such example of an H II region is the Horsehead Nebula in the constellation of Orion, seen in [Figure 1.2](#).

The ionising source within the H II region typically produces photons with energies more than sufficient to ionise hydrogen. Hence, some of the remaining photon energy is distributed amongst the surrounding gas as heat. The heating of the H II region creates a large pressure difference compared to the gas outside the region, and thus the H II region begins to expand outward into the surrounding molecular gas cloud. The edge of the H II region is known as the ‘ionisation front’ ([Anderson et al. 2009](#)).

With an abundance of (predominantly) hydrogen ions and electrons in the H II region plasma, it is inevitable that recombination between an electron and a positively-charged ion will occur. However, it is important to note that the recombined electron may not necessarily enter the ground state of the newly-formed hydrogen atom; rather, the hydrogen atom may be formed in an excited state. If so, the hydrogen atom may de-excite and emit a photon with energy equal to the energy gap between the two transitioning levels. If the photon is the result of de-excitation from the $n = 2$ to the $n = 1$ state (the ground state), this photon may be absorbed upon interaction with another neutral hydrogen atom in the ground state, either within the H II region or in the photodissociation region (PDR) outside the H II region ([Anderson et al. 2009](#)). Thus, it is difficult for photons of this energy and wavelength (10.2 eV, $\lambda = 1215 \text{ \AA}$, also known as Lyman-alpha; $\text{Ly-}\alpha$) to escape from the nebula. However, since most neutral hydrogen is found in the ground state, photons



Figure 1.2 The Horsehead Nebula, an H II region in the Orion Molecular Cloud Complex, in the constellation of Orion. Image taken from Astronomy Picture of the Day (APOD).

resulting from transitions between the $n = 3$ or higher levels to $n = 2$ more easily escape the nebula. These photons are referred to as the ‘Balmer series’ of hydrogen (Balmer 1885). The spectral lines in the Balmer series are given names depending on in which energy level the electron began before transitioning to the $n = 2$ level. The photon resulting from the $n = 3$ to $n = 2$ level is referred to as a ‘hydrogen-alpha’ photon, or simply $H\alpha$, and is the most abundant emission line in the Balmer series. The $n = 4$ to $n = 2$ transition produces an $H\beta$ photon, and so on. The Balmer series dominates the spectrum from an H II region, and hence emission lines such as $H\alpha$ and $H\beta$ are used as indicators of star formation.

Interstellar Shocks

When a fluid is compressed, it experiences changes in its properties. The density, pressure, and temperature all increase as the volume that the fluid occupies reduces. If the speed of compression is sufficiently slow, the changes in the different properties of the fluid will be

continuous and smooth. However, if the compression occurs too quickly, the fluid is forced to move faster than the speed at which it can compress (the sound speed in the medium). In such an event, the changes in the fluid's variables become instantaneous at the boundary of compression, resulting in a discontinuity in the fluid flow. Such a propagating disturbance is called a shock wave.

Shock waves occur in galaxies, through multiple mechanisms. Such mechanisms include supernova explosions, stellar winds, and outflows from either the protostellar disks of low-mass stars, or AGN (Machida 2017; Dopita & Sutherland 2003). In each listed case, the shock progenitor is capable of providing enough energy to forcefully compress interstellar gas. Two main types of shocks exist:

- shocks in which some or all of the flow variables change more continuously as the shock propagates. Such shocks are called continuous shocks, or *C-shocks* to emphasise their continuity, rather than discontinuity. For such a phenomenon to occur, the velocity required is relatively low, roughly 50 kms^{-1} and less.
- shocks which behave more in the manner previously explained, where a discontinuous boundary is formed in the fluid. Such shocks are referred to as jump shocks, or *J-shocks*, in reference to the instantaneous 'jump' experienced by the fluid variables at the shock boundary. The velocity required for this discontinuity to occur is typically $\sim 100 - 200 \text{ kms}^{-1}$ and greater (Dopita & Sutherland 2003). This thesis is mainly concerned with J-shocks, rather than C-shocks.

In the case of J-shocks, the shock is comprised of potentially six main zones:

- **Equipartition zone:** this zone immediately follows the shock front. The matter in the shocked plasma begins to relax towards equipartition of energy. A unique postshock temperature for all elements in the plasma can now be defined. Relative to the timescales of other processes relevant to the shock or plasma, the timescale required for equipartition of energy is usually very short.
- **Ionisation zone:** Due to the large increase in temperature following the shock, the ionisation state of the plasma rapidly increases. Provided the velocity of the shock is high enough (\gtrsim a few hundred kms^{-1}), the plasma will reach collisional ionisation equilibrium. If not, energy losses from radiative de-excitation will occur.
- **Cooling zone:** Beyond the ionisation zone, in what is known as the cooling zone, the plasma begins to cool isobarically. The temperature decreases, corresponding to an increase in density. Much of the cooling occurs through the release of hydrogen-ionising EUV photons. If the temperature of the shock is high enough, thermal X-rays may also be produced. The cooling zone is what gives rise to the notion of a *photoionised shock precursor*. Half of the EUV photons emitted in the cooling zone will travel upstream and beyond the shock front, thus ionising the preshock gas.
- **Photoionisation zone:** Once the temperature of the postshock gas decreases beyond $\sim 10^4 \text{K}$, the hydrogen atoms begin to absorb the EUV photons emitted from the hotter gas in the cooling zone. If the shock velocity is sufficiently high ($\gtrsim 200 \text{ kms}^{-1}$), a photoionisation zone will develop, where the gas is in photoionisation equilibrium.

- **Recombination zone:** Once the EUV photons are lost from the system, recombination begins, further cooling the plasma through the emission of recombination photons.
- **Molecular formation zone:** Beyond the recombination zone, the temperature decreases to roughly 3000 K and below. Provided the plasma is dense enough, these conditions favour the formation of molecules from the atoms in the gas (Dopita & Sutherland 2003).

Additional Sources of Ionisation

As mentioned previously, the ionising sources of AGN, H II regions, and interstellar shocks, are the primary focus of this thesis. However, it should be noted that other sources of ionisation and excitation of the ISM do exist, and in some cases can produce spectra similar to the above three.

One such source of ionisation is post-AGB stars. Similar to the previous case of new stellar populations in an H II region, aging stars have also been shown to adequately ionise the surrounding ISM. Studies such as those performed by Binette et al. (1994), Stasińska et al. (2008), and Cid Fernandes et al. (2010) have shown that the old stellar populations in galaxies which are no longer forming new stars (sometimes referred to as ‘retired galaxies’; e.g. Stasińska et al. 2008) can provide an adequate explanation for the amount of Lyman-continuum photons observed from these galaxies. In fact, Stasińska et al. (2008) and Cid Fernandes et al. (2010) show that the emission from retired galaxies can mimic closely the emission from an AGN, thus leading to possible confusion. In a similar way, diffuse ionised gas (DIG) can also produce a spectrum with emission line fluxes similar to that from AGN or shocks. DIG is described more in Section 2.7.2.

1.2. Optical Spectroscopy and Integral Field Units

Much of the science in astrophysics is performed by first obtaining the spectrum of an object. A spectrum can lead to identifying the composition of a star or gas cloud, calculate the velocity of a celestial object, or identify the source of ionisation within a region, among other examples. In this thesis, spectroscopy is a tool used to identify the ionising source within a region of a galaxy.

Example galaxy spectra are shown in Figure 1 from Ho (2008), shown here in Figure 1.3. The three types of spectra displayed in Figure 1.3 are from a Seyfert 2 galaxy, a LINER galaxy, and a star-forming galaxy, whose spectrum is primarily from H II regions.

1.2.1. Integral Field Spectroscopy

Traditional long-slit spectroscopy involves placing a single slit aperture across a galaxy. What results is a single spectrum from the galaxy, with limited information about where certain emission lines arise from within the field-of-view of the aperture. Integral field spectroscopy (IFS) revolutionises this method by providing a spectrum of an object which is spatially resolved. Rather than a single slit placed across the galaxy, the aperture is

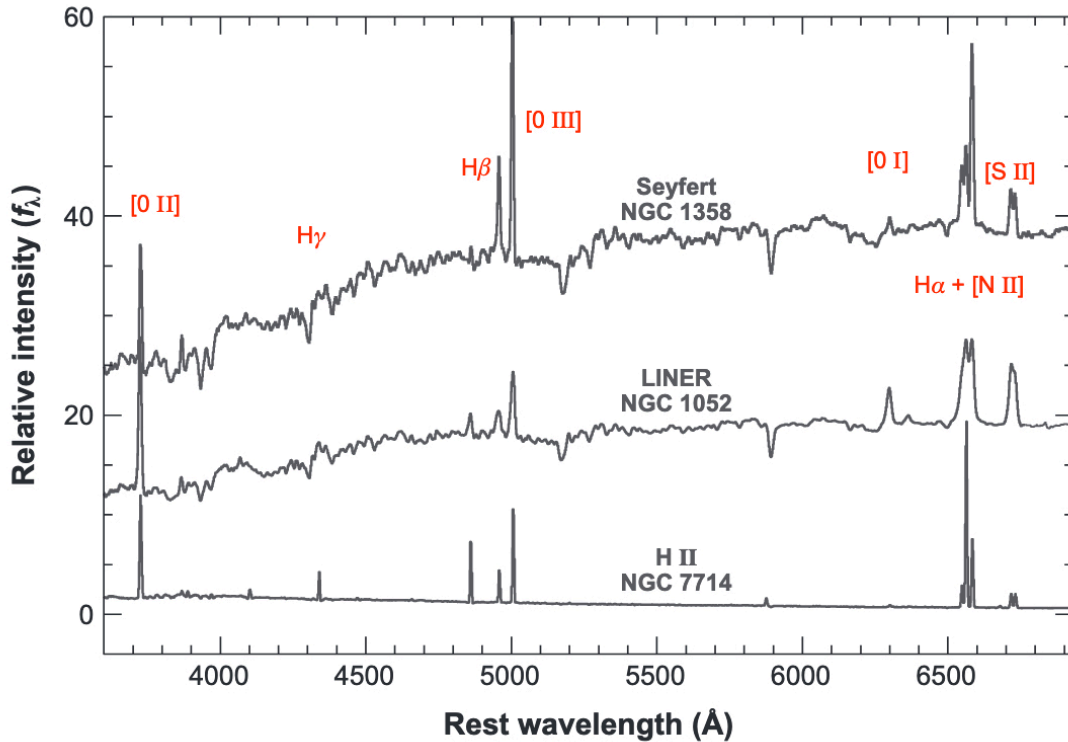


Figure 1.3 Figure 1 from Ho (2008), showing the spectra of several different galaxy types. Certain strong emission lines are labelled.

divided into an array of fibres which each capture a spectrum of their own. An example of imaging a galaxy using an integral field unit (IFU) is shown in Figure 1.4. The result of IFS is that different processes, identified through differences in their spectra, can be observed in various regions of a galaxy. The product of IFS is called a ‘datacube’, due to the three dimensions it possesses: two spatial dimensions, and one wavelength dimension. An illustration of the dimensions in a datacube is provided in Figure 1.5. The pixels in the image of an IFS datacube are known as ‘spaxels’ (spatial pixels).

1.2.2. Emission-Line Diagnostics

The sources of star formation, shocks, and AGN provide different spectral signatures, allowing the separate identification of each. As mentioned in Section 1.1.1, hydrogen recombination lines, such as $H\alpha$, $H\beta$, $H\gamma$ etc. are indicators of recent star formation. A large flux of ‘forbidden’ lines such as $[O\ III]\lambda 5007$ or $[N\ II]\lambda 6584$ hint at a much harder ionising source than star formation. Forbidden emission lines are named as such because their electron transitions are not allowed by classical selection rules. They are denoted with square brackets around the ion from which the emission line arises – the above examples of $[O\ III]\lambda 5007$ and $[N\ II]\lambda 6584$ convey the emission lines are from O^{++} and N^+ ions respectively, with wavelengths of 5007 and 6584 angstrom (\AA). Forbidden lines are also referred to as ‘collisionally-excited’ lines, since the electrons involved in these transitions are excited by collisions.

Collisionally-excited lines such as $[N\ II]\lambda 6584$ and $[O\ III]\lambda 5007$ are useful indicators of phenomena such as shocks and AGN. The ionisation potentials of the two ions, amongst

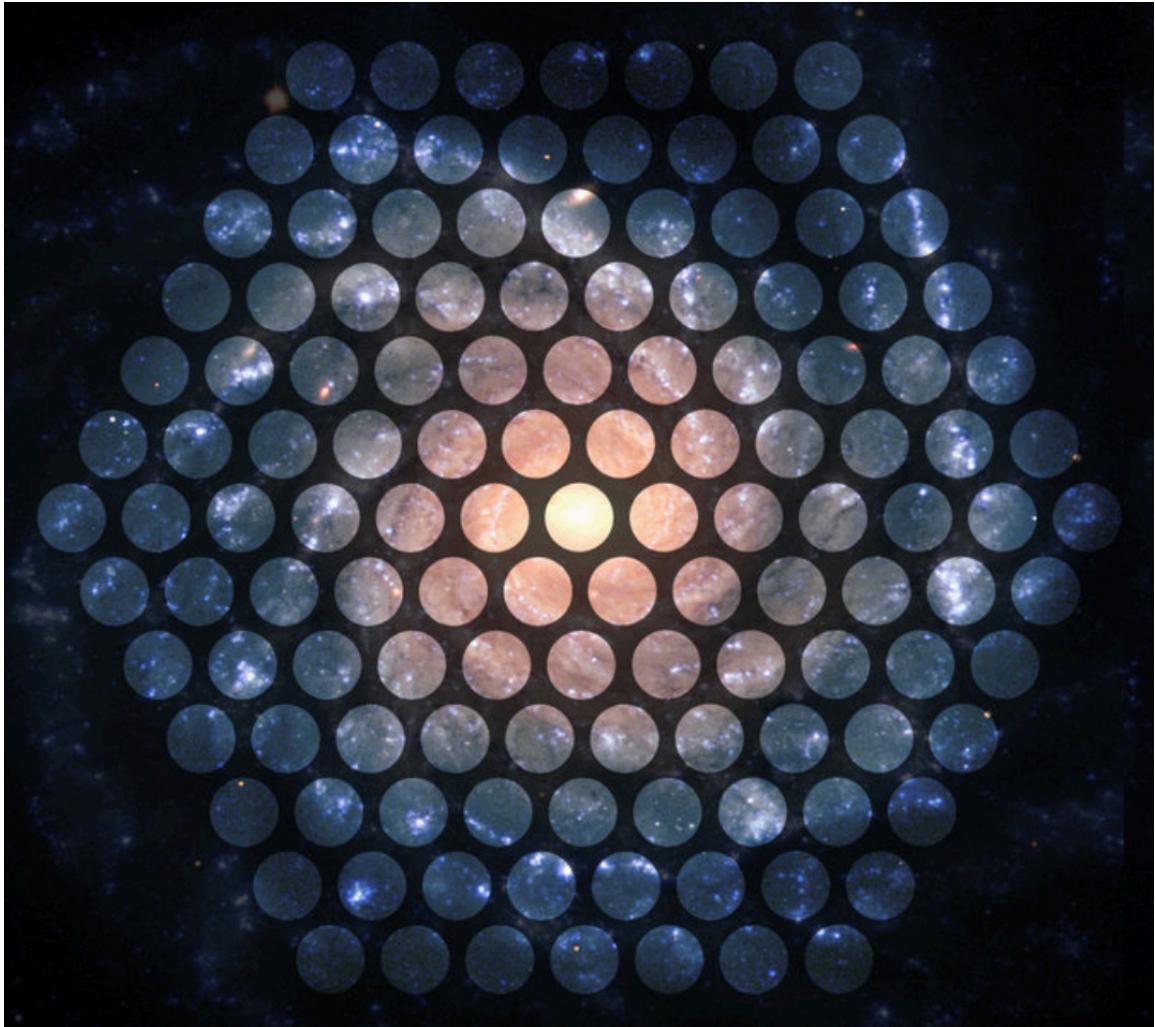


Figure 1.4 A spiral galaxy with an integral field unit from the MaNGA survey (Bundy et al. 2015) superimposed. Each circle represents a single fibre on the IFU.

others, are much higher than that for hydrogen (e.g. Dopita & Sutherland 2003), and hence a high flux of collisionally-excited lines requires a much harder radiation field. Shocks and AGN are capable of ionising such ions, as the extreme ultraviolet (EUV)/X-ray radiation field produced by the accretion disk of an AGN, or from the cooling zone of an interstellar shock, is much harder than the radiation field produced from star formation (e.g. Groves et al. 2004; Kewley et al. 2006, 2013a).

All of this information can be used when studying the spectrum of a galaxy, to determine the dominant source of ionisation and excitation. A common emission-line diagnostic diagram used to separate star formation and additional hard components is the $[\text{O III}]/\text{H}\beta$ vs $[\text{N II}]/\text{H}\alpha$ diagram from Baldwin et al. (1981) (commonly referred to as the ‘BPT diagram’). Further diagrams used to aid in this separation include the $[\text{O III}]/\text{H}\beta$ vs $[\text{S II}]\lambda\lambda 6716, 31/\text{H}\alpha$ and $[\text{O III}]/\text{H}\beta$ vs $[\text{O I}]\lambda 6300/\text{H}\alpha$ diagrams, introduced by Veilleux & Osterbrock (1987). Examples of these three diagnostic diagrams are shown in Figure 1 of Kewley et al. (2006), shown here in our Figure 1.6. The line ratios chosen in any of the diagnostic diagrams mentioned help separate star formation from other sources of ionisation: emission from star formation will contain high fluxes of $\text{H}\alpha$ and $\text{H}\beta$, meanwhile sources such as AGN and shocks will increase the line ratios with higher fluxes of collisionally-excited lines. Regions

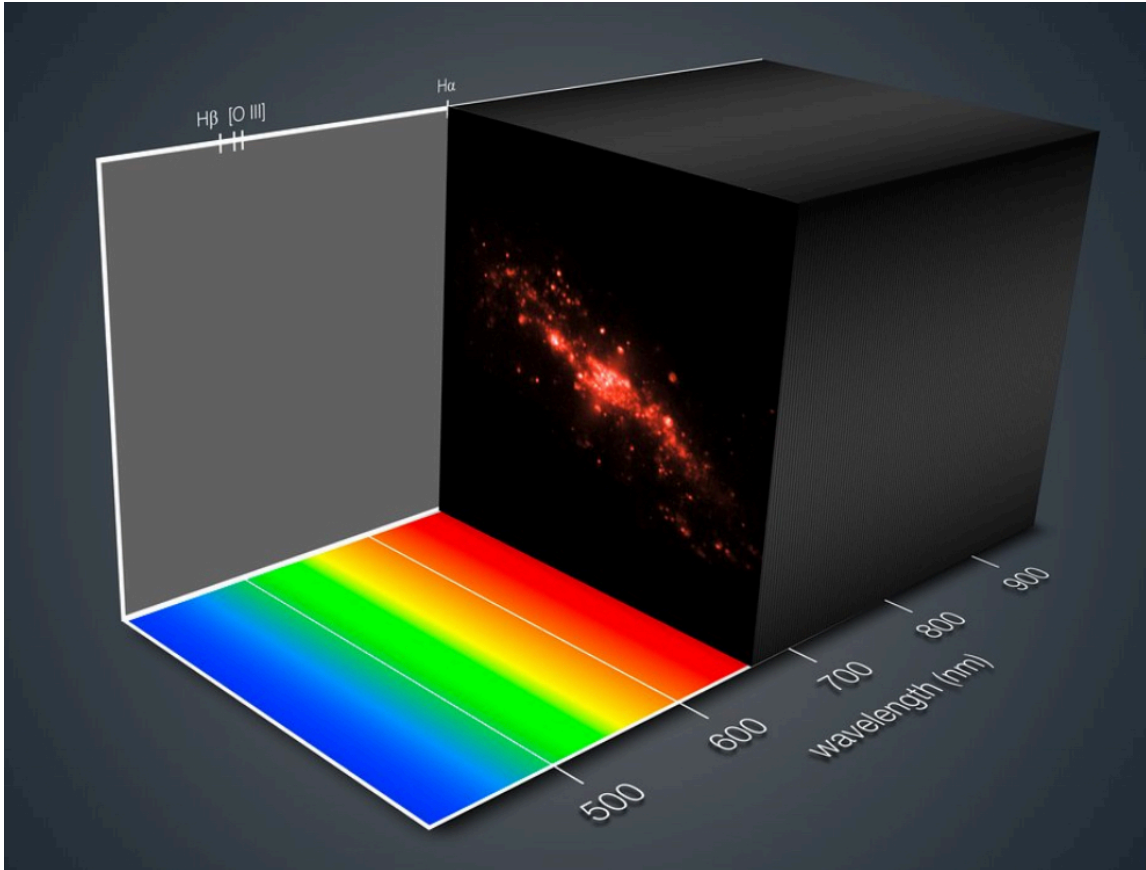


Figure 1.5 Illustration of a datacube, showing the two spatial dimensions providing the image, and a third wavelength dimension. Credit: ESO/MUSE consortium/R. Bacon/L. Calçada. <https://www.eso.org/public/images/eso1407a/>.

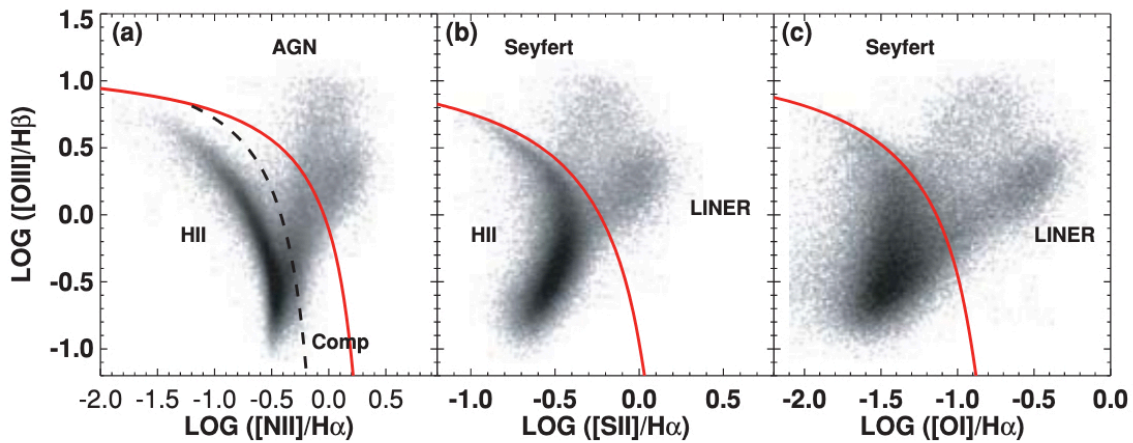


Figure 1.6 Emission-line diagnostics of Baldwin et al. (1981) and Veilleux & Osterbrock (1987), taken from Kewley et al. (2006). Data points are a subset of the Sloan Digital Sky Survey (SDSS) Data Release 4 (Adelman-McCarthy et al. 2006, see Kewley et al. 2006 for full details).

of the diagnostic diagrams where various sources dominate are labelled in the panels of Figure 1.6. The emission lines used in the ratios contain lines which are close in wavelength. Such a choice reduces the variation in the ratios from flux calibration issues, and from the effect of interstellar reddening.

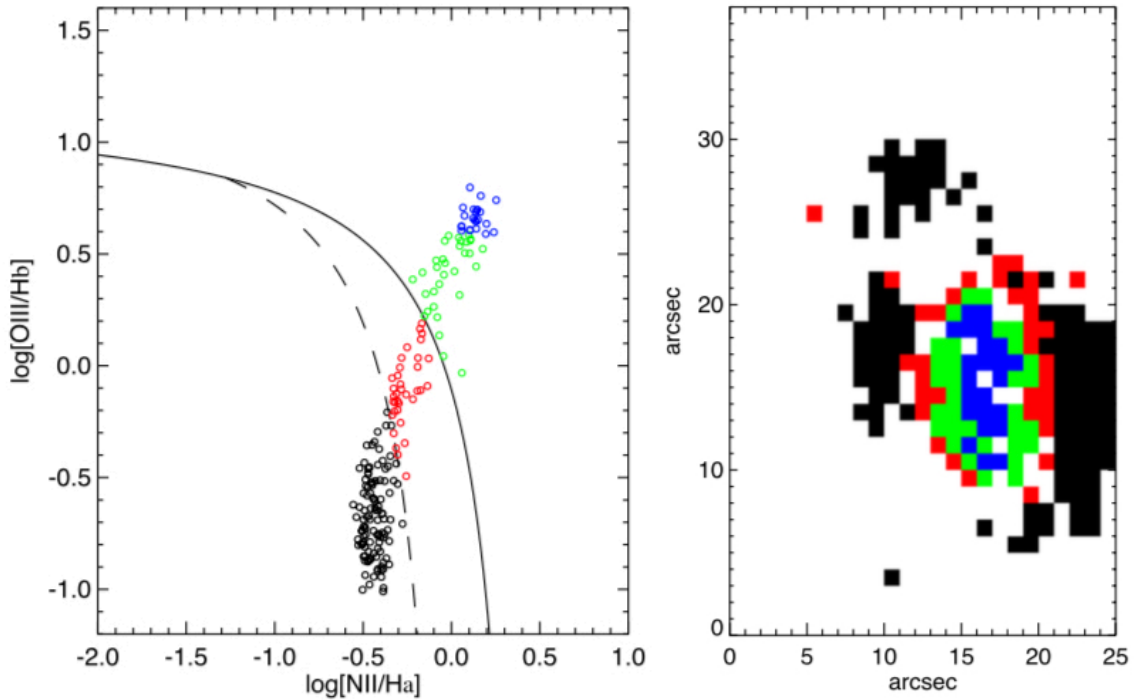


Figure 1.7 BPT diagram and corresponding map of NGC 7130, from [Davies et al. \(2014a\)](#). The colour-coding between the two panels is identical. Spaxels found towards the edge of the galaxy are shown with low $[\text{O III}]/\text{H}\beta$ and $[\text{N II}]/\text{H}\alpha$ ratios, and spaxels found towards the centre have high emission-line ratios.

When combined with emission-line diagnostic diagrams, integral field spectroscopy becomes a powerful tool. The spatially-resolved spectrum, combined with a method to aid in the separation of ionising sources, allows the separation to be studied visually. Such an example is shown in [Figure 1.7](#), which shows two figures from [Davies et al. \(2014a\)](#) (the left and right panels are [Figures 4a](#) and [5b](#) from [Davies et al. 2014a](#), respectively).

1.3. Photoionisation Modelling

A photoionisation model computes the spectrum emitted by an astrophysical gas cloud, as a result of ionisation and excitation from an external radiation source. Examples of ionising sources which produce the radiation field in photoionisation models include stellar clusters (forming an H II region; e.g. [Kewley et al. 2001](#); [Nicholls et al. 2014](#)), the NLR of an AGN (e.g. [Groves et al. 2004](#); [Thomas et al. 2016](#)), and astrophysical shocks (e.g. [Dopita & Sutherland 1995](#); [Allen et al. 2008](#)). Importantly, photoionisation models allow us to study the effect of incident radiation on matter in the ISM, to better understand how galaxies form and evolve in the big picture.

Fundamentally, regardless of the ionising radiation source, the principles of each photoionisation model remain the same. Incident photons are emitted from the source, and interact with matter in the surrounding nebula. These resultant interactions can be in the form of many different atomic processes. Such processes, including photoionisation, radiative transitions, collisional excitation, radiative recombination, two-photon emission, and charge exchange, amongst many others, need to be well-understood and accounted for in the photoionisation model in the form of equations and calculations.

The calculation of the model progresses incrementally, with the physical properties of the nebula (i.e. temperature, density, ionisation state and abundance of each element and ion) calculated at each step. Such a calculation is typically simulated as one-dimensional, however certain approaches to the input allow for geometric effects. For example, the radiation may be diluted with distance from the ionising source, simulating the illumination of a sphere. The completed model provides various results, such as detailed and accurate measurements for the fluxes of emission lines, chemical abundances, and the temperature and density structure throughout the nebula.

A photoionisation model is mainly influenced by the following parameters:

- Elemental abundances. Increased abundances of large atoms can affect the state of the plasma. Ionisation of atoms with more electrons provides more free electrons to the nebula, influencing the rate of radiative recombination. Higher abundances of metals (defined in astronomy as any element heavier than helium) also leads to an increased rate of cooling through radiative transitions.
- Gas pressure, P . Increased pressure in the nebula directly heightens the rate of collisions, leading to a larger rate of collisional excitation. Such an increase will provide a larger flux of collisionally-excited emission lines. Conversely, if the pressure is high enough such that the density is also sufficiently high, the rate of collisional de-excitation will also increase. Hence, the flux of collisionally-excited emission lines may be suppressed. The pressure, temperature, and density of the nebula are all closely related through the ideal gas law $P = nkT$, where P is the pressure, n is the number density of particles, T is the temperature, and k is Boltzmann's constant.
- Ionisation parameter, q . The ionisation parameter measures the ratio between the ionising photon flux and the number density in the plasma. A higher flux of ionising photons, and hence a higher value of q , will increase the overall ionisation present in the nebula. Alternatively, the ionisation parameter may be written as a dimensionless parameter, $U = q/c$, where c is the speed of light.
- The input ionising spectrum. As previously mentioned, this can be assumed to originate from a myriad of sources, such as a stellar cluster, fast shocks, or the NLR of an AGN. In each case, the input spectrum and the resultant model will be unique. Many assumptions and parameters themselves are also included in the production of the input spectrum. As the energy source for the model, this parameter is by far the most significant.

1.4. Thesis Overview

This thesis combines theory and observations to better constrain and understand the physical phenomena surrounding star formation, AGN, and shocks. The thesis climaxes with the development of a new framework, intended to further help the understanding of the mixing between all three aforementioned processes. The work completed during the candidature is explained in four chapters, each in the form of a journal article:

- Chapter 2 expands on the theory behind photoionisation modelling, specifically H II region modelling. Many different models and values exist for the input ionising spectrum and nebular parameters. Chapter 2 explores the systematic differences and uncertainties between these various models.
- Chapter 3 advances the previous work on star formation-AGN mixing using the BPT diagram. Photoionisation models are included to calculate the star formation and AGN fractions theoretically, rather than empirically.
- Chapter 4 begins to expand on the calculation of star formation-AGN mixing by considering the contribution from a third ionising source: shocks. With the BPT diagram insufficient for this separation of three mixing sources, Chapter 4 demonstrates a new, three-dimensional diagnostic diagram.
- Chapter 5 uses the three-dimensional diagram from Chapter 4 to calculate the relative contribution from star formation, shocks, and AGN activity in IFU data. Many aspects from the star formation-AGN mixing method presented in Chapter 2 are retained but expanded upon in Chapter 5, such as the use of photoionisation models.
- Chapter 6 discusses future directions of the work presented in this thesis.

An introduction and further background information to each topic is provided in the relevant chapters.

Statement of Contribution

This thesis is submitted as a Thesis by Compilation in accordance with https://policies.anu.edu.au/ppi/document/ANUP_003405

I declare that the research presented in this Thesis represents original work that I carried out during my candidature at the Australian National University, except for contributions to multi-author papers incorporated in the Thesis where my contributions are specified in this Statement of Contribution.

Title and authors: D'Agostino, J. J., Kewley, L. J., Groves, B., Byler, N., Sutherland, R. S., Nicholls, D., Leitherer, C., Stanway, E. R., 2019, "Comparison of Theoretical Starburst Photoionisation Models for Optical Diagnostics", ApJ, 878, 2

Current status of paper: Not Yet Submitted/Submitted/Under Revision/Accepted/Published

Contribution to paper: All but the CLOUDY photoionisation model shown in Figure 2.26

Senior author or collaborating authors endorsement:  BRENT GROVES

Joshua D'Agostino
Candidate - Print Name


Signature

11/7/2019
Date

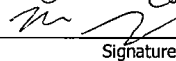
Endorsed

LISA KEWLEY
Chair of Supervisory Panel - Print Name


Signature

9/7/2019
Date

Mark Krumholz
Delegated Authority - Print Name


Signature

11/7/2019
Date

CHAPTER 2

H II Region Modelling

The pessimist sees difficulty in every opportunity. The optimist sees opportunity in every difficulty.

– Winston Churchill

The contents of this chapter have previously been published as ‘Comparison of Theoretical Starburst Photoionisation Models for Optical Diagnostics’, D’Agostino, J. J., Kewley, L. J., Groves, B., Byler, N., Sutherland, R. S., Nicholls, D., Leitherer, C., Stanway, E. R., 2019, ApJ, 878, 2. The abstract is as follows:

We study and compare different examples of stellar evolutionary synthesis input parameters used to produce photoionisation model grids using the MAPPINGS V modelling code. The aim of this study is to (a) explore the systematic effects of various stellar evolutionary synthesis model parameters on the interpretation of emission lines in optical strong-line diagnostic diagrams, (b) characterise the combination of parameters able to reproduce the spread of local galaxies located in the star-forming region in the Sloan Digital Sky Survey, and (c) investigate the emission from extremely metal-poor galaxies using photoionisation models. We explore and compare the stellar input ionising spectrum (stellar population synthesis code [Starburst99, SLUG, BPASS], stellar evolutionary tracks, stellar atmospheres, star-formation history, sampling of the initial mass function) as well as parameters intrinsic to the H II region (metallicity, ionisation parameter, pressure, H II region boundedness). We also perform a comparison of the photoionisation codes MAPPINGS and CLOUDY. On the variations in the ionising spectrum model parameters, we find that the differences in strong emission-line ratios between varying models for a given input model parameter are small, on average ~ 0.1 dex. An average difference of ~ 0.1 dex in emission-line ratio is also found between models produced with MAPPINGS and CLOUDY. Large differences between the emission-line ratios are found when comparing intrinsic H II region parameters. We find that low-metallicity galaxies are better explained

by a density-bounded H II region and higher pressures better encompass the spread of galaxies at high redshift.

The CLOUDY model grid used in Figure 2.26 was produced by co-author Nell Byler.

2.1. Introduction

The ratios of emission lines have been used to separate extragalactic objects according to their dominant power source (referring to ionisation and excitation) since 1981, after Baldwin et al. (1981) pioneered the technique. Baldwin et al. (1981) used the combination of two ratios created from strong optical emission lines, including the classical $[\text{N II}]\lambda 6584/\text{H}\alpha$ versus $[\text{O III}]\lambda 5007/\text{H}\beta$ or ‘BPT’ diagram, to demonstrate that the ionisation mechanism of emission-line regions could be determined.

Veilleux & Osterbrock (1987) revised and formulated this method, describing how diagnostic line ratios should be selected, including proximity in wavelength to minimise reddening corrections while maximising diagnostic power. They found that the BPT diagram, along with the $[\text{O III}]\lambda 5007/\text{H}\beta$ versus $[\text{S II}]\lambda(6716+6731)/\text{H}\alpha$ and $[\text{O III}]/\text{H}\beta$ versus $[\text{O I}]\lambda 6300/\text{H}\alpha$ diagrams could clearly distinguish between galaxies dominated by star-formation from galaxies containing an active galactic nucleus (AGN).

The theory underlining this clear separation was demonstrated by Kewley et al. (2001) using modelled stellar ionising spectra and photoionisation models. They found that the emission from star-forming galaxies (i.e. H II regions) could populate only a certain region of the diagnostic diagrams, even after accounting for variation in the gas-phase abundances and gas ionisation state. Only a hard ionising radiation field such as from the accretion disk surrounding the supermassive black hole could drive emission lines to the region in the diagnostic diagram populated by AGN. Using these models they parameterised an extreme starburst line, to be used in classifying galaxies into starburst or AGN type. They also suggested that the distance of a galaxy from this line could be used to determine the fractional contribution of an AGN to a galaxy spectrum.

The large number of galaxy spectra from the Sloan Digital Sky Survey (SDSS; York et al. 2000; Stoughton et al. 2002) revealed fully where galaxies could lie in the $[\text{O III}]/\text{H}\beta$ vs $[\text{N II}]/\text{H}\alpha$ and $[\text{O III}]/\text{H}\beta$ vs $[\text{S II}]/\text{H}\alpha$ diagrams. Measuring the strong emission lines in a sample of roughly 122,000 galaxies in a redshift range of $0.02 < z < 0.3$, Kauffmann et al. (2003) found that galaxies showed a continuous distribution from being star-formation dominated to being AGN dominated (see Fig. 2.1). Based on this distribution, they created an empirical diagnostic line for separating AGN galaxies from star-forming galaxies on the BPT diagram, based on the theoretical shape of the Kewley et al. (2001) line, with this diagnostic developed further by Kewley et al. (2006).

While both the Kewley et al. (2001) and Kauffmann et al. (2003) lines signify the upper limit of star formation from a theoretical and empirical point of view, respectively, the line described by Kewley et al. (2001) predicts much larger BPT emission-line ratios for maximum star formation than the line by Kauffmann et al. (2003). This difference is the result of using the PEGASE stellar population synthesis (SPS) code (Fioc & Rocca-Volmerange

1997), which uses the Clegg & Middlemass (1987) planetary nebula nuclei (PNN) atmosphere models to model Wolf-Rayet stars. These PNN atmospheres produce spectra that are harder in the 1-4 ryd range than spectra modelled using other W-R atmospheres explored by Kewley et al. (2001), and hence these models were used to classify the extreme theoretical starburst line. Furthermore, the lines of Kewley et al. (2001) and Kauffmann et al. (2003) are slightly different in their interpretations; the Kewley et al. (2001) line signifies the extreme upper limit above which star formation can no longer be considered the dominant power source within the galaxy. The Kauffmann et al. (2003) line, however, was derived as a pure star formation line, above which the contribution to the emission-line ratios from star formation is no longer 100%. The boundary of pure star-forming galaxies, which was reduced empirically by Kauffmann et al. (2003), was further refined through photoionisation modelling by Stasińska et al. (2006) and was shown to be similar to the Kauffmann et al. (2003) demarcation line.

Contemporary work considers the region of the BPT diagram found below the Kauffmann et al. (2003) line as the pure star-forming classification region and the region found above the Kewley et al. (2001) line as the pure AGN classification region. Even with this clear separation of ionisation mechanism, galaxies show a large spread on diagnostic emission-line diagrams such as the BPT. Within each classification region, such as the star-formation-dominated region, this spread is driven by the variation of the physical conditions within the emission-line regions, such as gas-phase metallicity, ionisation state, and the age of the stellar population. Galaxies, or integral field unit (IFU) spaxels, found between the two lines of Kewley et al. (2001) and Kauffmann et al. (2003) are considered to have multiple ionisation mechanisms (such as AGNs, shocks and/or star-formation) occurring within the same galaxy.

Photoionisation modelling can be used to determine the physical conditions within the galaxies based on their emission-line ratios, including the gas-phase metallicity, density, and ionisation parameter. Yet the interpretation of emission lines relies greatly on the photoionisation models used to provide the calibrations, as demonstrated by Kewley et al. (2001), Groves et al. (2004), Stasińska et al. (2006), and Levesque et al. (2010).

These photoionisation models are heavily dependent on the input ionising spectrum. Without independent confirmation, the wide range of possible ionising spectra leads to large systematic uncertainties on the derived parameters from emission-line galaxies using these models. In the case of star-forming galaxies, large differences in resulting emission lines are observed between models owing to different stellar atmospheres, different stellar evolutionary tracks, and differences in treating stellar winds, star formation histories (SFHs) and even binary star evolution (e.g. Kewley et al. 2001; Morisset et al. 2016; Stanway et al. 2016; Wofford et al. 2016). As such, differences between the resulting theoretical emission-line spectra are indications of the true systematic uncertainties in these models.

Furthermore, despite the ongoing work and development of these stellar population models and photoionisation grids, as of yet no model can explain the entire sequence of local star-forming galaxies in the SDSS galaxy survey, particularly in the low-metallicity regime. This problem has been further highlighted by recent observations of high-redshift ($z \approx 2 - 3$) galaxies (e.g. Kewley et al. 2013a,b; Steidel et al. 2014), which reveal that star-forming galaxies at these epochs appear offset to higher $[\text{O III}]/\text{H}\beta$ values for given $[\text{N II}]/\text{H}\alpha$ values

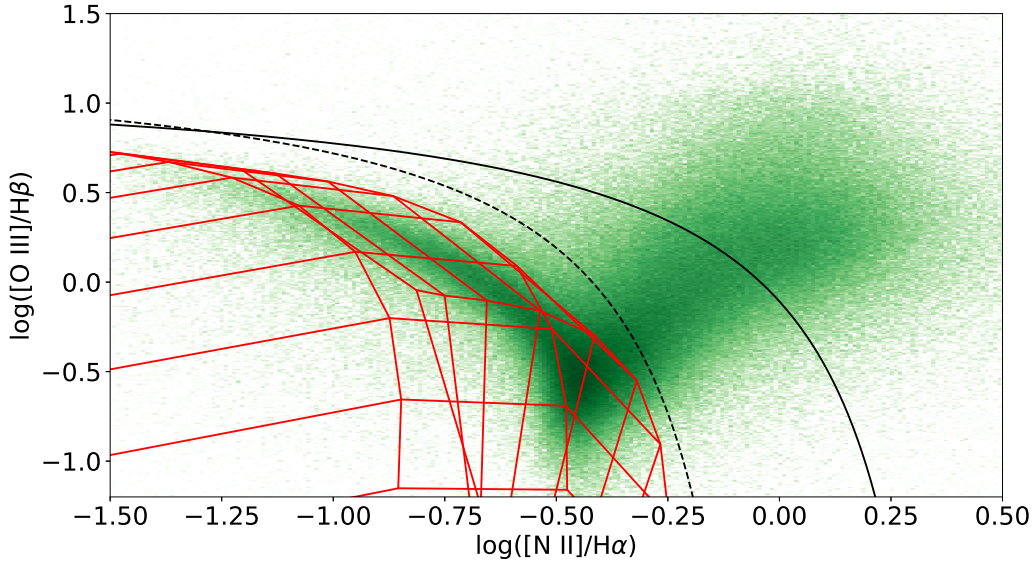


Figure 2.1 Example of a photoionisation grid used by many in the astrophysics community in recent years, overlaid on the distribution of galaxies from SDSS DR7 (Abazajian et al. 2009).

when compared to SDSS galaxies.

Our work is motivated by three main aims: (i) to explore how the emission-line ratios on the BPT diagram are affected by the differences in the parameters used and physics within the SPS models; (ii) to explain the offset of high-redshift galaxies from the local star-forming spread on the BPT diagram; and (iii) to explain the position of extremely metal-poor star-forming galaxies on the BPT diagram. In the coming years, telescopes such as the *James Webb Space Telescope* and *Wide Field Infrared Survey Telescope* will allow strong optical lines to be obtained for unprecedented numbers of galaxies at intermediate and high redshift. Understanding the effects of intrinsic interstellar medium (ISM) properties on emission lines is critical for the success of these future surveys. Furthermore, the growing wealth of data from recent IFU surveys such as SAMI (Bryant et al. 2015), MaNGA (Bundy et al. 2015), CALIFA (Sánchez et al. 2012a; Husemann et al. 2013a) and TYPHOON/PrISM (M. Seibert et al. in preparation) has made it increasingly necessary to perform an in-depth study into these photoionisation model grids and their systematics.

In this paper, we present a comparison of photoionisation model grids, extending the work of previous photoionisation model studies, such as those performed by Kewley et al. (2001) and Levesque et al. (2010). We reference several galaxy samples throughout this paper, and describe the samples in Section 3.2. We use the photoionisation modelling code MAPPINGS v and detail the updates made from the previous version, MAPPINGS IV, in Section 2.3. In Section 2.4, we introduce the various parameters associated with the input ionising radiation field that we explore, detailing differences amongst varying input models. Such parameters explored are the SPS code, stellar evolutionary tracks, stellar atmospheres, SFH, and stellar age, as well as the sampling of the initial mass function (IMF). In Section 2.5 we describe the photoionisation modelling input parameters used to produce the H II region; several of the parameters shown in Section 2.5 are also explored throughout the scope of this paper,

such as the H II region pressure and H II region boundedness. Section 2.6 showcases the systematic differences in each of the parameters explored, by firstly assessing the differences in the spectra in Section 2.6.1 before exploring differences in the resulting BPT diagrams in Section 2.6.2. All BPT diagrams include the Kewley et al. (2001) and Kauffmann et al. (2003) lines for reference. We address our aims and raise further points for discussion in Section 2.7 before providing our concluding statements in Section 2.8.

2.2. Sample Description

In this paper, we discuss and compare photoionisation models to several datasets. The first is SDSS Data Release 7 (DR7; Abazajian et al. 2009), featuring spectra from approximately 930,000 galaxies combined from the SDSS Legacy Survey (Abazajian et al. 2003), SEGUE (Yanny et al. 2009), and the SDSS-II SN survey (Frieman et al. 2008).

Second, we also consider a combined sample of metal-poor galaxies, constituting the Small Isolated Gas Rich Irregular Dwarf galaxy (SIGRID) sample from Nicholls et al. (2014), and low-metallicity subsets of SDSS, described in Izotov et al. (2006, 2012). The sample taken from Izotov et al. (2006) is truncated to only include galaxies with $Z < Z_{\odot}$ to compare with the models used in Nicholls et al. (2014). The galaxies in the SIGRID sample were selected for observation based on the criteria detailed in Nicholls et al. (2011). A further selection criterion was the detection of the [O III] λ 4363 line, making possible calculations of the electron temperature and the gas-phase oxygen abundance. A similar cut was made on the data in Izotov et al. (2006) and Izotov et al. (2012), specifically stating that the [O III] λ 4363 line should have a detection greater than 1σ and 2σ , respectively.

2.3. MAPPINGS V

In this work, we make use of the photoionisation modelling code MAPPINGS V. This version is a significant improvement on the previous version MAPPINGS IV. A summary of the previous version of MAPPINGS IV can be found in Nicholls et al. (2014) and references therein. Major changes from MAPPINGS IV to MAPPINGS V include updated atomic data, including version 8 of the CHIANTI database (Dere et al. 1997; Del Zanna et al. 2015), which gives atomic data for up to 80,000 spectral lines. Updated elemental depletion files are also included from Jenkins (2014). A much higher precision exponential integral function is included for calculation of the collisional ionisation rates, based on the functional form of Cody & Thacher (1968) and Cody & Thacher (1969), giving enhanced stability and accuracy (to at least 18 significant figures) during the modelling. Optical, near-UV and near-IR H I and He II wavelengths were reevaluated, although the wavelengths of hydrogen lines are largely similar. The new and former values of the optical, near UV, and near IR H I and He II lines agree to four significant figures, and in some cases five significant figures. Updates were also made to input spectral libraries such as the AGN atmosphere library and the planetary nebula stellar library.

Photoionisation model codes such as MAPPINGS (e.g. Sutherland & Dopita 1993) and CLOUDY (e.g. Ferland et al. 2013) require the input of nebula-specific parameters, as well

as an input ionising spectrum. In the following sections we detail the parameters involved in the MAPPINGS simulations by first describing the parameters used to produce the input stellar ionising spectrum, followed by other necessary parameters to produce the models. Unless otherwise stated, the individual parameters mentioned in each section are to be assumed for all models in this work.

2.4. Stellar Radiation Field

In this section, we compare various models that constitute the input ionising stellar radiation field. A summary of all the models used, along with references, can be found in Table 2.1.

2.4.1. SPS Codes

Single Stellar Populations

SPS codes compute the spectrum of a stellar population of given physical parameters such as SFH, age, and metallicity. These codes take theoretical stellar evolutionary tracks and populate these tracks with stars, distributed according to an IMF describing the number of stars per unit mass at the beginning of the formation of the stellar cluster, and assuming an age for the stars. The spectral output of the stellar population is determined through matching these stars with libraries of stellar atmosphere spectra. The final output is created by integrating simple stellar populations of given ages over the SFH of the stellar population – the rate at which stars have formed over time.

Starburst99 (SB99; [Leitherer et al. 1999](#); [Vázquez & Leitherer 2005](#); [Leitherer et al. 2014](#)) and Stochastically Lighting Up Galaxies (SLUG; [da Silva et al. 2012](#); [Krumholz et al. 2015](#)) are two SPS codes that are quite different in nature. Whilst both codes produce ionising spectra and photometry for star clusters and galaxies given parameters such as

Parameter	Models	Reference
Stellar population synthesis code	Starburst99 (SB99) Stochastically Lighting Up Galaxies (SLUG) Binary Population and Spectral Synthesis (BPASS)	Leitherer et al. (1999) da Silva et al. (2012) ; Krumholz et al. (2015) Eldridge et al. (2008) ; Eldridge & Stanway (2009, 2012) ; Stanway et al. (2016)
Stellar evolutionary tracks	Geneva HIGH Padova TP-AGB	Meynet et al. (1994) Girardi et al. (2000) ; Vassiliadis & Wood (1993)
Stellar atmospheres	Kurucz Hillier + Miller Pauldrach	Lejeune et al. (1997) Hillier & Miller (1998) Pauldrach et al. (2001)

Table 2.1 Various stellar radiation field models used throughout this paper, with references.

the IMF, SFH, cluster mass function (CMF), cluster lifetime function (CLF), and possibly extinction, SLUG differs from SB99 in that it carries out explicit Monte Carlo sampling from the probability distribution functions (pdf's) describing the stellar population (such as IMF) and thus returns the pdf of output spectra rather than just the average (see [da Silva et al. 2012](#), for a detailed explanation on the methodology and technique of SLUG).

A major difference between the two codes is the interpolation method used to create isochrones (single age sequences) from the stellar evolutionary tracks and to interpolate from the stellar atmosphere libraries onto the stars populating these isochrones. These interpolation methods can have a large impact on the final spectrum, especially in the presence of poor sampling of the evolutionary tracks (described in Section 2.6.1) or spectral libraries (described in Section 2.6.1). SB99 uses quadratic interpolation along the isochrones in the ‘isochrone synthesis’ technique, described in detail in [Charlot & Bruzual \(1991\)](#). SLUG uses the same isochrone synthesis technique but uses the ‘Akima spline’ ([Akima 1970](#)) in place of quadratic interpolation. The Akima spline is more robust to outliers in comparison to quadratic interpolation, thus ensuring that its isochrone interpolation is performed to a higher accuracy. Interpolation via the Akima spline requires five points, with the point of interest at the centre. In the absence of five points, SLUG reverts to linear interpolation. For comparison, SB99 only reverts to linear interpolation once only two points are available.

Binary Populations

We also explore the differences in output spectra between single stellar population models and the Binary Population and Spectral Synthesis code (BPASS; see [Eldridge et al. 2008](#); [Eldridge & Stanway 2009, 2012](#); [Stanway et al. 2016](#)). The findings of [Stanway et al. \(2016\)](#) when considering binary populations, amongst other findings, include a boosted (50-60%) ionising flux in stellar populations at low metallicities ($0.05Z_{\odot} \leq Z \leq 0.3Z_{\odot}$) and a more modest 10-20% increase in the flux at higher (near-solar) metallicities, compared to single-star stellar populations. [Eldridge & Stanway \(2009\)](#) show that binary populations tend to be bluer with fewer red supergiants than in single stellar populations, leading to a significantly smaller flux in the *I* band and subsequent longer wavelengths. [Eldridge & Stanway \(2009\)](#) also find W-R stars emerging over a wider range of ages, with populations of ages up to 10 Myr being found to host W-R stars.

BPASS models use a different set of model atmospheres for all stars other than OB stars than those used by SLUG and SB99, explained in Section 2.4.5. For stars with surface temperatures $< 25,000\text{K}$, BPASS uses the BaSeL V3.1 model atmosphere library ([Westera et al. 2002](#)). Stars with surface temperatures greater than 25,000K are treated as OB stars and are modelled with the high-resolution atmosphere libraries of [Smith et al. \(2002\)](#) (using the OB atmospheres of [Pauldrach et al. 2001](#)). The atmospheres of W-R stars (defined in BPASS as stars with a surface hydrogen mass fraction $X < 0.4$ and effective temperature $\log(T_{\text{eff}}/\text{K}) \geq 4.45$) are modelled using the Potsdam group’s theoretical atmospheres ([Hamann et al. 2006](#), see [Eldridge & Stanway 2009](#) for a detailed summary on the use of the Potsdam libraries for differing W-R types).

The stellar evolution models used by BPASS are those from the Cambridge STARS code ([Eggleton 1971](#); [Eldridge et al. 2008](#), and references therein). The STARS models include

not only a detailed set of single-star models, but also an extensive set of detailed binary star models. BPASS does not interpolate between the stellar tracks, as binary stellar evolution has more free parameters. Rather, each stellar model is weighted by a Salpeter IMF in order to calculate a stellar evolutionary track for stars of varying initial masses and binary parameters.

The various BPASS models available differ in the slope and endpoints of the IMF used to produce the spectral energy distribution. In order to accurately compare spectra of binaries produced using BPASS to single stellar models, we choose the BPASS model that resembles the IMF described in Section 2.4.3 as closely as possible. As a result, our BPASS model contains an IMF with power-law indices of $\alpha_1 = -1.30$ between masses of 0.1 and 0.5 M_{\odot} , and $\alpha_2 = -2.35$ between masses of 0.5 and 100 M_{\odot} . All instantaneous SFH BPASS models are for a $10^6 M_{\odot}$ cluster, and all continuous SFH BPASS models are for a cluster undergoing constant star formation at a rate of $1 M_{\odot} \text{yr}^{-1}$.

2.4.2. SFH and Age

We consider two simplistic treatments for the SFHs of our stellar populations: an instantaneous burst of star formation (i.e. a single aged stellar population), and a constant SFH. In both cases we assume that the stellar population is of a single metallicity. Both types of SFH are applicable in different situations. A constant SFH is thought to be a reasonable approximation when modelling the integrated spectra of galaxies, as new stellar populations emerge repeatedly. An instantaneous burst, on the other hand, is assumed when studying individual H II regions, where a single stellar population dominates the ionising spectrum. Cases where an instantaneous SFH may be applicable include galaxies whose star formation may be triggered by merger events, the sudden accretion of gas clouds within the IGM, or other situations where the star formation phase may be short-lived.

For the constant SFH models we adopt an age of 5 Myr (that is, a constant star formation of $1 M_{\odot} \text{yr}^{-1}$ occurring over the past 5 Myr) for both SB99 and SLUG (known as the ‘galaxy’ model in SLUG). As shown by Kewley et al. (2001), after 5 Myr, the spectrum of a constant SFH stellar population reaches equilibrium. However, when studying the effects of continuous SFH stellar cluster age on the emission-line ratios, we use cluster ages up to 10 Myr for reasons described in Section 2.6.2. For the instantaneous burst scenario we explore all ages up to 6 Myr, as $\sim 95\%$ of the total ionising radiation emitted by a stellar population over its lifetime has been emitted by this age (Dopita et al. 2006). By exploring the different ages, we demonstrate the impact of short-lived but active phases of a stellar population such as W-R stars on the stellar spectrum.

For our fiducial model we choose the constant SFH at 5 Myr following the work of Levesque et al. (2010). They report that a continuous SFH produces a better agreement with the emission-line ratios found in their galaxy sample, made up of local ($z < 0.1$) star-forming galaxies from a sample of SDSS described in Kewley et al. (2006), the Nearby Field Galaxy Survey (NFGS; Jansen 2000), a sample of blue compact galaxies from Kong & Cheng (2002) and Kong et al. (2002), and a sample of metal-poor galaxies described in Brown et al. (2008).

2.4.3. Initial Mass Function

We use the IMF of [Kroupa \(2002\)](#), particularly Equation (5). The IMF describes the number of stars present in the cluster at a given stellar mass. The [Kroupa \(2002\)](#) IMF is a broken power law, consisting of three different power-law segments. The segments start at $0.01M_{\odot}$, with further breakpoints at 0.08 and $0.5M_{\odot}$, and ending at $120M_{\odot}$. The power-law indices within each segment are $\alpha_1 = 0.3$, $\alpha_2 = 1.3$, and $\alpha_3 = 2.3$, respectively.

2.4.4. Stellar Tracks and Metallicities

Stellar evolutionary tracks follow a star of a given initial mass as it evolves during its lifetime from the time on the main sequence until its end point as a supernova or white dwarf. SPS codes use these tracks to interpolate onto an isochrone, representing the distribution of a population of stars of a single age and metallicity.

During this work, we use the Geneva group’s “High” (HIGH) mass-loss tracks. First published in [Meynet et al. \(1994\)](#), these tracks are intended to better reflect the mass-loss rates of low-luminosity W-R stars and blue-to-red supergiant ratios in both the Large and Small Magellanic Clouds ([Schaller et al. 1992](#); [Meynet 1993](#)) by including higher mass-loss rates than those found in the Geneva group’s “Standard” (STD) mass-loss evolutionary tracks. These high mass-loss rates are derived by doubling the mass-loss rates in the “standard” tracks for WNL and Population I stars (except W-R stars) found in [de Jager et al. \(1988\)](#), except for WNE W-R stars, as well as WC and WO W-R stars, which were left unchanged.

We compare the Geneva HIGH tracks with stellar evolutionary tracks from the Padova group. The Padova tracks we use during this paper contain thermally pulsing asymptotic giant branch (TP-AGB) stars and are described in [Girardi et al. \(2000\)](#) with an addition from [Vassiliadis & Wood \(1993\)](#). We make a distinction between the TP-AGB Padova tracks and the non-TP-AGB option described in [Bressan et al. \(1993\)](#), [Fagotto et al. \(1994a,b,c\)](#), and [Girardi et al. \(1996\)](#), yet we note that the AGB phase of stellar evolution begins at ~ 100 Myr ([Vázquez & Leitherer 2005](#)). Since the maximum age of our simulations in this work is 10 Myr, AGB stars are not present in the clusters generated. However, the TP-AGB Padova tracks are computed following major updates in the input physics from the non-AGB Padova tracks and so must be distinguished from one another. A summary of the differences in the input physics between the two sets of Padova tracks can be found in [Girardi et al. \(2000\)](#). On occasion, the TP-AGB Padova tracks may be referred to as simply the “Padova tracks,” and the Geneva HIGH tracks as simply the “Geneva tracks.” The input physics between the Geneva and Padova tracks are different; some differences include the chemical composition and abundances, reaction rates and neutrino losses, equation of state, convection processes, and chemical opacities. [Vázquez & Leitherer \(2005\)](#) provide an excellent and detailed comparison between the two sets of stellar evolutionary tracks.

The Geneva and Padova sets of tracks immediately differ on the values of metallicity used. Both sets of tracks use five metallicities, with three ($Z = 0.004$, $Z = 0.008$, $Z = 0.020$) being equal. They differ at both the low-metallicity end ($Z = 0.001$ for Geneva, $Z = 0.0004$ for Padova) and at the high-metallicity end ($Z = 0.040$ for Geneva, $Z = 0.050$ for Padova), with the Padova tracks ultimately encompassing a larger range of metallicity.

The reaction rates also differ between the two sets, with the Geneva models having been calculated using the reaction rates from [Caughlan et al. \(1985\)](#), whilst the Padova tracks utilised the rates calculated by [Caughlan & Fowler \(1988\)](#). The largest disagreement in the reaction rates between the two sets of tracks is in the $^{12}\text{C}(\alpha, \gamma)^{16}\text{O}$ rate as part of the CN cycle. The rate adopted by the Padova tracks provides the lower rate and hence provides a lower conversion rate of carbon to oxygen. Overall, this leads to an increase in the lifetime of the helium core burning of several percent.

Both Geneva and Padova use the [de Jager et al. \(1988\)](#) parametrisation for mass-loss rates, although the Geneva HIGH mass-loss tracks differ slightly from this parametrisation by doubling the mass-loss rates for WNL W-R stars and Population I stars. Both use identical mass-loss rates for remaining W-R stars, using the mass-dependent mass-loss rates compiled by [Langer \(1989\)](#). The limit for initialisation of W-R evolution differs for both Geneva and Padova, who adopt a limit of hydrogen surface abundance below 40% and 30%, respectively.

The most significant difference between the Geneva and Padova tracks comes in the W-R phase. Due to W-R stars' extended atmospheres, the radius and effective temperature (T_{eff}) of the stellar atmosphere become ambiguous. The calculation for such quantities depends on the definition of opacity in the atmosphere. The Geneva tracks aim to solve this issue by adopting a mean-weighted opacity $\kappa = \sigma_e(1 + \text{FM})$ from the radiation-driven wind theory. Here, σ_e is the electron scattering opacity, and FM is the ‘‘force multiplier,’’ which provides contribution from absorption lines. The radius and effective temperature are finally calculated by adding both the electron scattering and mean-weighted opacities. The Padova tracks, however, performed no such correction to the temperature of the W-R stars' atmospheres from outflows. As a result, the definition of effective temperature is the same for all stars in the Padova tracks, leading to an increase in the temperatures of W-R stars when compared to the Geneva models.

2.4.5. Stellar Atmospheres

The choice of stellar atmospheres used in the simulation is important in creating the ionising spectrum. Differences in atmospheric opacities can have a large impact in the final ionising spectrum, because emission lines of certain elements may be enhanced or hindered, depending on the favourability of the atmospheres.

Our chosen SPS codes, SB99 and SLUG, have several choices of stellar atmosphere libraries when synthesising the spectrum of a stellar population. The different stellar atmosphere choices we consider are formed from combinations of the three atmosphere models of the [Lejeune et al. \(1997\)](#) atmospheres (hereafter Kurucz), [Hillier & Miller \(1998\)](#) W-R atmospheres (hereafter Hillier), and [Pauldrach et al. \(2001\)](#) OB atmospheres (hereafter Pauldrach). The Kurucz atmospheres can be selected as a stand-alone choice, with the option to include the Hillier W-R atmosphere models (Kurucz + Hillier) and the Pauldrach OB atmosphere models (Kurucz + Pauldrach). The final stellar atmosphere choice consists of the Kurucz atmospheres with both the Hillier W-R models and the Pauldrach OB models (Kurucz + Hillier + Pauldrach; hereafter the SB99 atmosphere).

Both [Hillier & Miller \(1998\)](#) and [Pauldrach et al. \(2001\)](#) expand on the Kurucz atmospheres modelled by [Lejeune et al. \(1997\)](#) by modelling stars with spherically expanding

atmospheres. [Hillier & Miller \(1998\)](#) further expand on the Kurucz atmospheres by including a technique to model line blanketing in W-R stars. The updated W-R atmospheres are shown by [Hillier & Miller \(1998\)](#) to strengthen several optical CNO lines emitted by W-R stars by a factor of 2-5. [Pauldrach et al. \(2001\)](#) improve on the Kurucz atmospheres by including updated metal opacities in the OB stellar atmospheres. The inclusion of these updated opacities was aimed at solving the problems of line blanketing (as with [Hillier & Miller 1998](#)) and line blocking. The [Pauldrach et al. \(2001\)](#) atmospheres also include an improved atomic data archive, as well as a revised EUV and X-ray radiation model as a result of shock cooling zones in the OB stellar winds.

2.5. Photoionisation Models

2.5.1. Abundance Sets

For our nebular models, we adopt the solar reference abundances of [Anders & Grevesse \(1989\)](#), corresponding to a solar value of $Z = 0.020 \equiv 12 + \log(\text{O}/\text{H}) = 8.93$. Abundances at other metallicities of $Z = 0.001$, $Z = 0.004$, $Z = 0.008$, and $Z = 0.040$ are obtained by applying the Local Galactic Concordance (LGC) abundance scaling prescription described by [Nicholls et al. \(2017\)](#). Typically nebular models adopt a linear scaling for abundances with metallicity, with the exception of a few elements (e.g. He, C, and N). The LGC abundances model the individual scaling of elements with the overall nebular metallicity, based on empirical fits to stellar abundance data. These abundances account for the nonlinear scaling of alpha elements (including oxygen) with iron and account for primary and secondary production mechanisms for carbon and nitrogen. The variation with O/H of several elements, such as C, N, and Fe, is shown in [Nicholls et al. \(2017\)](#). We note that this abundance scale is calibrated from MW stellar abundances and may not be appropriate for dwarf galaxies or galaxies with instantaneous SFHs (see [Nicholls et al. 2017](#), for a detailed explanation of abundance scaling with metallicity). The abundance values are found in [Table 2.2](#). Through our simulations, we match the stellar abundance to the overall metallicity of the stellar evolutionary tracks (with the exception of $Z = 0.050$ Padova tracks, for which we use the $Z = 0.040$ abundance set). Whilst the Padova tracks also differ at the low-metallicity end with a metallicity of $Z = 0.0004$ rather than $Z = 0.001$, SLUG sets the low-metallicity end of the Padova tracks to $Z = 0.001$ for reasons described in [Section 2.6.2](#)). The direction of increasing metallicity in the model grids can be seen from [Figure 2.2](#).

2.5.2. Depletion Factors

The depletion factors used are those from [Jenkins \(2014\)](#), using a logarithmic base depletion of -1.50 for iron. Depletion values for each element are detailed in [Table 2.2](#). Throughout our simulations, we keep the depletion factors constant as a function of metallicity and set to the diffuse ISM values within the Milky Way. Hence, we neglect the possible variation in the depletion of each element amongst H II regions.

Element	$12 + \log(X/H)$	Depletion value
H	12.00	0.00
He	10.99	0.00
Li	1.16	-0.22
Be	1.15	-0.40
B	2.60	-0.58
C	8.56	-0.16
N	8.05	-0.04
O	8.93	-0.11
F	4.56	-0.09
Ne	8.09	0.00
Na	6.33	-0.42
Mg	7.58	-0.70
Al	6.47	-0.70
Si	7.55	-0.71
P	5.45	-0.11
S	7.21	0.00
Cl	5.50	-0.09
Ar	6.56	0.00
K	5.12	-0.62
Ca	6.36	-1.95
Sc	3.10	-0.69
Ti	4.99	-1.95
V	4.00	-2.17
Cr	5.67	-1.45
Mn	5.39	-1.27
Fe	7.67	-1.50
Co	4.92	-1.64
Ni	6.25	-1.57
Cu	4.21	-0.90
Zn	4.60	-0.20

Table 2.2 Solar abundance reference set from [Anders & Grevesse \(1989\)](#), and depletion values using the method from [Jenkins \(2014\)](#) for each element with a logarithmic base depletion of iron of -1.50.

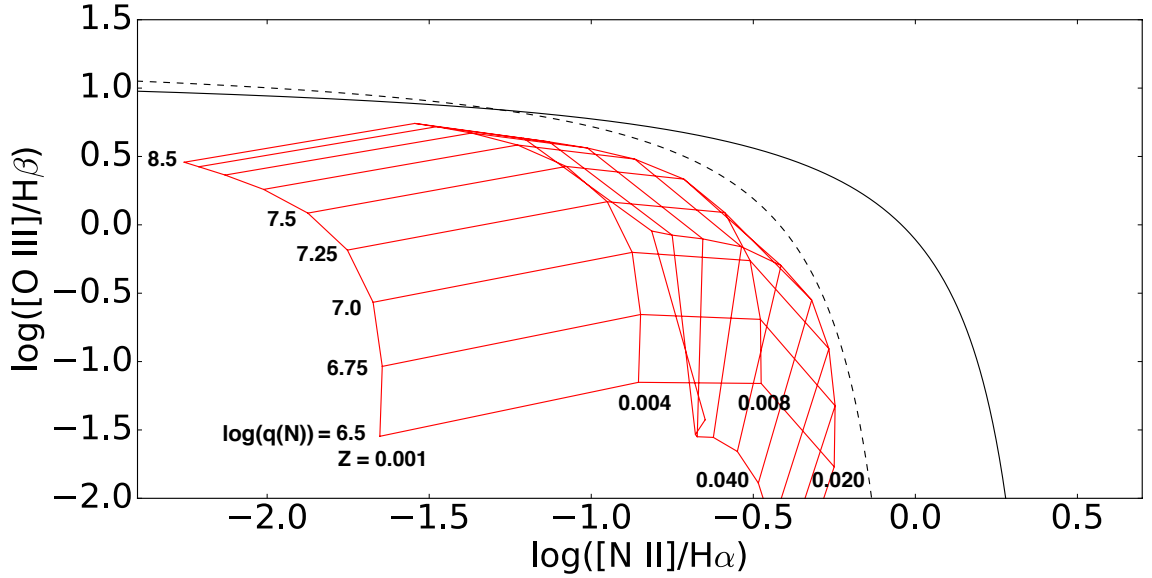


Figure 2.2 Model grid computed with the SLUG SPS code, using the SB99 combination atmosphere and Geneva HIGH tracks, assuming a continuous SFH at 5 Myr, truncated at 99% hydrogen recombination. The model is annotated showing directions of increasing metallicity Z and ionisation parameter $\log(q(N))$. Five metallicities are used in the model grids: $Z = 0.001, 0.004, 0.008, 0.020,$ and 0.040 . The values of the ionisation parameter used in the model grids range between $\log(q(N))/(\text{cm s}^{-1}) = 6.5$ and 8.5 inclusive, in 0.25 dex increments. The annotations shown on this figure are identical for all models on subsequent figures, unless otherwise stated.

2.5.3. Model Geometry

The geometry of the H II region is determined by the radiation source’s position relative to the molecular cloud that it ionises. In the simplest case, the geometry of the region may be considered to be spherical if the ionising source is found within the cloud. If the ionising source is external to the molecular cloud that it ionises, the geometry may be considered to be plane-parallel. Further, the geometry of the model can be either ‘open’ or ‘closed.’ Closed-geometry models are applicable when all ionising radiation is assumed to be incident on a molecular cloud (i.e. for a stellar cluster within an H II region), whereas open-geometry models imply that a fraction of ionising radiation is lost to the ISM (e.g. when modelling a narrow-line region photoionised by the accretion disk of a supermassive black hole). In all simulations, we assume a closed spherical shell assumed to be empty or optically thin, such that the inner surface of the H II region receives the same unobscured flux from the ionising central cluster.

2.5.4. Pressure and Density

The pressure of the H II region is important for the resulting emission from the nebula. Differences in pressure alter the density structure of the H II region. For a constant-pressure (isobaric) model, density increases towards the edge of the H II region owing to the decrease in temperature farther away from the central stellar cluster, resulting in different mean densities amongst differing ions throughout the nebula. We adopt an isobaric model for our simulations, with a total pressure of $P/k = 8 \times 10^5 \text{ cm}^{-3} \text{ K}$, derived from an initial total density of $n = 100 \text{ cm}^{-3}$ and initial temperature of 8000 K .

Setting the initial total density $n = 100 \text{ cm}^{-3}$ is widely supported, within the order of magnitude. [Dopita et al. \(2006\)](#) put a constraint of $n \leq 100 \text{ cm}^{-3}$ when computing H II region spectra for pressure values of $\log(P/k) = 6$. Meanwhile, [Kewley et al. \(2001\)](#) found an average electron density of $n = 350 \text{ cm}^{-3}$ for the [Kewley et al. \(2000\)](#) sample of warm infrared starburst galaxies (maximum redshift < 0.1). An average value of $n = 222^{+172}_{-128} \text{ cm}^{-3}$ was found by [Kashino et al. \(2017\)](#), using their sample from the FMOS-COSMOS survey ($1.4 \leq z \leq 1.7$), and also by work done by [Shimakawa et al. \(2015\)](#) and [Sanders et al. \(2016\)](#) ($n = 291$ and $n = 225^{+119}_{-4}$ $[\text{O II}]$ doublet, $n = 290^{+88}_{-169}$ $[\text{S II}]$ doublet cm^{-3} , at redshifts of $z = 2.5$ and 2.3 , respectively).

However, there have also been reported findings of galaxies with electron densities on the order of $n = 1000 \text{ cm}^{-3}$ from the likes of the FMOS-COSMOS sample presented in [Kashino et al. \(2017\)](#), and from high-redshift ($z \approx 3.3$) galaxies shown in [Onodera et al. \(2016\)](#). This leads [Kashino et al. \(2017\)](#) to conclude that H II regions in high-redshift galaxies do have an electron density a few to several times larger than that of local galaxies on average. This increase in electron density in high-redshift galaxies is thought to be linked to the increase in star-formation rate (SFR) of galaxies at high redshift (e.g. [Madau & Dickinson 2014](#)). [Kaasinen et al. \(2017\)](#) show that any offset in the electron density between local and high-redshift star-forming galaxies disappears if comparisons are performed between local and high-redshift galaxies matched in SFR or mass. They show an electron density in local galaxies ($z < 0.1$) in their COSMOS-[O II] sample of $26.8^{+0.2}_{-0.2} \text{ cm}^{-3}$, which increases to 98^{+4}_{-4} and $98^{+5}_{-5} \text{ cm}^{-3}$ when choosing galaxies matched to high-redshift galaxies in SFR and both SFR and mass, respectively. For the entire sample at $z \sim 1.5$, they measure an average electron density of $114^{+28}_{-27} \text{ cm}^{-3}$, leading to an agreement within errors for the electron densities at both low and high redshift. Throughout their sample, [Kaasinen et al. \(2017\)](#) also show instances of high-redshift galaxies with electron densities calculated to be $\sim 1000 \text{ cm}^{-3}$.

2.5.5. Ionisation Parameter

For the ionisation parameter $q(N)$ (ionising photon number density relative to the number density of all ions in the nebula), we use a range of values for $\log(q(N)/(\text{cm s}^{-1})) = 6.5 - 8.5$ with 0.25 dex increments. These values of $\log q(N)$ correspond to values of the dimensionless ionisation parameter $\log U(N) = q/c \approx -4$ to -2 , with 0.25 dex increments (nine values in total). The direction of increasing ionisation parameter in the model grids can be seen from [Figure 2.2](#).

[Rigby & Rieke \(2004\)](#) find a range of $-3.2 \lesssim \log U(N) \lesssim -0.9$ within local starburst galaxies. Whilst our values of the ionisation parameter are slightly lower than those found by [Rigby & Rieke \(2004\)](#), they compare well with those used by [Kewley et al. \(2001\)](#) within the errors, who use a range of $-4.3 \lesssim \log U(N) \lesssim -2.5$.

2.5.6. Boundedness

Boundary conditions can have a profound effect on the final emission-line fluxes. Radiation-bounded models represent an H II region where ionisation and excitation within are limited by the amount of ionising radiation from its ionising source, and it is assumed that all

ionising photons are absorbed by the nebula. Radiation-bounded simulations are terminated once a certain fraction of H II has recombined to H I (usually considered to be a high fraction, such as 95-99%).

It is possible that some fraction of the ionising radiation escapes the nebula, meaning that the gas column is not sufficient to absorb all photons. This is known as a ‘density-bounded’ nebula. These density-bounded situations are associated with ‘leaky H II regions’ (e.g. Pellegrini et al. 2012; Zastrow et al. 2013), which may give rise to diffuse ionised gas (DIG; described in Section 2.7.2) and play a key role in the reionisation of the universe. Our density-bounded models are truncated at a given optical depth at 13.6 eV, corresponding to the ionisation potential of hydrogen.

For individual H II regions, the escape of ionising photons is an important consideration. On typical galaxy scales, estimates place the escape fraction at $< 3\%$ (e.g. Inoue et al. 2006). However, for dwarf galaxies, where a star forming region can have a large impact, density-boundedness may be important. Nicholls et al. (2014) explored the ISM conditions within a sample of dwarf galaxies. They found that these dwarf galaxies were unable to be explained by radiation-bounded photoionisation models. The emission lines of the dwarf galaxies indicated a low metallicity, but with line ratios outside of the standard model predictions. By moving to a density-bounded regime, they found that lower optical depths may in fact offer explanations for the observed emission lines. Through the mass-metallicity relation (Tremonti et al. 2004), the low-metallicity galaxies seen in Nicholls et al. (2014) are also at a low mass, leading to a weaker gravitational pull on the material within the galaxy. Thus, supernova explosions in these low-mass galaxies have a greater effect on the surrounding material, by expelling and clearing gas far more easily. The result is a higher ionising photon escape fraction due to a larger mean free path, which ultimately results in a decrease in the optical depth of the galaxy (Trebitsch et al. 2017). The same principle can be applied to H II regions, because supernovae in low-mass galaxies cause more porous H II regions, thus increasing the ionising photon escape fraction.

2.5.7. Fiducial Model

Throughout this work, we adopt and compare various models for the parameters listed in Sections 2.4 and 2.5. When exploring the systematic differences amongst variations in a single parameter associated with the photoionisation grids, we keep all other parameters constant. Unless otherwise stated, we assume a solar metallicity ($Z = 0.020$), constant star formation rate ($1M_{\odot} \text{ yr}^{-1}$) with an age of 5 Myr, created using SLUG with a Kroupa IMF, the Geneva HIGH tracks, and combination (Kurucz + Hillier + Pauldrach) atmospheres. All spectra shown in Section 2.6.1 are first normalised to an SB99 spectrum of a 5 Myr cluster undergoing constant star formation at $1 M_{\odot} \text{ yr}^{-1}$, treating all stars as pure blackbodies. This reference spectrum is shown in Figure 2.3. The SFR and the age of the cluster provide a cluster mass of $5 \times 10^6 M_{\odot}$. The H II region model assumes a spherical, radiation-bounded, isobaric structure with $P/k = 8 \times 10^5 \text{ cm}^{-3} \text{ K}$, terminated once 99% of hydrogen recombination has occurred. Our abundances are solar, and the models include dust, following the depletion factors detailed in Section 2.5.2. Our models do not allow grain destruction, and the grain size distribution follows the MRN distribution (Mathis

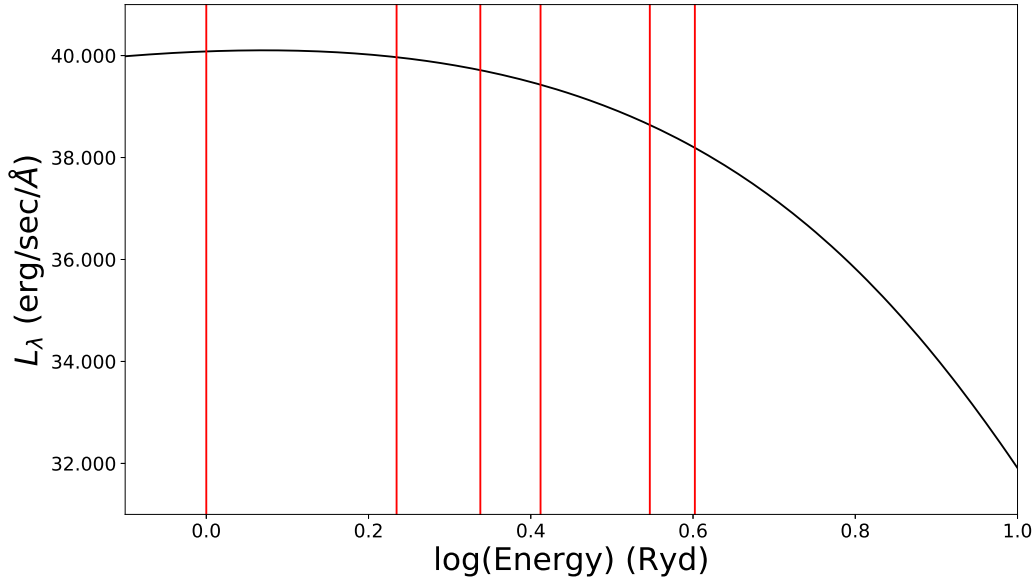


Figure 2.3 SB99 spectrum of a 5 Myr cluster undergoing constant star formation at $1 M_{\odot} \text{ yr}^{-1}$, treating all stars as pure blackbodies. This is the spectrum to which all spectra in Section 2.6.1 are first normalised.

et al. 1977). Finally, we include polycyclic aromatic hydrocarbons (PAHs), with a carbon dust depletion fraction of 0.3.

2.6. Model Comparisons

2.6.1. Ionising Radiation Field

Cluster Age

The spectra of instantaneous SFH stellar clusters at various ages are shown in Figure 2.4. When assuming an instantaneous SFH, we end the simulation at 6 Myr. Beyond the ages of 6 Myr, the flux of H^0 -, He^0 - and He^+ -ionising photons from a single stellar cluster decreases considerably (e.g. Wofford et al. 2016). Hence, we neglect ages beyond 6 Myr. A gradual decrease in the flux of the ionising spectrum continues up until 3.5 Myr. At this point, the beginning of a distinct and large increase in the ionising spectrum at high energies can be seen, corresponding to the evolution of the W-R stars, as a subset of evolved OB stars (Conti 1976; Lamers et al. 1991; Groh et al. 2013).

Using spectroscopic techniques, Vacca et al. (1996) calculated the masses of OB stars of many spectral types (O3-9.5, B0-0.5) and luminosity classes (Ia, III, and V). Averaged over the spectral type and luminosity class, Vacca et al. (1996) find an average OB star mass of $35.5 \pm 24.8 M_{\odot}$. This value is in very close agreement with the value calculated by Martins et al. (2005), who calculate an average OB star mass of $34.99 M_{\odot}$ with an average error of approximately $15 M_{\odot}$, using a very similar technique. At masses of $\sim 40 M_{\odot}$, Lamers et al. (1991) calculate the main-sequence lifetime of OB stars to be 2.5 – 4 Myr, coinciding with the W-R emergence time frame shown in Figure 2.4. The spectra of W-R stars contain very

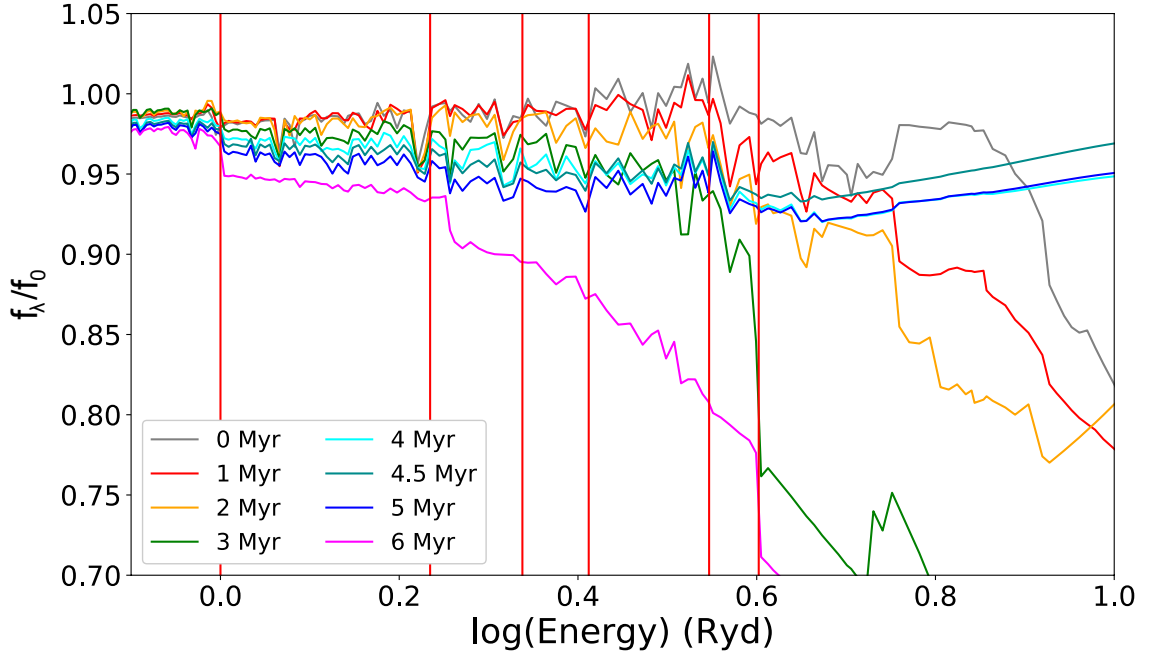


Figure 2.4 SLUG spectra for an instantaneous SFH cluster of mass $10^6 M_{\odot}$ for ages 0 – 6 Myr in steps of 0.5 Myr. f_{λ}/f_0 is the input spectrum normalised to the blackbody spectrum shown in Figure 2.3. All spectra are at a metallicity of $Z = 0.020$. The red vertical lines represent the ionisation potentials of important ISM species; from left to right: H^0 , S^+ , N^+ , O^+ , C^{2+} , He^+ .

strong broad emission lines of specifically helium, carbon, nitrogen, oxygen, and silicon, with hydrogen lines either weak or absent (Crowther 2007). Lamers et al. (1991) showed W-R stars to be late stages in the evolution of massive stars, which have removed their hydrogen-rich outer layers in a stellar wind. The loss of the outer layers exposes a bare core, leading to an increased detection of heavier elements.

The increase in the hardness of the spectrum continues for the duration of the lifetime of W-R stars (~ 0.5 Myr at a mass of $40M_{\odot}$; Meynet & Maeder 2005); Figure 2.4 shows the beginning of the distinct increase in hardness of the spectrum at 4 Myr, peaking at 4.5 Myr before decreasing at 5 Myr.

Stellar Evolutionary Tracks

The spectra for the Geneva and Padova stellar evolutionary tracks are shown in Figure 2.5, at continuous and instantaneous SFH cluster ages of 0 Myr (10 kyr), 3 Myr, and 5 Myr. Each spectrum in Figure 2.5 is shown normalised to a continuous SFH spectrum at 5 Myr treating all stars as blackbodies, produced using SB99. Only the spectra at metallicities where the tracks are directly comparable are shown ($Z = 0.004$, 0.008 , and 0.020 ; the tracks differ at the lowest and highest metallicities). Spectra for continuous and instantaneous SFH are shown at identical ages. Seen in Figure 2.5, the spectra at varying ages between the continuous SFH Geneva and Padova models are extremely similar for energies below $\log(E/\text{ryd}) \lesssim 0.6$, agreeing in flux to within $\sim 0.5\%$. In this energy regime, any noticeable trend in the difference in the spectra between the two sets of tracks with age or metallicity is difficult to determine. The difference between the spectra produced from both sets of tracks is more easily seen when using the spectra from an instantaneous SFH

cluster. Without continually emerging young stellar populations contributing to the overall spectrum, the dependence of stellar evolution on the choice of stellar evolutionary tracks becomes clearer. The Padova tracks are seen to produce a consistently higher flux than the Geneva tracks when considering the evolution of an instantaneous SFH cluster over time. The systematically higher flux from the Padova tracks is a result of the larger zero-age main-sequence (ZAMS) effective temperature and luminosity of the Padova tracks by ~ 0.03 and ~ 0.02 dex, respectively. The evolution of T_{eff} and luminosity is also similar over time in the two sets of tracks, with the exception of the W-R phase (Vázquez & Leitherer 2005).

At high energies, more noticeably as age increases, the difference between the spectra of the two sets of tracks becomes extremely large. This large difference in the flux between the Padova and Geneva tracks typically begins at $\log(E/\text{ryd}) \gtrsim 0.6$ ($E \gtrsim 4 \text{ ryd} \Rightarrow \lambda \lesssim 366 \text{ \AA}$), increasing in size with energy. Vázquez & Leitherer (2005) attribute this large discrepancy in ionising flux between the two tracks to the presence of W-R stars. The different definition of T_{eff} between the two models, as well as the subsequent higher effective temperature in the Padova tracks, has large ramifications once W-R stars begin to emerge in the cluster. This is reflected in the relative ionising fluxes of photons at shorter wavelengths, capable of ionising He^0 and He^+ ($\lambda \lesssim 504$ and 228 \AA , respectively). At a cluster age of 4 Myr, Vázquez & Leitherer (2005) show the relative difference in the number of ionising photons in the He II continuum to be roughly 4 – 8 orders of magnitude in favour of the Padova tracks, depending on the choice of stellar atmosphere. At ~ 6 Myr, this difference is increased to roughly 10 orders of magnitude. Beyond ~ 6.3 Myr, the number of W-R stars left within the cluster becomes negligible (see also Leitherer et al. 1999), and hence the relative difference in the number of He^+ -ionising photons decreases rapidly towards zero. Figure 2.5 shows a sustained large difference in the ionising flux at high energies in the continuous SFH spectra, as W-R stars continue to emerge for the duration of the simulation. SLUG calculates the flux for a minimum wavelength of 91 \AA . At a wavelength of 91 \AA , the difference between the total integrated ionising fluxes from the Geneva and Padova tracks calculated by SLUG is roughly 8 orders of magnitude.

Stellar Atmospheres

Spectra produced using each of the atmosphere models we consider are shown in Figure 2.6 for 0 Myr clusters on the left and clusters of ages 5 and 4.5 Myr assuming a continuous and instantaneous SFH, respectively, on the right. An age of 4.5 Myr for the instantaneous SFH clusters in Figure 2.6 was chosen to coincide with maximum W-R activity shown in Figure 2.4.

The W-R atmospheres added to the Kurucz atmospheres by Hillier & Miller (1998) make little difference to the overall shape of the ionising spectra of the stellar clusters, including once W-R activity is at a maximum at 4.5 Myr. The atmospheres used to model OB stars produced by Pauldrach et al. (2001) improved on the OB stellar models used in the Kurucz atmospheres by introducing metal opacities into the atmospheres of the OB stars. The metals introduced into the OB stellar atmospheres undergo excitation and ionisation through the absorption of internal stellar photons, and subsequent emissions from these metals result in differences in the strength of particular emission lines from the surrounding nebula. This can be seen in the left panels of Figure 2.6. The spectra that include the

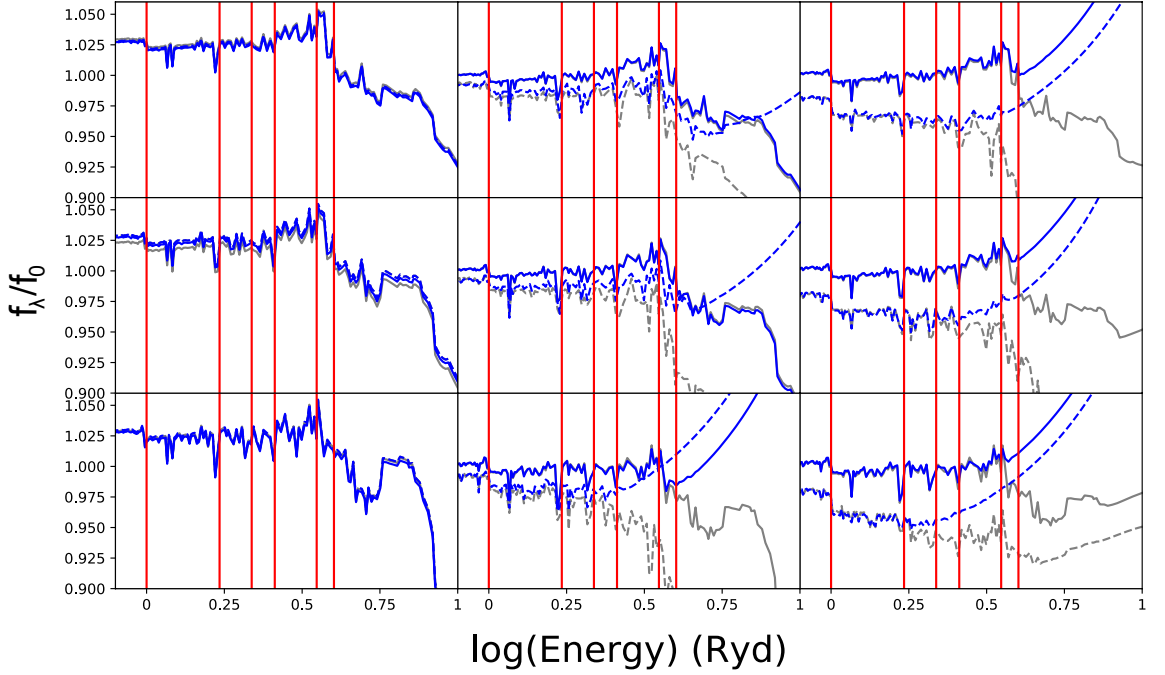


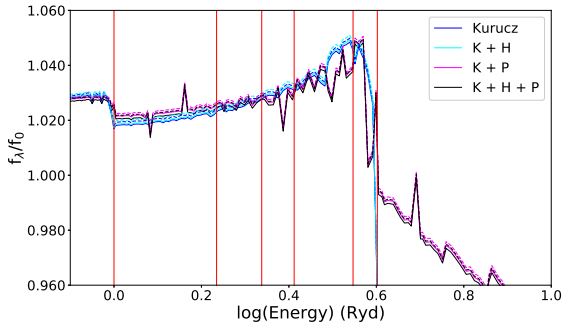
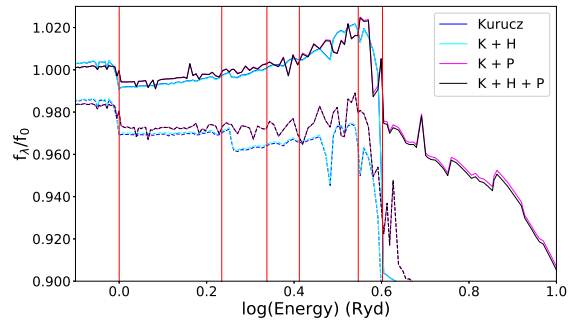
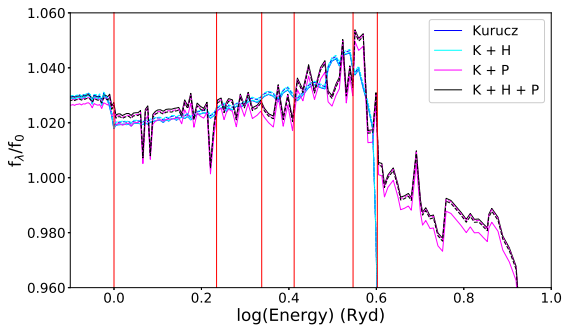
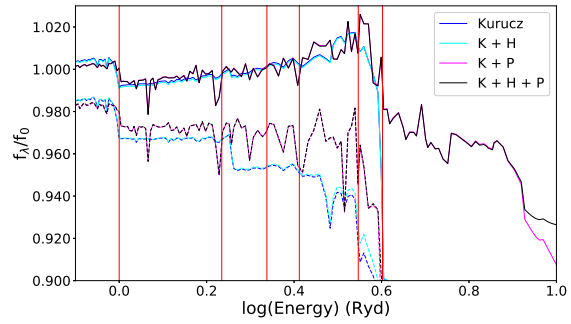
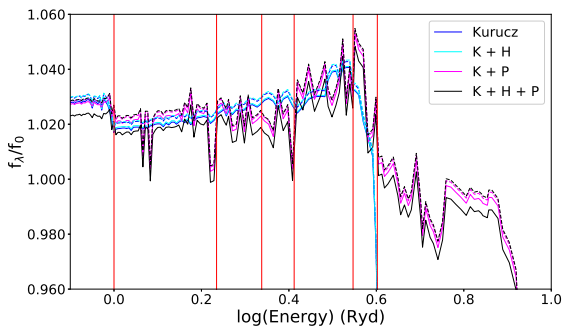
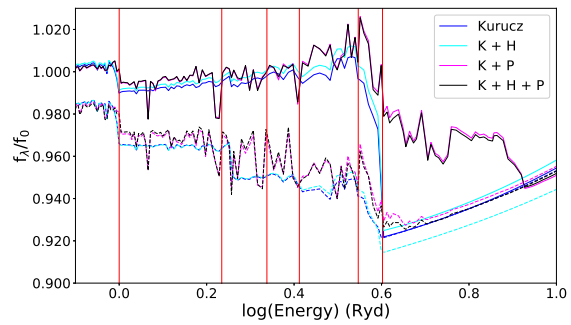
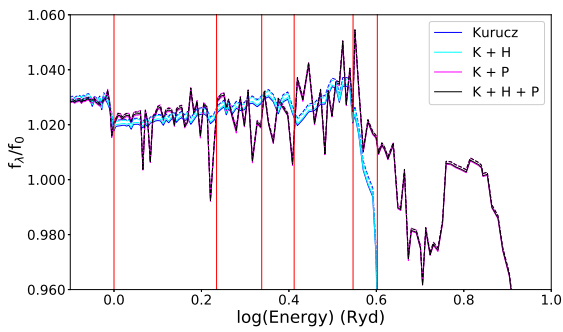
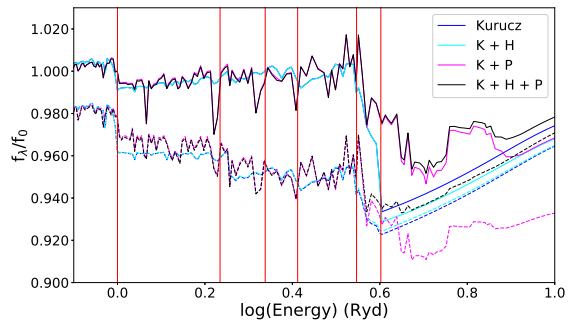
Figure 2.5 Input spectra (flux in units $\text{erg sec}^{-1} \text{\AA}^{-1}$ vs. energy) of the Geneva HIGH tracks (grey) and the Padova tracks with thermally pulsing AGB stars (blue). f_λ represents the individual input spectra, and f_0 is the blackbody spectrum shown in Figure 2.3. Solid lines are for continuous SFH clusters undergoing star formation at a rate of $1M_\odot \text{ yr}^{-1}$. Dashed lines are for instantaneous SFH clusters of mass $10^6 M_\odot$. The continuous SFH spectra shown at 0 Myr (10 kyr) are for clusters undergoing star formation at a rate of $100M_\odot \text{ yr}^{-1}$, ensuring that the continuous SFH cluster has a mass of $10^6 M_\odot$ for direct comparison to the instantaneous SFH clusters. Each column shows a different cluster age; from left to right: 0 Myr (10 kyr), 3 Myr, 5 Myr. Each row shows a different metallicity; from top to bottom: $Z = 0.004$, $Z = 0.008$, $Z = 0.020$. The red vertical lines represent the ionisation potentials of important ISM species; from left to right: H^0 , S^+ , N^+ , O^+ , C^{2+} , He^+ .

Pauldrach et al. (2001) OB atmospheres show increased absorption or emission at various photon energies throughout the spectrum. The spectra at 0 Myr in Figure 2.6 show an increased luminosity across all metallicities at the ionisation potential for O^+ ($\log(E/\text{ryd}) \approx 0.6$), whereas the luminosity at the ionisation potential for N^0 ($\log(E/\text{ryd}) \approx 0.3$) remains relatively constant with metallicity.

Stellar Population Synthesis Codes

Single stellar populations We first explore the differences in the ionising spectra produced by the two SPS codes SB99 and SLUG. Even with the same input parameters and libraries, differences in the spectra between two SPS codes can still arise owing to the different assumptions and computational methods within the codes. In Figure 2.7 we show the relative difference between the two ionising spectra generated using SB99 and SLUG for an individual cluster of mass $10^6 M_\odot$ at ages 0 – 6 Myr, in 1 Myr increments. It should be noted that for all our simulations using SLUG, 10 kyr has been used as an approximation to 0 Myr; SLUG requires a simulation starting time greater than 0. Both codes produce spectra that agree at the ZAMS (0 Myr; Figure 2.7a), because the main sequence is well sampled and understood.

However, at later ages, differences in the ionising spectra arise owing to the difficulty in

(a) Metallicity $Z = 0.001$ (b) Metallicity $Z = 0.001$ (c) Metallicity $Z = 0.004$ (d) Metallicity $Z = 0.004$ (e) Metallicity $Z = 0.008$ (f) Metallicity $Z = 0.008$ (g) Metallicity $Z = 0.020$ (h) Metallicity $Z = 0.020$

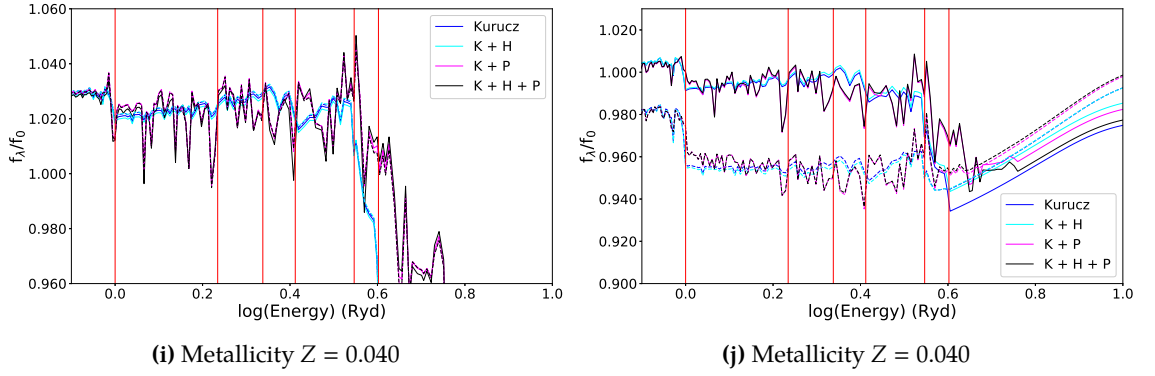
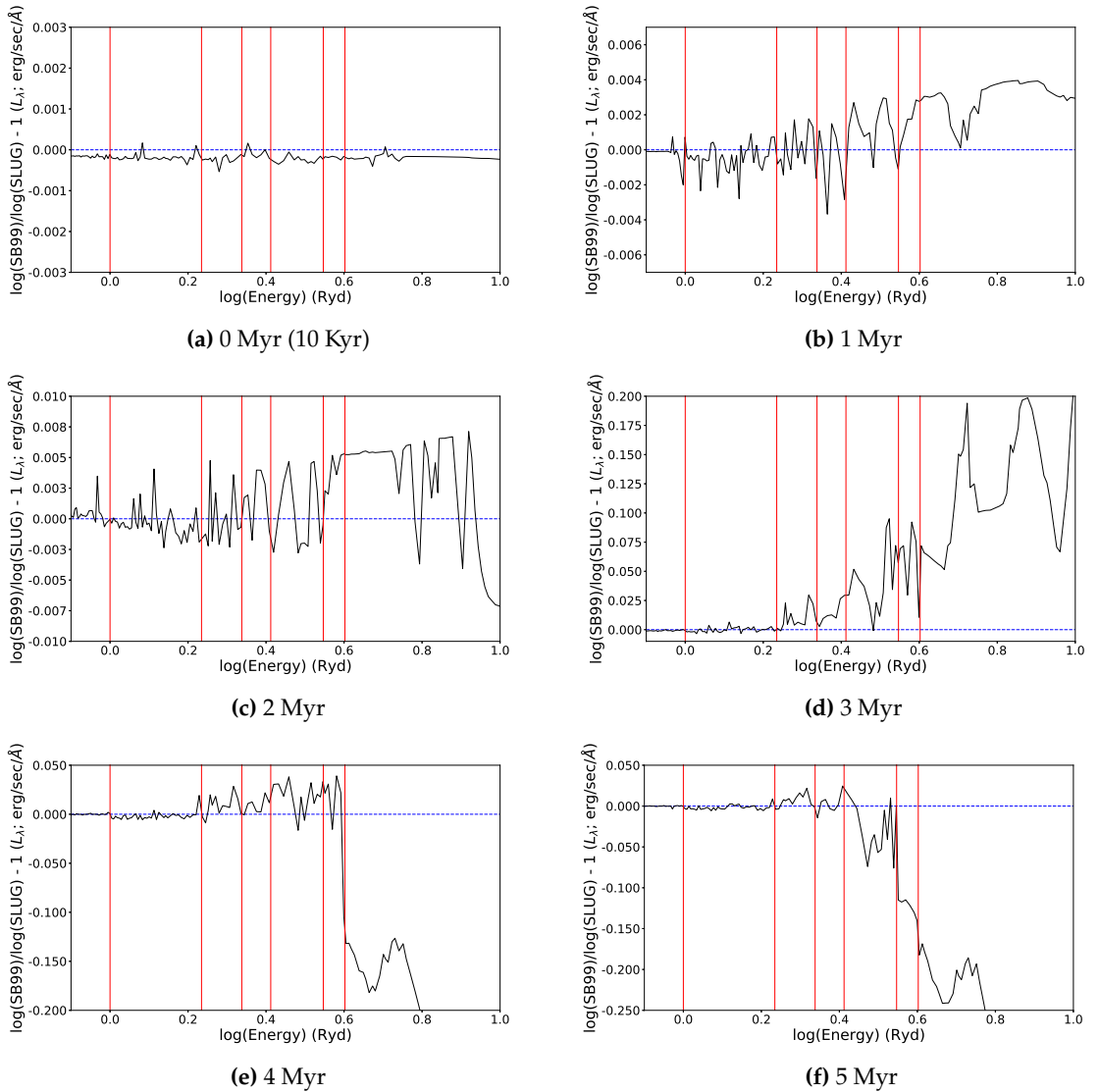


Figure 2.6 Input spectra (flux in units $\text{erg sec}^{-1} \text{\AA}^{-1}$ vs. energy) of each of the four SLUG atmospheres for each metallicity value used in the grids. f_λ represents the individual input spectra, and f_0 is the blackbody spectrum shown in Figure 2.3. The atmospheres used in each plot are Kurucz, Kurucz + Hillier (K + H), Kurucz + Pauldrach (K + P), and Kurucz + Hillier + Pauldrach (K + H + P). The left panels show both continuous SFH (solid lines) and instantaneous SFH (dashed lines) clusters of mass $10^6 M_\odot$ at ages of 0 Myr (10 kyr). The right panels show continuous SFH clusters at 5 Myr and instantaneous SFH clusters of mass $10^6 M_\odot$ at 4.5 Myr. The age of 4.5 Myr for the instantaneous SFH cluster was chosen to coincide with maximum W-R activity shown in Figure 2.4. The red vertical lines represent the ionisation potentials of important ISM species; from left to right: H^0 , S^+ , N^+ , O^+ , C^{2+} , He^+ .



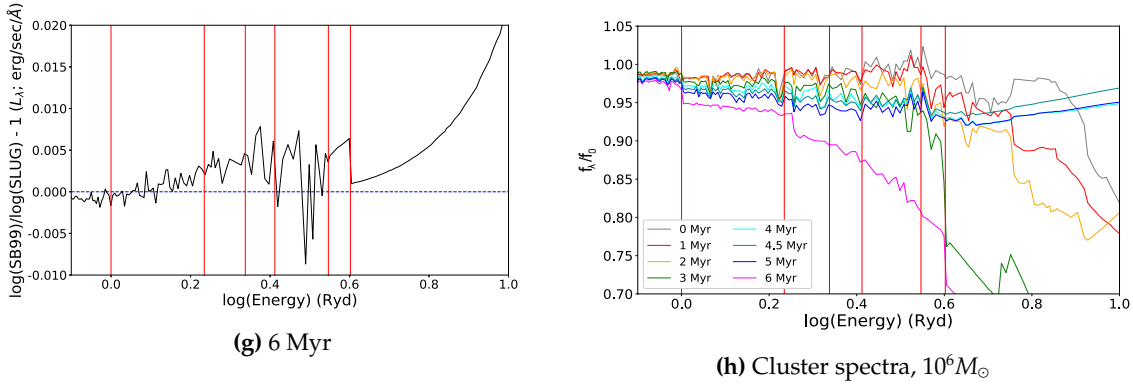


Figure 2.7 Relative difference between spectra of an instantaneous SFH $10^6 M_\odot$ cluster computed with SB99 and SLUG. The relative difference is shown at ages of 0 Myr (10 Kyr) to 6 Myr inclusive, in increments of 1 Myr. Instantaneous SFH cluster spectra produced with SLUG for each age are shown in panel (h). f_λ in (h) represents the individual input spectra, and f_0 is the blackbody spectrum shown in Figure 2.3. The blue dashed line represents a relative difference of 0. The red vertical lines represent the ionisation potentials of important ISM species; from left to right: H^0 , S^+ , N^+ , O^+ , C^{2+} , He^+ .

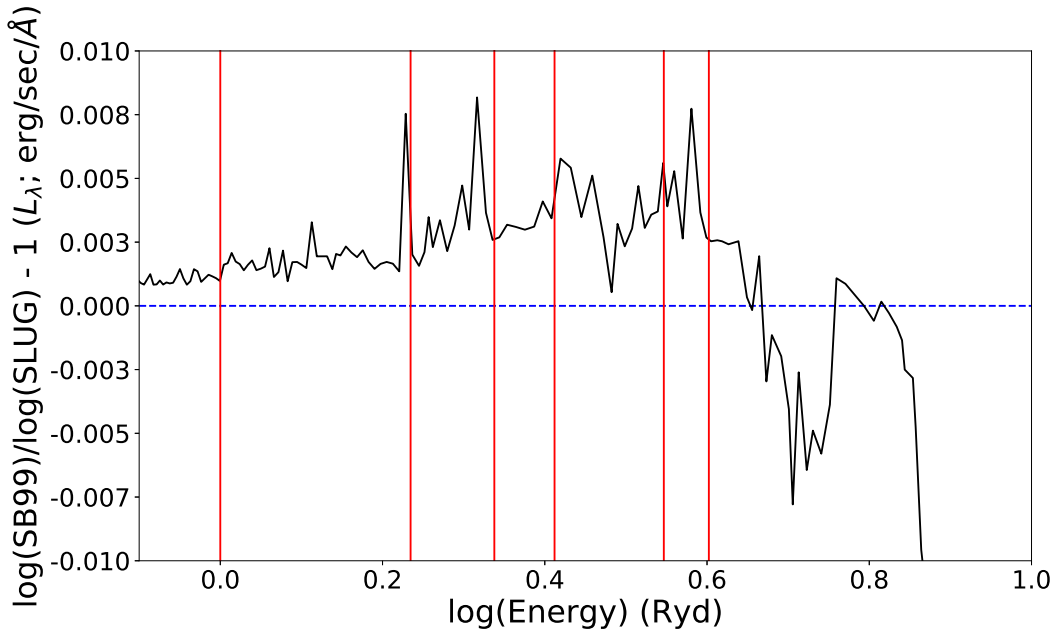


Figure 2.8 Relative difference between the spectra of SB99 and SLUG for a continuous SFH cluster at $Z = 0.020$ and at an age of 5 Myr. The red vertical lines represent the ionisation potentials of important ISM species; from left to right: H^0 , S^+ , N^+ , O^+ , C^{2+} , He^+ .

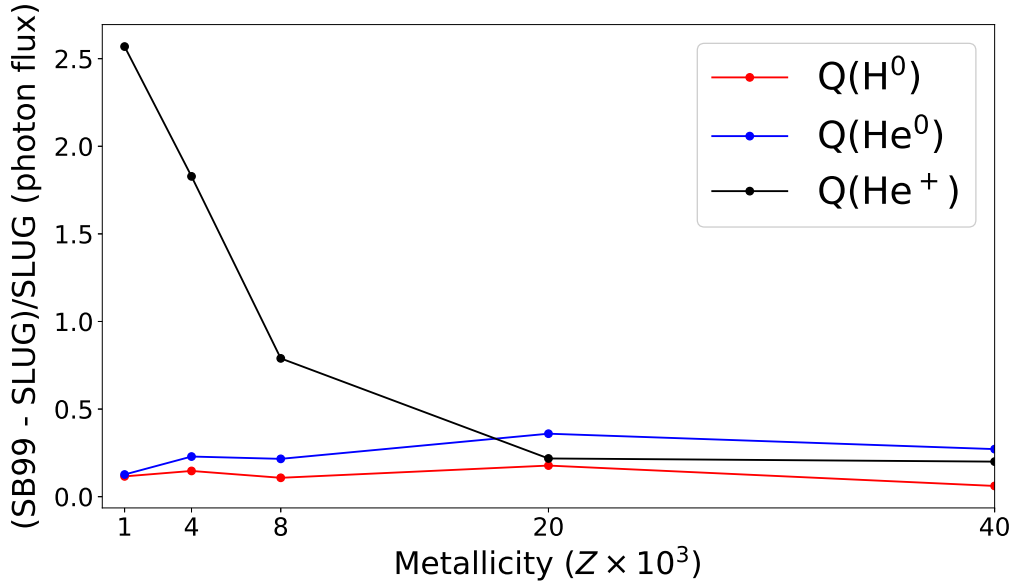


Figure 2.9 Relative difference between SB99 and SLUG in the number of H^0 -, He^0 - and He^+ -ionising photons vs. Z . All model parameters and input are equal to those in Figure 2.8.

modelling high-mass stars (Figures 2.7b-g). High-mass stars ($M \sim 120M_{\odot}$) evolve rapidly off the main sequence and go through several phases of evolution (e.g. red supergiant, blue supergiant post helium flash, with also possibilities for W-R, luminous blue variables, yellow hypergiants). As a result, their position on the Hertzsprung-Russell (H-R) diagram can alter drastically and quickly (see, e.g., Figure 5.2 of [Binney & Merrifield 1998](#)). Furthermore, mass sampling of massive-star evolutionary tracks used for isochrone interpolation is sparse, due to the difficulty in modelling, and obtaining constraining observations of high-mass stars (more on this in Section 2.7.1). Hence, the resulting stellar spectrum is heavily dependent on the specific stellar masses of the evolutionary tracks, as well as the interpolation method itself.

Shown in Figure 2.8 is the relative difference between SB99 and SLUG for a 5 Myr old cluster undergoing continuous star formation at a rate of $1M_{\odot} \text{ yr}^{-1}$. The difference in luminosity between the two spectra is less than 1%, with SB99 producing the more luminous ionising spectrum for most energies. At energies of $\log(E/\text{ryd}) > 0.6$, SLUG is shown to produce the harder ionising spectrum. Figure 2.9 also shows the more luminous ionising spectrum overall produced by SB99, by showing a relative increase in the flux of H^0 -, He^0 - and He^+ -ionising photons for all Z .

Stochastic sampling of IMF A main difference between SB99 and SLUG is the method by which each SPS code infers values for the parameters of the stellar cluster. SLUG regards each parameter as a probability distribution and will draw values for each parameter through Monte Carlo simulations. One such parameter for which this applies is the IMF. Here we show the effect of stochastic sampling of the IMF on the resulting stellar spectrum by comparing the spectra of SLUG and SB99 – the latter of which does not include stochasticity – at varying cluster masses. The size of the cluster is known to make a differ-

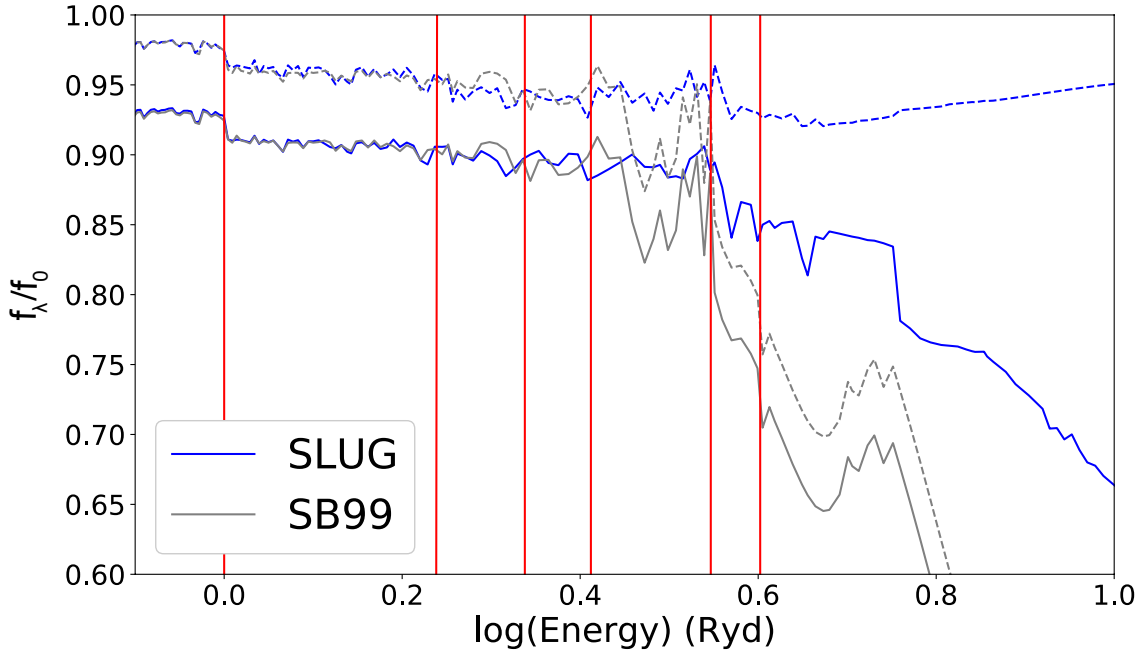


Figure 2.10 Spectra for instantaneous SFH clusters of age 5 Myr at masses of $10^4 M_{\odot}$ (solid) and $10^6 M_{\odot}$ (dashed), produced with SB99 and SLUG. All spectra are at a metallicity of $Z = 0.020$. f_{λ} represents the individual input spectra, and f_0 is the blackbody spectrum shown in Figure 2.3. The red vertical lines represent the ionisation potentials of important ISM species; from left to right: H^0 , S^+ , N^+ , O^+ , C^{2+} , He^+ .

ence to the cluster’s final ionising spectrum, because at low cluster masses undersampling from the IMF may lead to a skew in the stellar masses.

Assuming that the IMF is a pdf like in SLUG, [Cerviño et al. \(2013\)](#) and references therein show for cluster masses of $\lesssim 10^4 M_{\odot}$ that there is a significant scatter in the mass of the most massive star within the cluster. Hence, at a cluster mass of $10^4 M_{\odot}$ and below, variations in the distribution of individual stellar masses in the cluster can lead to very different ionising spectra (and hence a different spectrum for each SPS code execution). From the mass-luminosity relation (first proposed by [Eddington 1924](#)), it can be shown that stellar mass and flux are proportional. Hence, large variations in the masses of the stars within the cluster will lead to similarly large variations in the ionising spectra. This is shown in Figure 2.10 for stellar spectra produced stochastically through SLUG and nonstochastically through SB99 for cluster masses of $10^4 M_{\odot}$ and $10^6 M_{\odot}$. Each spectrum produced using SLUG is the result of one Monte Carlo experiment. For SPS codes that populate a stellar cluster simply according to the distribution of the IMF (such as SB99), the stellar spectra of the 10^4 and $10^6 M_{\odot}$ clusters have the same shape, with the total luminosity varying by a scale factor. However, if the stellar cluster is populated through the stochastic sampling of the IMF (as in SLUG), the resulting stellar spectra at cluster masses of 10^4 and $10^6 M_{\odot}$ will likely be very different.

Binary populations We compare spectra produced using both BPASS and SLUG, showing the relative difference between instantaneous SFH spectrum luminosities with cluster age in Figure 2.11, and for a continuous SFH cluster at 5 Myr in Figure 2.12. Seen in Figure 2.11, neither spectrum is systematically harder at all ages. The luminosity of spectra

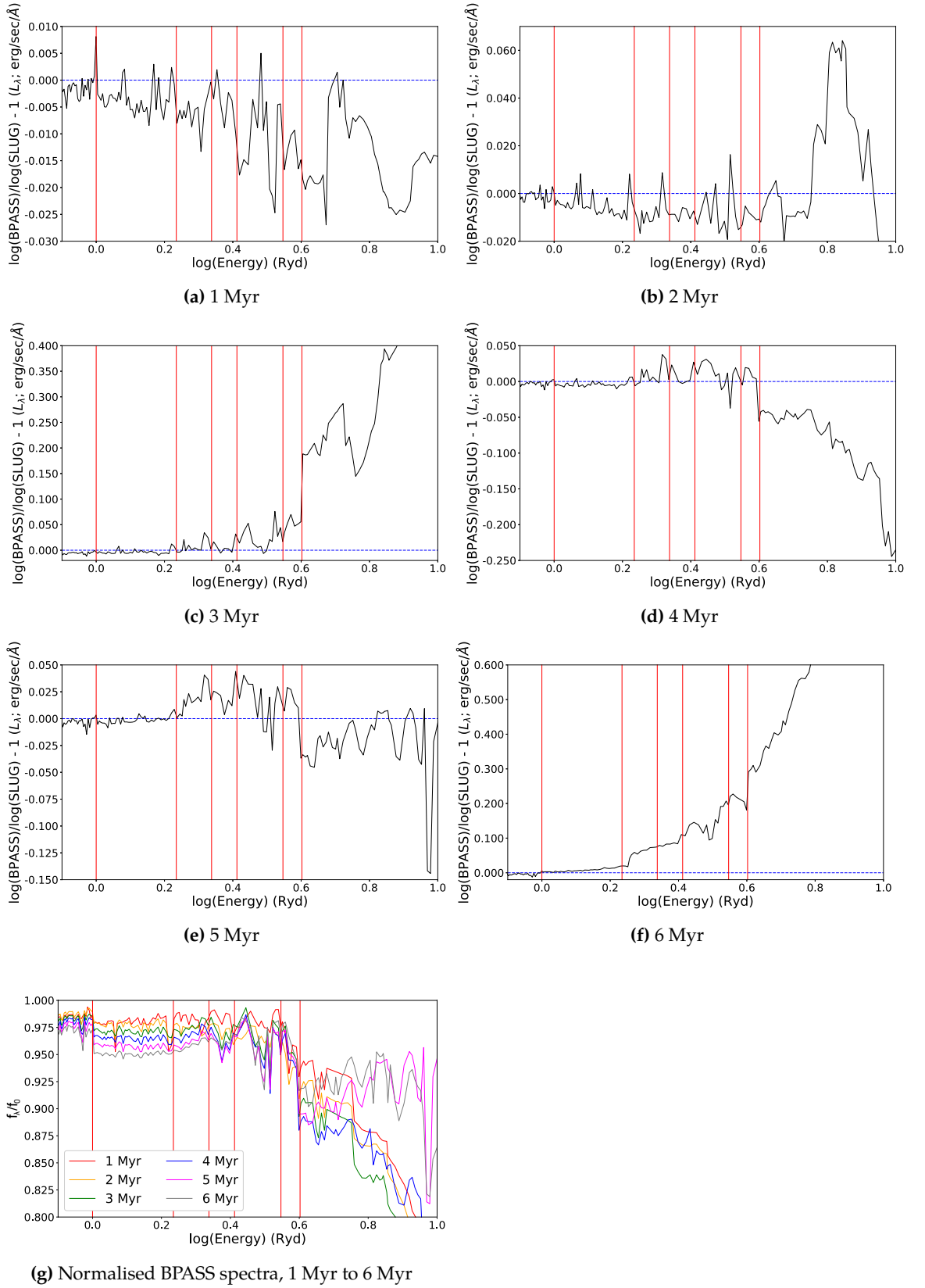


Figure 2.11 Relative difference between spectra of an instantaneous SFH $10^6 M_{\odot}$ cluster computed with BPASS and SLUG. The relative difference is shown at ages of 1 – 6 Myr inclusive, in increments of 1 Myr. Instantaneous SFH binary cluster spectra produced with BPASS for each age are shown in panel (g). f_{λ} in panel (g) represents the individual input spectra, and f_0 is the blackbody spectrum shown in Figure 2.3. The red vertical lines represent the ionisation potentials of important ISM species; from left to right: H^0 , S^+ , N^+ , O^+ , C^{2+} , He^+ .

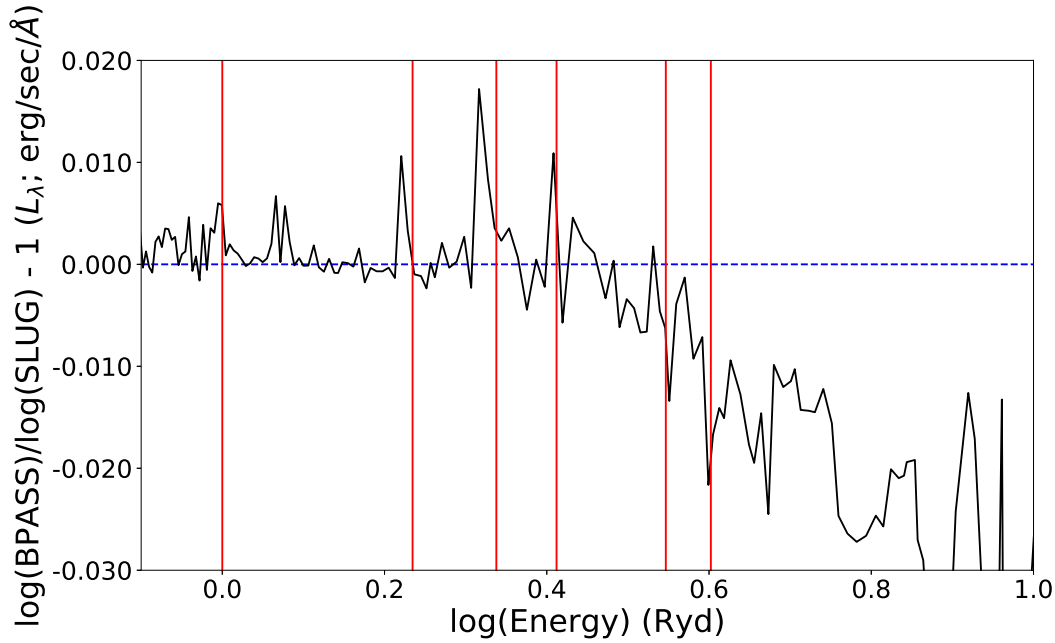


Figure 2.12 Relative difference between the spectra of BPASS and SLUG for a continuous SFH cluster at $Z = 0.020$ and at an age of 5 Myr. The red vertical lines represent the ionisation potentials of important ISM species; from left to right: H^0 , S^+ , N^+ , O^+ , C^{2+} , He^+ .

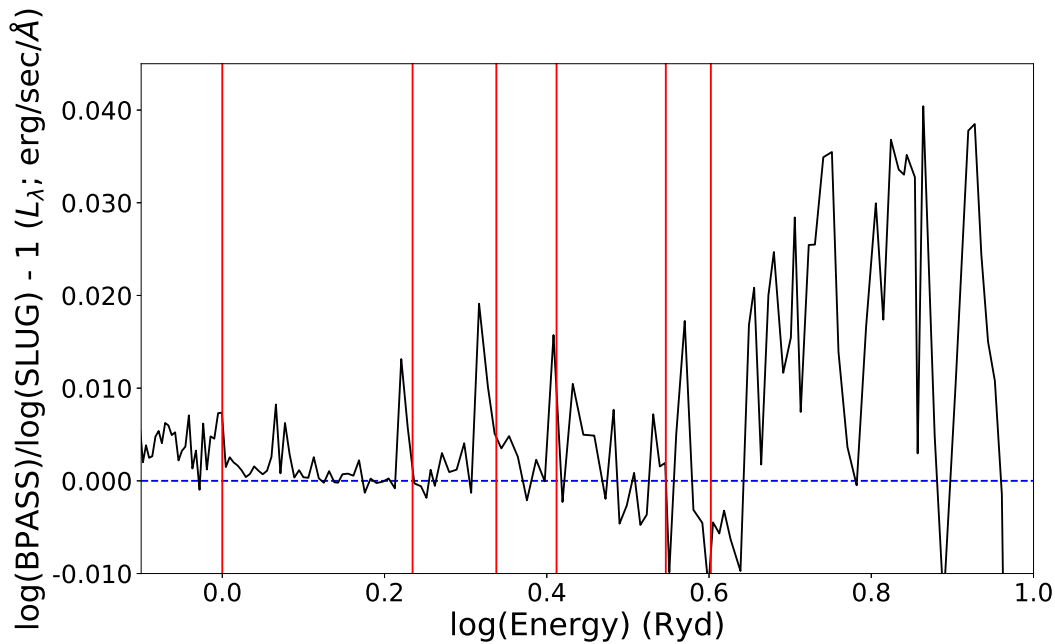


Figure 2.13 Relative difference between the spectra of BPASS and SLUG for a continuous SFH cluster at $Z = 0.020$ and at ages for which the stellar spectrum has reached equilibrium (5 Myr for SLUG, and 10 Myr for BPASS, seen in Figure 2.14a). The red vertical lines represent the ionisation potentials of important ISM species; from left to right: H^0 , S^+ , N^+ , O^+ , C^{2+} , He^+ .

from SLUG increases drastically between cluster ages of 3 and 4 Myr, coinciding with the emergence of W-R stars in the cluster. As a result, SLUG spectra at these ages are harder than those from BPASS. However, as high-mass stars and W-R stars reach the end of their lives at $\sim 5 - 6$ Myr in the single-star population produced with SLUG, W-R stars in the binary population produced with BPASS still continue to emerge, continuing to increase the far-UV (FUV) photon flux. Hence, BPASS spectra are harder than SLUG spectra at ages beyond 5 Myr. The relative difference in the spectra for continuous SFH populations between SLUG and BPASS shown in Figure 2.12 shows BPASS to produce a larger flux for photons of lower energies, with SLUG providing a harder flux for photons with energies $\gtrsim 0.6$ in $\log(E/\text{ryd})$. Ultimately, SLUG and BPASS use different models for the stellar tracks and atmospheres, which inevitably lead to differences in the output spectra. Treatments for W-R stars differ between the two SPS codes owing to the use of disparate atmospheres to model W-R star atmospheres; hence relative differences in the spectra between the two SPS codes are to be expected, particularly in the FUV part of the spectrum. Differences in synthesis procedure such as the aforementioned stellar track sampling, interpolation method, and stellar atmosphere grid sampling are also very important in the differing spectra produced using the two codes, for all other identical input parameters.

The high-energy region of the spectrum ($\sim 0.6 - 1$ in $\log(E/\text{ryd})$) produced by BPASS is still relevant up to an age of 6 Myr, seen in Figures 2.11f and 2.11g. This is in stark contrast to the spectra produced by SLUG up to similar cluster ages, where luminosity decreases rapidly in the same region of the spectrum as a result of high-mass star and W-R star deaths. We only consider BPASS cluster ages up to and including 6 Myr in order to directly compare with the clusters produced using SLUG. However, we note that significant ionising radiation produced by clusters simulated with BPASS is present from clusters of ages beyond 6 Myr. Wofford et al. (2016) show that BPASS models at varying metallicity continue to produce ionising radiation at cluster ages beyond 10 Myr, stating three main processes for the sustainment of ionising radiation at later ages. Firstly, stars in binary systems may be ‘rejuvenated’ towards the end of their lifetimes through mass transfer as a result of Roche lobe overflow (RLOF; e.g. Dray & Tout 2007, and references therein). Hence, the rejuvenated star appears younger and may evolve similarly to a younger star of its new mass (although this is not always the case; Dray & Tout 2007). Second, and similarly to rejuvenation through mass transfer, binary stars may be rejuvenated through mergers, thus forming a single star that appears younger than the original age of the binary system (e.g. Schneider et al. 2016, and references therein). These two rejuvenation processes cause higher-mass stars to be present at later ages of the simulation, far beyond the time frames expected with single stellar models. The third process is envelope removal from RLOF, leading to low-luminosity W-R stars and helium stars at later ages than found in single stellar clusters. Note that envelope removal will typically lead to low-luminosity W-R stars of high- Z and/or high-luminosity (and subsequently high mass) owing to a thin hydrogen layer remaining, which requires removal from sufficiently high stellar winds (Smith 2014; Trani et al. 2014, and references therein).

We adopt an age of 5 Myr for a stellar cluster undergoing constant star formation at a rate of $1M_{\odot} \text{ yr}^{-1}$ for our fiducial model because 5 Myr is the age at which the spectrum from a continuous SFH stellar population reaches equilibrium (Kewley et al. 2001). Also, when considering a single stellar cluster, we neglect the spectra from ages beyond 6 Myr

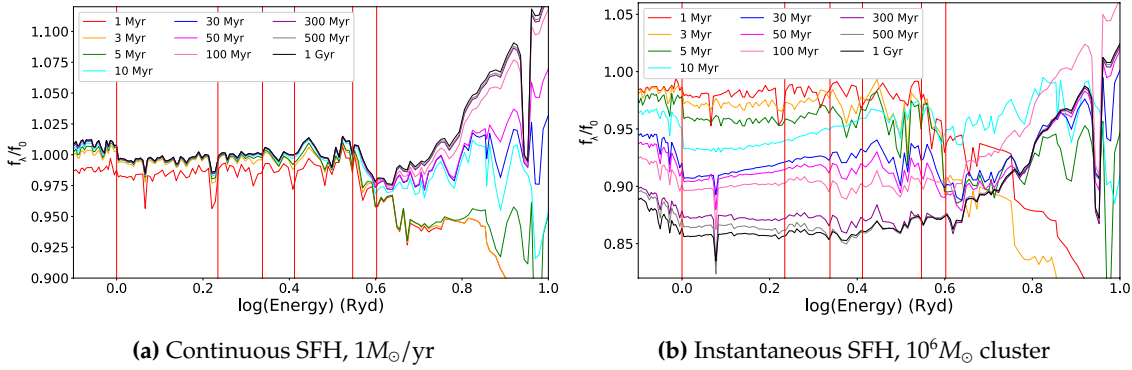


Figure 2.14 Spectra of clusters produced with BPASS assuming a continuous and instantaneous SFH in panels (a) and (b), respectively. f_λ represents the individual input spectra, and f_0 is the blackbody spectrum shown in Figure 2.3. The red vertical lines represent the ionisation potentials of important ISM species; from left to right: $\text{H}^0, \text{S}^+, \text{N}^+, \text{O}^+, \text{C}^{2+}, \text{He}^+$.

owing to the considerable decrease in ionising radiation at these ages (e.g. Wofford et al. 2016, and Figure 2.4). We note, however, that these ages associated with continuous and instantaneous SFH are based on single stellar clusters. Shown in Figure 2.14 are spectra produced using BPASS for clusters assuming both continuous and instantaneous SFHs. It is evident from Figure 2.14 that binary populations reach equilibrium at much later times than single-star populations, for the same three reasons (rejuvenation, mergers, and envelope removal) mentioned earlier. From Figure 2.14a, it can be seen that different regions of the spectrum produced by a continuous SFH binary population reach equilibrium at different ages. Up until the He II continuum (below ~ 0.6 in $\log(E/\text{ryd})$), the shape of the spectrum stabilises at an age of roughly 10 Myr. At energies within the He II continuum, however (above ~ 0.6 in $\log(E/\text{ryd})$), the spectrum only begins to approach a constant shape and luminosity at ages approaching 1 Gyr. This is a result of the unpredictability of W-R and He star emergence in binary clusters, which drastically increase the flux in the FUV part of the spectrum.

Figure 2.13 shows the relative difference in the spectra between the two SPS codes for a metallicity of $Z = 0.020$, at ages for which the stellar spectrum has reached equilibrium (5 Myr for SLUG, 10 Myr for BPASS). At these ages, the spectrum produced from BPASS is almost uniformly more luminous for all photon energies than that produced using SLUG, supporting the findings of Stanway et al. (2016).

W-R and He star emergence and impact are seen more clearly when considering the evolution of a single binary cluster (Figure 2.14b). For high-metallicity ($Z = 0.014$) BPASS models, Wofford et al. (2016) show a gradual decrease in the number of H^0 - and He^0 -ionising photons with increasing age. However, distinct increases in the number of He^+ -ionising photons emitted by the binary cluster are seen at ~ 10 Myr and again at ~ 80 Myr (their Figure 2). This is supported through Figure 2.14b, showing distinct increases in the spectrum luminosity at ages of 10 Myr and 80 Myr for energies > 0.6 in $\log(E/\text{ryd})$, while showing a constant gradual decrease in the spectrum luminosity for lower energies.

2.6.2. BPT Diagrams

SFH and Age

Figure 2.15 shows the $\log(q(N)/(\text{cm s}^{-1})) = 7.25$ branch of the photoionisation models for both a continuous and instantaneous SFH cluster at varying ages. We show variation with age in a continuous SFH cluster using both the Geneva HIGH tracks and the Padova TP-AGB tracks in Figures 2.15(a) and (b), respectively. In general, the $[\text{O III}]/\text{H}\beta$ and $[\text{N II}]/\text{H}\alpha$ emission-line ratios decrease with age when assuming a continuous SFH. This decrease in the emission-line ratios corresponds to aging stellar populations that produce a softer spectrum, as well as continually emerging young stellar populations that produce a higher flux in hydrogen recombination lines such as $\text{H}\alpha$ and $\text{H}\beta$. Eventually, however, the shape and position of the photoionisation models stabilises, as the stellar population reaches equilibrium. The age at which this stabilisation occurs differs for the two sets of tracks. The age of stabilisation for models using the Geneva HIGH tracks was found to be 8 Myr by Kewley et al. (2001). This age agrees with our models using the Geneva HIGH tracks in Figure 2.15a. Kewley et al. (2001) also find the age of stabilisation for models using the Padova tracks to be 6 Myr, albeit using an earlier version of the stellar track models described by Bressan et al. (1993). Figure 2.15b appears to show different ages of stabilisation for different model metallicities. At low metallicity, the models only truly stabilise at 10 Myr. At higher metallicity ($Z = 0.020$), the age of stabilisation is roughly 6 Myr. At the maximum metallicity used in the Padova tracks ($Z = 0.050$), the position and evolution of the grids are never seen to stabilise for the ages used. If desiring a stellar age for which models using the Padova TP-AGB tracks are stable, an age of 10 Myr should be chosen. Sources such as Charlot & Longhetti (2001) and Feltre et al. (2016) show that in general 10 Myr is the age at which 99.9% of ionising photons have been released for a single stellar generation; thus, no further evolution in the shape of the ionising spectrum is seen past 10 Myr.

With no new stellar populations emerging within the cluster, the instantaneous SFH models never reach a stabilisation point. The emission-line flux ratios for the models shown in Figure 2.15c continually decrease with age, excluding the ages for which the hardness of the spectrum increases with the emergence of W-R stars. W-R stars are more abundant in higher-metallicity environments, believed to be the result of mass-loss rate dependence on metallicity (Crowther 2007; Mokiem et al. 2007; Georgy et al. 2015). Hence, the BPT emission-line flux ratios show a larger increase as the metallicity in the models increases, due to the presence of W-R stars. Considering the ages at which W-R stars do not contribute to the spectra, the emission-line flux ratios decrease with age faster for increasing metallicity. Higher-metallicity stars spend a larger fraction of photons ionising the more abundant metals in their atmospheres. Therefore, there are fewer ionising photons emitted from stars in order to ionise and excite the surrounding ISM for increasing metallicity (Snijders et al. 2007).

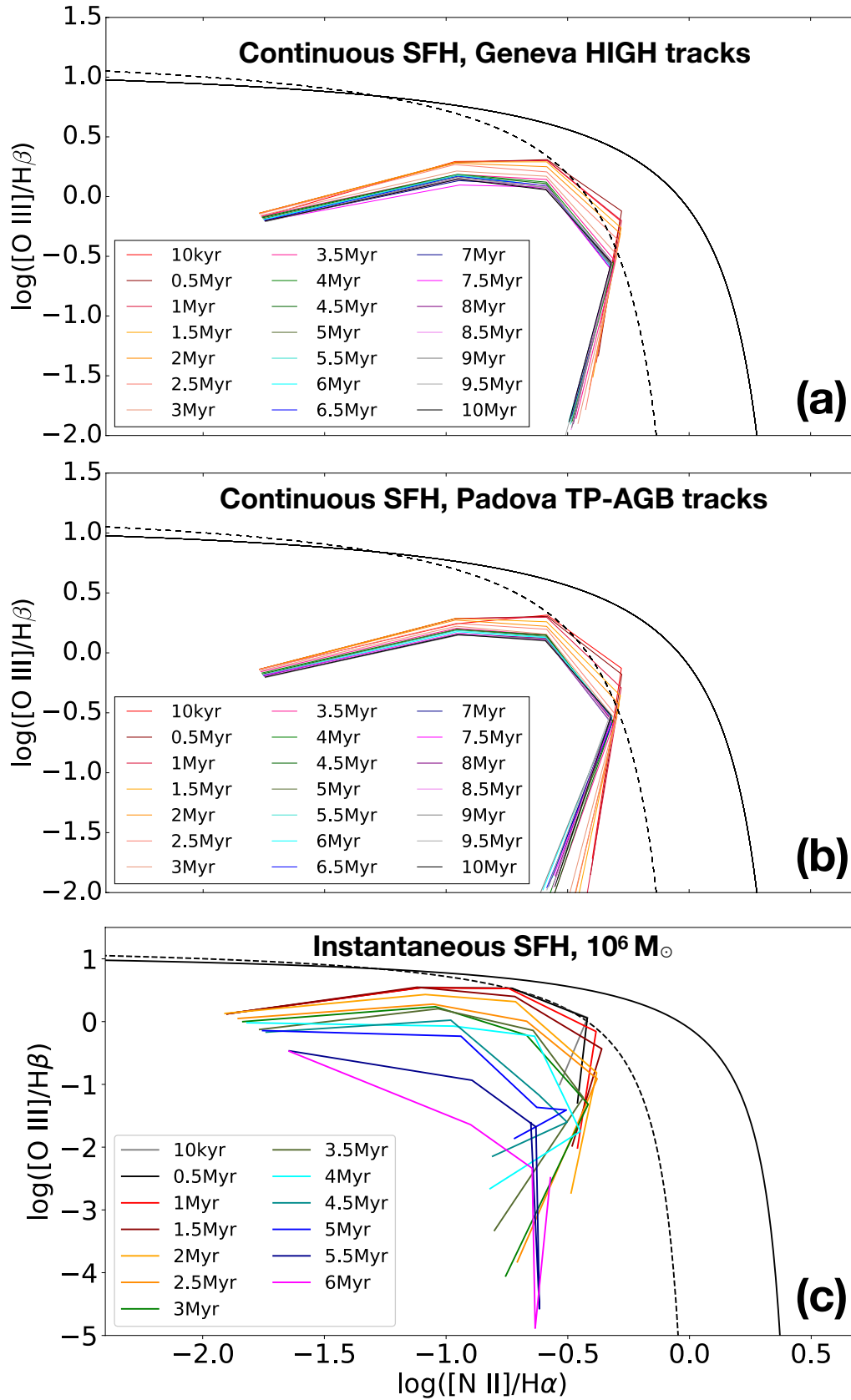


Figure 2.15 The $\log(q(N)/(\text{cm s}^{-1})) = 7.25$ branch shown at varying ages for continuous SFH clusters in panels (a) and (b), and an instantaneous SFH cluster of mass $10^6 M_{\odot}$ in panel (c). Panel (a) is a continuous SFH cluster using the Geneva HIGH stellar tracks, while panel (b) uses the Padova TP-AGB tracks. Ages for the continuous SFH cluster extend from 0 Myr (10 kyr) to 10 Myr in 0.5 Myr increments. Ages for the instantaneous SFH cluster range from 0 Myr (10 kyr) to 6 Myr in 0.5 Myr increments.

Stellar Evolutionary Tracks

Model grids incorporating both the Geneva HIGH and Padova TP-AGB stellar tracks for a continuous SFH population at an age of 5 Myr can be seen together in Figure 2.16a. Overall, the grids are extremely similar, with the largest difference apparent at the high-metallicity end. Recall that the two sets of stellar tracks differ in their allocation of highest metallicity. The Geneva tracks use a high metallicity of $Z = 0.040$, whereas the Padova tracks use a final metallicity of $Z = 0.050$. Therefore, a difference in the emission-line flux ratios at the high-metallicity end of the model grids is expected owing to the increased ionisation of stellar atmospheric metals and hence inhibition to ionise and excite the surrounding ISM (Snijders et al. 2007). The Geneva and Padova tracks also differ at the low-metallicity end ($Z = 0.001$ and 0.0004 respectively), yet the difference in the emission-line flux ratios between the two tracks is negligible. The reasoning for this is computational, rather than physical. The lowest metallicity available for use in both the Kurucz and Pauldrach atmospheres is $Z = 0.001$. Hence, SLUG proceeds with the calculation of the ionising spectrum using this value, setting the low-metallicity end of the Padova tracks equal to that of the Geneva tracks. At the common metallicities between the two sets of tracks, the emission-line flux ratios from the Padova tracks are higher than those for the Geneva tracks. This modest difference in emission-line flux ratio between the Padova and Geneva tracks is a result of the slightly increased temperature (~ 0.03 dex; Vázquez & Leitherer 2005) present in the Padova tracks. An increase in temperature enhances the collisional rate in the nebula, leading to an increase in the fluxes of collisionally excited lines such as [O III] and [N II]. Differences may be larger for instantaneous bursts in the W-R phase.

Stellar Atmospheres

The photoionisation model grids using each of the atmospheres we consider are shown in Figure 2.16b. A slight increase in emission-line ratios is seen in the Kurucz + Hillier grid when compared to the Kurucz grid, following the increased W-R strength added by Hillier & Miller (1998). The largest difference between these two atmospheres seen in Figure 2.16b is ~ 0.1 dex in both emission-line ratios, seen at higher metallicities. Since W-R stars are likely to be found in higher-metallicity environments (Leitherer et al. 1999; Crowther et al. 2006; Crowther 2007; Georgy et al. 2015, and references therein), the increase in the emission-line ratios primarily towards the higher-metallicity end of the grid is expected. However, a maximum increase in emission-line flux ratio of 0.1 dex is still small, despite a factor of 2–5 increase in the strength of the flux emitted from W-R stars in the Hillier atmospheres. With $\sim 10\%$ the amount of W-R stars as O stars in the cluster (Leitherer et al. 1999), the W-R flux increase added by Hillier & Miller (1998) is noticeable, yet small nonetheless. Hence, changes in emission-line strength are not significant.

The improvements to line blanketing made by Pauldrach et al. (2001) overall lead to a cooler nebula when the Pauldrach atmospheres are added to the Kurucz atmospheres; the ionic temperatures of O^{2+} and N^+ decrease by $\sim 3\%$ at a metallicity of $Z = 0.020$ and $\sim 6\%$ at a metallicity of $Z = 0.040$. This decrease in temperature is small, yet it nevertheless results in a noticeable difference in the emission-line ratios in Figure 2.16b. For almost all metallicities in the models (with the exception of $Z = 0.001$, where the effects of line

blanketing are negligible), the difference in the $[\text{N II}]/\text{H}\alpha$ line ratios between the Kurucz and Kurucz + Pauldrach atmospheres becomes larger, towards a maximum of ~ 0.2 dex. The lower temperature of the nebula results in a lower collisional excitation rate, leading to a decreased flux of $[\text{N II}]$ provided by the Kurucz + Pauldrach atmospheres. The $[\text{O III}]/\text{H}\beta$ line ratios, however, tend to increase with metallicity when Pauldrach atmospheres are added, up to $Z = 0.040$, where they experience a sharp decrease (~ 0.4 dex). The spectra in Figure 2.6 show that adding Pauldrach atmospheres results in a small increase in the luminosity of the spectrum at the ionisation potential of O^+ , leading to an increased abundance of O^{2+} ions in the nebula. Meanwhile, the spectra show no such feature at the ionisation potential of N^0 , resulting in no significant increase in the abundance of N^+ ions in the nebula. Despite the cooler nebular temperature, the increase in the number of O^{2+} ions provides a larger $[\text{O III}]$ flux and hence $[\text{O III}]/\text{H}\beta$ ratio. At a metallicity of $Z = 0.040$, the effects of line blanketing become more prominent. When combined with the decrease in temperature already expected from an increase in the abundance of metals, the collisional excitation rate decreases further, resulting in lower $[\text{O III}]/\text{H}\beta$ ratios than seen when using the Kurucz atmospheres.

The model produced using the combination of all three atmospheres very closely resembles the model produced using the Kurucz + Pauldrach atmospheres. With a W-R/O ratio of $\sim 10\%$, the emission-line strength increase from the Hillier atmospheres is only relevant for $\sim 10\%$ of the total stars at higher metallicities. Hence, the W-R atmospheric additions from the Hillier atmospheres are dwarfed by the OB atmospheric additions from the Pauldrach atmospheres, resulting in a small difference in emission-line ratios between the Kurucz + Pauldrach atmospheres and the Kurucz + Hillier + Pauldrach atmospheres.

SPS Codes

Single stellar populations Shown in Figure 2.16c are the two grids produced using SLUG and SB99. Overall the grids are similar, with a difference of ~ 0.1 dex at high metallicity in the $[\text{O III}]/\text{H}\alpha$ and $[\text{N II}]/\text{H}\beta$ line ratios, and negligible difference at low metallicity. A systematic offset is present in Figure 2.16c, as a result of SB99 producing a slightly harder stellar spectrum for a continuous population at 5 Myr (Figure 2.8). Fig. 2.16c shows that SLUG and SB99 produce models that agree to within 0.1 dex on the BPT diagram. This offset is within the error range typically assumed through photoionisation modelling (~ 0.1 dex; e.g. Kewley et al. 2001).

Stochastic sampling of IMF The photoionisation grids for $10^4 M_\odot$ and $10^6 M_\odot$ clusters produced using SLUG and SB99 are shown in Figure 2.17. The varying shape of the stellar spectrum between clusters of masses $10^4 M_\odot$ and $10^6 M_\odot$ when produced stochastically with SLUG leads to differences in emission-line ratios and hence photoionisation grids of varying shape. The differences in the emission-line ratios for the grids of differing cluster mass produced using SLUG range from < 0.1 to ~ 0.5 dex. Conversely, the grids that use spectra produced using SB99 are identical. Figure 2.17 shows that clusters of mass 10^4 and $10^6 M_\odot$ synthesised using SB99 produce spectra that are identical in shape, differing only by a scale factor in luminosity. Luminosity is negligible in the creation of BPT photoionisation grids, because both BPT line ratios contain emission lines from the Balmer sequence. The

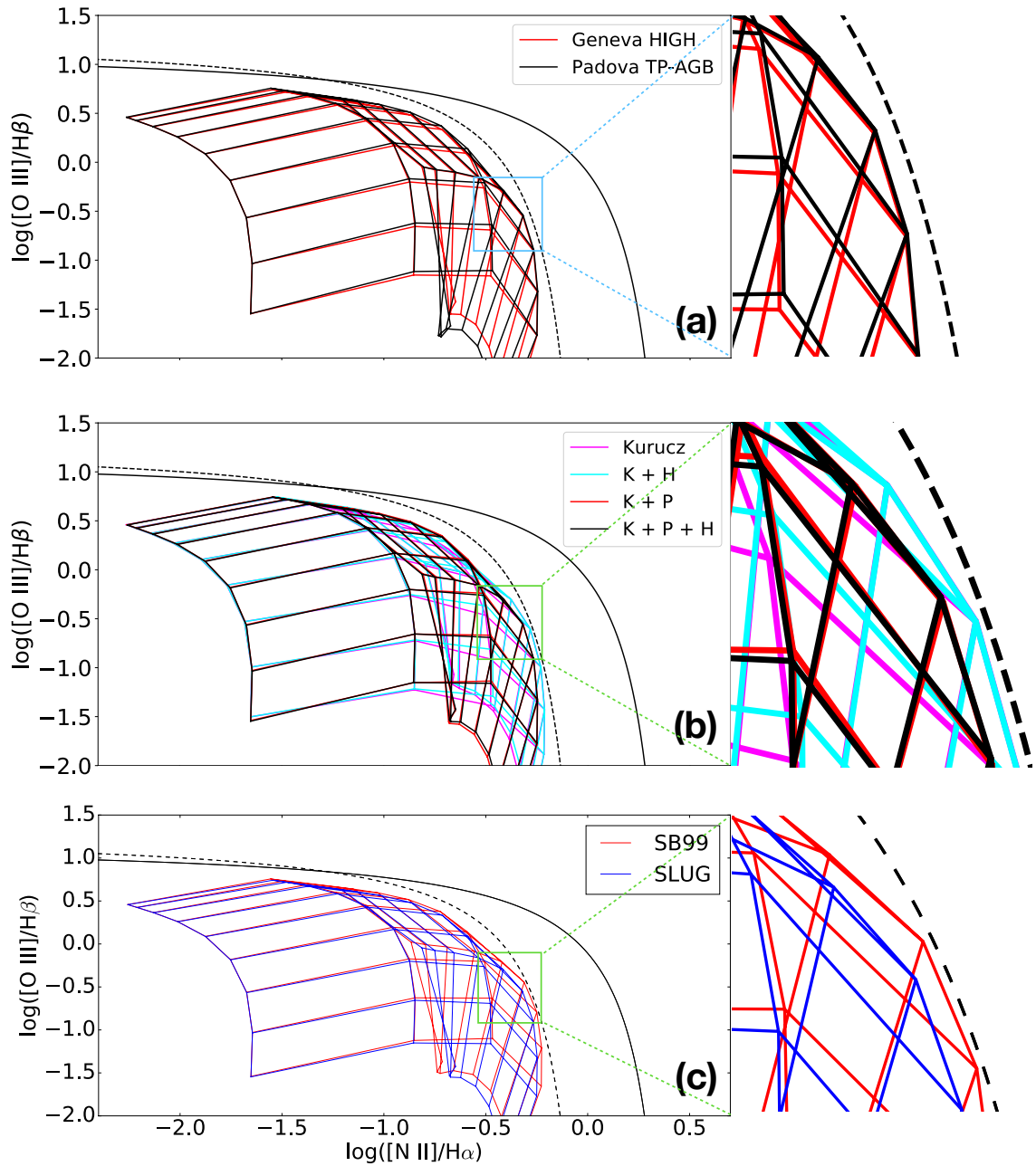


Figure 2.16 (a) Model grids produced using both the Geneva HIGH tracks and the Padova TP-AGB tracks for a continuous SFH population at age 5 Myr. (b) Model grids produced using different stellar atmospheres for a continuous SFH population at 5 Myr. The atmospheres included in the models are Kurucz, Kurucz + Hillier (K + H), Kurucz + Pauldrach (K + P), and Kurucz + Hillier + Pauldrach (K + H + P). (c) Model grids produced using SLUG and SB99. All parameters associated with these grids are fiducial.

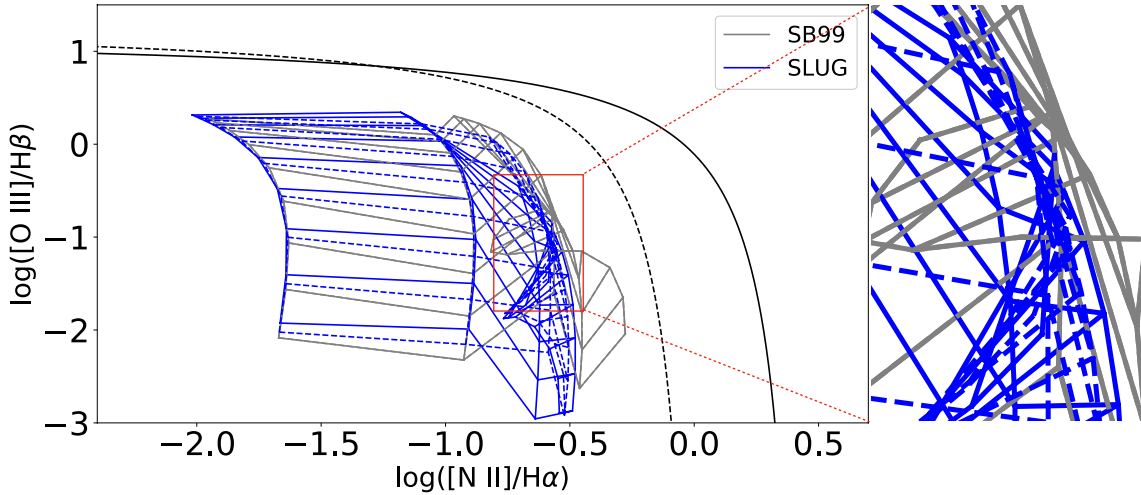


Figure 2.17 Instantaneous SFH grids of ages 5 Myr produced by SLUG and SB99, for cluster masses of $10^4 M_{\odot}$ (solid) and $10^6 M_{\odot}$ (dashed). The stochastic sampling of the IMF demonstrated by SLUG produces spectra of different shapes for clusters at 10^4 and $10^6 M_{\odot}$, leading to differences in the emission-line ratios. The lack of stochastic IMF sampling shown by SB99 leads to identically shaped ionising spectra for the $10^4 M_{\odot}$ and $10^6 M_{\odot}$ clusters, as shown in Figure 2.10.

flux of Balmer lines is directly proportional to the ionising radiation emitted by the stellar cluster (e.g. [Dopita et al. 2002c](#), and references therein). Hence, calculating the emission-line ratios with lines from the Balmer series removes luminosity dependence on the BPT diagram. Thus, the $10^4 M_{\odot}$ and $10^6 M_{\odot}$ grids have identical values of emission-line ratios for each grid point, leading to equal grids.

Binary populations Shown in Figure 2.18a are model grids produced using input spectra from BPASS and SLUG, using the remaining fiducial parameter set. Overall, the differences in emission-line ratios for a 5 Myr old continuous SFH cluster are small between BPASS and SLUG, with the largest differences occurring at high metallicity. The largest difference in the emission-line ratios between the two grids is ~ 0.1 dex in the $[\text{N II}]/\text{H}\alpha$ ratio and ~ 0.2 dex in the $[\text{O III}]/\text{H}\beta$ ratio, with SLUG producing the larger emission-line ratios. Figure 2.18a shows that, in general, at an age of 5 Myr for both single-star and binary clusters, the spectrum produced with SLUG produces emission-line ratios that are slightly greater than those produced by BPASS. However, at an age of 5 Myr, the binary cluster has yet to reach equilibrium. As shown in Section 2.6.1, the age at which the continuous SFH binary cluster simulated using BPASS reaches equilibrium is at ~ 10 Myr. Figure 2.18b shows model grids produced using input spectra from SLUG and BPASS, for ages at which both the single-star and binary clusters are at equilibrium (5 Myr for SLUG, 10 Myr for BPASS). At these ages, the emission-line ratios from the BPASS model are consistently higher (albeit by small amounts; less than 0.1 dex in emission-line ratio) than those from the SLUG model across all metallicities covered in the models. This is consistent with the findings of [Stanway et al. \(2016\)](#), concerning a boosted ionising photon flux in binary populations when compared to single-star populations. A harder ionising radiation field leads to a higher average nebular temperature and hence an increase in the collisional rate of ions, increasing the flux of collisionally excited lines such as $[\text{O III}]$ and $[\text{N II}]$.

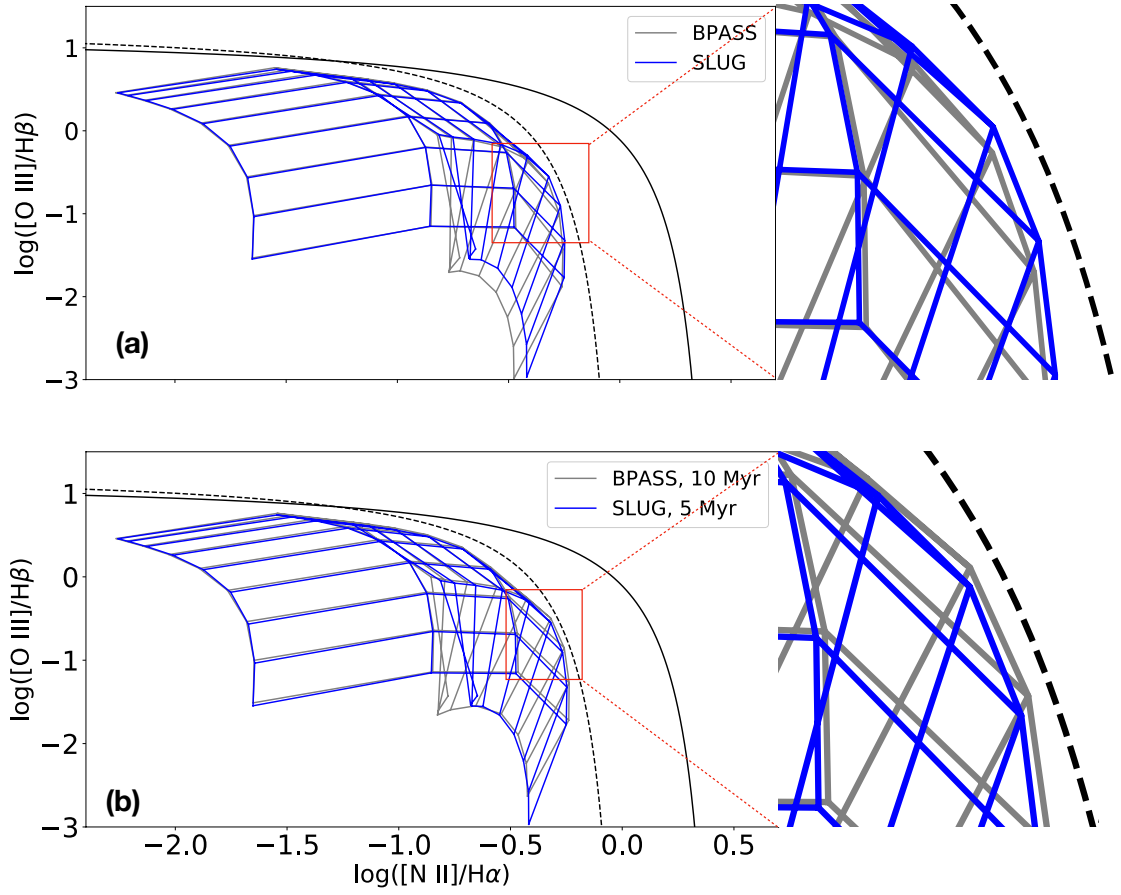


Figure 2.18 (a) Model grids produced using BPASS and SB99, both assuming a continuous SFH at an age of 5 Myr. (b) Model grids produced using BPASS and SB99, using SLUG and BPASS continuous SFH input spectra at ages for which the respective stellar cluster reaches equilibrium. All remaining parameters associated with these grids are fiducial.

Pressure and Density

We vary the P/k value by varying the initial electron density of the H II region, assuming an initial temperature of 8000K. This was partially explored by [Nicholls et al. \(2014\)](#), where they show that a higher P/k value increases the strength of certain emission-line ratios. Here we explore this further, sampling a pressure ranging from P/k values of $8 \times 10^3 \text{ cm}^{-3} \text{ K}$ to $8 \times 10^7 \text{ cm}^{-3} \text{ K}$ in steps of 1 dex, corresponding to initial densities of $n = 1, 10, 100, 1,000,$ and $10,000 \text{ cm}^{-3}$ (assuming an inner initial temperature of $T_e = 8000 \text{ K}$). It should be noted that a density of $n = 10,000 \text{ cm}^{-3}$ is far higher than the densities observed in local galaxies (see Section 2.5.4), and hence the models produced assuming a density of $n = 10,000 \text{ cm}^{-3}$ do not apply to the SDSS sample.

Seen in Figure 2.19, the BPT line ratios increase with pressure in general. The increase in line ratio with pressure is more noticeable at high metallicity. At high metallicity, the nebula is more susceptible to the effects of cooling, due to an increased abundance of coolants. At very low pressures ($\log(P/k) \sim 5$ and below), the density in the nebula is still below the critical density of several strong cooling lines (namely, [C II] $157.7 \mu\text{m}$, [N II] $205.3 \mu\text{m}$, and [O III] $88.4 \mu\text{m}$; e.g. [Abdullah et al. 2017](#)), allowing cooling to occur, which decreases the temperature at high metallicity. Hence, the strength of collisionally excited

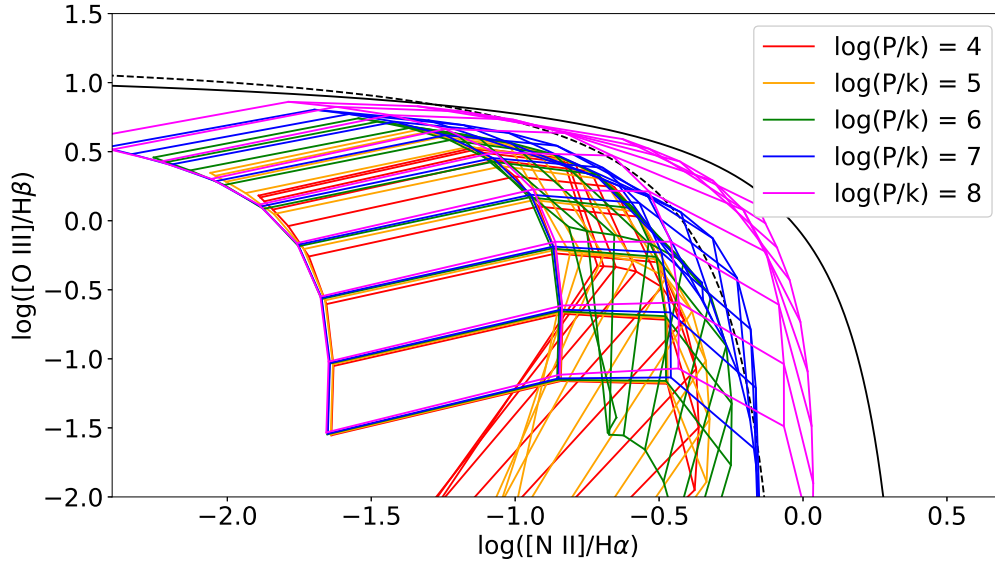


Figure 2.19 Model grids of varying pressure for a continuous SFH population at age 5 Myr, from $P/k = 8 \times 10^3$ ($\log(P/k) \sim 4$) to $P/k = 8 \times 10^7 \text{ cm}^{-3} \text{ K}$ ($\log(P/k) \sim 8$), in increments of 1 dex.

lines such as $[\text{N II}]$ and $[\text{O III}]$ is weakened. An increase in pressure, however, begins to suppress the fine-structure far-infrared cooling lines through collisional de-excitation, which increases the temperature. Our models show the $[\text{C II}] 157.7\mu\text{m}$ and $[\text{N II}] 205.3\mu\text{m}$ lines to be the dominant cooling lines affected, with both decreasing in flux by a factor of 100 from a pressure of $8 \times 10^3 \text{ cm}^{-3} \text{ K}$ to $8 \times 10^7 \text{ cm}^{-3} \text{ K}$. The rise in temperature then increases the strength of collisionally-excited lines, leading to increased line ratios on the BPT diagram. Due to the low abundance of coolants at low metallicity, this effect is still present, yet much weaker.

Shown in Figure 2.20 are the three models of the highest pressure taken from Figure 2.19, superimposed on the SDSS data. Figure 2.20 shows that the star-forming datapoints in the SDSS sample are well described by models with $\log(P/k) \sim 6$.

Boundedness

We explore the changes in emission-line ratios as the models progress from radiation-bounded situations to density-bounded ones. To do this, we study the evolution of the models as a function of optical depth, as well as the evolution as a function of hydrogen recombination percentage at the point of truncation. Both sets of models can be explained through the same process. Shown in Fig. 2.21 are the relative ionic fractions of individual species as a function of distance through the H II region for $\log(q) = 6.5$ and $Z = 0.004$. Figure 2.21 shows that truncating the model at earlier values of hydrogen recombination means truncating at a smaller distance into the nebula, which corresponds to a lower optical depth within the H II region. The models that vary with hydrogen recombination percentage allow us to study the differences along the ionisation front in the H II region much more finely than we can with the optical depth models.

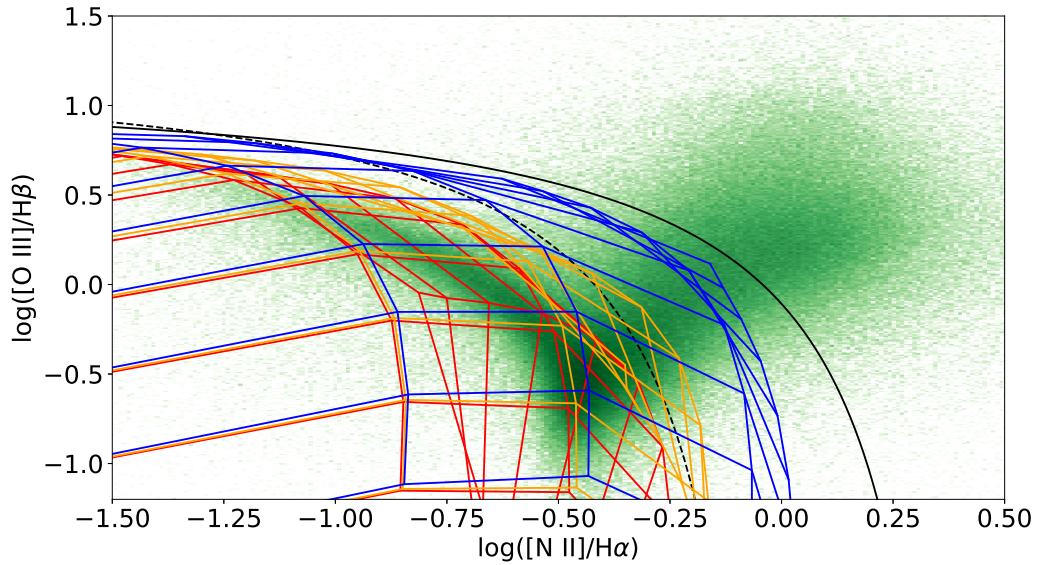


Figure 2.20 Grids of the three highest pressures (red $\Rightarrow P/k = 8 \times 10^5$, orange $\Rightarrow P/k = 8 \times 10^6$, blue $\Rightarrow P/k = 8 \times 10^7$) from Fig. 2.19 plotted with the SDSS DR7 sample. The models show that the SDSS star-forming galaxies are well described by models with pressure $\sim 8 \times 10^5 \text{ cm}^{-3} \text{ K}$. All parameters are fiducial.

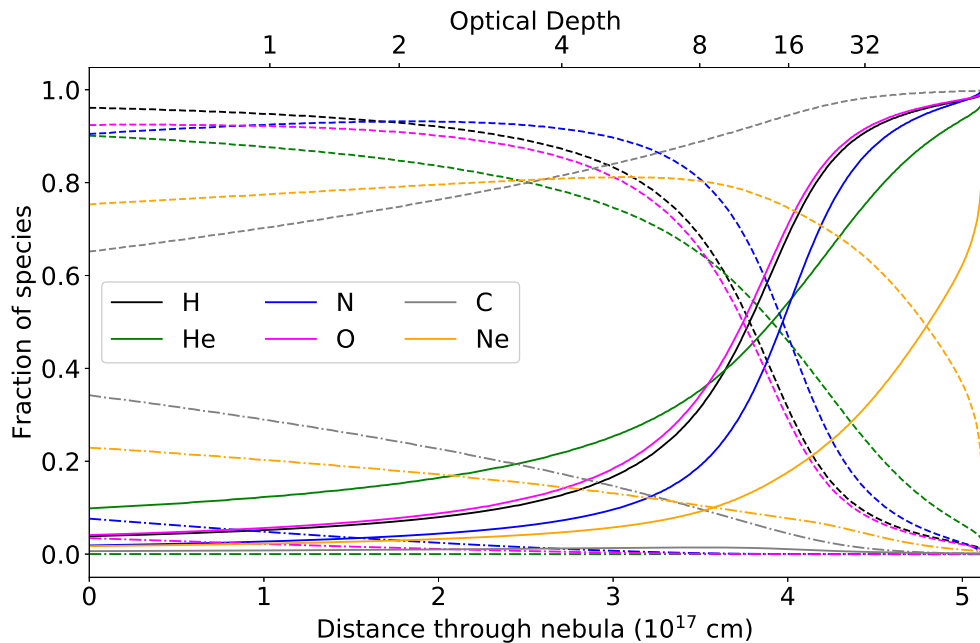


Figure 2.21 Ion fractions of species within the H II region as a function of distance from the ionising source. The corresponding optical depth is also shown. Solid lines show neutral (I) species, dashed lines show singly ionised (II) species, and dot-dashed lines show doubly ionised (III) species. Parameters for this plot are $\log(q) = 6.5$ and $Z = 0.004$. This particular model has been truncated with 1% of H II remaining. All other parameters are fiducial.

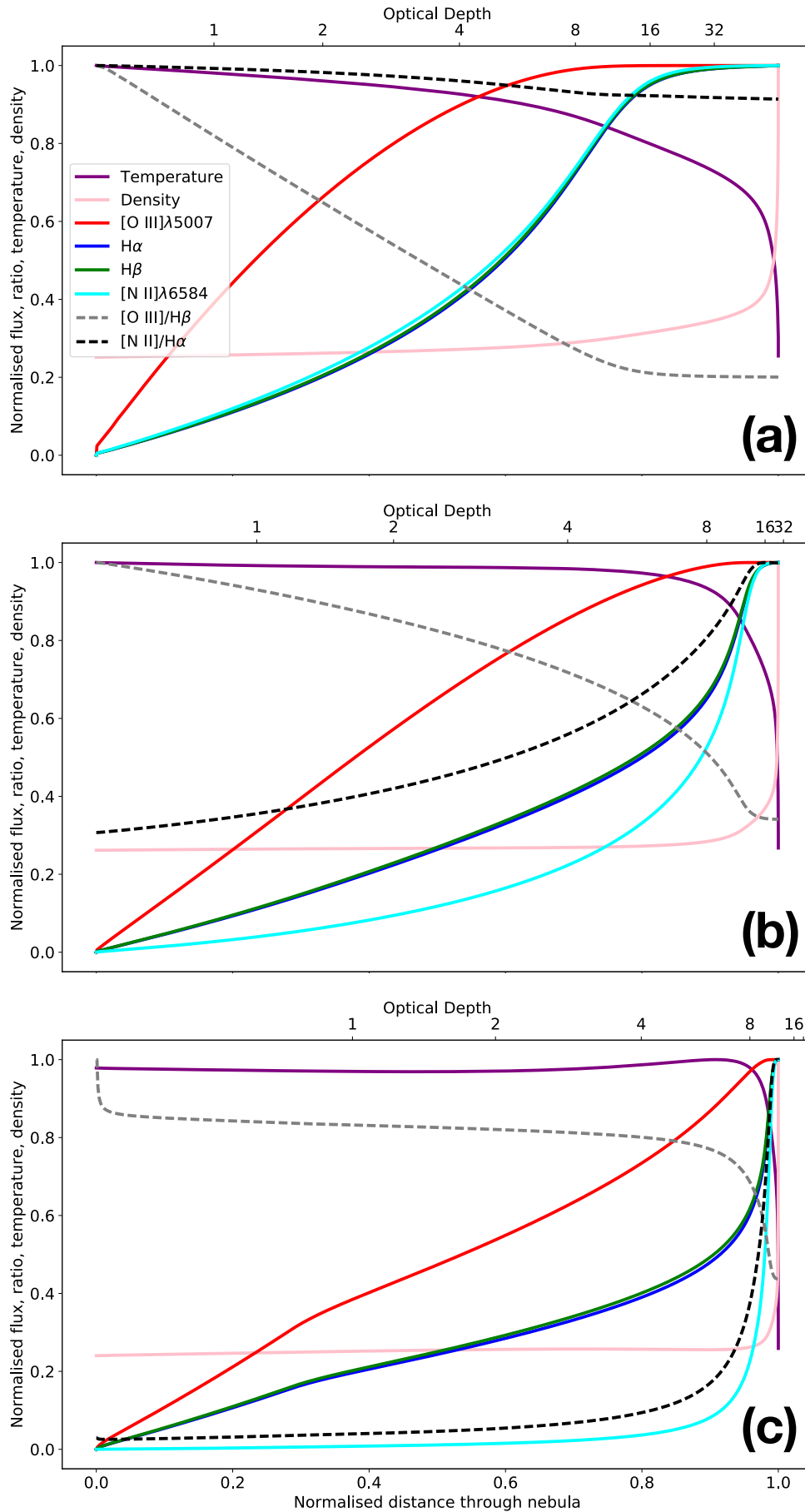


Figure 2.22 Cumulative growth of the BPT emission lines and emission-line ratios as a function of distance through the nebula, normalised to their maximum value, for $\log(q) = 6.5, 7.5$, and 8.5 in panels (a), (b), and (c), respectively. The normalised temperature and density distribution throughout the nebula are also shown. The metallicity for all plots is set to $Z = 0.004$. All other parameters are identical to Figure 2.21.

Figure 2.22 shows the cumulative growth of the BPT emission lines as a function of distance through the nebula, normalised to their maximum value. It also shows the resulting emission-line ratios (also normalised to their maximum value) if the nebula was to be truncated at a given radius, as in the case of density-bounded H II regions. The trends seen in the variation of emission-line ratios with optical depth are reflected in the shape and position of the model grids, shown in Figures 2.23(a) and (b) for hydrogen recombination percentage and optical depth variation, respectively. The optical depth grids in Figure 2.23(b) use the same values of τ as Nicholls et al. (2014), although differences between this work and that presented in Nicholls et al. (2014) include the P/k value, input spectrum, and version of MAPPINGS used (Nicholls et al. 2014 use the MAPPINGS IV photoionisation code; see Dopita et al. 2013; Nicholls et al. 2014, for details). In general, Figure 2.22 shows that the [O III]/H β ratio continues to increase as the optical depth and hydrogen recombination percentage lower. This trend is independent of the value of ionisation parameter, although it is far more noticeable at lower values. The [N II]/H α ratio, however, is seen to either increase or decrease at lower values of optical depth and hydrogen recombination, with a strong dependence on the ionisation parameter. Lower values of the ionisation parameter ($\log(q/(\text{cm s}^{-1})) \sim 6.5$) lead to an increase in the [N II]/H α ratio with decreasing optical depth and hydrogen recombination percentage, whilst at higher values of the ionisation parameter ($\log(q/(\text{cm s}^{-1})) \gtrsim 6.75$), the opposite is seen, with the [N II]/H α ratio decreasing with lowering optical depth.

Upon failure to reproduce the emission-line ratios for all data points in their combined sample, Nicholls et al. (2014) suggest that the off-grid points are the result of H II regions that are optically thin. This is supported by the fact that the majority of the off-grid data points are from the SDSS data release 7 (DR7) subsample from Izotov et al. (2012), which focused on selecting low-metallicity galaxies ($12 + \log(\text{O}/\text{H})$ between ~ 7.1 and ~ 7.9). As mentioned previously, low-metallicity galaxies tend to have a low stellar mass (Tremonti et al. 2004), which corresponds to a higher photon escape fraction from the impact of supernovae (Trebitsch et al. 2017), leading to a lower optical depth. Density-bounded models may provide an explanation for the off-grid data points seen in the SIGRID sample from Nicholls et al. (2014) and in the low-metallicity sample of SDSS from Izotov et al. (2012). Seen in Figure 2.24 is the SIGRID sample from Nicholls et al. (2014) (yellow points), the low-metallicity DR7 SDSS subset from Izotov et al. (2012) (black points), and a further DR3 SDSS subset from Izotov et al. (2006) (red points). Also shown in Figure 2.24 is a radiation-bounded photoionisation model from Nicholls et al. (2014) along with our density-bounded photoionisation model, truncated at an optical depth of $\tau = 1$ and with a pressure of $P/k = 8 \times 10^7 \text{ cm}^{-3} \text{ K}$. Figure 2.24 shows that the density-bounded model describes all of the data points in the Nicholls et al. (2014) SIGRID sample, Izotov et al. (2006) sample, and Izotov et al. (2012) sample simultaneously, suggesting that the metal-poor galaxies in both samples contain optically thin H II regions. A density-bounded regime is necessary to encompass all data points from the Nicholls et al. (2014) combined sample. We show this in Figure 2.25, by comparing the model truncated at $\tau = 1$ from Figure 2.24 with a model truncated at 99% of hydrogen recombination. The density-bounded model shows both decreases in the [N II]/H α ratio and increases in the [O III]/H β ratio, sufficient to explain the low-metallicity data points. A pressure of $P/k = 8 \times 10^7 \text{ cm}^{-3} \text{ K}$ ($\log(P/k) \sim 8$) is necessary to completely encompass all data points seen in Figure 2.24, which is a likely

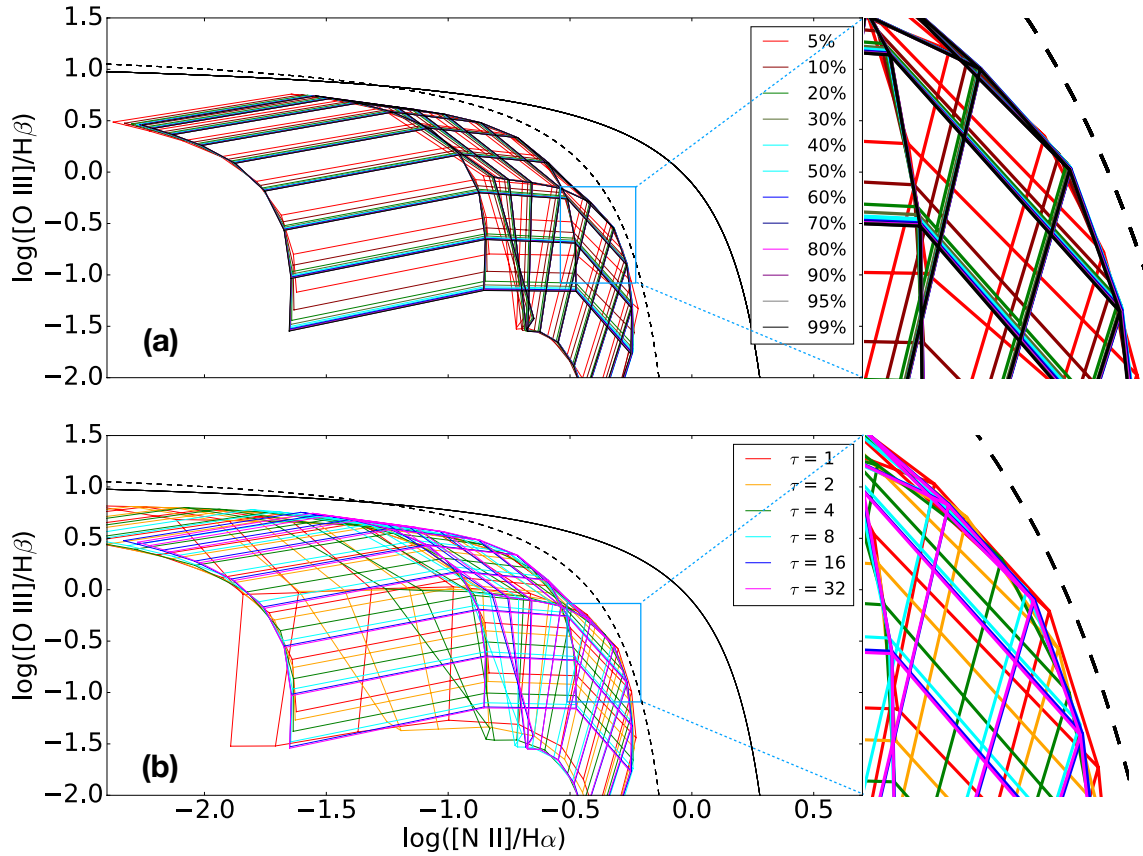


Figure 2.23 (a) Model grids computed with varying H II ionisation bounds, given as percentages. The percentage given is the fraction of H II that has undergone recombination to H I. (b) Model grids computed with varying optical depths at the threshold of hydrogen. The optical depth values used are identical to those used by [Nicholls et al. \(2014\)](#).

unphysical value for the pressure. D. C. Nicholls et al. (in preparation) note a significant X-ray deficit currently exists in H II region modelling spectra, which prevents current H II region models from producing high enough emission-line ratios needed to describe all possible data points – in particular those from the [Nicholls et al. \(2014\)](#) combined sample. D. C. Nicholls et al. (in preparation) aim to resolve this issue by including an X-ray excess in the model spectra.

Comparing MAPPINGS and CLOUDY

We provide a concentrated comparison between the latest models of the two photoionisation modelling codes, MAPPINGS and CLOUDY ([Ferland 1996](#)) version 13.03, described in [Ferland et al. \(2013\)](#). Small-scale comparisons between the two codes have been performed in the past. [Byler et al. \(2017\)](#) compare a constant SFH model grid produced using CLOUDY with the MAPPINGS IV model shown in [Dopita et al. \(2013\)](#). Both models are matched in ionisation parameter and metallicity (except for the highest metallicity in both grids), as well as gas-phase abundance. The two models show agreement in overall coverage of the star-forming region of the BPT diagram, yet there is significant disagreement between points of equal metallicity and ionisation parameter between the models. [Byler et al. \(2017\)](#) suggest that this is due to the difference in metallicity between the grids at the high-metallicity end,

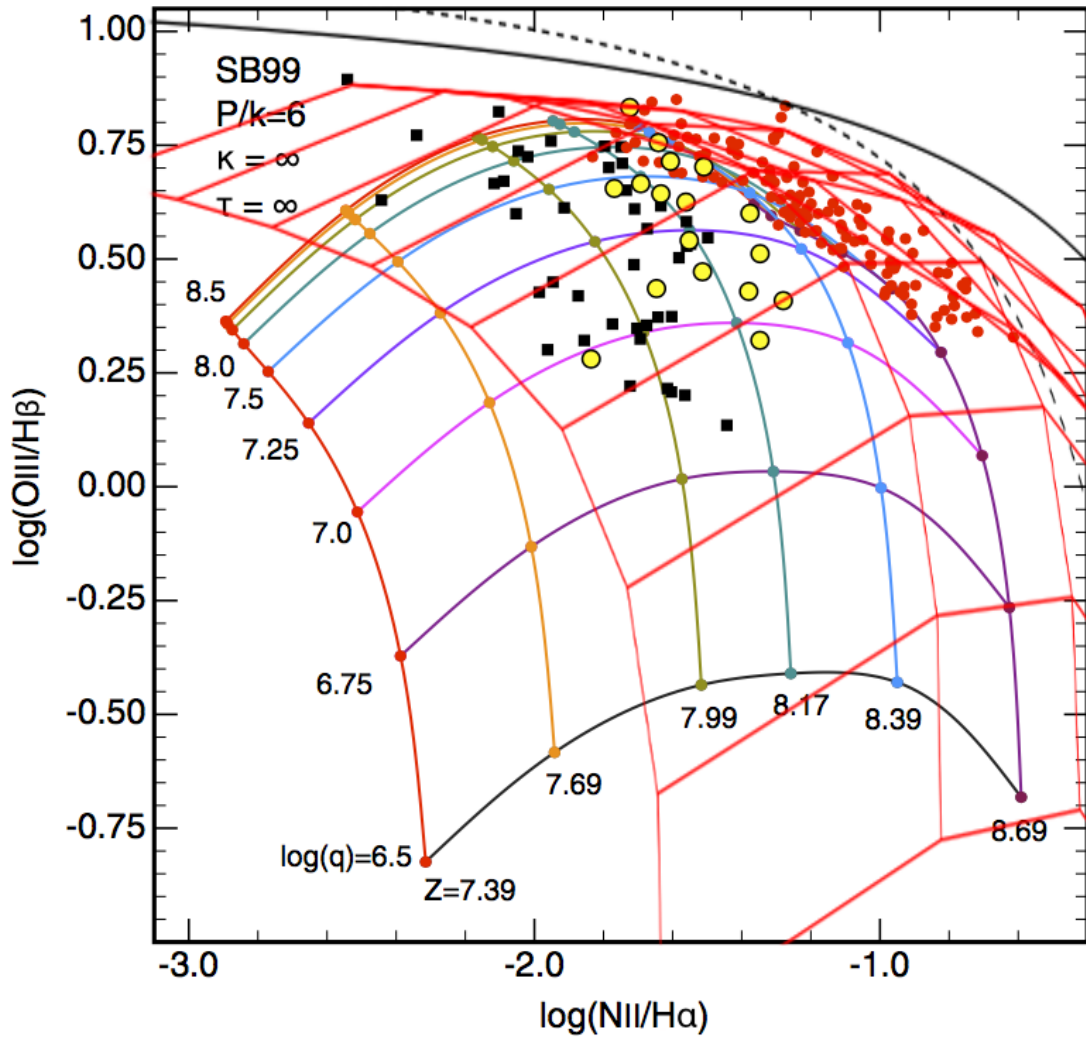


Figure 2.24 Density-bounded ($\tau = 1$) grid (red) with pressure $P/k \sim 8 \times 10^7 \text{ cm}^{-3} \text{ K}$, corresponding to an initial electron density $n = 10,000 \text{ cm}^{-3}$ under the assumption of an initial electron temperature of 8000K, shown over the top of the SIGRID sample and grid taken from Nicholls et al. (2014) (multicoloured). The yellow points show the SIGRID sample from Nicholls et al. (2014), the black points show the low-metallicity DR7 SDSS subset from Izotov et al. (2012), and the red points show the DR3 SDSS subset from Izotov et al. (2006). Metallicity values Z are in units of $12 + \log(\text{O}/\text{H})$. Ionisation parameter values are consistent with those used in this paper. All other parameters are fiducial. The density-bounded model better fits the data and helps explain the off-grid data points in Nicholls et al. (2014). The very high value of $\log(P/k) \sim 8$ is likely to be unphysical and arises as a result of an X-ray deficit in the model ionising spectra.

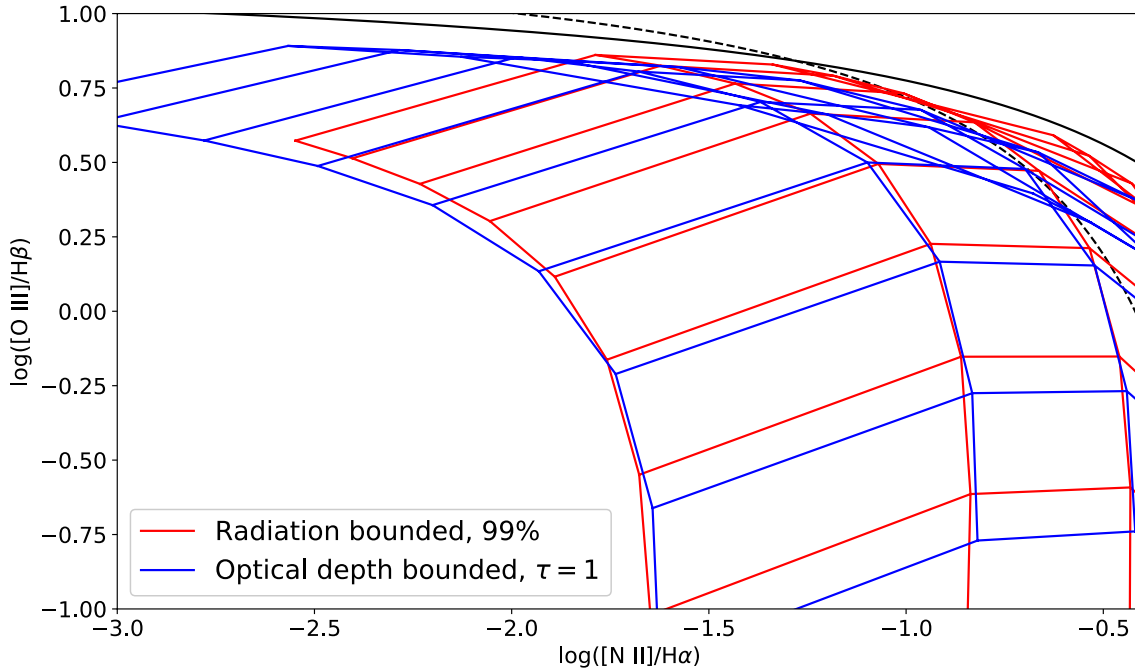


Figure 2.25 Isobaric models with pressure values of $P/k = 8 \times 10^7 \text{ cm}^{-3} \text{ K}$, assuming a density-bounded regime for the blue grid and radiation-bounded regime for the red grid. The density-bounded model is truncated at an optical depth of $\tau = 1$, and the radiation-bounded model is truncated at 99% of hydrogen recombination. The very high value of $\log(P/k) \sim 8$ is likely to be unphysical and arises as a result of an X-ray deficit in the model ionising spectra.

which has an effect on the gas-phase abundance. The CLOUDY model shown in [Byler et al. \(2017\)](#) ties the gas-phase abundance with the metallicity of the stellar population. Such a large disparity between the two models at the high-metallicity end will ultimately lead to differences in the synthesised stellar population. Differences in the synthesised stellar population between the two models may also arise as a result of the different SPS codes used. The input spectrum for the CLOUDY model grid is synthesised using the SPS code Flexible Stellar Population Synthesis (FSPS; [Conroy et al. 2009](#)), whereas [Dopita et al. \(2013\)](#) use Starburst99 to synthesise their stellar population. As discussed and shown in Sections 2.6.1 and later Section 2.6.2 when comparing the single-star SPS codes SLUG and Starburst99, different SPS codes may lead to variations in the input stellar spectrum, ultimately leading to differences in the emission-line ratios.

A BPT diagram showing photoionisation grids produced using MAPPINGS and CLOUDY is shown in Figure 2.26. Both the MAPPINGS and CLOUDY models are run with the exact same fiducial inputs, which includes the input ionising spectrum, ionisation parameters, abundances, depletion factors, and pressure. Hence, the differences seen in Figure 2.26 are the result of intrinsic differences between the two codes, such as atomic datasets, input physics, and model assumptions. Overall, the difference in emission-line ratios between the two models is ~ 0.1 dex on average across all metallicities explored.

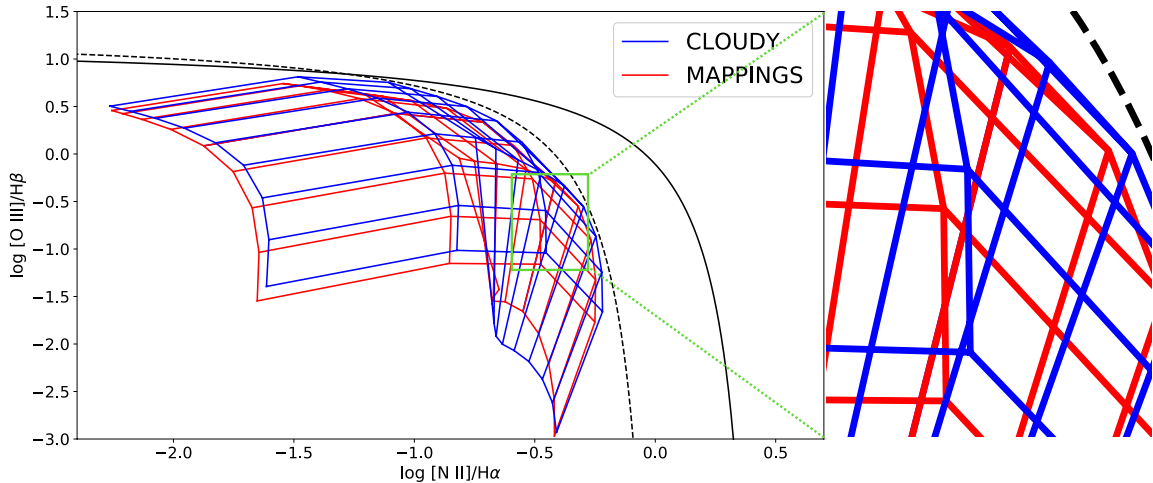


Figure 2.26 Model grids computed using the photoionisation modelling codes `MAPPINGS` and `CLOUDY`. All parameters associated with these grids are fiducial.

2.7. Discussion

2.7.1. Spread of SDSS galaxies

Ionising Radiation Field Parameters

The systematic differences in each of the ionising radiation field parameter variations are small and hence individually do not better explain or cover the spread in the star-forming SDSS galaxies. The average systematic difference in the emission-line ratios between varying model parameters is ~ 0.1 dex, ranging from < 0.1 dex to a maximum of ~ 0.5 dex more notably in the $[\text{O III}]/\text{H}\beta$ ratio at high metallicities in the model grids. As demonstrated by the relative variation in the ionising spectra (Figures 2.4 - 2.14), the impacts of stellar atmospheres, stellar tracks, and SPS codes on the ionising radiation spectra are much more visible at higher energies. This indicates that these variations will have a more significant impact on higher-ionisation species and temperature-sensitive emission lines than explored here. Even so, the impact of the uncertainties in modelling ionising spectra of clusters is visible in the BPT. Therefore, we recommend that a ~ 0.1 dex uncertainty be included when comparing model grids to data and that the most sophisticated model spectra be used when possible. We believe that the current best models include:

- The stellar atmosphere combination of Kurucz + Hillier + Pauldrach, which takes the Kurucz atmospheres compiled by [Lejeune et al. \(1997\)](#) and includes updates on the W-R and OB stars' atmospheres from [Hillier & Miller \(1998\)](#) and [Pauldrach et al. \(2001\)](#) respectively.
- The stellar evolutionary tracks to be used are dependent on the age of the cluster considered. For ages at which the TP-AGB phase is reached ($\sim 0.1 - 2$ Gyr), the Padova TP-AGB tracks described in [Girardi et al. \(2000\)](#) and [Vassiliadis & Wood \(1993\)](#) should be used. At lower stellar ages such as those considered in this paper, we favour the Geneva tracks for their sensible correction to the definition of effective

temperature at the W-R phase. The lack of an effective temperature correction for W-R stars in the Padova tracks leads to the same definition of T_{eff} for all stars, resulting in an order of magnitude of ~ 8 difference in the FUV spectra between the two sets of tracks as calculated by SLUG.

- SPS modelling still needs a large improvement in the high stellar mass regime. The sparse grid points at high stellar masses that aid in the interpolation of the stellar isochrone result in large uncertainties in the spectrum. Overall, both SPS codes Starburst99 and SLUG are suitable, as the differences produced between the two are negligible. However, the use of the Akima spline in SLUG results in less systematic uncertainties from outliers in the SLUG output. Similarly, the differences in emission-line ratios produced by BPASS are small when compared to single stellar SPS codes.

Intrinsic H II Region Parameters

The spread of the SDSS starburst galaxies as modelled by the photoionisation grids seen in Figures 2.1 and 2.20 is largely affected by variations in parameters associated with the H II region. The starburst spread in SDSS, defined as the galaxies below the [Kauffmann et al. \(2003\)](#) line, incorporates a large range of metallicities ($\sim 0.028 \pm 0.002$ in Z) and ionisation parameter ($\sim 2 \pm 0.13$ dex in $\log(q(N)/(\text{cm s}^{-1}))$).

Seen in Figure 2.20, models with a pressure of $\log(P/k) \approx 6$, which approximately corresponds to a density of $n = 100 \text{ cm}^{-3}$ cover the majority of the starburst spread. The extent of the $n = 100 \text{ cm}^{-3}$ model grid does not reach the [Kauffmann et al. \(2003\)](#) line, however, and hence there are areas of the star-forming region of the BPT that are yet to be explained. Increasing the density and hence pressure of the H II region does increase the strength of the emission-line ratios, offering a larger covering range on the BPT diagram. Overall, all galaxies in the SDSS star-forming sequence can be explained with a pressure between $6 \lesssim \log(P/k) \lesssim 7$. However, increasing the pressure of the H II region to pressures of $\log(P/k) \sim 7$ and above forces the models to include galaxies that may have a possible nonstellar (i.e. AGN) contribution to their emission-line spectrum. A discussion on the various other sources powering the emission from galaxies along the mixing sequence can be found in Section 2.7.2.

Different types of H II region boundedness do not better explain the spread of SDSS galaxies, of the boundedness types we have explored. At the metallicities of the star-forming SDSS galaxies ($0.002 \lesssim Z \lesssim 0.030$), the model grids are all largely similar for different bound situations at the same pressure, seen in Figures 2.23. Shown in Figure 2.20 are three model grids of $\log(P/k) \approx 6 \Rightarrow n = 100 \text{ cm}^{-3}$, $\log(P/k) \approx 7 \Rightarrow n = 1,000 \text{ cm}^{-3}$, and $\log(P/k) \approx 8 \Rightarrow n = 10,000 \text{ cm}^{-3}$, computed in a radiation-bounded situation truncated at 99% of H II recombination.

As explained and shown in Section 2.6.2 with the use of the combined SIGRID and [Izotov et al. \(2006, 2012\)](#) low-metallicity sample, density-bounded situations only appear applicable at extremely low metallicities. At the metallicities of the star-forming SDSS galaxies, a radiation-bounded situation is sufficient to explain and encompass the spread of galaxies. Variations in the metallicity and ionisation parameter values used in the models have not been explored in this paper; however, the star-forming sequence in SDSS is adequately

explained by the values of metallicity ($Z = 0.001 - 0.040$ inclusive) and ionisation parameter ($\log(q(N)/(\text{cm s}^{-1})) = 6.5 - 8.5$ inclusive) used in our models.

Massive-star Lifetimes

Whilst the stochasticity associated with star formation incorporated in SLUG may be seen as an improvement on the SB99 method, there are still fundamental issues surrounding the creation of an ionising spectrum through SPS. The massive stars that produce the majority of the ionising radiation in stellar populations are rare; hence, IMF sampling is an issue (discussed in Section 2.6.1). These massive stars also evolve rapidly, with short lifetimes. This rapid evolution, along with their rarity and obscuration by their still clearing birth clouds, provides difficulty in obtaining constraining observations, and hence the models are relatively unconstrained. Also, the very strong stellar winds from massive stars require a very finely detailed modelling of their atmospheres. These issues surrounding the modelling of massive stars lead to systematic uncertainties with the resulting emission lines from star forming regions.

2.7.2. Further Ionising Processes

It is possible that objects that lie below the [Kewley et al. \(2001\)](#) line may have contributions in their emission from non-star-formation-related processes. AGNs, shocks, and DIG all provide a means of altering the strong-line-to-hydrogen-line ratios. Shocks and radiation from AGNs provide an increased collisional rate that increases the strength of the strong, forbidden/collisionally excited lines.

The theory of DIG is still largely a mystery, with a common explanation not yet having been agreed upon. There is much evidence for the idea of ‘leaky H II regions’ from density-bounded H II regions ([Ferguson et al. 1996](#); [Oey & Kennicutt 1997](#); [Zurita et al. 2002](#)); however, simulations have also shown the formation of DIG through other processes, such as magnetic recombination ([Hoffmann et al. 2012](#)) and radiative cooling ([Bordoloi et al. 2016](#)).

2.8. Conclusions

Using MAPPINGS V, we have explored the common parameters used in the production of photoionisation model grids. We explore the effects of the variations on the resulting emission-line flux ratios in the optical emission-line diagnostic diagrams. Further, we search the parameter space for models that explain the spread of galaxies in SDSS and in a combined metal-poor sample consisting of data from the SIGRID survey ([Nicholls et al. 2011](#)) and data from [Izotov et al. \(2006, 2012\)](#). We find the following:

(i) Variations in the parameters associated with the ionising radiation field (SPS code, stellar atmospheres, stellar evolutionary tracks, IMF) are small, with an average systematic difference of ~ 0.1 dex in optical emission-line ratio between varying models. In this situation where spectra resulting from varying models are similar, we make the following recommendations:

- Kurucz + Hillier + Pauldrach atmospheres for the updated W-R and OB stellar input physics.
- Geneva HIGH mass-loss evolutionary tracks for younger stellar populations due to the W-R effective temperature definition correction. Padova TP-AGB evolutionary tracks for older stellar populations, where the thermally pulsing AGB phase is reached.
- Either SLUG or SB99 are suitable for modelling single stellar populations.

(ii) Similarly, both photoionisation modelling codes MAPPINGS and CLOUDY are suitable for modelling H II regions. The difference in emission-line ratios produced between the two codes is small, on the order of ~ 0.1 dex

(iii) Including the ionising input spectrum parameters listed above, the main star-forming spread of SDSS can be explained by using a photoionisation model with metallicity ranging from $Z = 0.001$ to 0.040 inclusive, ionisation parameter ranging from $\log(q(N)/(\text{cm s}^{-1})) = 6.5$ to 8.5 inclusive, and $\log(P/k) \approx 6$, corresponding to an initial electron density of approximately $n = 100 \text{ cm}^{-3}$ under the assumption of an initial temperature of 8000 K , and computed assuming a radiation-bounded situation where truncation occurs at 99% H II recombination. This is supported by work done by [Kewley et al. \(2001\)](#) that shows the electron density within local galaxies to be $n = 350 \text{ cm}^{-3}$.

(iv) The position of high-redshift galaxies on the BPT (e.g. [Kewley et al. 2013b](#)) is well explained by models at higher pressure. We find star-forming high-redshift galaxies to be well explained by photoionisation models containing a pressure value of $\log(P/k) \approx 7$. For comparison, the star-forming sequence of SDSS is well explained by models with $\log(P/k) \approx 6$. This supports work showing high-redshift galaxies to be observed with a higher electron density (e.g. [Kashino et al. 2017](#); [Onodera et al. 2016](#)).

(v) Low-metallicity galaxies can be explained using a density-bounded H II region model rather than a radiation-bounded one. From the mass-metallicity relation, these low-metallicity galaxies have lower stellar masses and hence contain a lower gravitational binding energy, leading to an increase in the number of escaped photons. Our density-bounded models show better agreement with the low-mass combined sample from the SIGRID survey ([Nicholls et al. 2011](#)) and [Izotov et al. \(2006, 2012\)](#), when compared to the radiation-bounded model used by [Nicholls et al. \(2014\)](#).

Our future work includes using the findings of this paper to model H II regions, in order to separate star-forming emission from other sources, such as AGNs and shocks. The theoretical nature of the H II region models allows us to discern physical properties about the star-forming regions of a galaxy, in addition to quantifying the amount of star-formation in IFU spaxels.

Acknowledgements

Parts of this research were conducted by the Australian Research Council Centre of Excellence for All Sky Astrophysics in 3 Dimensions (ASTRO 3D), through project No. CE170100013. B.G. gratefully acknowledges the support of the Australian Research Council as the recipient of a Future Fellowship (FT140101202).

Statement of Contribution

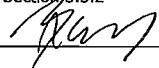
This thesis is submitted as a Thesis by Compilation in accordance with https://policies.anu.edu.au/ppl/document/ANUP_003405

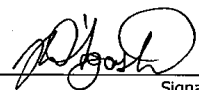
I declare that the research presented in this Thesis represents original work that I carried out during my candidature at the Australian National University, except for contributions to multi-author papers incorporated in the Thesis where my contributions are specified in this Statement of Contribution.

Title and authors: D'Agostino J. J., Poetrodjojo H., Ho I.-T., Groves B., Kewley L., Madore B. F., Rich J., Seibert M., 2018, "Starburst-AGN mixing: TYPHOON observations of NGC 1365, NGC 1068, and the effect of spatial resolution on the AGN fraction", MNRAS, 479, 4907

Current status of paper: Not Yet Submitted/Submitted/Under Revision/Accepted/Published

Contribution to paper: All but Figures 3.1, 3.4, 3.5, and Section 3.3.2

Senior author or collaborating authors endorsement:  BRENT GROVES

Joshua D'Agostino  1/7/2019
Candidate - Print Name Signature Date

Endorsed

LISA KEWLEY  9/7/2019
Chair of Supervisory Panel - Print Name Signature Date
Mark Krumholz  11/7/2019
Delegated Authority - Print Name Signature Date

CHAPTER 3

Star Formation-AGN Mixing with the TYPHOON/PrISM Survey

*I see now that the circumstances of one's birth are irrelevant.
It's what you do with the gift of life that determines who you are.*
– Mewtwo

The contents of this chapter have previously been published as ‘Starburst-AGN mixing: TYPHOON observations of NGC 1365, NGC 1068, and the effect of spatial resolution on the AGN fraction’, D’Agostino, J. J., Poetrodjojo, H., Ho, I., Kewley, L., Groves, B., Madore, B. F., Rich, J., Seibert, M., 2018, MNRAS, 479, 4907. The abstract is as follows:

We demonstrate a robust method of resolving the star-formation and AGN contributions to emission lines using two very well known AGN systems: NGC 1365, and NGC 1068, using the high spatial resolution data from the TYPHOON/PrISM survey. We expand the previous method of calculating the AGN fraction by using theoretical-based model grids rather than empirical points. The high spatial resolution of the TYPHOON/PrISM observations show evidence of both star formation and AGN activity occurring in the nuclei of the two galaxies. We rebin the data to the lower resolutions, typically found in other integral field spectroscopy surveys such as SAMI, MaNGA, and CALIFA. The results show that when rebinned from the native resolution of TYPHOON (< 200 pc/pixel) to 1 kpc/pixel, the effects include a ~ 3 kpc increase in the radius of measured AGN activity, and a factor of 2 – 7 increase in the detection of low surface brightness features such as shocks. All of this information is critical, because information on certain physical processes may be lost at varying resolutions. We make recommendations for analysing data at current IFU survey resolutions.

Figure 3.1 was generated by co-author I-Ting Ho. Figures 3.4 and 3.5 were produced by co-author Jeffrey Rich, who also performed the correction to the NGC 1068 datacube. Parts of Section 3.3.2, detailing the corrections made to the NGC 1068 datacube, were written by co-author Jeffrey Rich. The TYPHOON/PrISM observations were performed mainly by co-authors Mark Seibert and Jeffrey Rich. Myself and co-author Henry Peotrodjojo contributed to one observing run in August 2016. The raw data was reduced for science purposes by co-authors Mark Seibert and I-Ting Ho.

3.1. Introduction

Much work has been undertaken to establish the relationship between the accretion activity of supermassive black holes (SBH) and the evolution of their host galaxies (Cattaneo et al. 1999; Haehnelt & Kauffmann 2000; Cid Fernandes et al. 2001; Kauffmann et al. 2003; Granato et al. 2004; LaMassa et al. 2012). We now know that the mass of the SBH correlates with other properties of the galaxy, such as the velocity dispersion (M - σ relation; e.g. Ferrarese & Merritt 2000; Gebhardt et al. 2000; Tremaine et al. 2002; Gültekin et al. 2009; McConnell & Ma 2013), the stellar mass in the bulge (M_{BH} - M_* relation; e.g. Magorrian et al. 1998; Marconi & Hunt 2003; Bennert et al. 2011; McConnell & Ma 2013), and the luminosity of the bulge (M_{BH} - L ; e.g. Marconi & Hunt 2003; Gültekin et al. 2009; McConnell & Ma 2013). Therefore, one might expect that black hole activity correlates with star formation. Yet, all current theories that link these processes, such as mergers, starburst-driven winds or AGN-driven outflows (e.g. Yuan et al. 2010; Rafferty et al. 2011) have remained unconvincing. No theoretical model has successfully been able to explain the relationship between star formation and AGN (see the review by Alexander & Hickox 2012).

Emission lines such as $H\alpha$ are one of the key measures for the growth of the stellar mass and SBH in galaxies across cosmic time. However such lines can arise from both AGN and star-forming processes, making the determination of the relative rate of growths difficult when both are present. This confusion presents one of the difficulties in understanding the link between galaxy and SBH growth. Line ratio diagnostic diagrams, such as suggested by Baldwin et al. (1981); Veilleux & Osterbrock (1987); Kewley et al. (2001, 2006) can be used to determine the dominant power source within a galaxy. The flux from hydrogen recombination lines such as $H\alpha$ and $H\beta$ is proportional to the number of ionising photons emitted by a stellar cluster, which is proportional to the birthrate of massive stars (Dopita et al. 2002c, and references therein). Hence, the flux of $H\alpha$ specifically (rather than $H\beta$ which typically has a smaller flux due to the process that governs the two emission lines, as well as $H\beta$ being more prone to extinction and stellar absorption) is typically used as a star formation indicator. The [N II] λ 6584 and [O III] λ 5007 lines (hereafter simply [N II] and [O III] unless specified) are strong, forbidden lines and are easily measurable. These lines are AGN indicators because the extreme ultraviolet (EUV) radiation field from the accretion disk of the central AGN is harder than the radiation field from star formation (Groves et al. 2004; Kewley et al. 2006, 2013a).

Work on starburst-AGN mixing was first explored by Kewley et al. (2001), using previous spectroscopy techniques. These previous spectroscopy techniques (e.g. long-slit) obtained

a spectrum from a galaxy as a whole. As a result, galaxies were typically classified on the BPT diagram as either star-forming or from AGN, with the exception being when their line ratios placed them in the region of the BPT between the Kewley and Kauffmann demarcation lines (see Kewley et al. 2001; Kauffmann et al. 2003, respectively). These two lines are theoretical and empirical upper bounds of star formation in galaxies respectively. The region between these two lines is interpreted to imply mixing of both star formation and an additional hard component (from e.g. AGN, shocks, or diffuse ionised gas) in galaxies (Yuan et al. 2010). Through their work with starburst galaxy modelling, Kewley et al. (2001) demonstrated with their SDSS sample that a continuum of ionising sources (a ‘mixing sequence’) exists in galaxies. This notion was taken further by Kewley et al. (2006), who demonstrated that contributions from various ionising sources could be calculated and extracted from galaxies which show multiple sources of ionisation.

It is anticipated that the study of starburst-AGN mixing and uncovering the relationship between the two processes will become clearer with the advent of integral field spectroscopy (IFS). IFS, unlike previous methods, obtains spatially resolved spectra from individual spaxels across a galaxy, rather than a single spectrum that encompasses the galaxy as a whole. This allows both star formation and AGN processes in a single galaxy to be separated, and hence integral field unit (IFU) data is central to the study of starburst-AGN mixing. Starburst-AGN mixing using IFU data was first investigated by Davies et al. (2014a,b), who calculated the ‘AGN fraction’ for NCG 7130 from the Great Observatory All-Sky LIRG Survey (GOALS; Armus et al. 2009), and four galaxies (NGC 6394, NGC 2410, IC 0540, NGC 6762) from the Calar Alto Legacy Integral Field Area (CALIFA; Sánchez et al. 2012b; Husemann et al. 2013b). They make use of the concept of ‘star-forming distance’ defined in Kewley et al. (2006) to empirically fit each galaxy’s mixing sequence from the star-forming to the AGN regions on the BPT diagram. We expand on the work conducted by Davies et al. (2014a,b) by calculating the AGN fraction with new theoretical models, rather than the Davies et al. (2014a,b) empirical method.

Using data obtained from the TYPHOON/Progressive Integral Step Method (PrISM) survey, we analyse two galaxies: NCG 1365 and NGC 1068, described in Section 3.2. TYPHOON/PrISM is a survey of 100 of the nearest and largest spiral galaxies, resulting in an incredibly highly-resolved dataset. The survey and dataset is described further in Section 3.3. The high resolution of the dataset gives a clean separation of both star formation and AGN processes in each galaxy, allowing very accurate calculations of the contribution to emission lines from both star formation and AGN processes. We calculate the AGN fraction for both NGC 1365 and NGC 1068 using new theoretical models. The models are described in Section 3.4, and the new AGN fraction calculation is showcased in Section 3.5. Further, we explore systematically the impact of resolution on determining the true contributions to both processes in Section 3.6 by rebinning the data to lower spatial resolutions and repeating the analysis.

3.2. Sample Selection

3.2.1. NGC 1365

NGC 1365 is a large barred spiral galaxy (SB(s)b; [de Vaucouleurs et al. 1991](#)) located at a distance of roughly 18 Mpc in the constellation Fornax. NGC 1365 is roughly four times bigger than the Milky Way, with a semi major axis of ~ 32 kpc. NGC 1365 has a Seyfert 1.8 nucleus ([Véron-Cetty & Véron 2006](#)) with a rapidly rotating supermassive black hole of mass $M_{\text{BH}} \approx 2 \times 10^6 M_{\odot}$ and spin parameter $a > 0.84$ ([Reynolds 2013](#); [Risaliti et al. 2013](#)).

Large-scale outflows from NGC 1365 have been reported since the middle of the 20th century (for a detailed discussion on the history of reported outflows, see [Veilleux et al. 2003](#), and references therein). [Veilleux et al. \(2003\)](#) confirm previous studies by measuring a biconical outflow south-east and north-west from the nucleus of NGC 1365. The opening angle of the biconical outflow has been suggested to be $\sim 100^\circ$, with a position angle of 126° ([Hjelm & Lindblad 1996](#)). [Veilleux et al. \(2003\)](#) and [Sharp & Bland-Hawthorn \(2010\)](#) also show high [N II]/H α and [O III]/H β ratios particularly along the axis of the biconical outflow, up to values of 1.5 and 3 for each of the respective ratios (figures 6d and 7d respectively from [Veilleux et al. 2003](#)). The high emission line ratios suggest photoionisation from the central AGN. The biconical outflow structure is roughly aligned with a radio jet-like feature at a position angle of 125° , observed in [Sandqvist et al. \(1995\)](#) and [Morganti et al. \(1999\)](#).

3.2.2. NGC 1068

As the prototypical Seyfert galaxy, NGC 1068 has been the subject of much work in the astronomical community, leading to it being arguably the most-studied active galaxy in the local universe. A Seyfert 2 ([Osterbrock & Martel 1993](#)) (R)SA(rs)b ([de Vaucouleurs et al. 1991](#)) galaxy, it is located at a distance of roughly 12.5 Mpc in the constellation Cetus. The galaxy’s broad-line region is known to be obscured by an optically-thick torus (e.g. [Miller & Antonucci 1983](#); [Antonucci & Miller 1985](#); [Miller et al. 1991a](#); [García-Burillo et al. 2016](#)), and hence has largely been hidden from view due to extinction in the past ([Rigby 2006](#)). However, recent work such as [Marinucci et al. \(2016\)](#) and [García-Burillo et al. \(2016\)](#) has begun to resolve the nucleus and circumnuclear disk of NGC 1068.

NGC 1068 is also observed to have a large-scale biconical outflow structure (e.g. [Cecil et al. 1990](#); [Arribas et al. 1996](#); [Pogge 1988](#); [Crenshaw & Kraemer 2000](#)). Material within this bicone has been observed in the [O III] $\lambda 5007$ line to be moving outward from the nucleus at velocities of $\sim 3000 \text{ km s}^{-1}$ at a position angle of $\sim 32^\circ$, believed to be radiatively accelerated by the AGN at the galaxy’s centre ([Pogge 1988](#); [Cecil et al. 2002](#); [Dopita et al. 2002a](#)). The outflow in [O III] can be seen in Figure 3.3b with $\log([\text{O III}]/\text{H}\beta)$ values near unity, extending from the centre of the galaxy to the north-east. Material with high values of $\log([\text{O III}]/\text{H}\beta)$ are also seen to the south-west of the galaxy, partially obscured by the disk of the galaxy. This ejecta is aligned with the radio jet seen from this galaxy, which has a measured position angle of 34° (e.g. [Wilson & Ulvestad 1983, 1987](#); [Pogge 1988](#); [Gallimore et al. 1996](#)). The models from [Das et al. \(2006\)](#) (especially their Figure 10) which attempt to model the bicone give an opening angle of $\sim 80^\circ$ and position angle of $\sim 30^\circ$. Values

of parameters relating to the geometry of the bicone measured by [Das et al. \(2006\)](#) agree closely with those calculated by [Crenshaw & Kraemer \(2000\)](#), with the exception of the value for the bicone position angle for which [Crenshaw & Kraemer \(2000\)](#) suggest 15° . [Poncelet et al. \(2008\)](#) also measure a value for the bicone orientation using emission lines in the infrared which is in closer agreement to that suggested by [Crenshaw & Kraemer \(2000\)](#). [Poncelet et al. \(2008\)](#) suggest a bicone orientation with a position angle of $\sim 10^\circ$. The position angle suggested by [Poncelet et al. \(2008\)](#) is in better agreement with the *HST* [O III] image results from [Evans et al. \(1991\)](#). [Poncelet et al. \(2008\)](#) do however agree with the opening angle of the bicone calculated by [Das et al. \(2006\)](#), finding an opening angle of $\sim 82^\circ$. However, as mentioned by [Goosmann & Matt \(2011\)](#), derivation of the actual geometry of the ionisation bicone close to the centre is not straightforward when observations have large spatial scales. Instead, they propose X-ray polarimetry to constrain the geometry of the innermost outflows.

3.3. Observations and Data Reduction

3.3.1. Observations

TYPHOON is a survey which uses the Progressive Integral Step Method (PrISM), also known as the ‘step-and-stare’ or ‘stepped-slit’ method to construct 3D datacubes of 100 of the closest and largest galaxies in the southern hemisphere. The survey is being undertaken on the 2.5m du Pont telescope at the Las Campanas Observatory in Chile. Whilst not using an IFU *per se*, the observations are made by progressively stepping a long-slit aperture across a galaxy to mimic the effect of an IFU. Thus, the end product is a high spectral resolution datacube. The datacubes produced from the TYPHOON/PrISM survey are highly resolved, with a spatial resolution of $\sim 4\text{-}5$ pc at best ([Sturch & Madore 2012](#)). Further details about the TYPHOON/PrISM survey will be explained in a forthcoming publication (Seibert et al. in prep.)

NGC 1365 was observed using the Wide Field reimaging CCD (WFCCD) imaging spectrograph on the du Pont telescope. The WFCCD has a field of view of $25'$ and we construct the 3D data cube using a custom long-slit ($18' \times 1.65''; 0.5 \text{ arcmin}^2$) which was placed along the north-south direction and progressively scanned across the galaxy through stepping and staring. Each pointing position was integrated for 600 seconds before the slit was moved by one slit width in the east-west direction for the next integration. This procedure was repeated until the optical disk of NGC 1365 was covered. In total, 223 observations covering an area of approximately $6' \times 18'$ were taken during 15 nights over four observing runs in November 2011, January 2016, February 2016 and August 2016. NGC 1068 was also observed using the WFCCD imaging spectrograph on the du Pont telescope, with 63 observations taken between the 8th and 11th of October 2012 inclusive. The observations cover an area of $1.73' \times 18'$, centered on the nucleus and inner star-forming ring. Each exposure was also integrated for 600 seconds. Observations were performed only when the seeing was less than the slit-width of $1.65''$. Spectrophotometric flux standards were observed each night.

3.3.2. Data Reduction

The data are reduced using standard long-slit data reduction techniques. The wavelength calibration has a typical root-mean-square value 0.05\AA for the entire data set. Flux calibration is accurate to 2% at the spaxel scale over the range of 4500 to 7500 \AA . The reduced long-slit 2D spectra are tiled together to form the 3D data cube. The final reduced data cube covers a wavelength range of 3650 to 8150 \AA , with spectral and spatial samplings of 1.5 \AA and 1.65'', respectively. From fitting Gaussians to field stars in the reduced data cube, we estimate that the full-width half maximum of the point spread function is approximately 2'', which corresponds to approximately 169 pc at the assumed distance of roughly 18 Mpc. The instrumental dispersion is approximately 3.5 \AA (σ ; correspond to $R \approx 850$ at 7000 \AA).

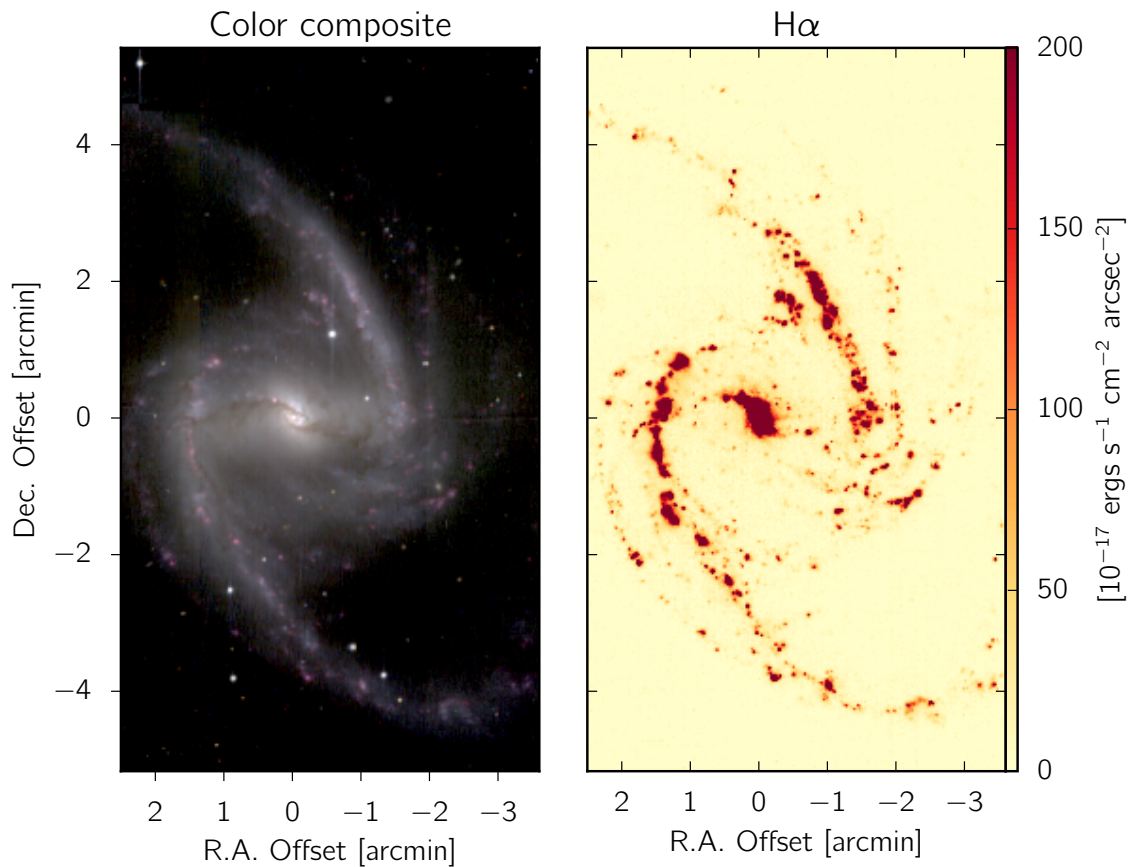
The colour-composite images extracted from the reduced datacube are shown in the left-hand panels of Figure 3.1 for both galaxies NGC 1365 and NGC 1068. The H α flux maps derived from the datacube for both galaxies are shown in the right-hand panels of Figure 3.1. We use the emission line fitting tool LZIFU (Ho et al. 2016; Ho 2016) to measure emission line fluxes from the raw data, following the method outlined in Ho et al. (2017). The flux of H α emission peaks at the centre of the galaxy for both galaxies. Hence we use the spaxel containing the highest value of H α flux as the centre of the galaxy, from which we measure our radial offsets.

The large-scale distribution of H α is seen to follow the spiral arms in both galaxies. However, the centres of both NGC 1365 and NGC 1068 have been shown to be dominated by harder-ionising processes, such as AGN and shocks (see Section 3.2), resulting in outflows seen in emission lines such as [O III] λ 5007. Their centres also contain significant star-formation, such as the nuclear 1kpc diameter starburst ring in NGC 1068 (e.g. Wilson et al. 1991). Therefore, while some clear AGN driven structures can be detected using single lines like the biconical outflow in the [O III] map of NGC 1365 in Figure 3.2, most lines towards the centre arise from some combination of star formation and AGN affected gas. This is most clearly seen in Figure 3.3, which shows increases towards the nucleus in both the [N II]/H α and [O III]/H β ratios. We note that the line ratio maps in Figure 3.3 do not show evidence of a biconical outflow in NGC 1365 due to low signal-to-noise in the H β line. Hence, we make use of the BPT diagram and each galaxy's mixing sequence to separate star formation and AGN activity. For this work, we apply a consistent signal-to-noise cut of 3 on all emission lines in the BPT diagram (H α , H β , [O III], [N II]).

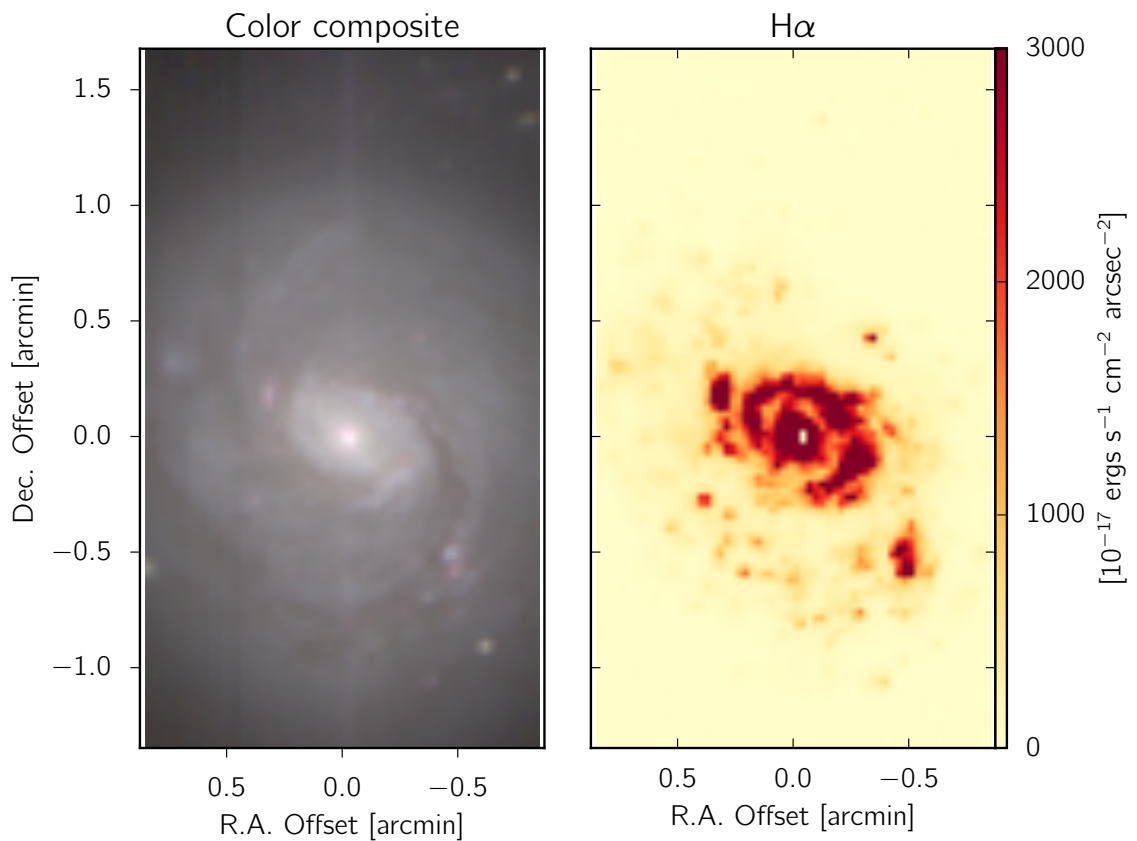
Correcting for Saturation in NGC 1068

The emission lines affected by saturated pixels include [O III] λ 4959,5007, H α and [N II] λ 6543,6584. In the pipeline, pixels that are saturated are flagged and carried through as 'NaN' pixels. We reproduce the line profile by performing a fit to the unsaturated emission line(s). For spaxels with saturated lines, we use IDL/MPFIT to fit the H β profile with a two-component gaussian.

The [O III] λ 4959,5007 profile with saturated (NaN) pixels is fit with IDL/MPFIT using a two-component gaussian with the redshift and velocity width of the gaussian components fixed to the values derived from the H β fit. The line peaks, continuum level and continuum slope are allowed to vary (the [O III] λ 4959,5007 ratio is held fixed at 1:3), using the Gaussian



(a) NGC 1365



(b) NGC 1068

Figure 3.1 Colour composite (*BVR*) and H α maps for NGC 1365 and NGC 1068 from the TYPHOON datacubes. For both images (and all hereafter), north is vertically upwards, and east to the left.

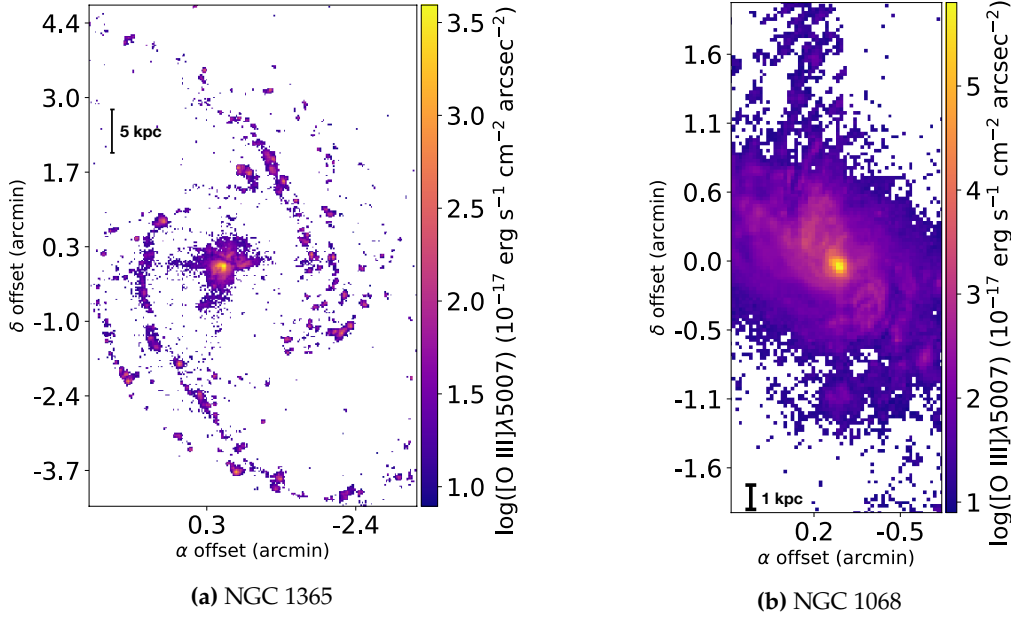


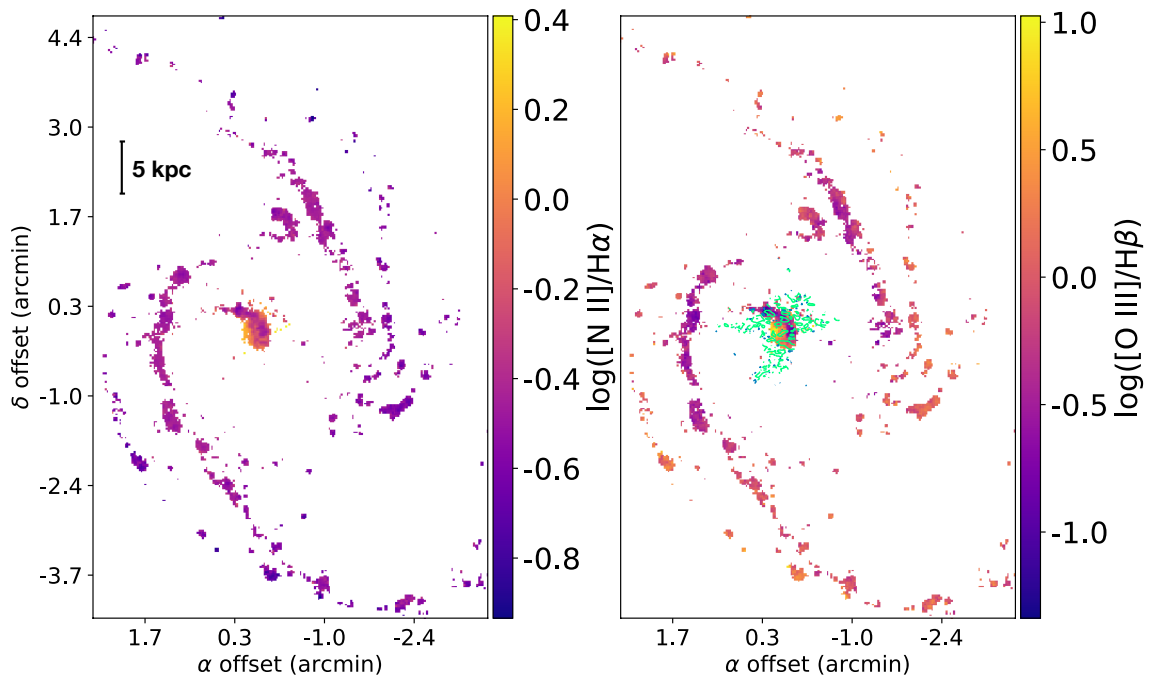
Figure 3.2 [O III] distribution maps for NGC 1365 and NGC 1068.

shape and the unsaturated wings of the line to constrain the missing data. Any ‘NaN’ pixels in the region of [O III] are replaced with the value from the resulting fit. This process is repeated using the [O I] $\lambda\lambda 6300,6363$ doublet to generate a two-component gaussian used to fit the [N II] $\lambda\lambda 6543,6584 + \text{H}\alpha$ region in the same fashion (redshift and width are fixed, the [N II] $\lambda\lambda 6543,6584$ ratio is fixed to 1:3, the peaks of the [N II] and $\text{H}\alpha$ lines are allowed to vary). The example in Fig. 3.4 shows the $\text{H}\beta$ (top left) and [O I] (bottom left) fits - a single component fit is shown in red and the two-component fit is shown in orange. The fits to [O III] (upper right) and [N II] $+\text{H}\alpha$ (bottom right) using the same gaussian components are shown on the right.

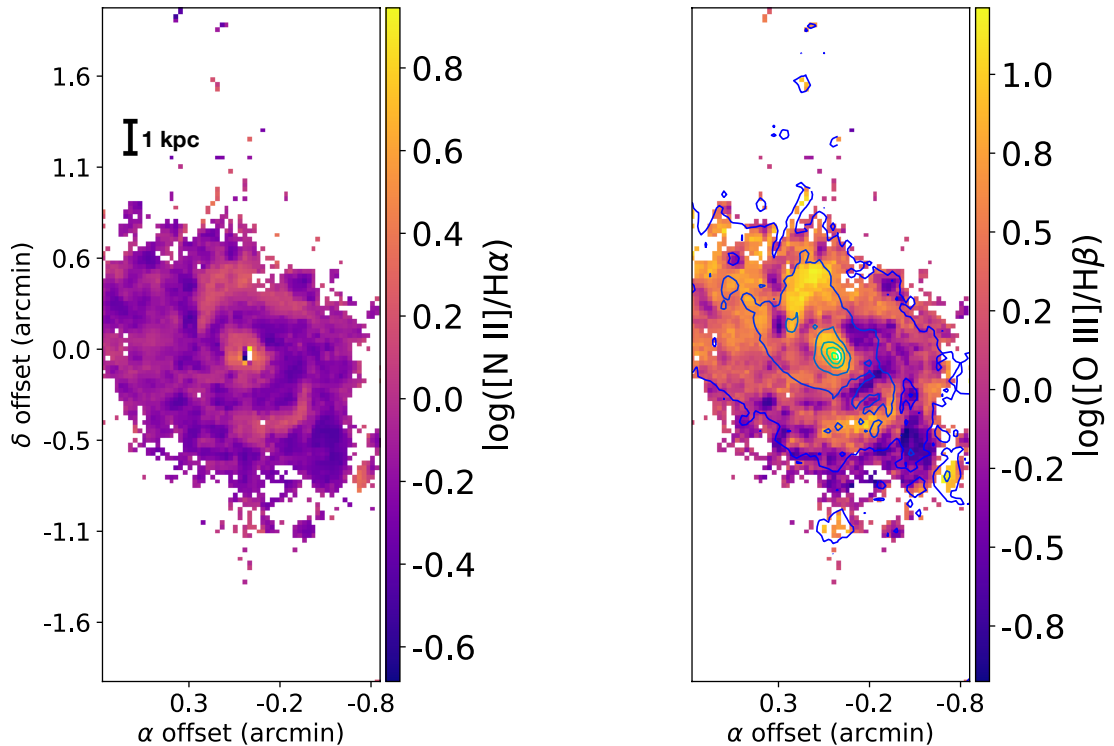
Finally, there are some spaxels where the signal-to-noise in the $\text{H}\beta$ profile is too low to provide a reliable fit to be used for the [O III] doublet. For these four spaxels, we fit the [O III] $\lambda 4959$ line to generate the two-component gaussian widths and redshifts, and apply the results to the [O III] $\lambda\lambda 4959,5007$ simultaneously with the resulting widths and redshifts fixed. In Fig. 3.5, the left panel shows the fit to [O III] $\lambda 4959$ and the right panel shows the combined [O III] $\lambda\lambda 4959,5007$ fit using the parameters from the [O III] $\lambda 4959$ fit. Again a single component gaussian is shown in red and a two-component gaussian is shown in orange.

The spaxels with these corrections applied are located at the following (α, δ) arcminute offsets from the centre of the galaxy): $(-0.028, -0.054)$, $(-0.055, -0.054)$, $(-0.028, -0.027)$, $(-0.055, -0.027)$, $(-0.028, 0.000)$, $(-0.055, 0.000)$, $(0.000, 0.027)$, $(-0.028, 0.027)$, $(-0.055, 0.027)$, $(0.000, 0.054)$, $(-0.028, 0.054)$, $(-0.055, 0.054)$, $(-0.028, 0.081)$, $(-0.055, 0.081)$.

In total, when considering spaxels with a signal-to-noise cut greater than 3 in all the emission lines on the BPT diagram, the percentage of spaxels with a correction applied is only 0.5%.



(a) NGC 1365



(b) NGC 1068

Figure 3.3 $[\text{N II}]/\text{H}\alpha$ and $[\text{O III}]/\text{H}\beta$ distribution maps for NGC 1365 and NGC 1068. Contours of $[\text{O III}]$ with a signal-to-noise ratio greater than 3 are included on the $[\text{O III}]/\text{H}\beta$ maps. The $[\text{O III}]$ contours are shown for the inner 7 kpc of NGC 1365, ranging from $\log([\text{O III}]) = 1.5$ (light green) to $\log([\text{O III}]) = 0.5$ (deep blue) $10^{-17} \text{ erg s}^{-1} \text{ cm}^{-2} \text{ arcsec}^{-2}$ in increments of 0.5 dex. For NGC 1068, contours for the whole map are shown, ranging from $\log([\text{O III}]) = 5.6$ (light green) to $\log([\text{O III}]) = 1.6$ (deep blue) $10^{-17} \text{ erg s}^{-1} \text{ cm}^{-2} \text{ arcsec}^{-2}$ in increments of 0.8 dex.

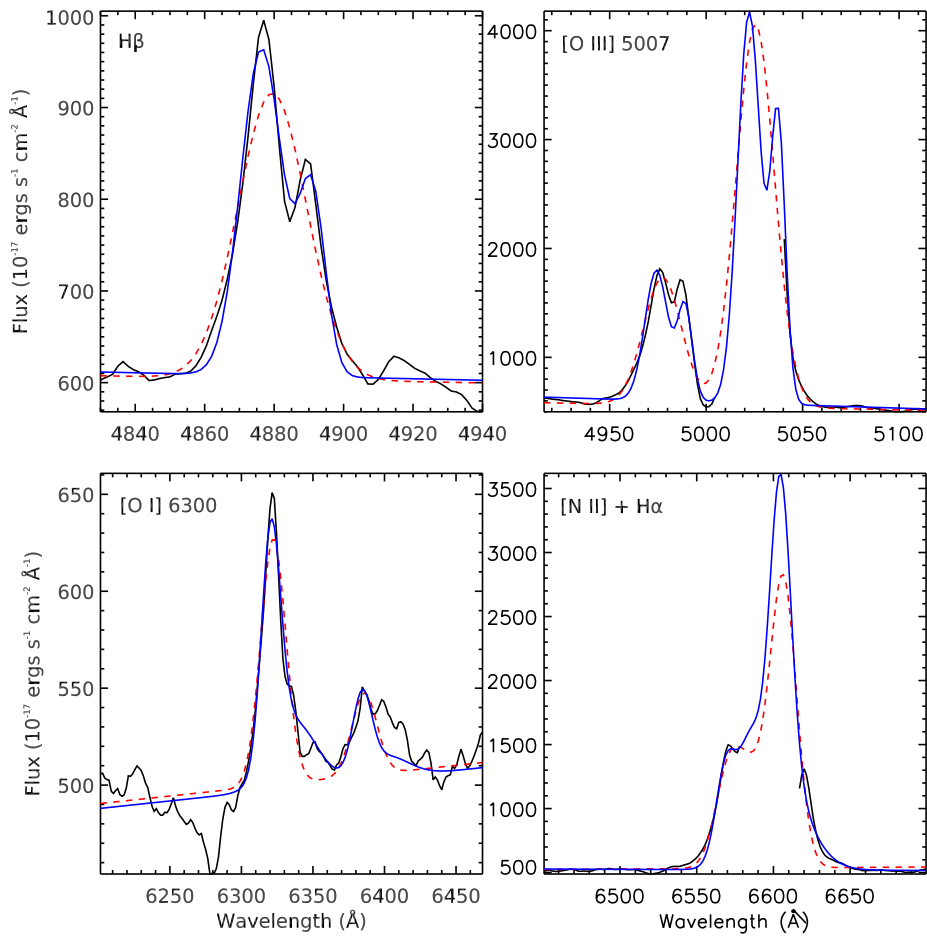


Figure 3.4 The fitting correction applied to the NGC 1068 datacube for NaN spaxels at the centre. Figure shows corrections to the H β , [O III], [O I], [N II], and H α emission lines. The one-component gaussian fits are shown in red, whilst the two-component fits are shown in blue.

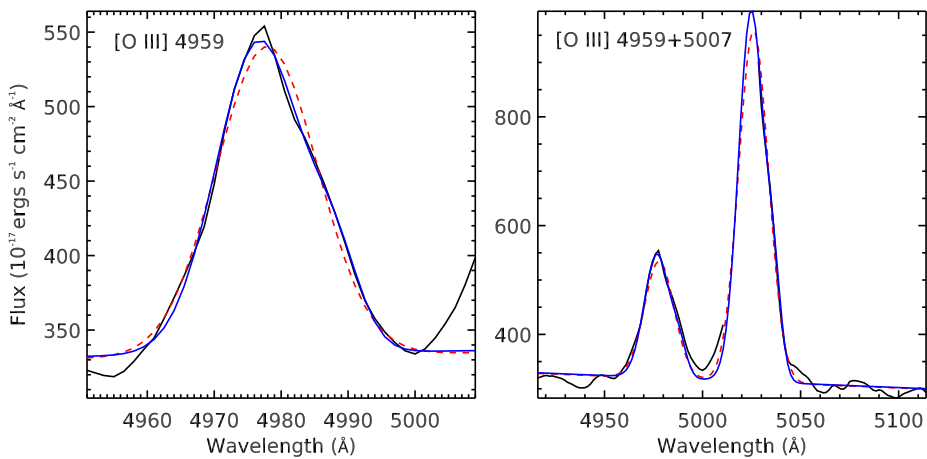


Figure 3.5 Figure showing the fit to the [O III] λ 4959, used to fit the [O III] λ 4959,5007 when the signal-to-noise in the H β profile is too low to provide reliable fit parameters. The one-component gaussian fits are shown in red, whilst the two-component fits are shown in blue.

3.4. Photoionisation Model Grids

The photoionisation grids used during this work were created using the photoionisation code MAPPINGS v.1. We compute separate model grids for both the star-formation region and the AGN region of the BPT diagram, described subsequently.

3.4.1. Starburst Model Grid

The parameters involved in the creation of the starburst model grid are based on the findings and recommendations given by D’Agostino et al. (2019a). We consider all aspects of the H II region, including a stellar cluster and physical structure of the region.

Ionising Stellar Spectrum

To synthesise the ionising stellar spectrum, we use the stellar population synthesis code Stochastically Lighting Up Galaxies (SLUG; da Silva et al. 2012; Krumholz et al. 2015). The stellar spectrum is created using the initial mass function of Kroupa (2002), the Geneva ”High” mass-loss (HIGH) stellar evolutionary tracks published in Meynet et al. (1994), and the stellar atmospheres of Lejeune et al. (1997) with the addition of updated Wolf-Rayet (WR) and OB star atmospheres from Hillier & Miller (1998) and Pauldrach et al. (2001) respectively. We favour the use of certain stellar models based on updates to the input physics from previous models. The Geneva group’s HIGH stellar tracks include a correction to the definition of stellar effective temperature at the WR phase. Similarly, specialised modelling of WR stars by Hillier & Miller (1998) and OB stars by Pauldrach et al. (2001) include updated physics to model both processes of line blanketing and line blocking, as well as a revised EUV and X-ray radiation model as a result of shock cooling zones in the OB stellar winds. We assume a stellar population at 10 Myr, undergoing constant star formation at a rate of $1M_{\odot} \text{ yr}^{-1}$. We use an age of 10 Myr, as 10 Myr is the age at which 99.9% of ionising photons have been released for a single stellar generation undergoing constant star formation (e.g. Charlot & Longhetti 2001; Feltre et al. 2016). Hence, the shape of the stellar spectrum varies negligibly beyond this point. Despite the fact that we resolve individual H II regions harbouring a single stellar cluster in galaxies using TYPHOON data, we use models which assume a continuous star-formation history. As we resolve individual H II regions across the entire galaxy (see Figure 3.6), it is fair to assume the initial conditions and rates of star formation within each H II region differs throughout the galaxy, especially considering galaxies containing an AGN with a rich history of large-scale outflows. Hence, our models consider radiation from stellar clusters of all ages up to and including 10 Myr.

H II Region Structure

We assume a spherical geometry for our H II region, and adopt the elemental abundance solar reference of Anders & Grevesse (1989), and metallicity scaling prescription of Nicholls et al. (2017), matching the stellar abundance to the overall metallicity of the stellar tracks. Our model includes dust, using the elemental depletion pattern of Jenkins

(2014), with a fraction of 0.3 of the carbon dust in the form of polycyclic aromatic hydrocarbons (PAHs). We use five metallicities in our starburst grid, with metallicities of $Z = 0.001, 0.004, 0.008, 0.020,$ and 0.040 . Z here refers to the mass fraction of heavy elements (elements heavier than helium), defined by the relationship $X(\text{H}) + Y(\text{He}) + Z = 1$. The range of metallicities sufficiently covers the metallicity range measured in both galaxies NGC 1365 and NGC 1068. We use the R_{23} metallicity diagnostic from Kobulnicky & Kewley (2004) to measure the range of metallicity in both galaxies. This is discussed further in Section 3.5.1. We include a range of the ionisation parameter $Q(N)$, defined as the number of ionising photons emitted from the source relative to the number density of all ions in the nebula, with values of $\log(Q(N) \text{ cm}^{-2}\text{s}^{-1})$ from 6.5 to 8.5 inclusive, in increments of 0.25 dex. The range of ionisation parameter is comparable to that used by Kewley et al. (2001). We compute our model in isobaric conditions, setting the initial pressure of the H II region to be $P/k = 8 \times 10^5 \text{ K cm}^{-3}$. Under the assumption of an H II region initial temperature of 8000K, this approximately corresponds to an electron density of $n = 100 \text{ cm}^{-3}$. Figure 3.7 shows the electron density distribution across both NGC 1365 and NGC 1068 calculated using the [S II] ratio, showing an electron density of $n = 100 \text{ cm}^{-3}$ to be a reasonable assumption in the star-forming regions of both galaxies. Our model is assumed to be radiation-bounded, and hence the model is terminated once 99% of H II recombination has occurred

3.4.2. AGN Model Grid

Our AGN models are computed assuming a plane-parallel geometry, and use the same definitions for the abundance pattern and metallicity scaling, and ionisation parameter as our starburst model described in Section 3.4.1. We use six metallicities when computing our AGN model grids, with values of $Z = 0.001, 0.004, 0.008, 0.020, 0.040$ and 0.060 . However, the low metallicities used in these grids are arguably redundant, as low-metallicity AGN are rare (e.g. Groves et al. 2006). In increments of 0.25 dex, the ionisation parameter varies from $\log(Q(N) \text{ cm}^{-2}\text{s}^{-1}) = 7.0$ to 11.0 inclusive.

We compute the AGN models also in isobaric conditions, however the value of initial pressure differs between the models used for NGC 1365 and NGC 1068. For NGC 1365, we use an initial pressure of $P/k = 2 \times 10^7$, and for NGC 1068, $P/k = 2 \times 10^8$. Under the assumption of a narrow-line region (NLR) initial temperature of 20,000K, this corresponds to electron densities of $n = 1000 \text{ cm}^{-3}$ and $n = 10,000 \text{ cm}^{-3}$ for NGC 1365 and NGC 1068 respectively, supported through the density calculation from the [S II] ratio in Figure 3.7.

The AGN region models are computed with a power-law spectrum of the form cv^α (Groves et al. 2004), fixing $\alpha = -1.2$. Lower values of α have been historically favoured (~ -1.4 to ~ -2.0 ; e.g. Groves et al. 2004; Belsole et al. 2006), however we find lower values of α fail to completely explain the TYPHOON data on the BPT diagram. Further justification on the use of $\alpha = -1.2$ is discussed in Appendix 3.8. The value of α however has been known to vary wildly amongst AGN (e.g. see detailed catalogue of AGN by Ackermann et al. 2011).

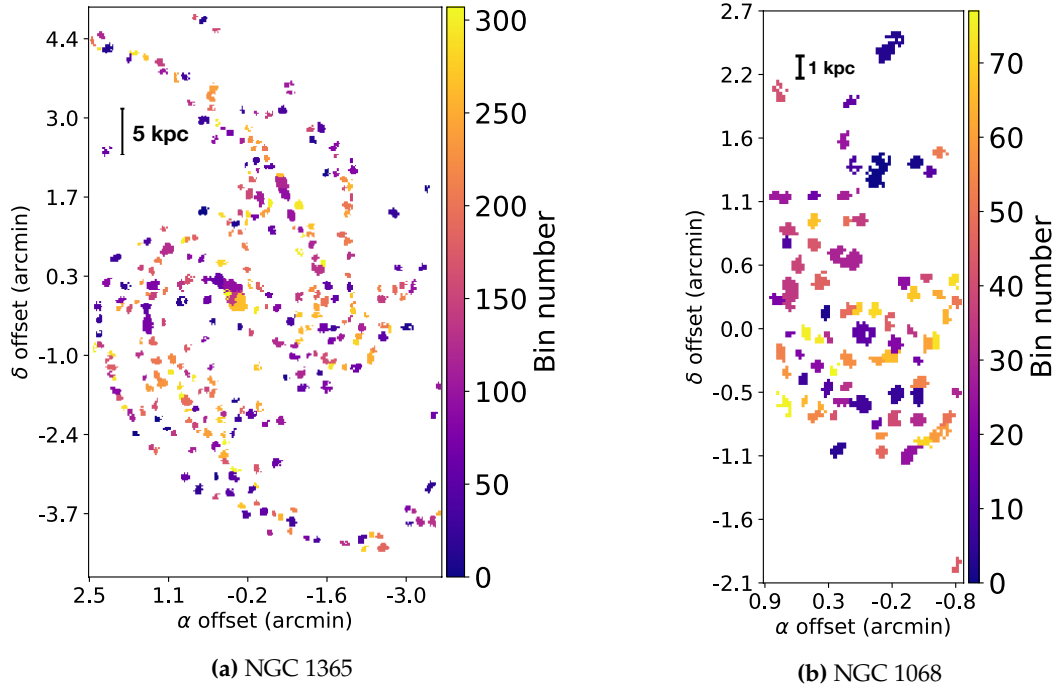


Figure 3.6 Figure showing location of H II regions in NGC 1365 in (a) and NGC 1068 in (b). These H II regions were identified using `npnpot`, developed by [Thilker et al. \(2000\)](#).

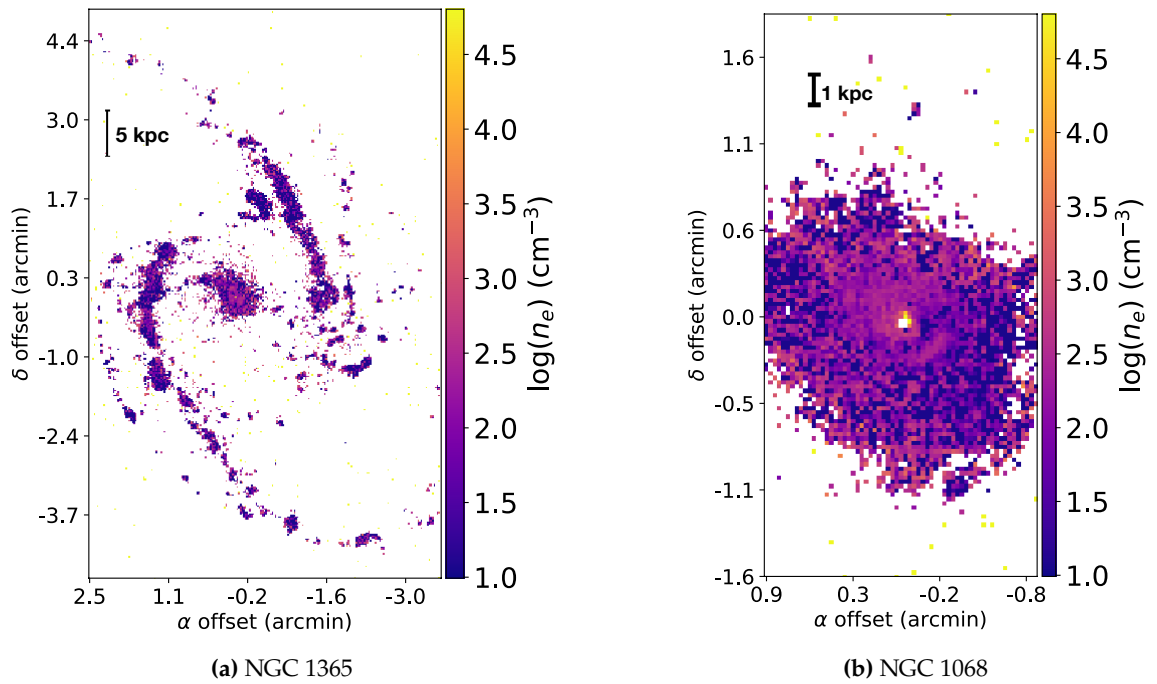


Figure 3.7 Figure showing range of electron density across both NGC 1365 in (a) and NGC 1068 in (b).

3.5. The Starburst-AGN Mixing Sequence

As demonstrated by [Kewley et al. \(2001\)](#) and [Kauffmann et al. \(2003\)](#), star-forming galaxies lie along a tight curve on the BPT diagram. However, as an AGN increases in activity until it completely dominates over emission from star formation, the galaxy moves off this star-forming sequence onto a ‘mixing sequence’ (e.g. [Kewley et al. 2006](#)). As discussed by [Kewley et al. \(2001\)](#) and demonstrated empirically by [Davies et al. \(2014a,b\)](#), the relative fractional contribution of star-formation and the AGN to the emission line luminosity can be determined from this mixing sequence.

[Davies et al. \(2014a,b\)](#) used ‘basis points’ to define empirical 100% starburst and 100% AGN positions on the BPT diagram. The starburst and AGN basis points were assigned to the spaxels which contained the lowest and highest $[\text{O III}]/\text{H}\beta$ ratio respectively. These basis points corresponded to 0% and 100% AGN activity, respectively. All other spaxels were assigned an AGN fraction between 0% and 100% corresponding to their star-forming distance (d_{SF} ; [Kewley et al. 2006](#)) along the line between the two basis points. The star-forming distance d_{SF} is a measure of a spaxel’s (or galaxy’s) offset in its $[\text{N II}]/\text{H}\alpha$ and $[\text{O III}]/\text{H}\beta$ ratios from the star-forming sequence on the BPT diagram, mapped out by pure star-forming galaxies in SDSS (see [Kauffmann et al. 2003](#)). The starburst basis point was defined as having a $d_{\text{SF}} = 0$. The complement to the AGN fraction with respect to 100% is considered to be the relative fraction of emission from star formation. Using data from the TYPHOON survey, we extend this method, described below.

The result of applying the method described by [Davies et al. \(2014a,b\)](#) to NGC 1365 from the TYPHOON survey is shown in Figure 3.10. The method from [Davies et al. \(2014a,b\)](#) when applied to IFU data shows AGN fractions of up to $\sim 50\%$ for several spaxels along the star forming sequence of NGC 1365. These spaxels are found below the Kauffmann line, which is considered to be the upper limit of pure star formation.

3.5.1. Use of Photoionisation Grids

We use the photoionisation grids described in Section 3.4 to aid in the selection of the basis points. The basis points selected by [Davies et al. \(2014a,b\)](#) for their starburst-AGN mixing work are purely empirical. Hence, the basis points contain no physical information about the galaxy. Through the use of photoionisation grids, star formation and AGN activity can be separated with the basis points containing physical information about the galaxy, such as the metallicities, ionisation parameters, pressures of both the H II and AGN regions, and hardness of the AGN power-law radiation field (Thomas et al. in prep.). In addition, theoretical models also allow the prediction of spectra at other wavelengths.

Galaxy	Metallicity (Z_{\odot})		Basis Point Coordinates ($\log([\text{N II}]/\text{H}\alpha)$, $\log([\text{O III}]/\text{H}\beta)$)				
	Edge	Centre	SB ₁	SB ₂	SB ₃	AGN ₁	AGN ₂
NGC 1365	0.55	1.42	(-1.01, 0.39)	(-0.64, -0.86)	(-0.42, -1.27)	(0.24, 1.14)	(0.46, 0.62)
NGC 1068	1.02	1.41	(-0.52, -0.19)	(-0.48, -0.99)	(-0.38, -1.49)	(0.22, 1.31)	(0.49, 0.71)

Table 3.1 Derived quantities for NGC 1365 and NGC 1068 for use on the BPT diagram.

To constrain the basis points of both the AGN and star-forming grids we use the independently determined gas-phase metallicity. The R_{23} metallicity diagnostic from Kobulnicky & Kewley (2004) (KK04) was used to diagnose metallicities from H II regions within the galaxy. These H II regions were identified using the IDL routine HIIPHOT, developed by Thilker et al. (2000). The H II regions were found to be located throughout the galaxy, thus making possible the calculation of metallicity gradients from the central regions to the outskirts of both galaxies. The location of the H II regions across NGC 1365 and NGC 1068 can be seen in Figure 3.6. The metallicities for the central and outer regions of both NGC 1365 and NGC 1068 can be found in Table 3.1.

Seen in Figure 3.8, coloured by radius from the centre of the galaxy, is the presence of a large star-forming sequence in NGC 1365. This star-forming sequence extends from the nucleus to the outermost regions of the galaxy. The starburst grid shows a metallicity gradient within this star-forming sequence, beginning at a high metallicity within the nucleus, and extending to a low metallicity at the edges of the galaxy.

We used the metallicity calculations to construct extra lines on the photoionisation grids, corresponding to the metallicities of the central and outer regions of the two galaxies. All basis points are positioned along these new grid lines, depending on the region of the galaxy for which they correspond. The positions of basis points SB1, SB2, and SB3 are defined by the starburst grid, whilst the positions of basis points AGN1 and AGN2 are defined by the AGN grid. Basis point SB1 is positioned along the line corresponding to the outer metallicity of the galaxy, at the edge of the star-forming sequence of spaxels. Basis points SB2 and SB3 are positioned along the line of central metallicity at the nuclear region of the star-forming sequence. Basis points AGN1 and AGN2 are also positioned along the line of central metallicity. The basis points are placed along the lines of constant metallicity such that they encompass the spread in ionisation parameter in the data (see Section 3.5.3). The starburst basis points SB1, SB2, and SB3 define the *starburst basis line*, described in Section 3.5.2. Basis points SB2, SB3, AGN1, and AGN2 altogether define the *nuclear column*, defined in Section 3.5.3. As an example, we show all five basis points located on the photoionisation grids in Figure 3.9, using the central and outer metallicities of NGC 1365 to determine their locations. Figure 3.9 also demonstrates the basis points defining the starburst basis line, and the nuclear column.

3.5.2. Starburst Basis Line

Davies et al. (2014a,b) assign a star-forming distance of $d_{\text{SF}} = 0$ to the high-metallicity end of the star-forming sequence, as the majority of AGN-dominated galaxies are shown to mix with high-metallicity H II regions (Groves et al. 2006). The high spatial resolution of the TYPHOON IFU data shows a star-forming sequence present in each individual galaxy, following the path mapped out by the pure star-forming galaxies in SDSS (see Kauffmann et al. 2003). By defining a single point as $d_{\text{SF}} = 0$, the spaxels on the star-forming sequence which extend out to lower metallicities are given progressively higher values for their star-forming distance. Seen in Figure 3.10, lower-metallicity star-forming spaxels are designated larger AGN fractions than expected.

We extend the notion of a starburst basis point defined as $d_{\text{SF}} = 0$, to a *starburst basis*

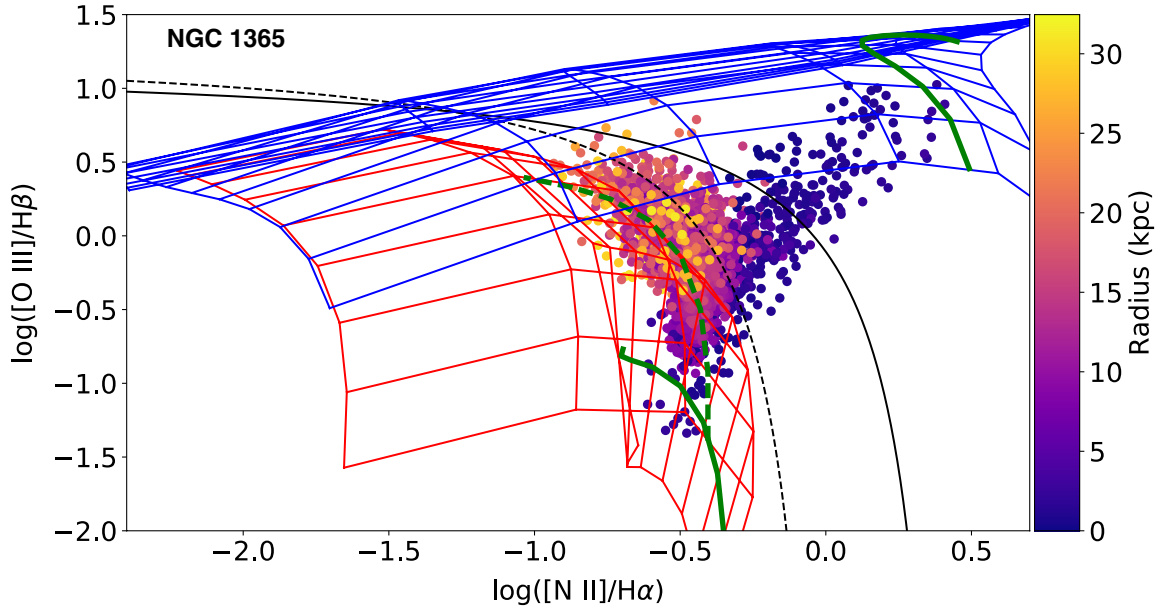


Figure 3.8 The BPT diagram of NGC 1365, with each spaxel coloured according to radius from the centre of the galaxy. The black dashed curve is the [Kauffmann et al. \(2003\)](#) empirical maximum starburst line, and the black solid line is the [Kewley et al. \(2001\)](#) theoretical maximum starburst line. The H II region grid is shown in red, and the AGN grid is shown in blue. The solid green grid lines on both grids represent the metallicity at the centre of the galaxy, and the dashed green grid line on the H II region grid represents the metallicity at the edge of the galaxy. Both metallicity values are stated in Table 3.1.

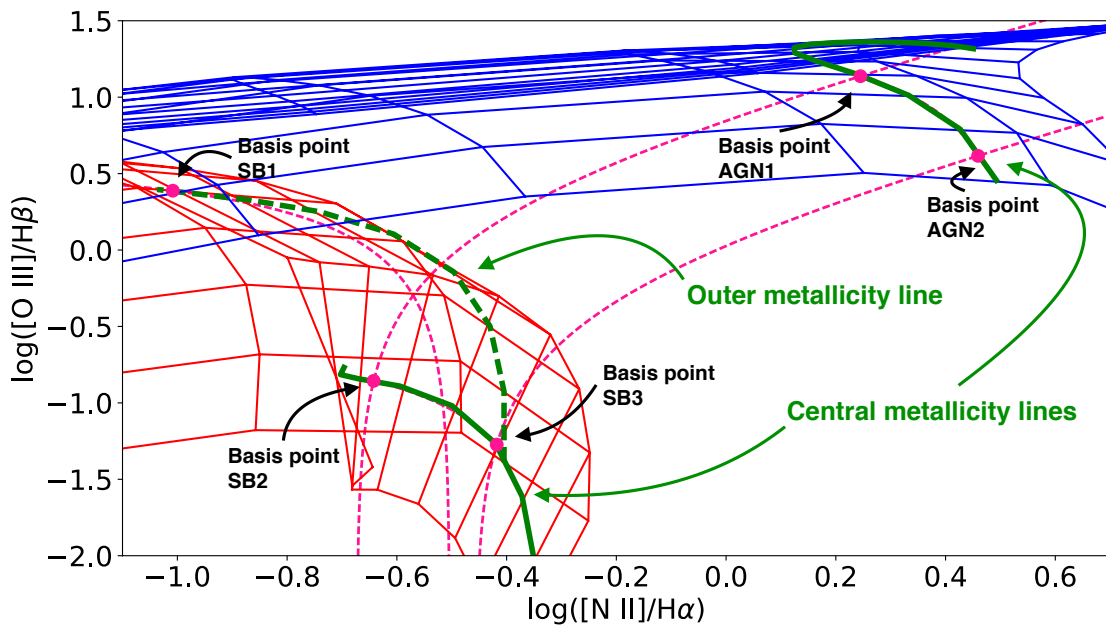


Figure 3.9 The basis points exhibited on the photoionisation grids, with the location of each constrained using the metallicity measurements of NGC 1365. The starburst basis points SB1, SB2, and SB3 define the starburst basis line, while the basis points SB2, SB3, AGN1, and AGN2 together define the nuclear column.

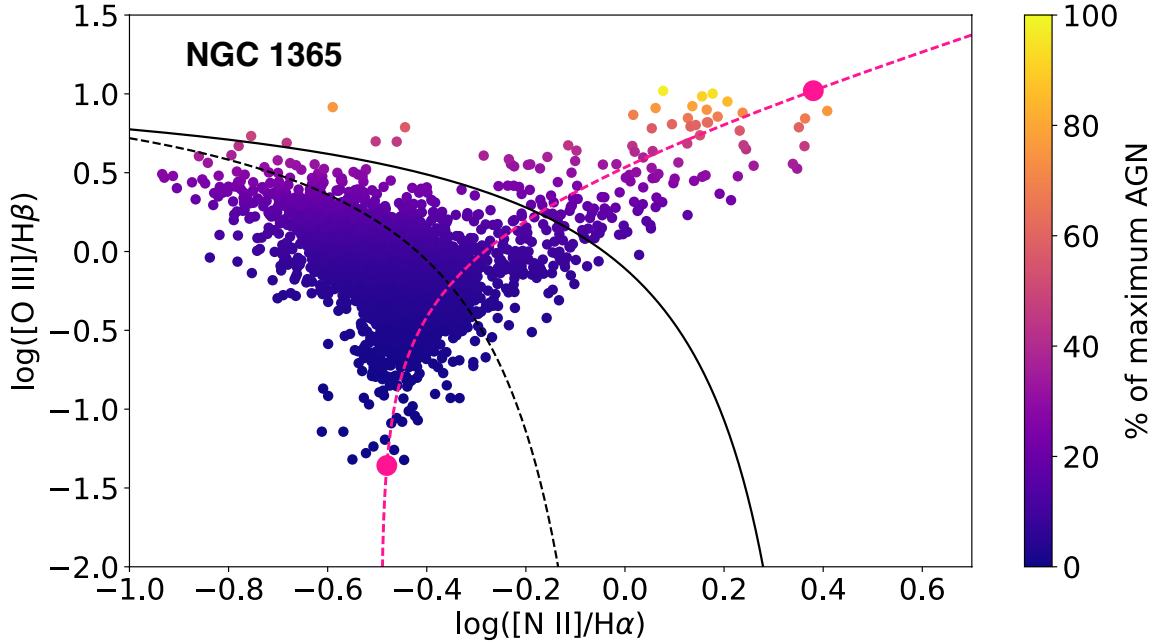


Figure 3.10 The AGN fraction for NGC 1365, using the old calculation by Davies et al. (2014a,b). The method from Davies et al. (2014a,b) gives AGN fractions of up to $\sim 50\%$ for some spaxels below the Kauffmann line – a well-known empirical line which signifies the upper limits of pure star formation.

line. Any spaxel present along the line is defined as having $d_{\text{SF}} = 0$. This line is indicated on Figure 3.12, extending between the starburst basis point SB1, and the midpoint of the starburst basis points SB2 and SB3.

3.5.3. Nuclear Column

Interestingly, all spaxels seen in the mixing sequence of NGC 1365 in Figure 3.8 are located in the nucleus, showing both star formation and AGN activity occurring as nuclear processes. Seen along this mixing sequence in Figure 3.8 is a clear spread in the ionisation parameter. We further extend the method displayed by Davies et al. (2014a,b) by increasing the number of basis points located at either end of the mixing sequence from one to two, in order to account for this spread in ionisation parameter ($\Delta \log Q(N) \sim 0.5$ dex). The result is defined as the *nuclear column*, and indicated in Figure 3.12 as extending between the 100% nuclear starburst line, and the 100% measurable AGN line. The nuclear column ensures the star-forming distance in the spaxels along the mixing sequence remains consistent, despite the changes in ionisation parameter. The AGN fraction for each spaxel is then determined by each spaxel's distance along a unique line projected between the 100% nuclear starburst line and the 100% AGN line.

3.5.4. Relative AGN Fractions

We calculate the relative AGN fractions for several emission lines for both NGC 1365 and NGC 1068, given as a percentage of the total emission. This calculation is identical to that displayed and described in Davies et al. (2014a). The complement of the AGN fraction with respect to 100% signifies the relative fraction of the total emission from star formation. The

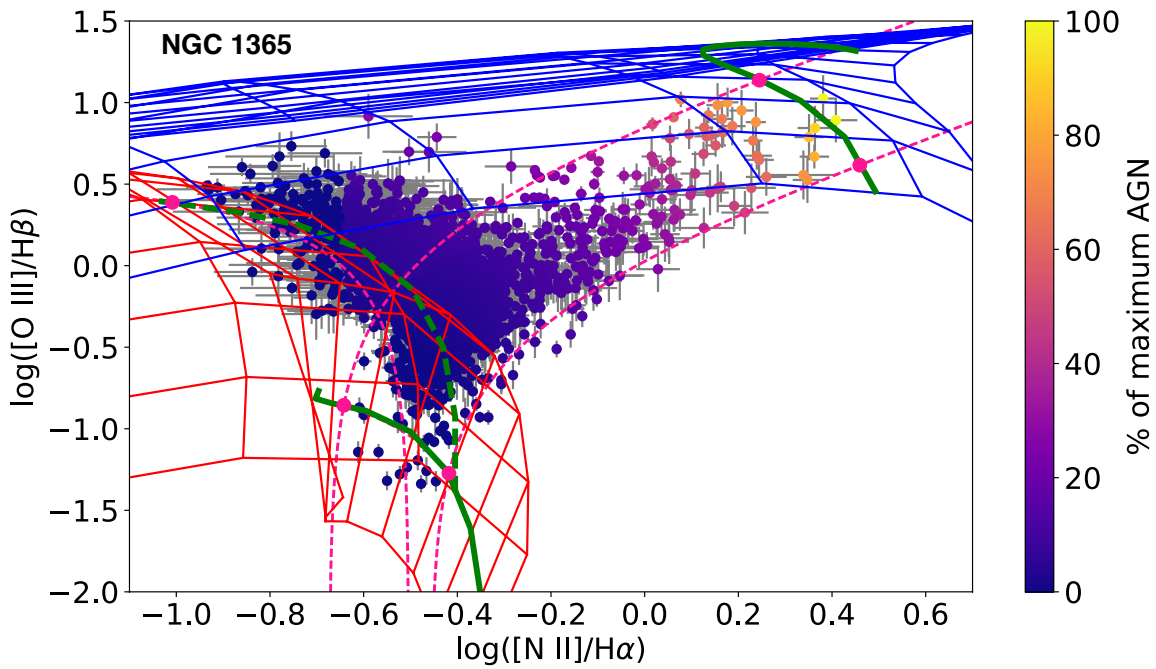


Figure 3.11 AGN fraction $[O\ III]/H\beta$ vs $[N\ II]/H\alpha$ diagram for NGC 1365.

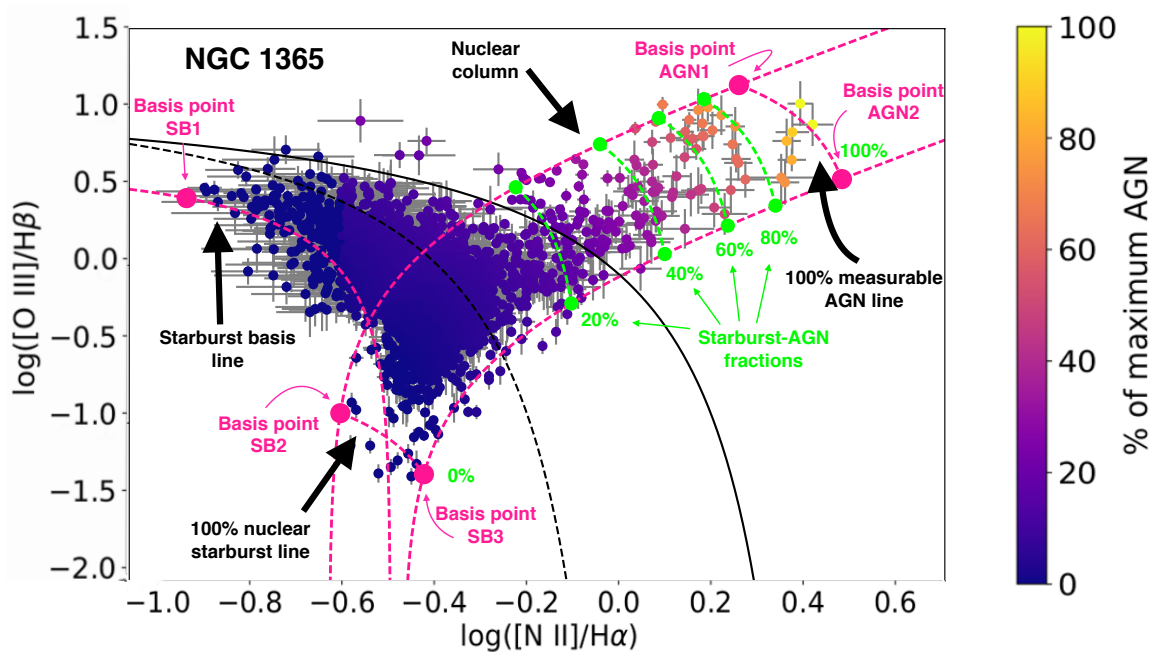


Figure 3.12 The BPT diagram for NGC 1365 showing the fractional contribution of AGN excited gas to the $H\alpha$ line using our new calculation method. This figure also overlays the original [Kauffmann et al. \(2003\)](#) and [Kewley et al. \(2001\)](#) AGN diagnostic lines (black lines, Figure 3.8), the new basis points and mixing curves based on our model grids (pink points and lines, Figure 3.9 and Section 3.5), and the resulting starburst-AGN mixing sequence (green curves).

total luminosity of any emission line in a given galaxy can be calculated by the following:

$$L_{\text{Tot}} = \sum_{i=1}^n L_i$$

where L_i is the luminosity in spaxel i for the emission line in question. The total luminosity of the emission line attributable to AGN activity can be calculated from

$$L_{\text{AGN}} = \sum_{i=1}^n f_i^{\text{AGN}} L_i$$

where f_i^{AGN} is the AGN fraction in spaxel i . It follows that the relative fraction of emission attributable to AGN activity for the given emission line is given by

$$f_{\text{Tot}}^{\text{AGN}} = \frac{L_{\text{AGN}}}{L_{\text{Tot}}}$$

Shown in Table 5.2 are the results of the above calculations for several emission lines. We discuss the results for NGC 1365 and NGC 1068 below individually.

NGC 1365

AGN activity from NGC 1365 has been inferred previously, with studies showing the nucleus of NGC 1365 to be luminous in hard x-rays (e.g. Risaliti et al. 2007, 2013), radio wavelengths (e.g. Sandqvist et al. 1982, 1995) and FUV radiation (e.g. Phillips et al. 1983). Further, the nucleus of NGC 1365 has been shown to produce large fluxes of collisionally-excited emission lines, with its high flux of [O III] very well documented (Phillips et al. 1983; Veilleux et al. 2003). Large [O III]/H β ratios in the nucleus of NGC 1365 (Phillips et al. 1983), as well as [O III]/H α ratios much larger than unity in the nucleus (Veilleux et al. 2003) have led previous authors to conclude the [O III] is produced by photoionisation from the central AGN of NGC 1365.

Our results of starburst-AGN mixing are in agreement with the AGN activity in the nucleus of NGC 1365. Seen in Figures 3.11 and 3.12 is the BPT diagram for NGC 1365, showcasing our new AGN fraction calculation. We note the presence of spaxels found below the 100% star formation lines, and spaxels found above the 100% AGN line. This indicates the uncertainties found within the photoionisation models, and may arise due to systematic uncertainties in the input ionising spectrum parameters (see D’Agostino et al. in prep. for a detailed discussion on the systematic uncertainties in input ionising stellar spectrum parameters in H II region modelling). Nevertheless, all spaxels which lie below the 100% star formation lines are set to 100% star formation, and all spaxels found above the 100% AGN line are set to 100% AGN. The map of the distribution of AGN fractions in NGC 1365 is shown in Figure 3.13a. Seen in Figure 3.13b is the nucleus of NGC 1365, coloured by AGN fraction. The nucleus of NGC 1365 shows regions of high AGN activity, corresponding to high [O III]/H β and [N II]/H α emission line ratios. However, regions of high star formation (low AGN fractions) are also seen in the nucleus, with a clean mixing evident between regions of low and high AGN fractions. Star formation in the nucleus of NGC 1365 is also confirmed in the BPT diagram of NGC 1365 coloured by radius from the centre of the galaxy, shown in Figure 3.8. Nuclear star formation in NGC 1365 has also been found

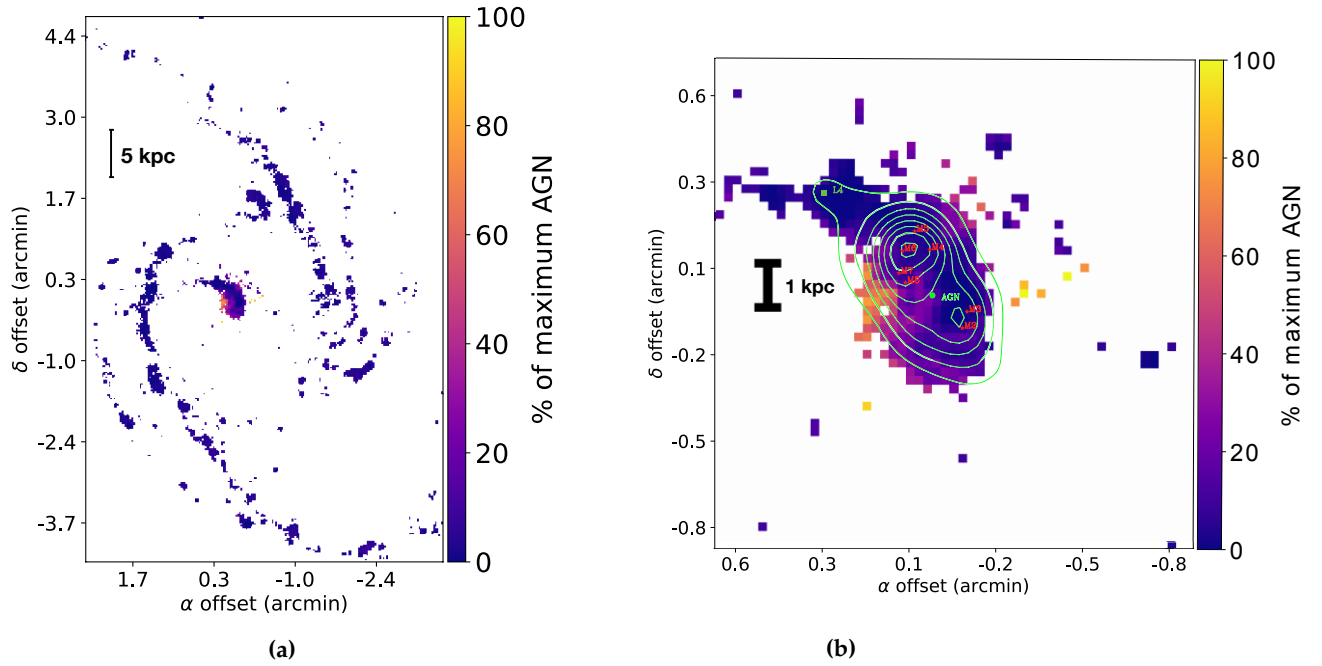


Figure 3.13 Map of NGC 1365 (a), with spaxels coloured to the $[\text{O III}]/\text{H}\beta$ vs $[\text{N II}]/\text{H}\alpha$ AGN fraction. The nucleus of NGC 1365 is shown in (b), overlaid with an image from [Alonso-Herrero et al. \(2012\)](#) showing star-forming clusters identified by [Galliano et al. \(2005\)](#) (red stars, M2, ..., M8), the $\text{H}\alpha$ hotspot L4 from [Alloin et al. \(1981\)](#) and [Kristen et al. \(1997\)](#), and light-green contours showing the $70\mu\text{m}$ flux distribution from Herschel PACS (square-root flux scaling, flux density of 85.5 Jy in the inner 15 arcseconds; [Alonso-Herrero et al. 2012](#)). The contours are in a square-root intensity scale, with flux of $70\mu\text{m}$ mid-IR emission.

previously (e.g. [Phillips et al. 1983](#); [Forbes & Norris 1998](#); [Galliano et al. 2008](#); [Alonso-Herrero et al. 2012](#), and references therein). In [Figure 3.13b](#), we show the position of several star-forming clusters shown in [Alonso-Herrero et al. \(2012\)](#), coinciding with regions of low AGN fractions (high star-forming emission) in the nucleus of NGC 1365. Contours of $70\mu\text{m}$ IR emission are also shown in [Figure 3.13b](#), taken from [Alexander & Hickox \(2012\)](#). The detection of mid-IR emission at $70\mu\text{m}$ (and other wavelengths; see [Alexander & Hickox 2012](#)) in the nucleus of NGC 1365 suggests an indirect detection of nuclear star formation, as a prominent dust lane surrounds the nuclear region of NGC 1365, obscuring a significant fraction of optical emission from our field of view ([Alexander & Hickox 2012](#)).

AGN activity south-east of the nucleus matches the biconical outflow seen in [Veilleux et al. \(2003\)](#), supporting the claim made by [Veilleux et al. \(2003\)](#) that the outflowing material is the result of AGN activity. Very little AGN activity, and in general structure, is seen on the north-west side of the nucleus. However, the north-west component of the $[\text{O III}]$ biconical outflow is fainter than its south-east counterpart ([Figure 3.2](#) and [Veilleux et al. 2003](#)).

As a source of ionisation and excitation, the AGN of NGC 1365 is relatively weak. This can be seen when considering the fraction of strong collisionally-excited emission line fluxes as a result of AGN activity, as the flux of collisionally-excited emission lines such as $[\text{O III}]$ and $[\text{N II}]$ are greatly enhanced by the extremely hard radiation field from the accretion disk of AGN ([Kewley et al. 2006, 2013a](#)). We measure the fraction of $[\text{O III}]$ luminosity from AGN activity in NGC 1365 within the TYPHOON field-of-view to be $10.02 \pm 0.71\%$. Conversely, this implies that $\sim 90\%$ of the total $[\text{O III}]$ luminosity in NGC 1365 within the TYPHOON

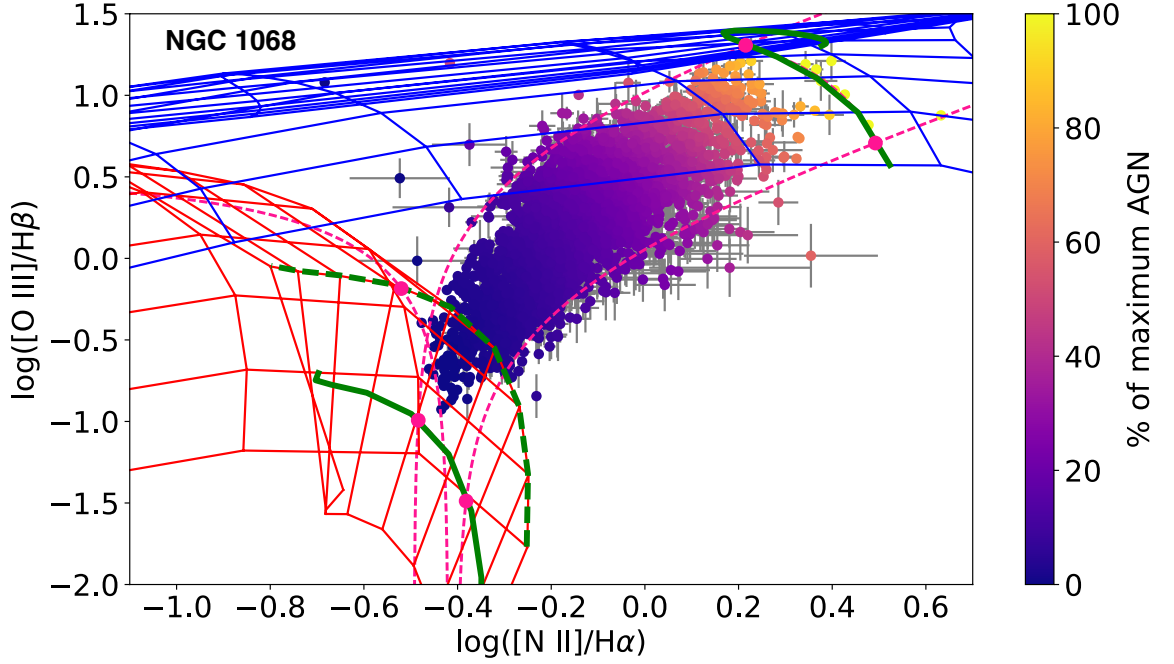


Figure 3.14 AGN fraction $[\text{O III}]/\text{H}\beta$ vs $[\text{N II}]/\text{H}\alpha$ diagram for NGC 1068.

field-of-view is from star formation, showing that star formation is the dominant process in NGC 1365. This is supported by the BPT diagram in Figure 3.8, which not only shows an extensive star-forming sequence, but also shows star formation occurring in the nucleus of NGC 1365 along with AGN activity. Further, we calculate the radius at which star formation and AGN activity dominate equally (AGN fraction = 50%) for NGC 1365 to be 1.350 ± 0.362 kpc. This calculation shows the majority of the AGN activity to be contained tightly within the nucleus with a very small radius of influence.

We calculate the fraction of the total $\text{H}\alpha$ luminosity attributable to AGN activity in NGC 1365 within the TYPHOON field-of-view to be $5.12 \pm 0.07\%$. As noted in Davies et al. (2014a), the AGN fractions in galaxies which display both processes indicate the degree of error imposed when using $\text{H}\alpha$ as a star formation rate (SFR) indicator. In the case of NGC 1365, SFRs calculated for NGC 1365 using $\text{H}\alpha$ can be considered largely accurate, as we observe $\sim 95\%$ of the total $\text{H}\alpha$ luminosity to be from star formation. At most, an overestimate of $\sim 5\%$ is expected when calculating SFRs in NGC 1365.

NGC 1068

Figures 3.14 and 3.15 show the BPT diagram and subsequent AGN fraction calculation for NGC 1068. The map of the AGN fraction for NGC 1068 is shown in Figure 3.16. Our findings support the claims made by Cecil et al. (2002) and Dopita et al. (2002a) regarding the driving force behind the large-scale outflows seen in NGC 1068. Material with a very high AGN fraction is seen in Figure 3.16a to both the north-east of the galaxy, and to the south-west through openings in the galactic disk, coinciding with the biconical structure shown in Das et al. (2006). This suggests that the large-scale outflowing plume of $[\text{O III}]$ seen in Pogge (1988) is the result of AGN-driven activity (shown in Figure 3.16a).

AGN-driven outflow from NGC 1068 has also been concluded from results in radio wavelengths.

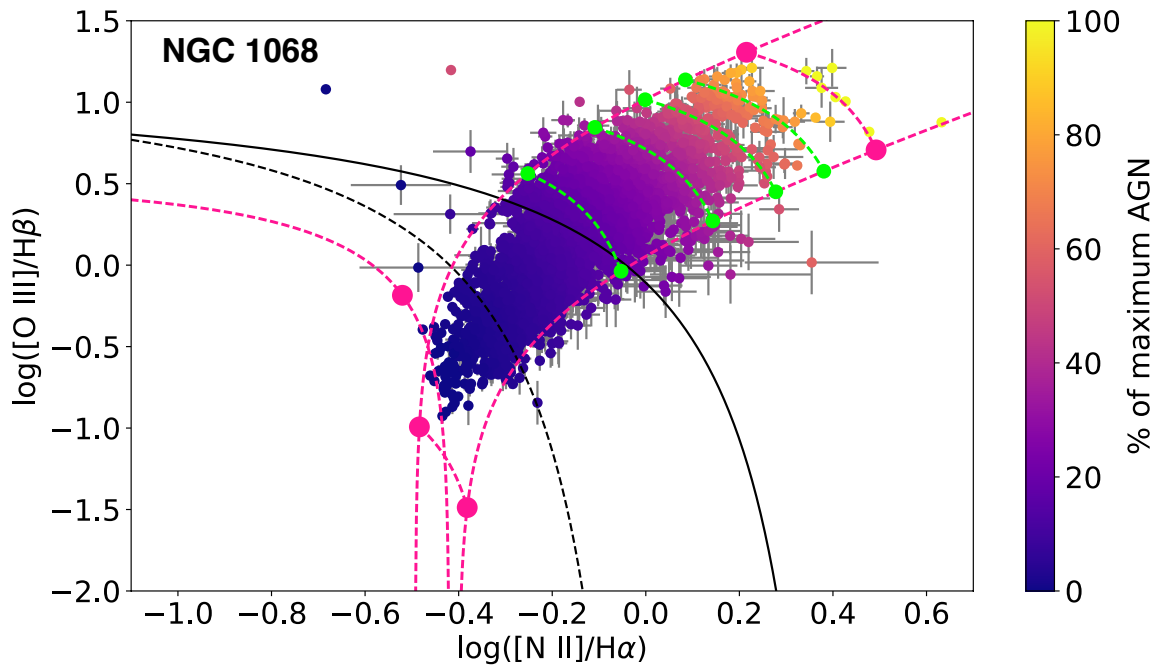


Figure 3.15 AGN fraction $[\text{O III}]/\text{H}\beta$ vs $[\text{N II}]/\text{H}\alpha$ diagram, without grids for clarity. Green dashed lines indicate 20%, 40%, 60%, and 80% AGN.

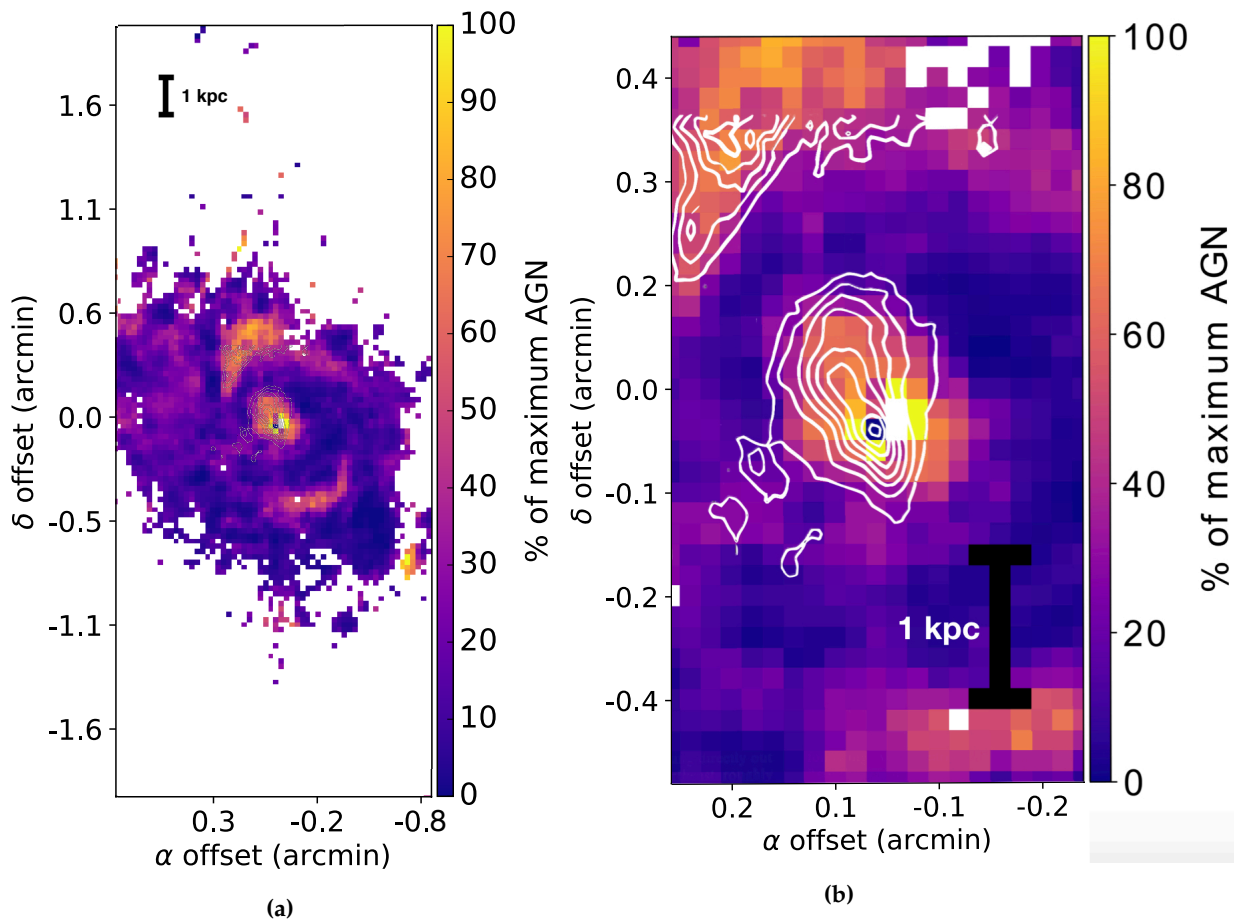


Figure 3.16 Map of NGC 1068 (a), with spaxels coloured to the $[\text{O III}]/\text{H}\beta$ vs $[\text{N II}]/\text{H}\alpha$ AGN fraction. The nucleus of NGC 1068 is shown in (b). The $[\text{O III}]/(\text{H}\alpha + [\text{N II}])$ contours from Pogge (1988) are shown on NGC 1068 in (a) and (b) in white.

Using data from ALMA, [García-Burillo et al. \(2014\)](#) map emission from a set of dense molecular gas tracers, namely CO(3-2), CO(6-5), HCN(4-3), HCO⁺ (4-3), and CS(7-6). Within the inner 50 – 400 pc, they report a massive outflow in all molecular gas tracers of $M_{\text{mol}} = 2.7^{+0.9}_{-1.2} \times 10^7 M_{\odot}$. They also show a tight correlation between the ionised gas outflow, the radio jet, and outward motions within the circumnuclear disk of NGC 1068, suggesting the outflow is AGN-driven. They strengthen this suggestion by noting the outflow rate in the circumnuclear disk is $63^{+21}_{-37} M_{\odot} \text{ yr}^{-1}$, much larger than the star formation rate calculated for NGC 1068 at these radii.

Star formation within the nucleus of NGC 1068 has been seen previously, with [Storchi-Bergmann et al. \(2012\)](#) locating young stars within the central 100 pc. The nuclear star formation rate in NGC 1068 is quite modest however, with estimates of $SFR_{\text{nuclear}} \sim 0.4 - 0.7 M_{\odot} \text{ yr}^{-1}$ out to a radius of 35 pc ([Davies et al. 2007](#)), $SFR_{\text{nuclear}} \sim 0.4 M_{\odot} \text{ yr}^{-1}$ out to a radius of 12 pc ([Esquej et al. 2014](#)), and $SFR_{\text{nuclear}} \sim 1 M_{\odot} \text{ yr}^{-1}$ out to a radius of 140 pc.

Further out from the nucleus, up to radii of a few kpc, the star formation rate in NGC 1068 has been shown to be enormous. [Thronson et al. \(1989\)](#) calculate a SFR of $\sim 100 M_{\odot} \text{ yr}^{-1}$ in the ring surrounding the circumnuclear disk. The starburst ring in NGC 1068 can be seen in our results in [Figure 3.16b](#) as a ring of spaxels with low AGN fraction surrounding the central region containing high AGN fractions. This large SFR is likely a consequence of the very large molecular mass in the circumnuclear region ($\sim 2 - 6 \times 10^9 M_{\odot}$), which appears to have been confined to the circumnuclear region by the bar at the centre of NGC 1068. As a result, star formation in NGC 1068 is seen to primarily take place in the star-forming ring surrounding the galaxy’s central region. Hence, observations showing extensive star formation towards the outermost regions of NGC 1068 have been rare. This finding is reflected in the BPT diagram of NGC 1068 shown in [Figure 3.14](#) which lacks a large star-forming sequence like that seen in [Figure 3.11](#) for NGC 1365. Our results suggest that star formation as a source of ionisation and excitation weakens at radii $\leq 2.246 \pm 1.277$ kpc, as these radii contain spaxels with AGN fractions greater than 50%.

We show star formation nevertheless is influential in the total emission from NGC 1068, despite the lack of a star-forming sequence and a relatively low nuclear SFR. Presumably a result of the enormous SFR surrounding the circumnuclear disk, we calculate roughly $\sim 59\%$ of the total [O III] luminosity to be from star formation within the TYPHOON field-of-view (shown as an AGN fraction of $41.68 \pm 0.28\%$ in [Table 5.2](#)). Our calculations in [Table 5.2](#) also show star formation to be the dominant process in the emission of all collisionally-excited lines considered within the TYPHOON field-of-view, with between $\sim 60 - 70\%$ of the total luminosity in the lines [O III] $\lambda 5007$ ($\sim 58\%$), [O II] $\lambda\lambda 3726, 3729$ ($\sim 68\%$), [S II] $\lambda\lambda 6716, 6731$ ($\sim 67\%$) and [N II] $\lambda 6854$ ($\sim 59\%$) attributable to star formation rather than AGN emission.

We claim the use of the total H α luminosity as a SFR indicator in NGC 1068 will overestimate the SFR by $\sim 25\%$. Shown in [Table 5.2](#), the luminosity of H α from AGN activity is calculated to be $24.38 \pm 0.12\%$, implying only $\sim 75\%$ of the luminosity from H α in NGC 1068 is from star formation.

3.6. Investigating the Effect of Spatial Resolution

We investigate the AGN fraction and other properties as a function of spatial resolution. We apply the same calculations and methods described in Section 3.5 to datacubes rebinned to 330, 500, and 1000 pc/pixel; resolutions found in other IFU surveys such as MaNGA, SAMI and CALIFA.

3.6.1. Effect of Resolution on the AGN Fraction

The AGN fraction calculations for NGC 1365 and NGC 1068 at differing resolutions are shown in Figures 3.18 and 3.21 as the BPT diagrams and in Figures 3.19 and 3.22 as maps of the galaxies. Figures 3.20 and 3.23 show maps of the AGN fraction in the nuclear regions of NGC 1365 and NGC 1068 respectively.

The basis point positions remain the same across all rebinned data for consistency, set to the values shown in Table 3.1. However, we do note following the work of Poetrodjojo et al. (2019), the metallicity gradient of a galaxy flattens with coarser resolution. Hence, if the metallicity gradient for both galaxies was recalculated using the rebinned data, the estimate for the central and outer metallicities would differ for each datacube, resulting in different positions for the basis points. We avoid this issue by noting the basis points are intended to represent line ratios associated with 100% star formation and 100% AGN emission. Binning together spaxels of AGN and star formation combines the processes in these spaxels, raising the overall contribution from AGN activity in the star-forming spaxels, and vice-versa. The result is a diminishing spread of spaxels on the BPT diagram with coarser resolution. Hence, as the resolution coarsens, the likelihood of a spaxel containing 100% emission from AGN activity or 100% emission from star-formation continues to decrease. This spread of spaxels on the BPT diagram is highest with the native resolution of both galaxies, suggesting the best indication of 100% AGN emission and 100% star-forming emission is provided by the highest-resolution datacubes available.

The increase in AGN contribution in spaxels as the data is rebinned is shown in Table 3.2 which gives a constant increase in the radius of equal starburst-AGN domination for both galaxies (the radius where the AGN fraction = 50%). It is also shown in Figure 3.17, showing an average increase in the percentage of spaxels with AGN fractions > 50% as resolution decreases. The AGN radiation field produces large [O III] and [N II] line strengths, which dominate over the weaker line strengths from star formation, even at low AGN fractions.

In general, the AGN fractions for several strong emission lines ($H\alpha$, $H\beta$, [O II] $\lambda\lambda$ 3726,3729, [O III] λ 5007, [S II] $\lambda\lambda$ 6716,6731, and [N II] λ 6584) may increase with coarser resolution (Table 5.2). Considering NGC 1365, we find no significant change in the AGN fractions within the error bounds of the aforementioned strong emission lines between native resolution and a resolution of 1 kpc/pix, averaged over all lines shown in Table 5.2. NGC 1068 however, shows an average increase of $17.67 \pm 7.09\%$ in the AGN fractions for the same strong emission lines between native resolution and a resolution of 1 kpc/pix. This has large ramifications for calculating the SFR in a galaxy. NGC 1068 shows an increase in the $H\alpha$ AGN fraction between native (121 pc/pix) and 1 kpc/pix resolutions of $14.59 \pm 0.14\%$.

As a result, in general, the SFR from a galaxy with AGN activity may be continually and further overestimated with coarser spatial resolution.

We find that there is no limiting spatial resolution which allows the AGN fraction to be reliably estimated. The radius of equal starburst-AGN domination continues to decrease as the resolution increases (seen in Table 3.2), as does the percentage of spaxels with AGN fraction greater than 50% (seen in Figure 3.17). As such, one can expect the measurable emission from AGN to continue to decrease once the resolution has increased beyond the resolutions of the TYPHOON galaxies (169 pc/pixel for NGC 1365; 121 pc/pixel for NGC 1068). Hence, when attempting to accurately measure and quantify the influence and emission from an AGN, one should obtain data at a resolution as high as possible.

3.6.2. Effect of Resolution on Low Surface Brightness Features

As the resolution decreases, low surface brightness (LSB) features become apparent. Seen in the BPT diagrams at lower resolutions are spaxels in the regions commonly associated with features such as shocks (for the position of shock features on diagnostic diagrams, see Rich et al. 2010, 2011; Kewley et al. 2013a). These LSB features typically have low signal-to-noise ratio values. The rebinning process produces an increase in the S/N of the LSB spaxels. Hence, LSB features become observable in the data. Table 3.2 shows the relative difference in spaxels with emission attributable to LSB features. In total, we see an increase in the percentage of spaxels which we attribute to low surface brightness features between the native resolution data and the rebinned data for both NGC 1365 and NGC 1068. The increase in the relative amount of spaxels attributed to LSB features differs for both galaxies, with up to a factor of ~ 12.5 increase in NGC 1365 with coarser resolution, and up to a factor of ~ 1.6 increase in NGC 1068. These spaxels are defined as being outside the nuclear column with moderate $[\text{O III}]/\text{H}\beta$ and moderate-high $[\text{N II}]/\text{H}\alpha$ ratios, in the region of the BPT where LSB features are typically found.

Shocks

Shocks (or shock waves) are compression waves which propagate at a speed greater than the sound speed in the medium. Due to the supersonic nature of the shock wave, instantaneous changes in properties of the medium (such as density, pressure and temperature) occur at the shock front, causing discontinuities in the values of these properties before and after the boundary of the shock. The source of supersonic compression may originate from astrophysical phenomena such as supernova explosions, stellar winds, or outflows from young stellar clusters or AGN (Dopita & Sutherland 2003, and references therein).

Shocks are typically diagnosed and categorised by their high velocity dispersions (typically $\sim 100 - 500 \text{ kms}^{-1}$; Rich et al. 2010, 2011, 2014; Ho et al. 2014). Figure 3.24 shows the velocity dispersion maps across all resolutions considered for NGC 1365. Regions of high velocity dispersion ($\sigma \sim 160 \text{ kms}^{-1}$) can be seen around the nucleus of NGC 1365 across all resolutions. However, the high velocity dispersion regions surrounding the nucleus grow in size as resolution decreases. The high- σ areas surrounding the nucleus are aligned with the biconical outflow in $[\text{N II}]/\text{H}\alpha$ and $[\text{O III}]/\text{H}\beta$ shown in NGC 1365 from Veilleux et al. (2003)

Percentage of spaxels from low surface brightness features				
Resolution	Native	330 pc/pix	500 pc/pix	1 kpc/pix
NGC 1365	0.03%	0.61%	0.77%	0.20%
NGC 1068	1.29%	2.04%	0.66%	2.11%
Radii of equal starburst-AGN domination				
Resolution	Native	330 pc/pix	500 pc/pix	1 kpc/pix
NGC 1365	1.35 ± 0.36 kpc	2.49 ± 1.12 kpc	2.79 ± 0.92 kpc	4.26 ± 2.08 kpc
NGC 1068	2.26 ± 1.27 kpc	3.55 ± 1.89 kpc	5.00 ± 1.81 kpc	6.97 ± 2.98 kpc

Table 3.2 (i) The percentage of spaxels showing emission from low surface brightness features. Spaxels showing emission from low surface brightness features are defined as being below the nuclear column. (ii) The radius of equal starburst and AGN domination (AGN fraction = 50%) for varying resolutions for both NGC 1365 and NGC 1068. Values are calculated as averages of distances for spaxels with AGN fractions between 45% and 55%. The errors on these values represent the standard deviation of these sets of distances.

(shown in Figure 3.25), suggesting the shocks in NGC 1365 are the result of outflow from the central AGN.

The number of regions of high velocity dispersion along the spiral arms of NGC 1365 increases as the resolution decreases, with velocity dispersions up to $\sigma \sim 300 \text{ km s}^{-1}$ at a resolution of 1 kpc/pix. The high levels of star formation in the spiral arms of NGC 1365 shown in Figures 3.11 and 3.13a suggest that regions of high velocity dispersion within the spiral arms are a result of shocks from stellar sources, such as supernova explosions and stellar winds. It appears that shocks from stellar sources are intensified and enhanced with coarser resolution.

NGC 1068 also shows evidence of shocks. Seen in the velocity dispersion maps for NGC 1068 in Figure 3.26, regions of high velocity dispersion can be seen away from the central AGN, notably along the biconical outflowing material. An accreting supermassive black hole will produce thermal x-rays which provide a radiation pressure on nearby gas, causing expulsion of the gas in the form of a wind. The biconical outflow, believed to be the result of AGN activity (Pogge 1988; Cecil et al. 2002; Dopita et al. 2002a, and our Figure 3.16) is radiatively accelerated to high velocities ($\sim 3000 \text{ km s}^{-1}$ in the case of NGC 1068; Cecil et al. 2002) by the AGN wind. Once the wind enters the ISM, the high-velocity material interacts with the ISM material, which is travelling at a velocity on the order of the sound speed in the medium (\sim a few tens of km s^{-1} ; Dopita & Sutherland 2003). The high-velocity outflowing material, travelling at a velocity higher than the sound speed in the medium, compresses the ISM material upon interaction, causing shocks through the ISM (Zubovas & King 2012). Hence, it is expected that regions of high velocity dispersion which correspond to shocks appear within the biconical outflowing material found in NGC 1068. The number and relative amount of the high velocity dispersion regions along the biconical outflow continues to increase as the resolution decreases. The spaxels in the area concerning shocks on the BPT diagrams for NGC 1068 shown in Figure 3.21 are assigned large radii ($r > 5$ kpc), constraining these spaxels to be outside the disk of NGC 1068.

NGC 1365				
Resolution	Native (169 pc/pix)	330 pc/pix	500 pc/pix	1 kpc/pix
H α	4.85 \pm 0.07%	5.43 \pm 0.06%	5.75 \pm 0.06%	6.34 \pm 0.05%
H β	4.41 \pm 0.27%	4.86 \pm 0.26%	5.09 \pm 0.24%	5.54 \pm 0.20%
[O II] $\lambda\lambda$ 3726,3729	4.78 \pm 1.76%	5.23 \pm 1.13%	5.60 \pm 1.02%	6.35 \pm 0.81%
[O III] λ 5007	10.06 \pm 0.71%	11.96 \pm 0.72%	12.35 \pm 0.66%	13.25 \pm 0.52%
[S II] $\lambda\lambda$ 6716,6731	5.65 \pm 0.30%	6.47 \pm 0.28%	6.97 \pm 0.26%	7.93 \pm 0.21%
[N II] λ 6584	6.95 \pm 0.20%	8.49 \pm 0.20%	9.17 \pm 0.18%	10.32 \pm 0.15%
NGC 1068				
Resolution	Native (121 pc/pix)	330 pc/pix	500 pc/pix	1 kpc/pix
H α	25.23 \pm 0.13%	39.40 \pm 0.10%	39.07 \pm 0.08%	39.82 \pm 0.05%
H β	26.40 \pm 0.81%	38.91 \pm 0.51%	39.26 \pm 0.38%	42.31 \pm 0.25%
[O II] $\lambda\lambda$ 3726,3729	32.23 \pm 6.81%	25.27 \pm 2.50%	31.56 \pm 2.18%	42.68 \pm 1.54%
[O III] λ 5007	42.69 \pm 0.28%	68.19 \pm 0.16%	68.75 \pm 0.12%	68.88 \pm 0.07%
[S II] $\lambda\lambda$ 6716,6731	33.38 \pm 0.79%	43.32 \pm 0.43%	44.15 \pm 0.38%	46.16 \pm 0.21%
[N II] λ 6584	41.52 \pm 0.31%	64.58 \pm 0.15%	66.02 \pm 0.11%	67.62 \pm 0.07%

Table 3.3 AGN fractions for several strong emission lines at varying resolutions for both NGC 1365 and NGC 1068 within the TYPHOON field-of-view. Percentage indicates fraction of luminosity attributable to AGN activity for each line.

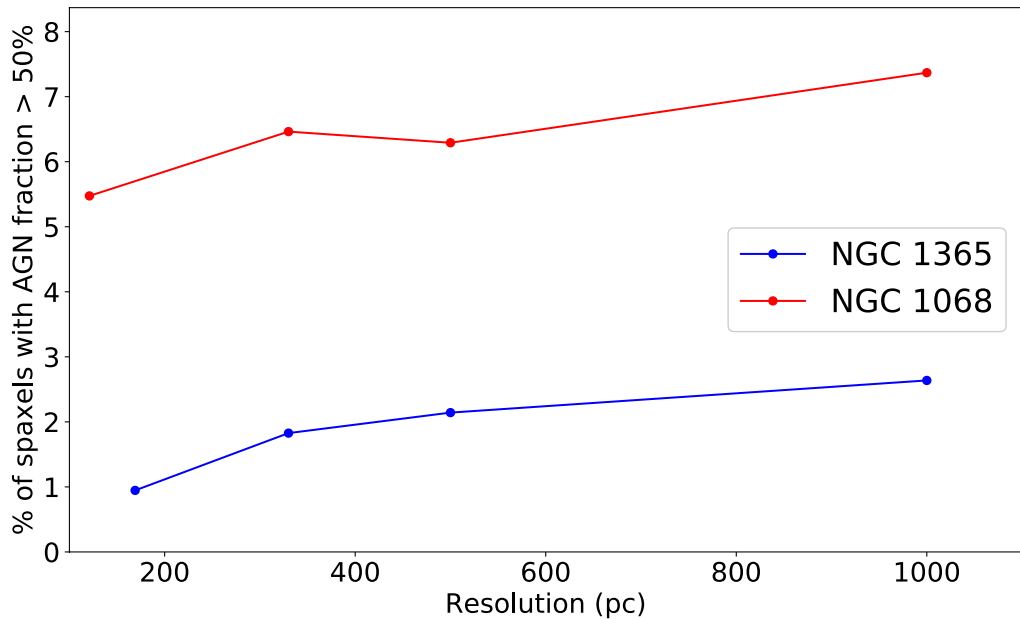


Figure 3.17 The percentage of spaxels in the BPTs of both NGC 1365 and NGC 1068 with AGN fractions of greater than 50% as a function of spatial resolution. The four markers indicate (in order): native resolution (169pc and 121pc for NGC 1365 and NGC 1068 respectively), 330pc, 500pc, and 1000pc (1kpc).

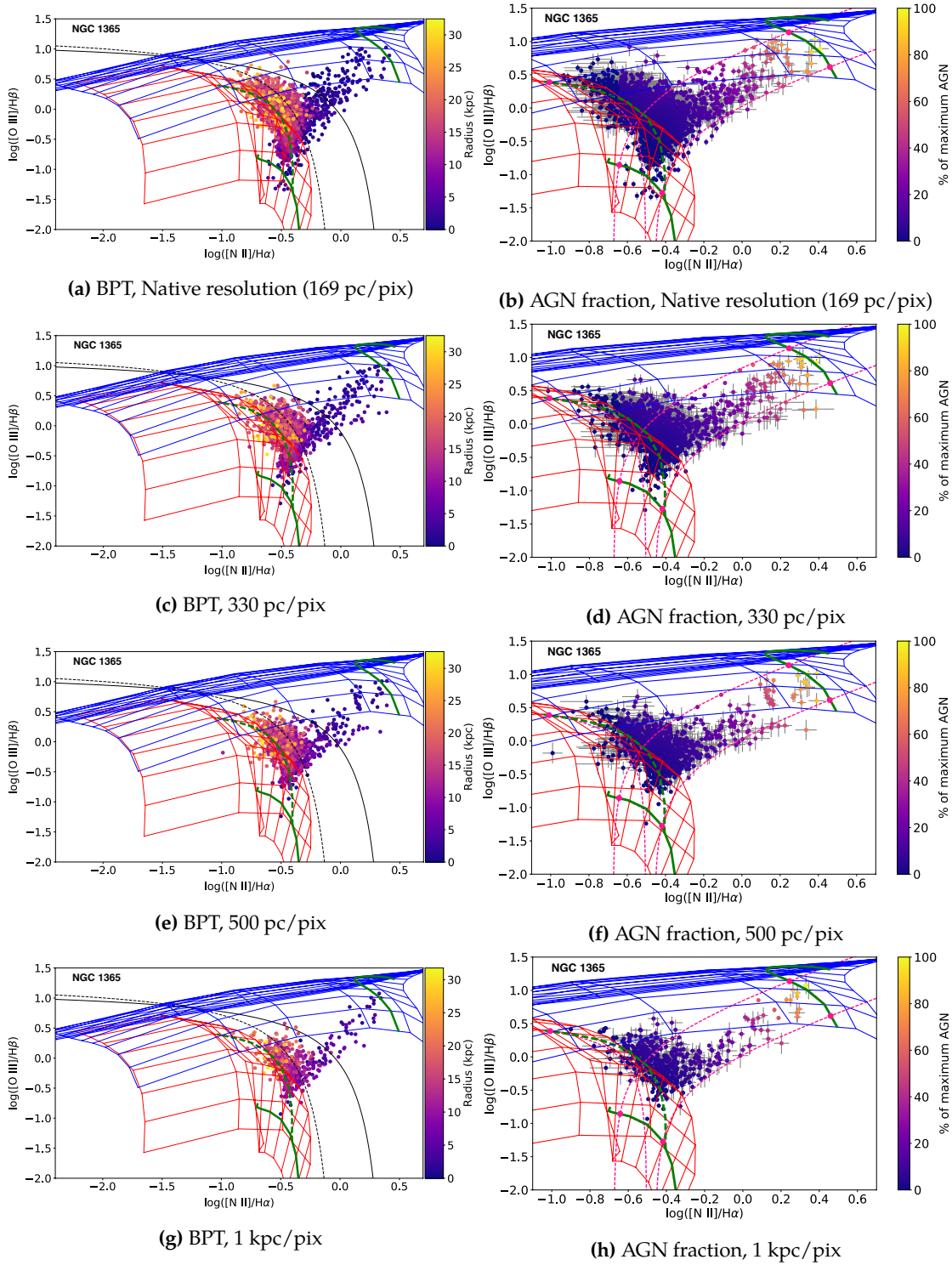


Figure 3.18 The AGN fractions and BPT diagrams coloured by radius for NGC 1365, after rebinning to lower spatial resolutions. Errors for the spaxels on the BPT diagrams are the same as those on the AGN fraction plots.

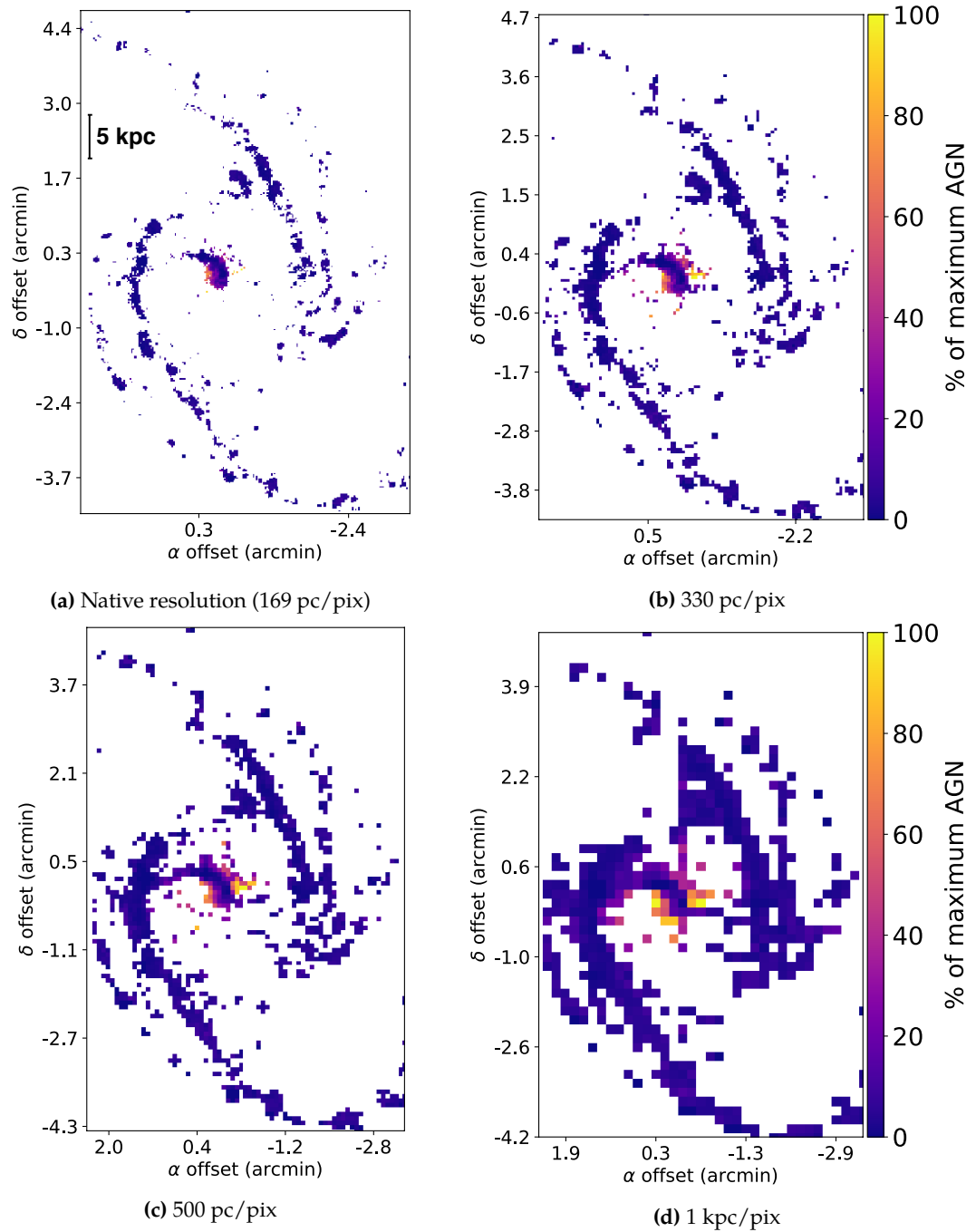


Figure 3.19 The $[\text{O III}]/\text{H}\beta$ vs $[\text{N II}]/\text{H}\alpha$ AGN fraction map for NGC 1365, after rebinning to lower spatial resolutions.

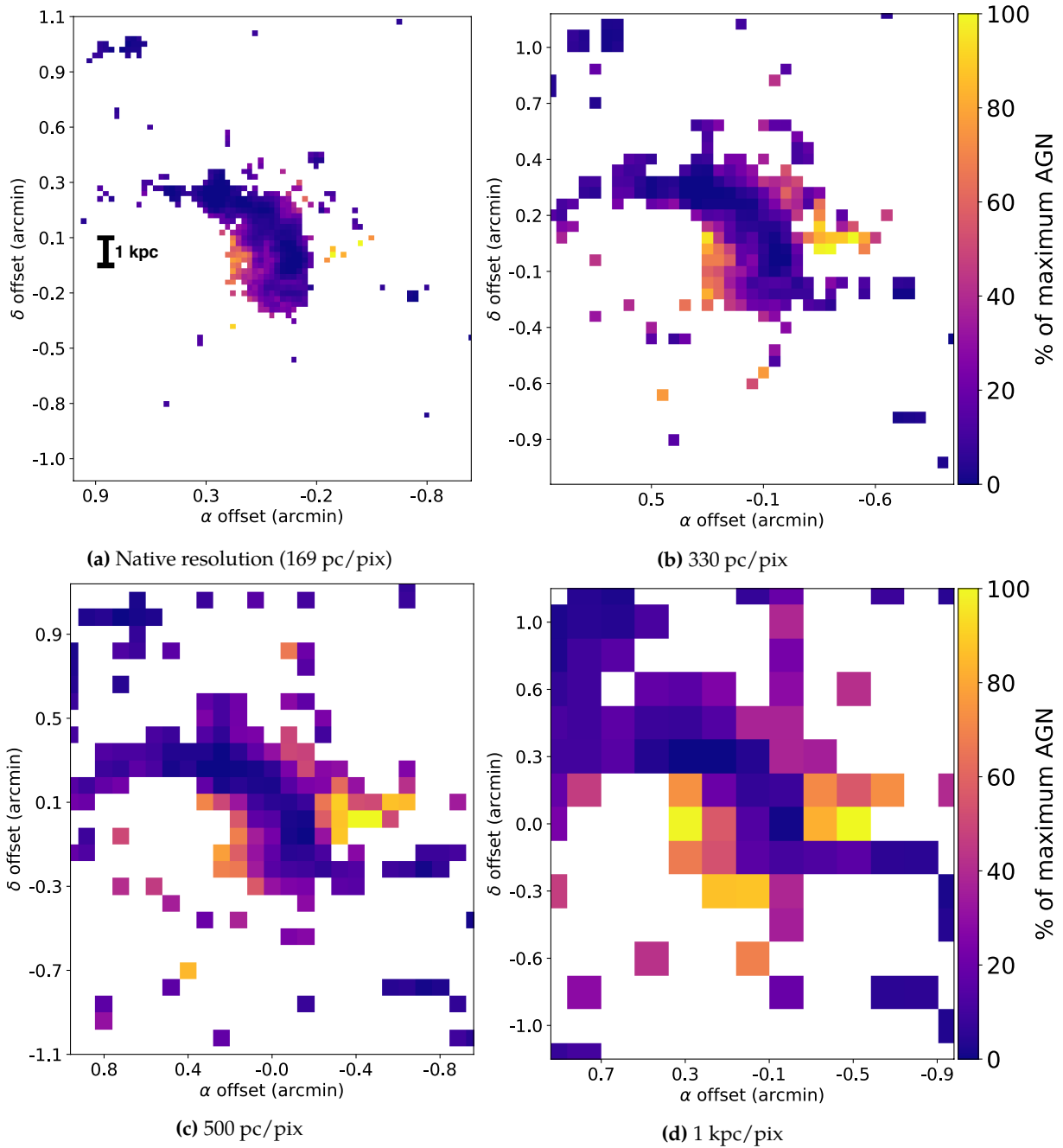


Figure 3.20 Images from Figure 3.19 with a zoom on the nuclear region of NGC 1365

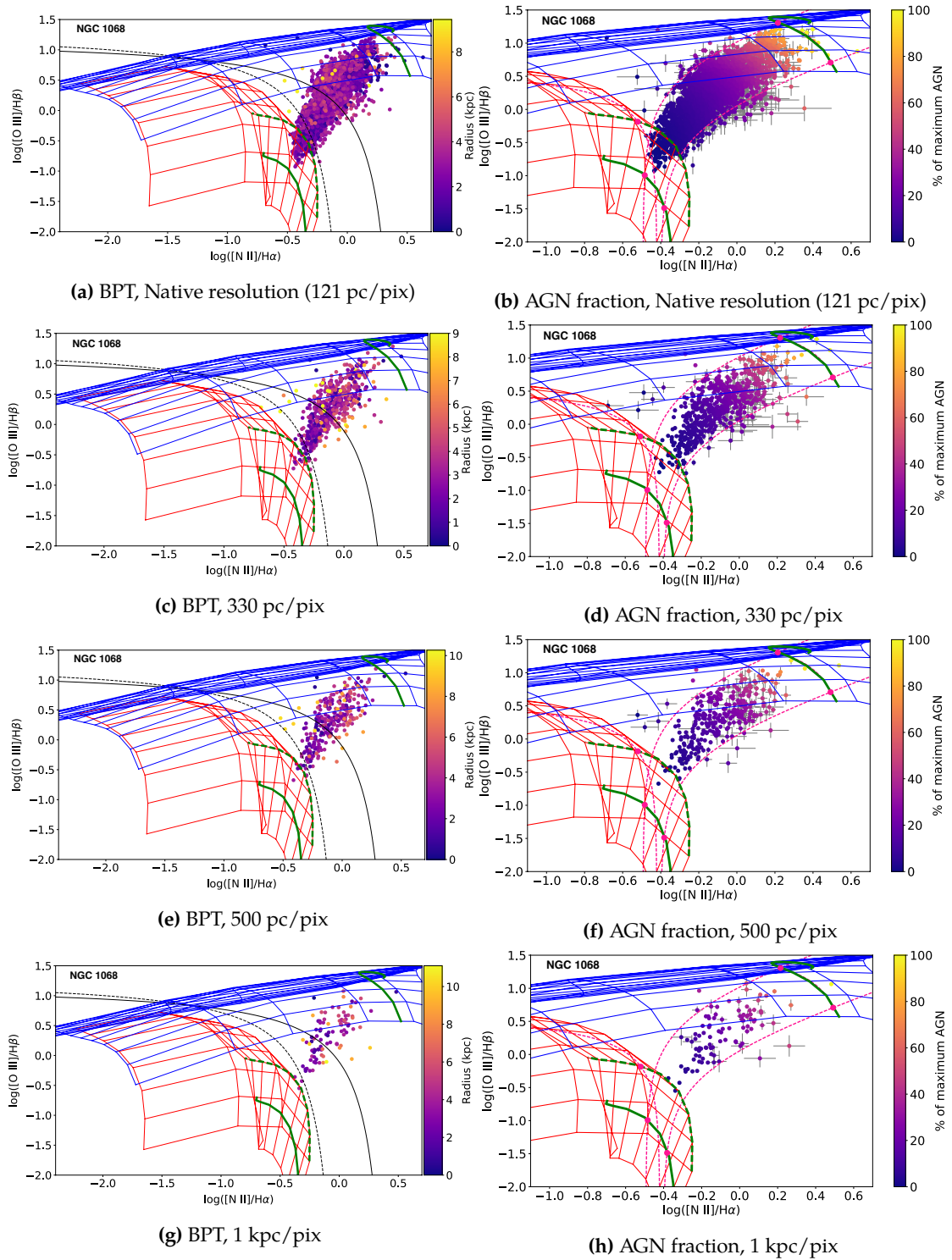


Figure 3.21 The AGN fractions and BPT diagrams coloured by radius for NGC 1068, after rebinning to lower spatial resolutions. Errors for the spaxels on the BPT diagrams are the same as those on the AGN fraction plots.

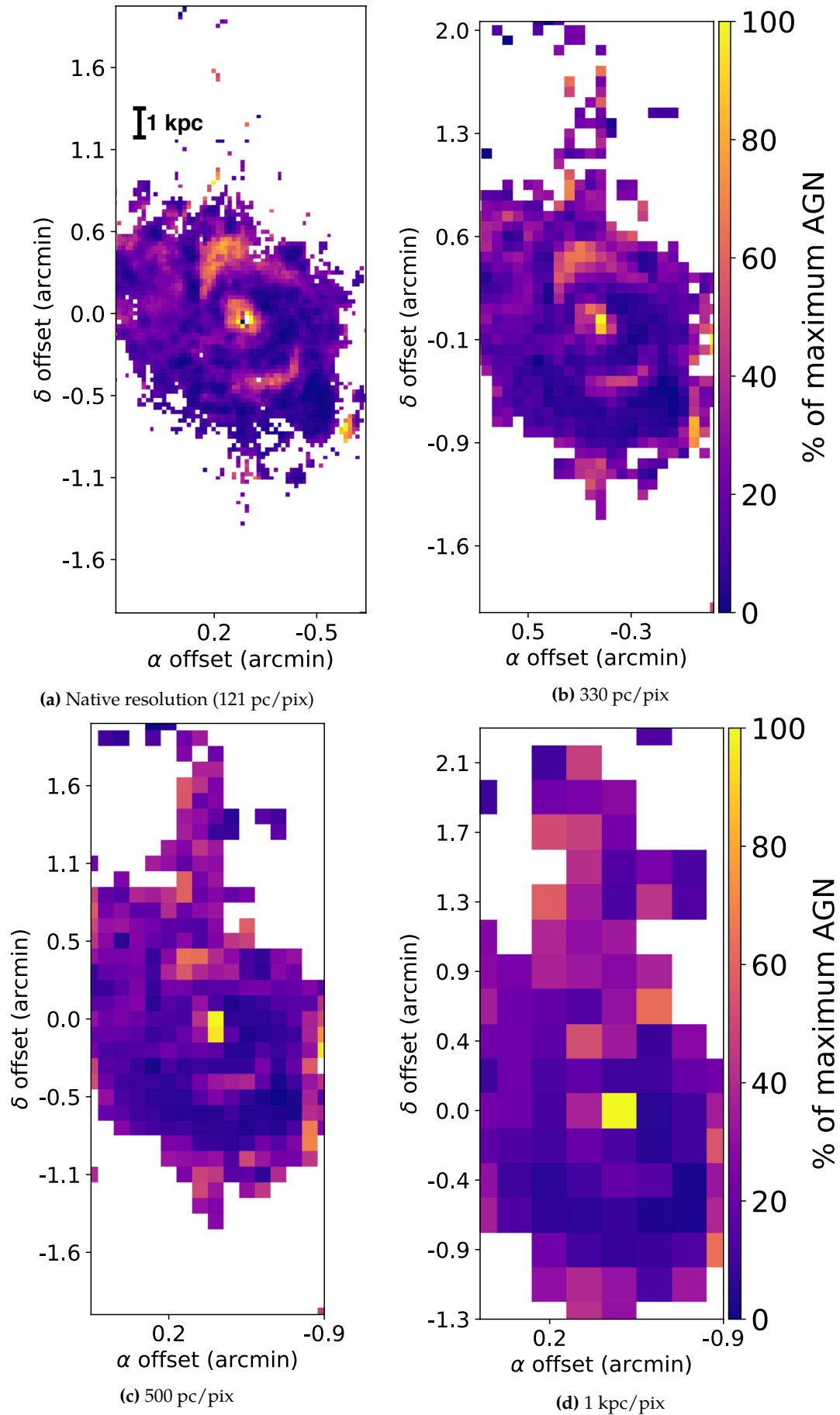


Figure 3.22 The $[\text{O III}]/\text{H}\beta$ vs $[\text{N II}]/\text{H}\alpha$ AGN fraction map for NGC 1068, after rebinning to lower spatial resolutions.

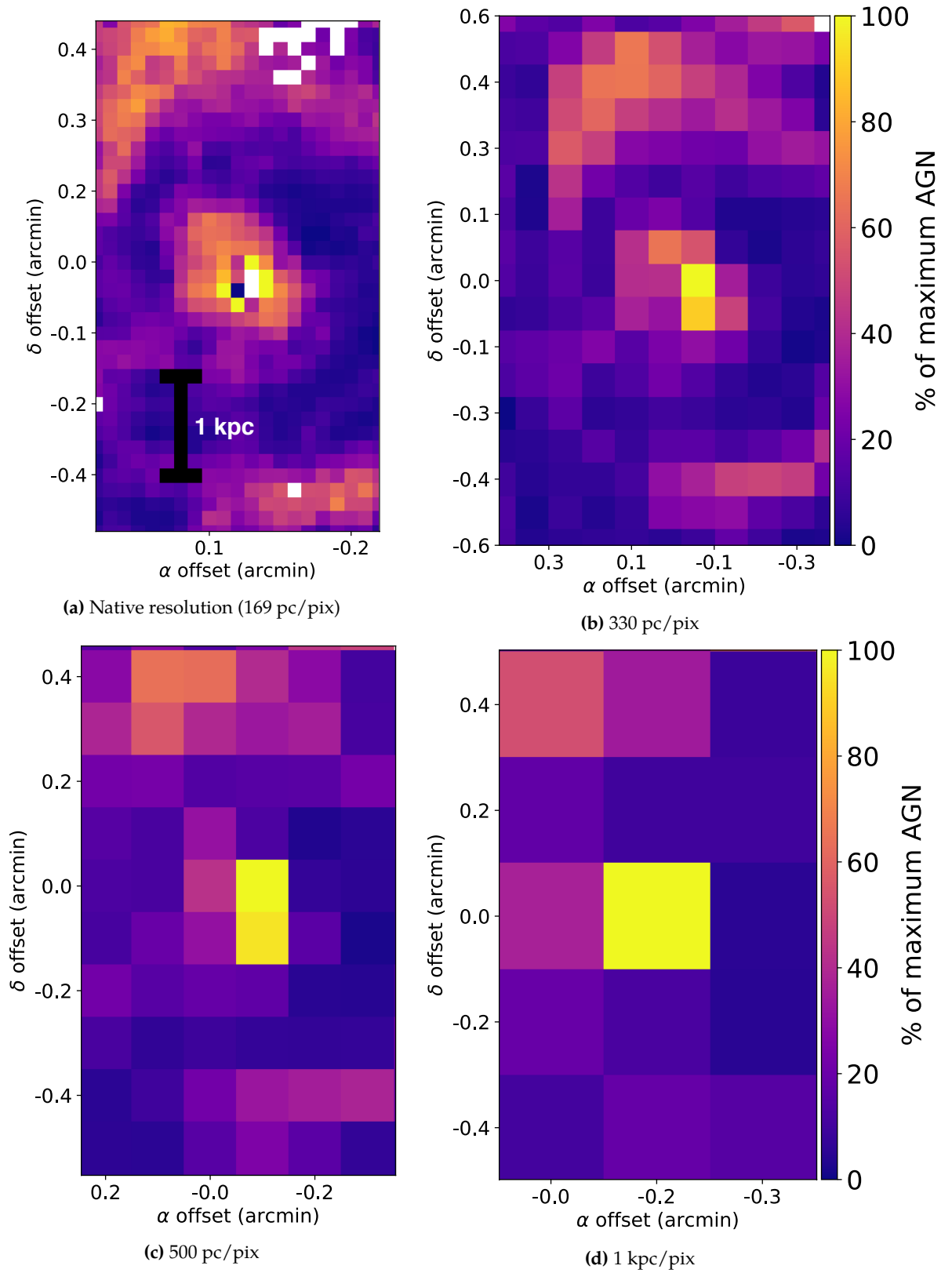


Figure 3.23 Images from Figure 3.22 with a zoom on the nuclear region of NGC 1068

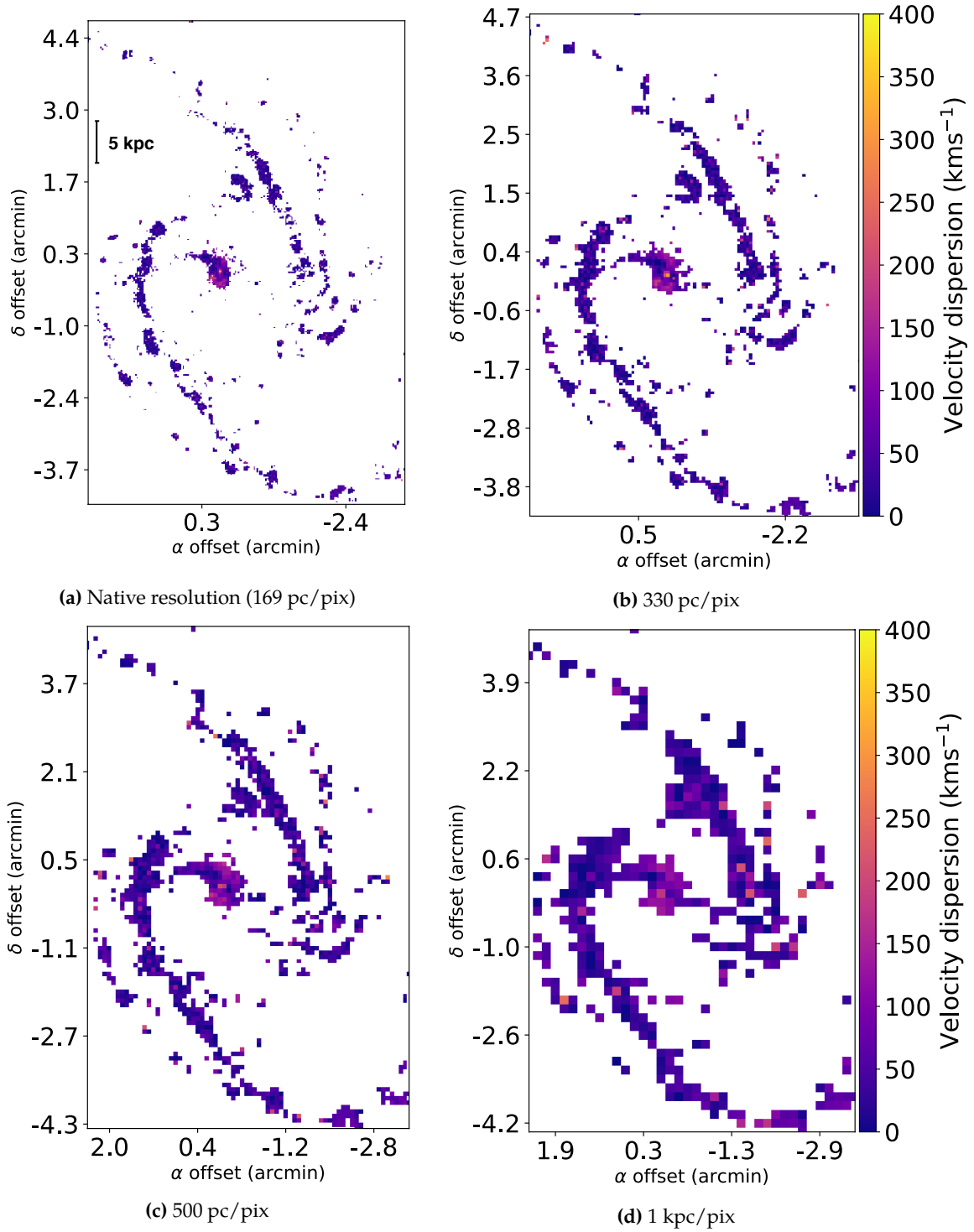


Figure 3.24 The velocity dispersion maps for NGC 1365, after rebinning to lower resolutions.

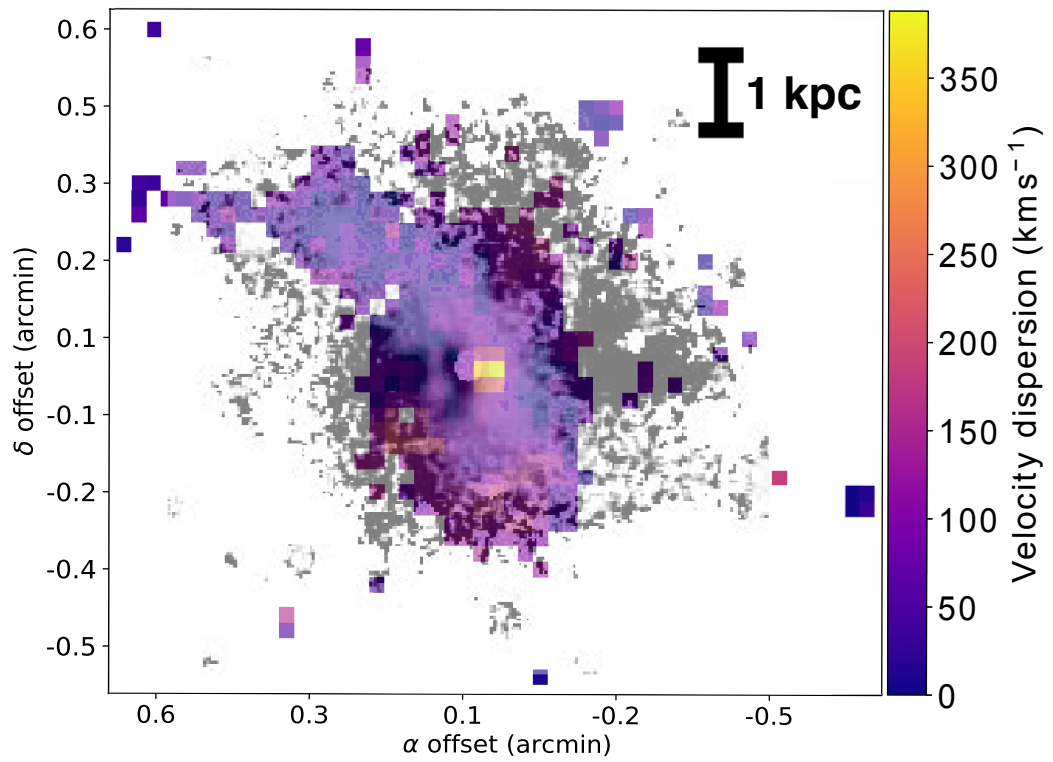
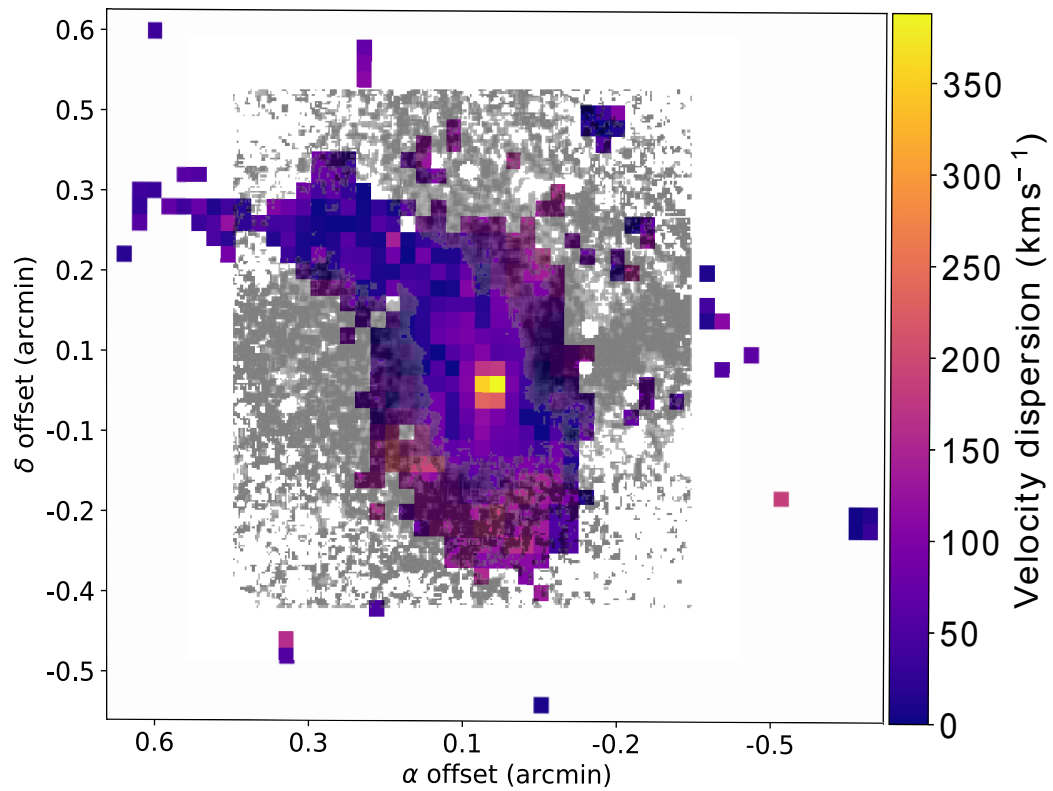
(a) $[\text{O III}]/\text{H}\beta$ (b) $[\text{N II}]/\text{H}\alpha$

Figure 3.25 Outflows in $[\text{O III}]/\text{H}\beta$ (a) and $[\text{N II}]/\text{H}\alpha$ (b) seen in the nucleus of NGC 1365 from [Veilleux et al. \(2003\)](#), coinciding with regions of high velocity dispersion. The $[\text{O III}]/\text{H}\beta$ values in (a) range from 0 at the lightest to 3 at the darkest. The $[\text{N II}]/\text{H}\alpha$ values in (b) range from 0 at the lightest to 1.5 at the darkest.

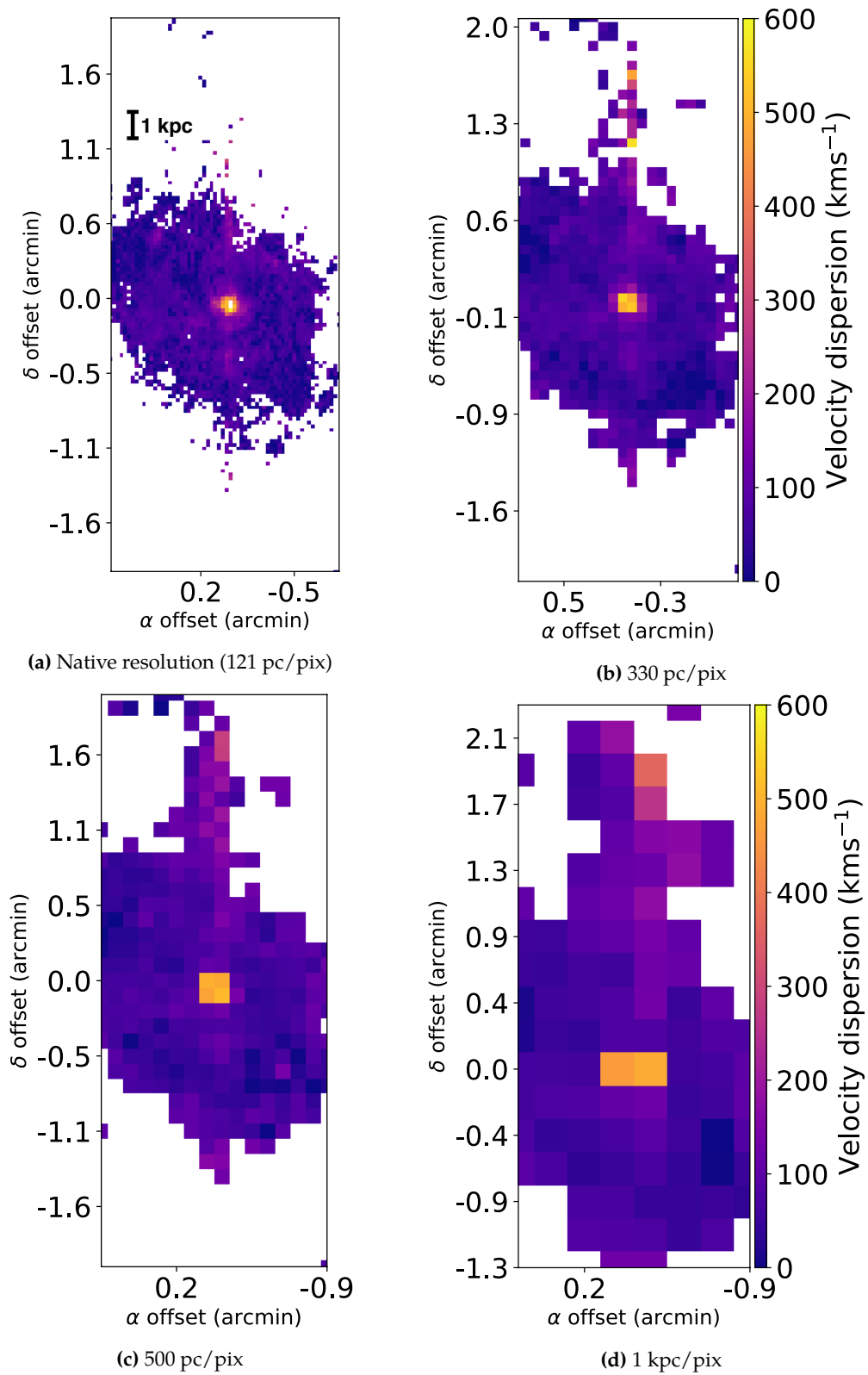


Figure 3.26 The velocity dispersion maps for NGC 1068, after rebinning to lower resolutions.

3.7. Conclusions

Using high spatial resolution data from the TYPHOON/PrISM survey, we analyse two AGN host galaxies NGC 1365 and NGC 1068. We extend the work of [Davies et al. \(2014a,b\)](#) by using photoionisation grids to introduce a new method to calculate the AGN fraction of a galaxy from the BPT diagram. We also perform the same AGN fraction calculations on datacubes of NGC 1365 and NGC 1068 which have been rebinned to lower spatial resolutions. We report the following:

- (i) IFU datacubes with resolutions as high as those used by TYPHOON (169 pc/pix for NGC 1365; 121 pc/pix for NGC 1068) show both star formation and AGN activity occurring in the nucleus of an AGN host galaxy.
- (ii) The AGN in NGC 1365 is relatively weak, with only $\sim 10\%$ of the total $[\text{O III}]\lambda 5007$ luminosity and $\sim 5\%$ of the total $\text{H}\alpha$ luminosity from NGC 1365 being attributable to AGN activity within the TYPHOON field-of-view. This shows that the vast majority of the emission from NGC 1365 is from star formation. The AGN in NGC 1068 is stronger, accounting for $\sim 42\%$ of the total $[\text{O III}]$ luminosity and $\sim 24\%$ of the total $\text{H}\alpha$ luminosity within the TYPHOON field-of-view. This shows that whilst AGN activity in NGC 1068 is considerable, star formation does have a large influence in the total emission from NGC 1068. The fraction of $\text{H}\alpha$ emission from AGN activity also has consequences for the calculation of SFRs in both of these galaxies. An overestimate of $\sim 5\%$ and an overestimate of $\sim 24\%$ on the SFR of NGC 1365 and NGC 1068 respectively will occur if $\text{H}\alpha$ for the calculation.
- (iii) Low surface brightness features such as shocks in galaxies and certain outflows (such as that in NGC 1365) only appear at lower resolutions. Features with a low S/N ratio gain a S/N increase when binned with spaxels containing a higher S/N ratio, or when observed with a higher S/N feature in the same spaxel. Increases in the number of spaxels attributable to low surface brightness features up to factors of ~ 12.5 and ~ 1.6 are noticed with coarser resolution in NGC 1365 and NGC 1068 respectively. Hence, certain features within a galaxy are lost when the resolution of the observations increases.
- (iv) The contribution of AGN to total galaxy emission increases with coarser resolution. An average 18.05% increase from the emission from AGN activity in NGC 1068 is seen in several strong lines as the resolution decreases from their respective native resolutions to a resolution of 1 kpc/pix. As the resolution lowers, the AGN fraction in individual spaxels and also individual emission lines increases, showing a larger effect from the AGN. This is also seen by the radius of equal starburst-AGN domination increasing with coarser resolution, with a roughly equal factor of 3 increase in the radius of equal domination for both NGC 1365 and NGC 1068 as the resolution decreases from their respective native resolutions to a resolution of 1 kpc/pix.

For optimal results when calculating the contribution of emission from AGN activity, the highest possible resolution data should be sought. We show that with finer resolution, the relative contribution from AGN in the total emission within the galaxy continuously decreases. Furthermore, the zone of influence of the AGN is also shown to be continually overestimated with coarser resolution. Hence, only the highest possible resolution will provide the most accurate measure of the AGN activity within a galaxy.

We intend to extend this project in the future. Emission in galaxies may arise from sources other than AGN or star formation, such as shocks. Hence, future work will include the separation of emission from shocks in addition to AGN and star formation in IFU data.

Acknowledgements

Parts of this research were conducted by the Australian Research Council Centre of Excellence for All Sky Astrophysics in 3 Dimensions (ASTRO 3D), through project number CE170100013. The authors would also like to thank referee Santiago García-Burillo, who provided valuable input and helped improve the condition of the publication.

3.8. Appendix: Power-Law Spectral Index

Here we show BPT diagrams of NGC 1365 and NGC 1068, with AGN model grids featuring power-law spectral indices of $\alpha = -1.4$ and -1.7 . In both $n = 1000 \text{ cm}^{-3}$ and $n = 10000 \text{ cm}^{-3}$ cases for NGC 1365 and NGC 1068 respectively, lowering the spectral index α lowers the $[\text{O III}]/\text{H}\beta$ and $[\text{N II}]/\text{H}\alpha$ fluxes produced by the models. Several caveats result from using a lower spectral index with these models:

- The line of constant metallicity representing the central region of the galaxy is moved further down the mixing sequence towards the starburst region of the BPT diagram, and in the case of NGC 1068, does not provide a good fit to the uppermost spaxels in the mixing sequence. The result of using such a model to define the 100% AGN region would be many spaxels saturated at 100% AGN. Further, the error in the photoionisation models of ~ 1.5 dex in emission line ratio (D’Agostino et al. in prep) does not account for the amount of spaxels above the central metallicity line.
- While a case may be made for the use of $\alpha = -1.4$ for NGC 1365 seen in Figure 3.27a, use of such a model (and models which decrease α even further) results in several off-grid spaxels which are not explained or defined by the model. At $\alpha = -1.7$ and below, increasing the metallicity of the $n = 1000 \text{ cm}^{-3}$ models fails to describe the off-grid spaxels, as the models begin to turn over at metallicities of $Z = 0.060$ and beyond, seen in Figure 3.27b. A turn in the shape of the model is not yet evident when using $\alpha = -1.4$ for the $n = 1000 \text{ cm}^{-3}$ model seen in Figure 3.27a, hence increasing the maximum metallicity shown in the model beyond $Z = 0.060$ may describe the off-grid spaxels. However, it should be noted that the maximum metallicity calculated in each galaxy ($1.42Z_{\odot}$ and $1.41Z_{\odot}$ for NGC 1365 and NGC 1068 respectively, where $Z_{\odot} \equiv Z = 0.020$) is far below the maximum already included in the models of $Z = 0.060$. Hence, using higher metallicities to explain the off-grid spaxels is inconsistent with our metallicity calculations, and such a high metallicity is possibly considered unphysical.

Hence, a power-law spectral index of $\alpha = -1.2$ is the only value considered which is consistent with the data and our metallicity calculations.

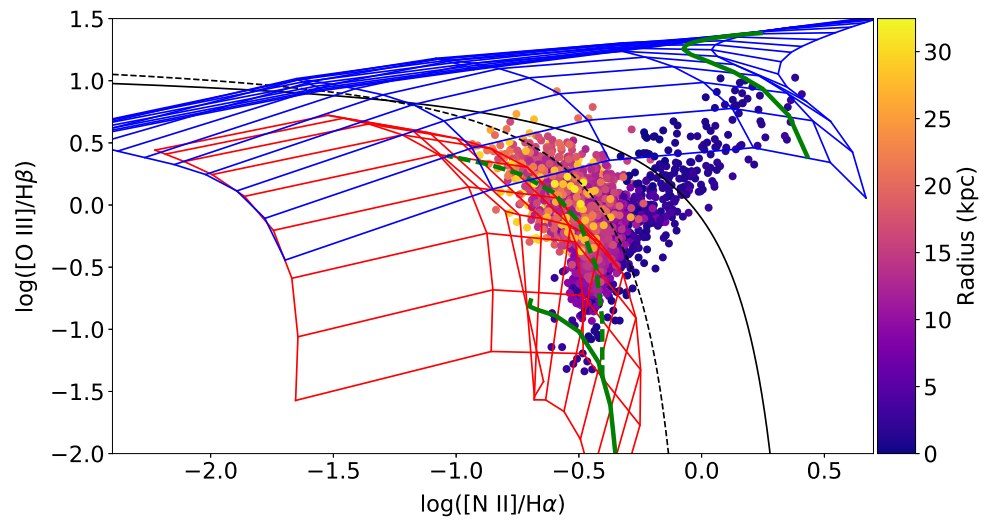
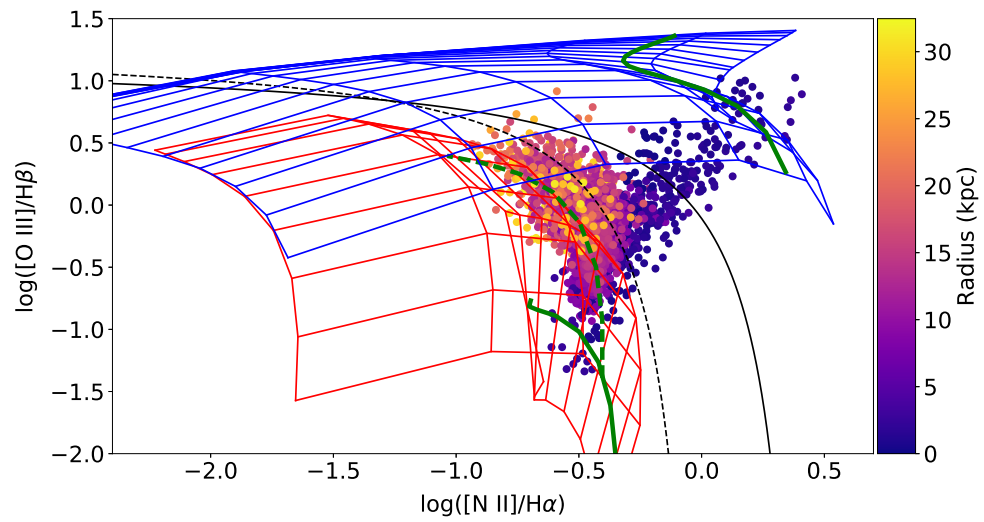
(a) $\alpha = -1.4$ (b) $\alpha = -1.7$

Figure 3.27 NGC 1365, showing $n = 1000 \text{ cm}^{-3}$ AGN model grids computed with power-law spectral indices of $\alpha = -1.4$ and -1.7 .

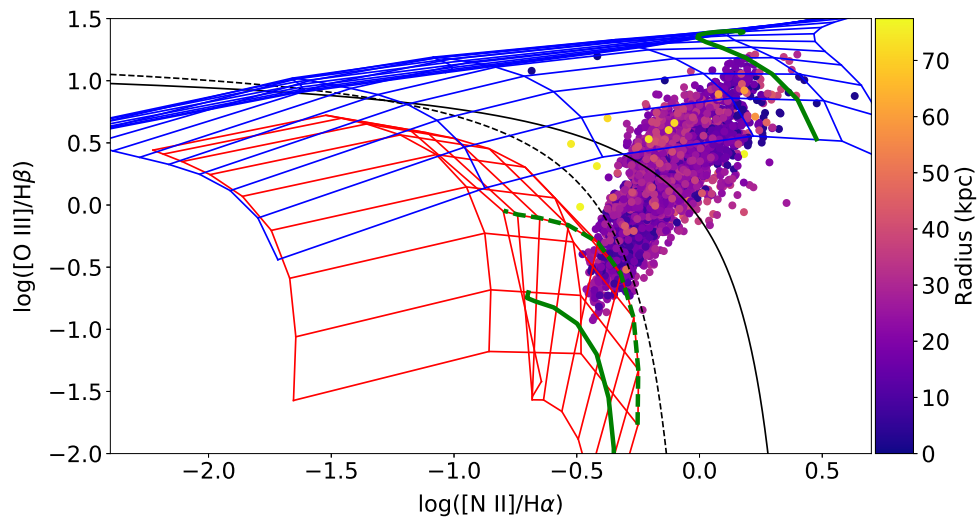
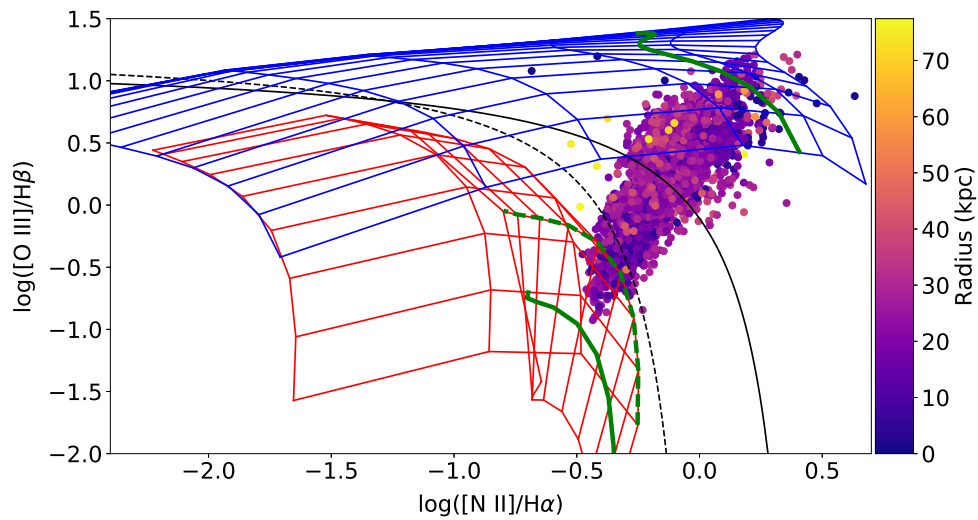
(a) $\alpha = -1.4$ (b) $\alpha = -1.7$

Figure 3.28 NGC 1068, showing $n = 10000 \text{ cm}^{-3}$ AGN model grids computed with power-law spectral indices of $\alpha = -1.4$ and -1.7 .

Statement of Contribution

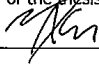
This thesis is submitted as a Thesis by Compilation in accordance with https://policies.anu.edu.au/ppi/document/ANUP_003405

I declare that the research presented in this Thesis represents original work that I carried out during my candidature at the Australian National University, except for contributions to multi-author papers incorporated in the Thesis where my contributions are specified in this Statement of Contribution.

Title and authors: D'Agostino, J. J., Kewley, L. J., Groves, B. A., Medling, A., Dopita, M. A., Thomas, A. D., 2019, "A new diagnostic to separate line emission from star formation, shocks, and AGNs simultaneously in IFU data", MNRAS, 485, L38

Current status of paper: Not Yet Submitted/Submitted/Under Revision/Accepted/Published

Contribution to paper: All work was done by the author of the thesis

Senior author or collaborating authors endorsement:  BRENT GROVES

Joshua D'Agostino  11/7/2019
 Candidate – Print Name Signature Date

Endorsed

LISA KEWLEY  9/7/2019
 Chair of Supervisory Panel – Print Name Signature Date

Mark Krumboltz  11/7/2019
 Delegated Authority – Print Name Signature Date

CHAPTER 4

The Three-Dimensional Diagnostic Diagram

I'm tired of reading about the achievements of better men.

– Samwell Tarly (Benioff/Weiss)

The contents of this chapter have previously been published as ‘A new diagnostic to separate line emission from star formation, shocks, and AGNs simultaneously in IFU data’, D’Agostino, J. J., Kewley, L. J., Groves, B. A., Medling, A., Dopita, M. A., Thomas, A. D., 2019, MNRAS, 485, L38. The abstract is as follows:

In the optical spectra of galaxies, methods for the separation of line emission arising from star formation and an additional hard component, such as shocks or active galactic nuclei (AGNs), is well-understood and possible with current diagnostics. However, such diagnostics fail when attempting to separate and define line emission which arises from shocked gas, and that arising from AGNs. We present a new three-dimensional diagnostic diagram for integral field unit data which can simultaneously separate the line emission amongst star formation, shocks, and AGNs within a galaxy. We show that regions we define as AGN-dominated correlate well with the hard X-ray distribution in our test case NGC 1068, as well as with known regions of AGN activity in NGC 1068. Similarly, spaxels defined as shock-dominated correlate strongly with regions of high-velocity dispersion within the galaxy.

All raw S7 data was reduced by co-author Adam Thomas, and released in the publication by [Thomas et al. \(2017\)](#).

4.1. Introduction

The mixing of line emission from gas ionised by star formation and active galactic nuclei (AGN) is a well-understood problem. The diagnostic diagram first described by [Baldwin et al. \(1981\)](#) (now known as the ‘BPT diagram’) and subsequent diagnostic diagrams shown by [Veilleux & Osterbrock \(1987\)](#) are powerful tools used in separating the emission from star formation and other excitation mechanisms. The BPT diagram in particular utilises the two emission line ratios $[\text{N II}]\lambda 6584/\text{H}\alpha$ and $[\text{O III}]\lambda 5007/\text{H}\beta$. The hard extreme ultraviolet (EUV) radiation field from the accretion disk of an AGN produces higher fluxes of collisionally-excited lines such as $[\text{N II}]$ and $[\text{O III}]$ ([Groves et al. 2004](#); [Kewley et al. 2006, 2013a](#)).

Initial work from [Kewley et al. \(2001\)](#) and subsequent work from [Kewley et al. \(2006\)](#), [Davies et al. \(2014a,b\)](#), and [D’Agostino et al. \(2018\)](#) has shown the existence of a ‘mixing sequence’ amongst AGN galaxies, and within individual galaxies when using data from an integral field unit (IFU). Mainly using the BPT diagram, spaxels originating in the star-forming region of the BPT diagram demonstrate a continuous spread towards the AGN classification region, indicated by high $[\text{N II}]/\text{H}\alpha$ and $[\text{O III}]/\text{H}\beta$ ratios. This spread of spaxels on the BPT diagram has led to the name ‘starburst-AGN mixing’ or ‘star formation-AGN mixing’ to describe the process. IFU data is particularly helpful when studying star formation-AGN mixing within individual galaxies, due to the spatially-resolved spectrum it provides.

The position of a galaxy spectra or spaxel on this mixing sequence can be used to determine the relative contribution of AGN. A problem with this method however, is that no other ionisation sources are considered. On the BPT diagram in particular, emission from shocked gas can produce $[\text{O III}]/\text{H}\beta$ and $[\text{N II}]/\text{H}\alpha$ ratios consistent with values along the mixing sequence, typically towards the AGN region of the diagram (see [Rich et al. 2010, 2011](#); [Kewley et al. 2013a](#)). This presents a problem with the results of star formation-AGN mixing, in that the ratio of true AGN emission within each spaxel is likely overestimated.

In this paper, we present a new diagnostic diagram capable of separating emission from star formation, shocks, and AGN simultaneously in IFU data.

4.2. Data Selection

We use data from the Siding Spring Southern Seyfert Spectroscopic Snapshot Survey (S7; [Thomas et al. 2017](#)). The S7 is an IFU survey conducted between 2013 and 2016. The Wide Field Spectrograph (WiFeS; [Dopita et al. 2007, 2010](#)) located on the ANU 2.3m telescope at Siding Spring Observatory was used for the survey. Data from the S7 is ideal to use for this work, due to the high spectral and spatial resolution of the survey. In particular, the high spectral resolution ($R \sim 7000$ in the red, 3000 in the blue) allows the study of independent velocity components in the emission lines, providing more information on shocked regions ([Ho et al. 2014](#)). For a full explanation of the S7, see [Thomas et al. \(2017\)](#).

To showcase our new diagnostic diagram, we use the Seyfert 2 galaxy NGC 1068. NGC 1068 is the perfect galaxy to use as an example, as emission from all three sources of star

formation, shocks, and AGN has been inferred within the nucleus. NGC 1068 has a large-scale biconical outflow structure, believed by many to be radiatively accelerated by the AGN (Pogge 1988; Cecil et al. 2002; Dopita et al. 2002a; D’Agostino et al. 2018). Observations have also shown evidence of shocked gas towards the edge of the central bar (Tacconi et al. 1994). Evidence of shocks within the system is further supported by the velocity of the outflowing material, calculated to be moving away from the nucleus at velocities in excess of 3000 kms^{-1} (Cecil et al. 2002). Furthermore, NGC 1068 has been shown to host a circumnuclear star-forming ring, with estimates of a star formation rate (SFR) of up to 100 $M_{\odot} \text{yr}^{-1}$ (Thronson et al. 1989).

4.3. Issues with Current Diagnostics

In Figure 4.1 we show a BPT diagram of NGC 1068, coloured by the maximum velocity dispersion in the spaxel. The maximum velocity dispersion in each spaxel is calculated by firstly fitting each emission line with three Gaussian components (see Ho et al. 2016). The recommended number of one, two, or three Gaussian components for each spaxel is then determined by a neural network (LZCOMP; Hampton et al. 2017). The maximum velocity dispersion in each spaxel is then defined as the velocity dispersion of the highest-order component. We refer to the velocity dispersion of each individual component as the ‘single-component velocity dispersion’ later in Section 4.4.

We show the maximum velocity dispersion in each spaxel in Figure 4.1 to highlight the prevalence of shocked gas along and within the mixing sequence of the galaxy. The spaxels on the diagram form a spread from low to high emission line ratios, indicating a large

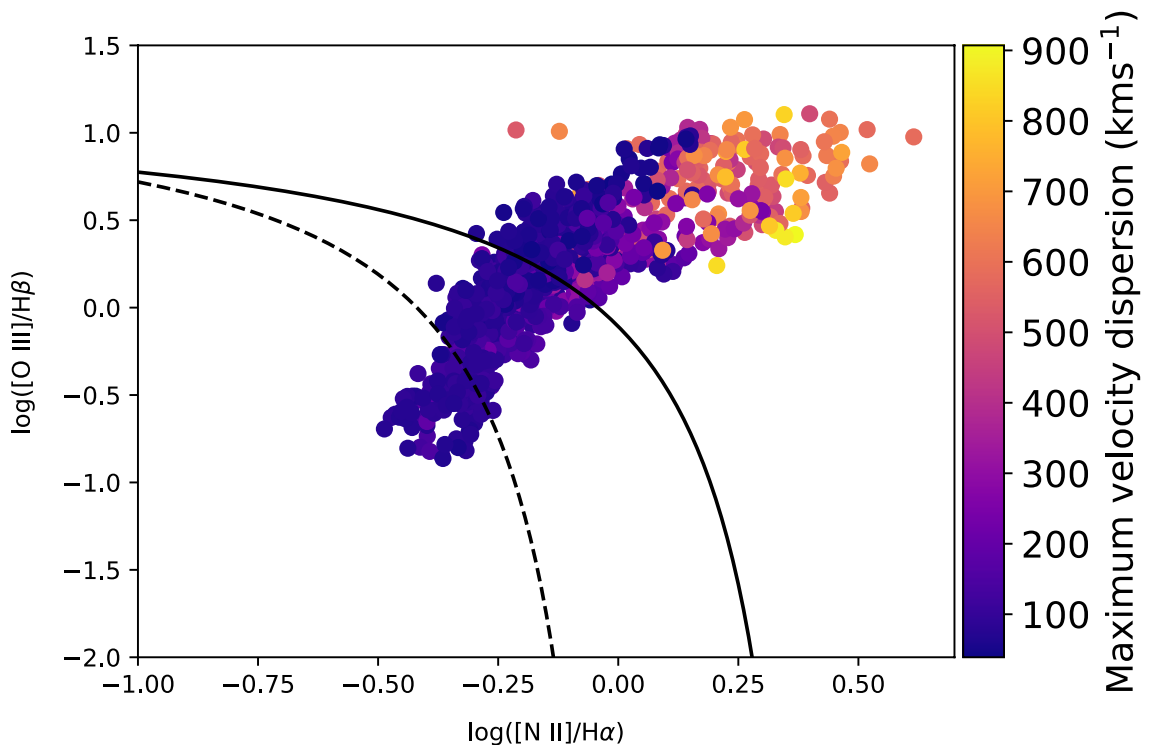


Figure 4.1 BPT diagram of NGC 1068, coloured by the maximum velocity dispersion in each spaxel.

contribution from the AGN. However, many of the spaxels found above the [Kewley et al. \(2001\)](#) line show velocity dispersions greater than 300 km s^{-1} . At these velocity dispersions and higher, fast shocks very likely contribute to the ionisation present in these spaxels (e.g. [Dopita 1995](#); [Rich et al. 2011](#); [Ho et al. 2014](#)). Yet the emission line ratios of the spaxels are high enough to be consistent with Seyfert emission ([Kewley et al. 2006](#)). Hence, Figure 4.1 shows that the BPT diagram is poor at successfully separating emission between AGN and shocks.

4.4. The 3D Diagnostic Diagram

We present a new three-dimensional diagnostic diagram to simultaneously separate emission amongst star formation, shocks, and AGN in IFU data. This diagram is shown for NGC 1068 in Figure 4.2. The emission line ratio information from the BPT diagram is still considered in this diagram, shown on the vertical axis as our emission line ratio (ELR) function. The functional form is given in Equation 5.1. The ELR function essentially traces the mixing sequence of the galaxy, shown in Figure 4.3. The purpose of the ELR function is to order the spaxels on the 3D diagram in terms of their combined $[\text{O III}]/\text{H}\beta$ and $[\text{N II}]/\text{H}\alpha$ ratios. It is important to note that the ELR function is data-dependent, and the range of values from 0 to 1 is arbitrary. The endpoints of 0 and 1 do not represent any physical phenomena, such as 100% star formation emission and 100% AGN emission respectively. The other axes of radius and velocity dispersion provide additional information on the data. As mentioned previously, the velocity dispersion is a suitable shock diagnostic. Furthermore, the radial values provide information on the mixing between AGN and other processes, as AGN emission is seen more towards the nucleus. In addition to this, when mixing with other processes, star formation is more likely seen towards the outskirts of the galaxy (e.g. [Davies et al. 2014a,b](#); [D’Agostino et al. 2018](#)). The single-component velocity dispersion used in Figure 4.2 refers to the velocity dispersion of individual components in each spaxel. If the neural network LZCOMP recommends multiple-component fits to a spaxel, then multiple data points for a single spaxel will be present on the 3D diagram. These data points will differ in their values for the velocity dispersion (with higher-order components having a greater velocity dispersion), yet will have the same radial and ELR function values. The ELR function value associated with these multiple components of a single spaxel is calculated from the total flux (‘zeroth’ component) of the spaxel. We use the single-component velocity dispersion on the 3D diagram, because the various components contain information about different processes. The first component (which contains the lowest velocity dispersions) is consistent with emission from H II regions, and the higher-order components (in particular, the third component if present) is consistent with emission from shocks ([Ho et al. 2014](#)).

$$\text{ELR function} = \frac{\log([\text{N II}]/\text{H}\alpha) - \min_{\log([\text{N II}]/\text{H}\alpha)}}{\max_{\log([\text{N II}]/\text{H}\alpha)} - \min_{\log([\text{N II}]/\text{H}\alpha)}} \times \frac{\log([\text{O III}]/\text{H}\beta) - \min_{\log([\text{O III}]/\text{H}\beta)}}{\max_{\log([\text{O III}]/\text{H}\beta)} - \min_{\log([\text{O III}]/\text{H}\beta)}} \quad (4.1)$$

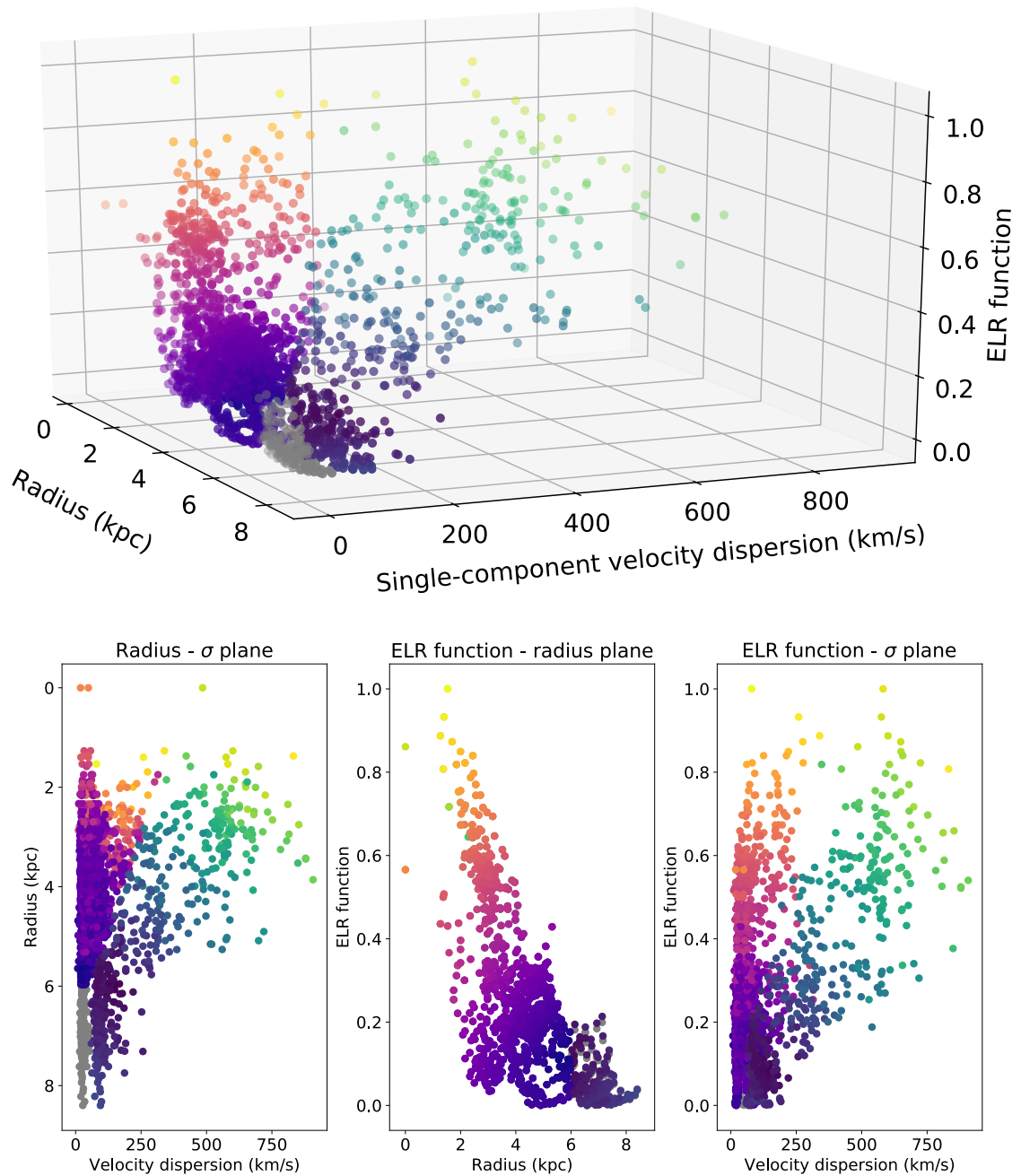


Figure 4.2 3D diagnostic diagram of NGC 1068, showing two distinct mixing sequences of spaxels. The velocity dispersion value is the velocity dispersion of the individual components. Each individual-component velocity dispersion is combined with the total flux ('zeroth' component), and the radius value for the spaxel to form a data point. The purple-to-yellow sequence is referred to as the 'first' sequence, and the deep blue-to-yellow sequence is referred to as the 'second' sequence. Grey spaxels are those which are not definitively in either sequence. The first sequence shows mixing between emission from star formation and AGN, and the second sequence shows the mixing between the star formation and shocks. Significant scatter appears between the two sequences, indicating mixing also between the AGN and shocked emission. The three panels below the 3D diagram show the projection in the radius-velocity dispersion plane, radius-ELR function plane, and velocity dispersion-ELR function plane. The separation into two sequences is seen more clearly when studying all three planes.

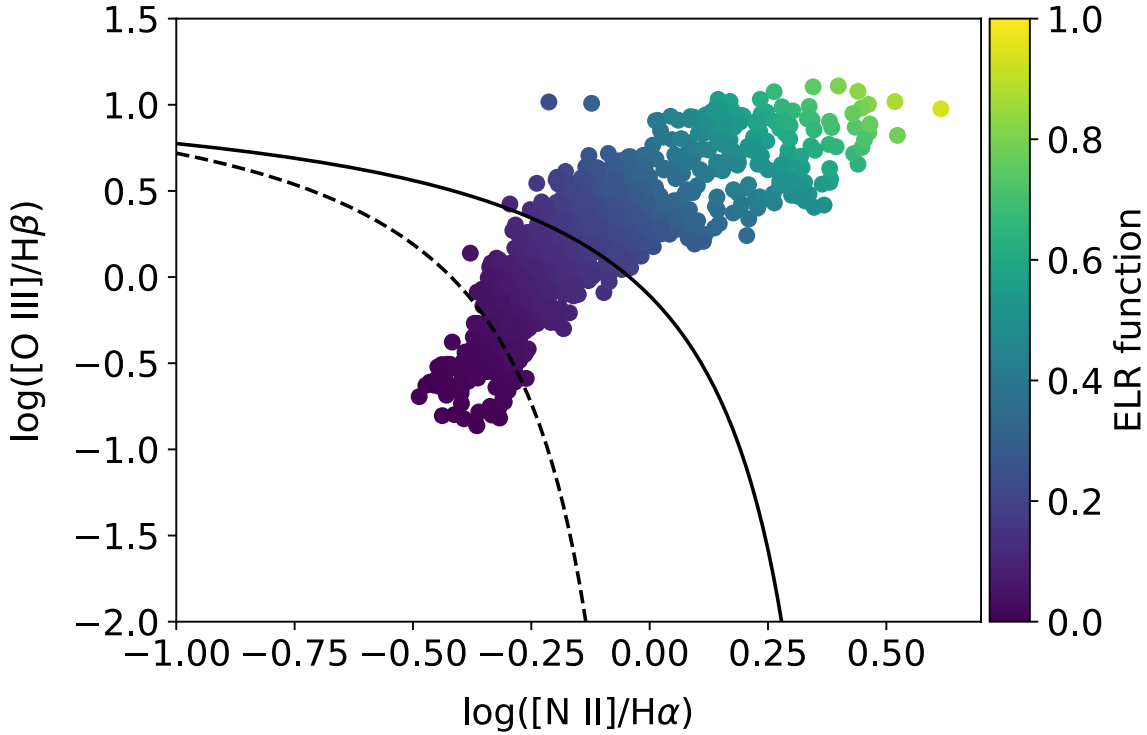


Figure 4.3 BPT diagram of NGC 1068, coloured by the ELR function value from Equation 5.1 in each spaxel. The black, solid line is the Kewley et al. (2001) demarcation line, and the black, dashed line is the Kauffmann et al. (2003) demarcation line.

4.5. Results

The 3D diagnostic diagram demonstrates two distinct sequences of spaxels, each advancing from a region of low ELR function values, to regions of high ELR function values. The two sequences separated by colour on Figure 4.2. Hereafter, we refer to the purple-to-yellow sequence as the ‘first’ sequence, and the deep blue-to-yellow sequence as the ‘second’ sequence. Grey spaxels are those which do not clearly belong to either sequence. The separation of the spaxels into two sequences is seen more clearly in the bottom panels of Figure 4.2, which shows the two sequences as viewed in the radius-velocity dispersion plane, radius-ELR function plane, and velocity dispersion-ELR function plane. In general, we find that the first and second sequences mostly contain spaxels of the first-component and third-component velocity dispersions respectively. However, a small fraction of first-component velocity dispersion spaxels are located in the second sequence. Second-component velocity dispersion spaxels are found within and between both sequences. Large scatter is seen between the two sequences, particularly at high ELR function values. Therefore, it should be noted that the separation made between the two sequences is only approximate.

We claim that the first and second sequences represent the star formation-AGN mixing and star formation-shock mixing respectively. We show this by studying the spatial distribution of the two sequences in Figure 4.4. The map of the first sequence in Figure 4.4a closely traces the 0.25-7.5 keV *Chandra* X-ray contours from Young et al. (2001). Furthermore, the distribution of the first-sequence spaxels in Figure 4.4a resembles the [O III] flare in NGC 1068, believed to be a result of photoionisation from the AGN. The alignment with the

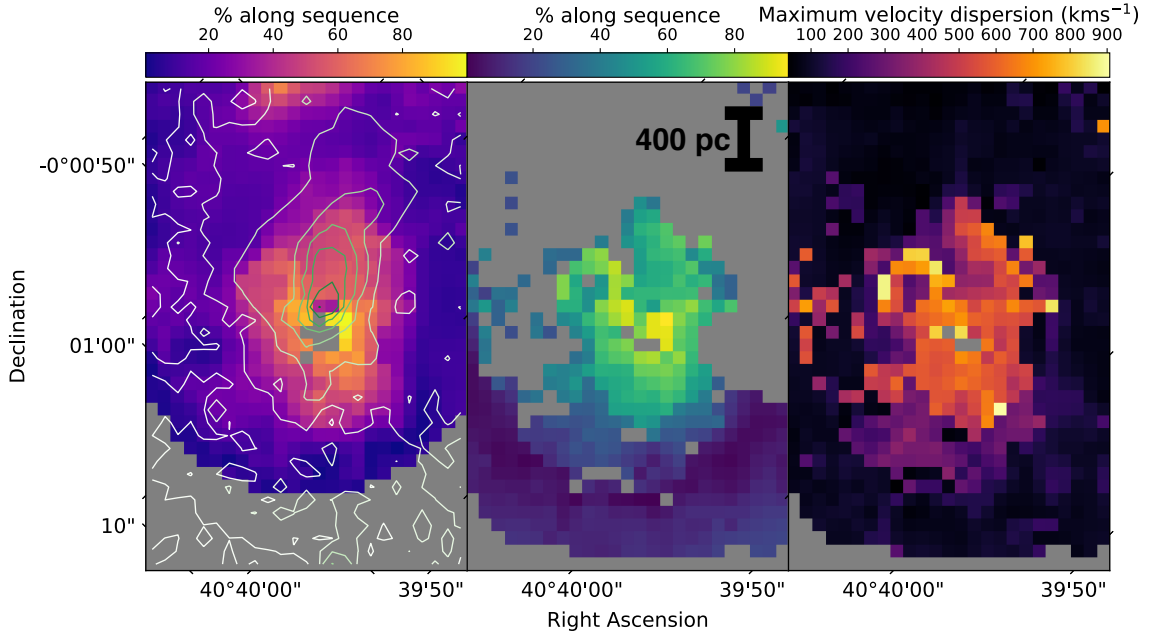


Figure 4.4 Maps of NGC 1068, showing the distribution of the first sequence of spaxels in (a), the second sequence in (b), and the velocity dispersion in (c). Spaxel colours for (a) and (b) are identical to Figure 4.2. 0.25-7.5 keV *Chandra* X-ray contours from Young et al. (2001) are also shown on (a).

X-ray and [O III] distributions is a strong indication that the first sequence represents the star formation-AGN mixing in each spaxel. Figures 4.4b and 4.4c however show a strong correlation between the second sequence of spaxels and the velocity dispersion distribution. Spaxels found towards the high ELR end of the second sequence also contain extremely high velocity dispersions. The combination of high ELR and velocity dispersion values indicate the emission in these spaxels is from shocked gas. Significant scatter between the two sequences exists at high ELR values, seen in Figure 4.2, indicating mixing also between the AGN- and shock-affected spaxels. This is to be expected however, as shocks can result from the accretion disk of the AGN (e.g. Spruit 1987; Molteni et al. 1994; Sponholz & Molteni 1994).

The star formation-AGN and star formation-shock mixing nature of the two sequences is also shown in Figure 4.5. Both sequences begin in the pure star-forming region of the BPT diagram (below the demarcation line of Kauffmann et al. 2003) before demonstrating a continuous spread towards and beyond the Kewley et al. (2001) demarcation line. The BPT diagrams show that both sequences contain mixing between pure star formation and additional hard components, demonstrated prior to be predominantly AGN and shocks for the first and second sequences respectively.

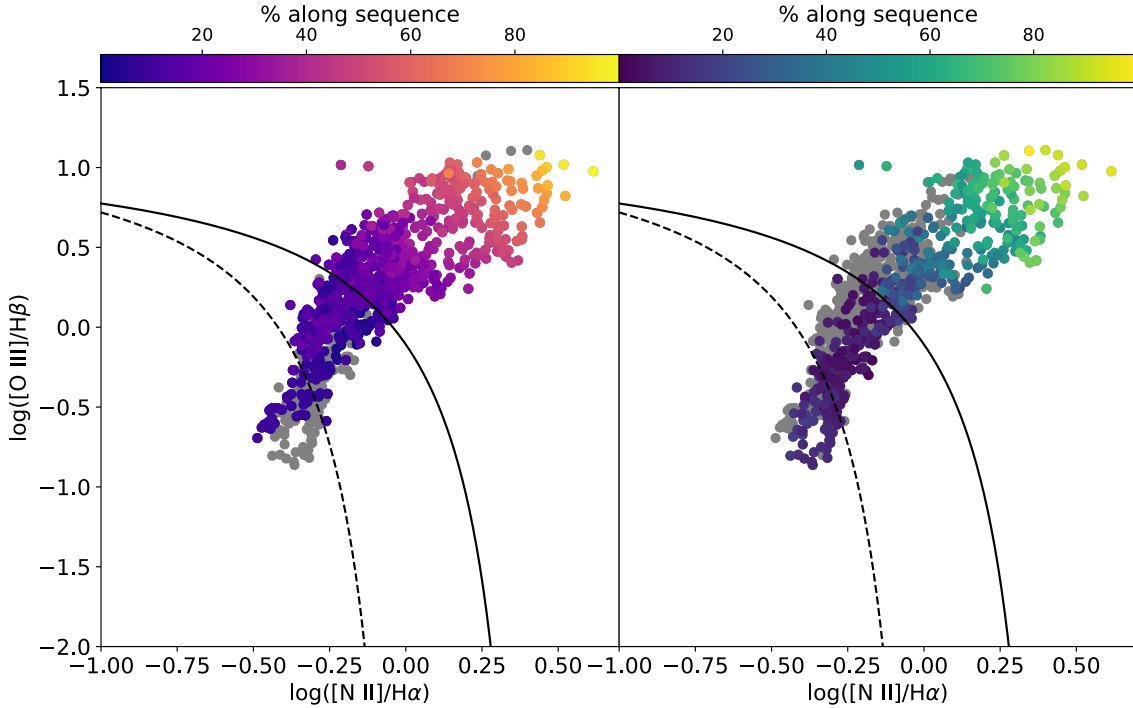


Figure 4.5 BPT diagrams showing the spread of spaxels in the first sequence on the left, and second sequence on the right. Spaxel colours are identical to Figure 4.2. The black, solid line is the Kewley et al. (2001) demarcation line, and the black, dashed line is the Kauffmann et al. (2003) demarcation line.

4.6. Summary and Future Work

We have shown that traditional methods used to distinguish non-stellar line emission are ineffective in separating AGN- and shock-excited gas. Instead, we have proposed and demonstrated a new three-dimensional diagnostic diagram which simultaneously separates emission from star formation, shocks, and AGN in IFU data. The diagram uses the radial information and velocity dispersion in each spaxel for two axes, while the third axis consists of a function of emission line ratios. The emission line ratio function used in the diagram is a combination of the BPT emission line ratios $[N II]\lambda 6584/H\alpha$ and $[O III]\lambda 5007/H\beta$, ensuring that the advantages of the BPT diagram are still retained.

Using the Seyfert galaxy NGC 1068 as a test case, we show that two distinct and clear sequences of spaxels are found on the 3D diagram. We claim these sequences represent the mixing between star formation and AGN, and star formation and shocks respectively. This is supported through maps of the spaxel distributions across the galaxy. The distribution of spaxels found in the star formation-AGN mixing sequence correlates well with the X-ray distribution in NGC 1068, as well as the $[O III]$ flare seen extending from the galaxy. The spaxels within the star formation-shock mixing sequence however correlate strongly with regions of high velocity dispersion in the galaxy. These results suggest the two sequences seen on the 3D diagnostic diagram indeed represent the star formation-AGN and star formation-shock mixing within the galaxy.

In an upcoming publication, we intend to use this method to quantify the relative contributions of star formation, shocks, and AGN to emission lines for galaxies undergoing mergers, as a function of merger stage.

Acknowledgements

Parts of this research were conducted by the Australian Research Council Centre of Excellence for All Sky Astrophysics in 3 Dimensions (ASTRO 3D), through project number CE170100013.

Statement of Contribution

This thesis is submitted as a Thesis by Compilation in accordance with https://policies.anu.edu.au/ppi/document/ANUP_003405

I declare that the research presented in this Thesis represents original work that I carried out during my candidature at the Australian National University, except for contributions to multi-author papers incorporated in the Thesis where my contributions are specified in this Statement of Contribution.

Title and authors: D'Agostino, J. J., Kewley, L. J., Groves, B. A., Medling, A. M., Di Teodoro, E., Dopita, M. A., Thomas, A. D., Sutherland, R. S., Garcia-Burillo, S., 2019, "Separating Line Emission from Star Formation, Shocks, and AGN Ionisation in NGC 1068", MNRAS, 487, 4153

Current status of paper: Not Yet Submitted/Submitted/Under Revision/Accepted/**Published**

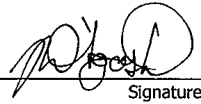
Contribution to paper: All but Figure 5.3

Senior author or collaborating authors endorsement: _____



BRENT GROVES

Joshua D'Agostino
Candidate – Print Name

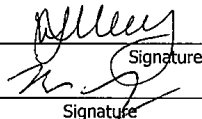


Signature

1/7/2019
Date

Endorsed

LISA KEWLEY
Chair of Supervisory Panel – Print Name



Signature

9/7/2019
Date

Mark Krumholz
Delegated Authority – Print Name



Signature

11/7/2019
Date

CHAPTER 5

Separating Line Emission from Star Formation, Shocks, and AGN Ionisation in NGC 1068

I find that the harder I work, the more luck I seem to have.

– Thomas Jefferson

The contents of this chapter have previously been published as ‘Separating Line Emission from Star Formation, Shocks, and AGN Ionisation in NGC 1068’, D’Agostino, J. J., Kewley, L. J., Groves, B. A., Medling, A. M., Di Teodoro, E., Dopita, M. A., Thomas, A. D., Sutherland, R. S., García-Burillo, S., 2019, MNRAS, 487, 4153. The abstract is as follows:

In the optical spectra of galaxies, the separation of line emission from gas ionised by star formation and an AGN, or by star formation and shocks, are very well-understood problems. However, separating line emission between AGN and shocks has proven difficult. With the aid of a new three-dimensional diagnostic diagram, we show the simultaneous separation of line emission from star formation, shocks, and AGN in NGC 1068, and quantify the ratio of star formation, shocks, and AGN in each spaxel. The AGN, shock, and star formation luminosity distributions across the galaxy accurately align with X-ray, radio, and CO(3-2) observations, respectively. Comparisons with previous separation methods show that the shocked emission heavily mixes with the AGN emission. We also show that if the H α flux is to be used as a star formation rate indicator, separating line emission from as many sources as possible should be attempted to ensure accurate results.

Figure 5.3 was generated by co-author Enrico Di Teodoro.

5.1. Introduction

One of the biggest mysteries in modern astrophysics is the link between supermassive black hole (SMBH) accretion and the evolution of its host galaxy. Studies have shown SMBH mass correlates with other galaxy properties, such as the velocity dispersion (M - σ relation; e.g. Ferrarese & Merritt 2000; Gebhardt et al. 2000; Tremaine et al. 2002; Gültekin et al. 2009; McConnell & Ma 2013), the stellar mass in the bulge (M_{BH} - M_* relation; e.g. Magorrian et al. 1998; Marconi & Hunt 2003; Bennert et al. 2011; McConnell & Ma 2013), and the luminosity of the bulge (M_{BH} - L ; e.g. Marconi & Hunt 2003; Gültekin et al. 2009; McConnell & Ma 2013). However, no such theory linking SMBH accretion and star formation, such as mergers, starburst-driven winds or AGN-driven outflows (e.g. Yuan et al. 2010; Rafferty et al. 2011) have been convincing. As a result, no theoretical model has successfully been able to explain the relationship between star formation and active galactic nuclei (AGN; see the review by Alexander & Hickox 2012).

Work on uncovering the link between star formation and AGN activity was explored by Kewley et al. (2001) through the use of several emission-line-ratio diagnostic diagrams given by Baldwin et al. (1981) and Veilleux & Osterbrock (1987). Kewley et al. (2001) defined a curve on each of the [O III]/H β vs [N II]/H α (commonly referred to as the ‘BPT diagram’; Baldwin et al. 1981), [O III]/H β vs [S II]/H α , and [O III]/H β vs [O I]/H α diagrams to represent the theoretical maximum of line emission from star formation, derived from photoionisation modelling using the MAPPINGS III code. Kauffmann et al. (2003) also defined a maximum starburst line on the BPT diagram, albeit empirically from their sample of SDSS galaxies. Contemporary work on star formation-AGN mixing treats line emission in the region below the Kauffmann et al. (2003) line on the BPT diagram as pure star formation, and line emission in the region above the Kewley et al. (2001) line is considered to be dominated by harder sources, such as AGN or shocks. The region on the BPT diagram which occupies the space between the two lines is considered to result from a mixture of star formation with an additional hard component.

The study of star formation-AGN mixing was furthered through the advent of integral field spectroscopy (IFS). Pioneered by Davies et al. (2014a,b), a spatially-resolved spectrum across a galaxy containing an AGN shows a very clear and smooth ‘mixing sequence’ between star formation towards the outer of the galaxy, and AGN activity towards the centre. To calculate the relative contributions to several strong emission lines from star formation and AGN activity across the galaxy, Davies et al. (2014a,b) empirically selected two ‘basis points’ from the data on the BPT diagram to represent 100% star formation and 100% AGN activity. The relative contribution from star formation and AGN in each spaxel was then calculated by finding each spaxel’s ‘star-forming distance’, defined in Kewley et al. (2006). D’Agostino et al. (2018) furthered this technique by selecting five basis points through the use of photoionisation model grids for H II regions and narrow-line regions (NLRs) using the MAPPINGS V photoionisation modelling code.

Despite improving upon the method showcased by Davies et al. (2014a,b), the theoretical calculation of the star formation-AGN fraction shown in D’Agostino et al. (2018) remains incomplete. Considering the line emission from a galaxy to be the result of two sources (star formation and AGN activity) is a vast oversimplification. The BPT diagram, which has

been a favoured tool for previous work on star formation-AGN mixing, fails to distinguish between star formation, AGN activity, and other sources of ionisation and excitation. In particular, shocked outflows have been shown to result from starburst galaxies (e.g. Heckman et al. 1987; Rupke et al. 2005), AGN (e.g. Cecil et al. 2002; Rupke & Veilleux 2011), and galaxy mergers (e.g. Rich et al. 2011, 2014; Rupke & Veilleux 2013). Furthermore, shocks can result from accretion disks. Simulations and analytical calculations have shown shocks to be prevalent among the accretion disks of black holes (Spruit 1987; Molteni et al. 1994; Sponholz & Molteni 1994) and have been observed in the accretion disk of the dwarf nova U Geminorum (Neustroev & Borisov 1998). Additionally, ionisation and excitation between an AGN and shocks can be further confused through differences in observed phenomena, such as in the AGN spectral energy distribution (SED) or continuum (e.g. Ferland & Mushotzky 1982; Kraemer et al. 2009), or even gas turbulence (particularly when using [N II] λ 6584 as a diagnostic; Gray & Scannapieco 2017). Yet on the BPT diagram, shocked line emission can be found in the same region as AGN-affected spaxels, or within the mixing sequence of the galaxy (for the position of shock features on diagnostic diagrams, see Rich et al. 2010, 2011; Kewley et al. 2013a). Hence, when studying a mixing sequence from a galaxy, simplifying the emission into a ratio between only star formation and AGN activity can lead to misleading if not erroneous results.

A three-component emission decomposition between star formation, shocks, and AGN activity was performed by Davies et al. (2017), by using the BPT diagram as well as the [O III]/H β vs [S II]/H α diagnostic diagram. Similarly to Davies et al. (2014a,b), the basis points to represent 100% star formation, shock and AGN line emission were selected empirically. Despite utilising another diagnostic diagram, the [O III]/H β vs [S II]/H α diagram is just as problematic as the BPT diagram when attempting to separate shocked line emission from star formation- and AGN-ionised line emission.

Throughout this work, we use a new three-dimensional diagnostic diagram first described in D’Agostino et al. (2019b), which shows the separation between star formation, shocks, and AGN line emission more clearly than the BPT diagram. Further, we follow D’Agostino et al. (2018) by using theoretical photoionisation modelling to define regions on the 3D diagnostic diagram of 100% star formation, shocks, and AGN. In Sections 5.2 and 5.3, we provide detail on the integral field unit (IFU) survey data used in this paper, as well as providing information on our test case NGC 1068. The main work of this paper is found in Section 5.5, which includes demonstrating the 3D diagnostic diagram, as well as calculating the star formation, shock, and AGN fractions in NGC 1068. We compare our results to data in wavelengths outside of the optical range in Section 5.6, before summarising our findings and describing future applications of this method in Section 5.7.

5.2. Siding Spring Southern Seyfert Spectroscopic Snapshot Survey (S7)

The Siding Spring Southern Seyfert Spectroscopic Snapshot Survey (S7) is an optical IFU survey performed between 2013 and 2016. The Wide Field Spectrograph (WiFeS; Dopita et al. 2007, 2010) was used for the S7 survey, located on the ANU 2.3m telescope at Siding Spring Observatory. WiFeS has a field-of-view of 38×25 arcsec² composed of a grid of 1×1

arcsec² spaxels. The S7 is an ideal choice for this work, due to the high spectral resolution and spatial resolution of the survey. In particular, the high spectral resolution ($R \sim 7000$ in the red, 3000 in the blue) allows the study of independent velocity components in the emission lines, providing more information on shocked regions (Ho et al. 2014). Full details of the S7, including wavelength ranges and selection criteria, can be found in Dopita et al. (2015a) and Thomas et al. (2017).

5.3. NGC 1068

NGC 1068 is the prototypical Seyfert 2 (Osterbrock & Martel 1993) (R)SA(rs)b (de Vaucouleurs et al. 1991) galaxy, roughly located at a distance of 12.5 Mpc (e.g. Schoniger & Sofue 1994) in the constellation Cetus. It has an optically-thick torus, which is known to obscure the broad-line region of the galaxy (e.g. Miller & Antonucci 1983; Antonucci & Miller 1985; Miller et al. 1991b; García-Burillo et al. 2016). However, contemporary work has begun to resolve the circumnuclear disk and nuclear region of NGC 1068 (Marinucci et al. 2016; García-Burillo et al. 2016).

A large-scale biconical outflow with position angle $\sim 32^\circ$ is seen from the centre of the galaxy, observed to be moving outward at velocities of $\sim 3000 \text{ km s}^{-1}$ (Cecil et al. 2002). Such an outflow is believed to be the result of radiative acceleration from the central AGN (Pogge 1988; Cecil et al. 2002; Dopita et al. 2002a; D’Agostino et al. 2018). This conclusion is supported by results at radio wavelengths. Emission from dense molecular gas tracers, in particular CO(3-2), CO(6-5), HCN(4-3), HCO+ (4-3), and CS(7-6), was mapped by García-Burillo et al. (2014) using ALMA. Using these maps, García-Burillo et al. (2014) show a large outflow in all molecular gas tracers in the inner 50 - 400 pc, with a mass of $M_{\text{mol}} = 2.7^{+0.9}_{-1.2} \times 10^7 M_\odot$. A tight correlation between the motions in the circumnuclear disk (CND), the radio jet, and the ionised gas outflow is also shown by García-Burillo et al. (2014). Such a correlation suggests an AGN-driven outflow. This notion is further supported when considering the outflow rate in the circumnuclear disk. García-Burillo et al. (2014) state that the CND outflow rate of $63^{+21}_{-37} M_\odot \text{ yr}^{-1}$ is much larger than the star formation rate (SFR) calculated at the same radii in NGC 1068. Furthermore, Tacconi et al. (1994) conclude that gas at the leading edge of the bar in NGC 1068 is shocked, through observations in the near-infrared.

Young stellar clusters towards the centre of NGC 1068 have previously been identified by Storchi-Bergmann et al. (2012), supporting the idea of nuclear star formation. However, the nuclear star formation in NGC 1068 is small, with nuclear SFR estimates of $SFR_{\text{nuclear}} \sim 0.4 - 1.0 M_\odot \text{ yr}^{-1}$ being calculated between radii of 12 - 140 pc (Davies et al. 2007; Esquej et al. 2014). This is in stark contrast to the SFR calculated away from the nucleus, up to radii of several kpc. Surrounding the CND, Thronson et al. (1989) calculate a SFR of $\sim 100 M_\odot \text{ yr}^{-1}$, likely a result of the high molecular mass found in the region ($\sim 2 - 6 \times 10^9 M_\odot$). Such a large mass is believed to have been confined to the region surrounding the CND by the bar at the centre of NGC 1068 (Thronson et al. 1989). Hence, the majority of star formation in NGC 1068 is seen in what is aptly named the ‘star-forming ring’ towards the central region of the galaxy. A corollary to such a statement is that extensive star formation towards the outskirts of NGC 1068 is very rarely seen.

5.4. Photoionisation Models

We use photoionisation models produced with MAPPINGS v.1 (Sutherland et al. 2018) to aid in the separation of star formation, shock and AGN line emission. Models of H II regions and NLRs are used to represent line emission from star formation, and shocks/AGN respectively. We use identical H II region and NLR models to those described in D’Agostino et al. (2018), with the exception of using a NLR model pressure of $P/k = 2 \times 10^7 \text{ cm}^{-3} \text{ K}$, corresponding to assumptions of an initial NLR temperature of 20,000 K and initial electron density of $n = 1000 \text{ cm}^{-3}$. An initial electron density of $n_e = 1000 \text{ cm}^{-3}$ for the NLR of NGC 1068 is justified through the electron density distribution shown in D’Agostino et al. (2018), calculated using the [S II] doublet ratio. An initial temperature of 20,000 K is considered to be within the typical range for NLRs (e.g. Woltjer 1959; Camenzind & Courvoisier 1983; MacAlpine 1986). We note however that an electron temperature of $\sim 20,000 \text{ K}$ is calculated using the [O III] ratio (e.g. Vaona et al. 2012), and the use of different emission line ratios (e.g. the [O II] or [S II] ratios) may lead to a broader range of possible calculated temperatures for the NLR (Taylor et al. 2003; Vaona et al. 2012). For a detailed explanation of the parameters associated with the H II region and NLR models, see D’Agostino et al. (2018).

5.5. Separating Line Emission from Star Formation, Shocks, and AGN

5.5.1. The Need for a New Diagnostic

Previous studies which considered separating line emission from star formation and an additional high energy component, such as shocks (e.g. Rich et al. 2010, 2011, 2014), or AGN (e.g. Kewley et al. 2001, 2006, 2013a,b; Davies et al. 2014a,b; D’Agostino et al. 2018) utilised the BPT diagram most favourably, as well as other diagnostic diagrams such as the [O III]/H β vs [S II]/H α and the [O III]/H β vs [O I]/H α diagnostic diagrams introduced by Veilleux & Osterbrock (1987). The radiation field produced by sources such as shocks or AGN is harder than that from star formation, leading to increased excitation of collisionally-excited emission lines, such as [N II] $\lambda 6584$, and [O III] $\lambda 5007$. Hence, separation of star formation and line emission from harder sources is straightforward on an emission line diagnostic diagram.

These diagnostic diagrams fail however, when attempting to separate line emission between shocks and AGN. Shocks and AGN can produce very similar values of the line ratios on the aforementioned diagnostic diagrams, leading to the two sources being indistinguishable if both shocks and AGN are present in a single galaxy. Furthermore, shocked spaxels on the BPT diagram in particular may coincide with spaxels along the galaxy’s mixing sequence (see Davies et al. 2014a,b; D’Agostino et al. 2018), leading to further confusion. Hence, in order to simultaneously separate line emission from star formation, shocks, and AGN activity in a single galaxy, a new diagnostic diagram must be explored.

5.5.2. The 3D Diagnostic Diagram

To simultaneously separate line emission from star formation, shocks, and AGN, we utilise the 3D diagnostic diagram first shown by [D’Agostino et al. \(2019b\)](#). We consider the 3D diagnostic diagram to be an extension of the BPT diagram, combining the BPT line ratios with distance and velocity dispersion. The information from the BPT diagram is retained by using a function of the two line ratios, defined as the emission-line-ratio (ELR) function. The ELR functional form is given in Equation 5.1. The ELR function is defined in such a way that any two hardness-sensitive line ratios may be used instead of those from the BPT diagram. We have chosen the BPT line ratios in particular, as the BPT diagram has been historically the most favoured diagnostic diagram for studying the separation of star formation, and AGN or shocks. Other diagnostic line ratios such as $[\text{O I}]/\text{H}\alpha$ or $[\text{S II}]/\text{H}\alpha$ may be easily substituted into the ELR function. The purpose of the ELR function is to simply order the spaxels on the 3D diagram in terms of their combined $[\text{O III}]/\text{H}\beta$ and $[\text{N II}]/\text{H}\alpha$ ratios. We emphasise that the ELR function is data-dependent, and the range of values from 0 to 1 is arbitrary. The endpoints of 0 and 1 do not represent any physical phenomena, such as 100% star formation emission and 100% AGN emission respectively.

Prior to the data being displayed on the 3D diagnostic diagram, we first reduce and flux-calibrate the emission-line fluxes in the raw cubes using LZIFU ([Ho et al. 2016](#)). LZIFU is capable of fitting multiple Gaussian components to each emission line, thereby resolving multiple velocity components. Once each emission line is fit with a maximum of three Gaussian components, the neural network LZCOMP ([Hampton et al. 2017](#)) is used to determine the recommended number of Gaussian components for each emission line in each spaxel. Maps showing the distribution across the galaxy of each resolved velocity component in each spaxel are shown in Figure 5.1. Full details of the S7 data reduction are provided in [Thomas et al. \(2017\)](#).

An example of the 3D diagnostic diagram showing data from NGC 1068 is shown in Figure 5.2. The data points shown on the 3D diagram represent each individual velocity component in the data. For every component present in each spaxel, the velocity dispersion of the individual component (hereafter referred to as the ‘single-component velocity dispersion’) is combined with the total flux (‘zeroth’ component) and the radial value for the spaxel to define the position on the figure. Full details of the 3D diagram can be found in [D’Agostino et al. \(2019b\)](#). Data points which contain the first-component, second-component, and third-component fits to the velocity dispersion are shown on the 3D diagram in Figure 5.2 in red, blue, and green respectively. The first, second, and third components are numbered in order of the narrowest to broadest velocity dispersion. Hence, higher-order components will have greater values of the single-component velocity dispersion. We include the higher-order component fits to the velocity dispersion on the 3D diagram, as shocks are typically diagnosed and categorised by high velocity dispersions ([Rich et al. 2010, 2011, 2014; Ho et al. 2014](#)). All relevant emission lines are corrected for extinction, in accordance with [Cardelli et al. \(1989\)](#). The extinction calculation from [Cardelli et al. \(1989\)](#) uses the colour excess $E(B-V)$, which itself uses the Balmer decrement $\text{H}\alpha/\text{H}\beta$.

$$\text{ELR function} = \frac{\log([\text{NII}]/\text{H}\alpha) - \min_{\log([\text{NII}]/\text{H}\alpha)}}{\max_{\log([\text{NII}]/\text{H}\alpha)} - \min_{\log([\text{NII}]/\text{H}\alpha)}} \times \frac{\log([\text{OIII}]/\text{H}\beta) - \min_{\log([\text{OIII}]/\text{H}\beta)}}{\max_{\log([\text{OIII}]/\text{H}\beta)} - \min_{\log([\text{OIII}]/\text{H}\beta)}} \quad (5.1)$$

Effects of beam smearing on the velocity dispersion

The finite beam size of a telescope inevitably leads to a phenomenon known as beam smearing (e.g. [Bosma 1978](#); [Begeman 1987](#)). The smearing of line emission across adjacent spaxels produces broader line profiles, which ultimately can be erroneously interpreted as a higher velocity dispersion in a given spaxel. This could prove problematic, because the 3D diagram from [D’Agostino et al. \(2019b\)](#) uses the velocity dispersion in a spaxel as a major shock diagnostic. Large velocity dispersions towards the centre of an AGN are predominantly the result of outflows from the NLR (e.g. [Freitas et al. 2018](#)). Thus, the impact of beam smearing may be small, yet potentially significant nonetheless.

To verify that the large velocity dispersions seen in NGC 1068 are not solely the result of beam smearing, we use the code ^{3D}BAROLO ([Di Teodoro & Fraternali 2015](#)) to recover the rotational kinematics of the galaxy. The results of using ^{3D}BAROLO are shown in Figure 5.3. The velocity field is fit using the H α line in the ^{3D}BAROLO model. The model panels in Figure 5.3 (right-hand-side panels) show maps of the line-of-sight velocity field and velocity dispersion of the derived rotation curve of the galaxy. We are only concerned with the central region of the galaxy, because beam smearing is associated with strong velocity gradients. Strong velocity gradients are more likely found towards the centre of a galaxy due to disk rotation, where the velocity field will transition between positive and negative velocities rapidly. Figure 5.3 shows that in the ideal model case, beam smearing will only increase the velocity dispersion at the centre of NGC 1068 slightly (seen as the small region of $\sim 100 \text{ km s}^{-1}$ spaxels in the model velocity dispersion panel). The data however, shows a much larger region with very high velocity dispersions. This provides confidence that the high velocity dispersions at the centre of NGC 1068 are physical, and not the result of beam smearing. Furthermore, high spatial resolution images from *Hubble Space Telescope (HST)* (e.g. [Cecil et al. 2002](#)) show high-velocity regions (up to $\sim 3000 \text{ km s}^{-1}$) within the central arcsecond of NGC 1068, supporting our claim of the physical nature of these high velocity dispersions.

Calculating the distance measurement in each spaxel

In order to assign each spaxel a distance value, we first check for local maxima in the [O III]/H β distribution across the galaxy. Local maxima in the [O III]/H β distribution are identified, and shown as red crosses in Figure 5.4a. Each maximum is treated as a centre, and a deprojected radius is calculated from each maximum, assuming the same values for the position angle and axis ratio for the galaxy. In the event where multiple maxima are detected (as in the case of NGC 1068), the deprojected radii calculated from each maximum are multiplied together, and then raised to the power of $1/n_{\text{maxima}}$, where n_{maxima} is the number of maxima detected (the ‘geometric mean’). If only a single peak

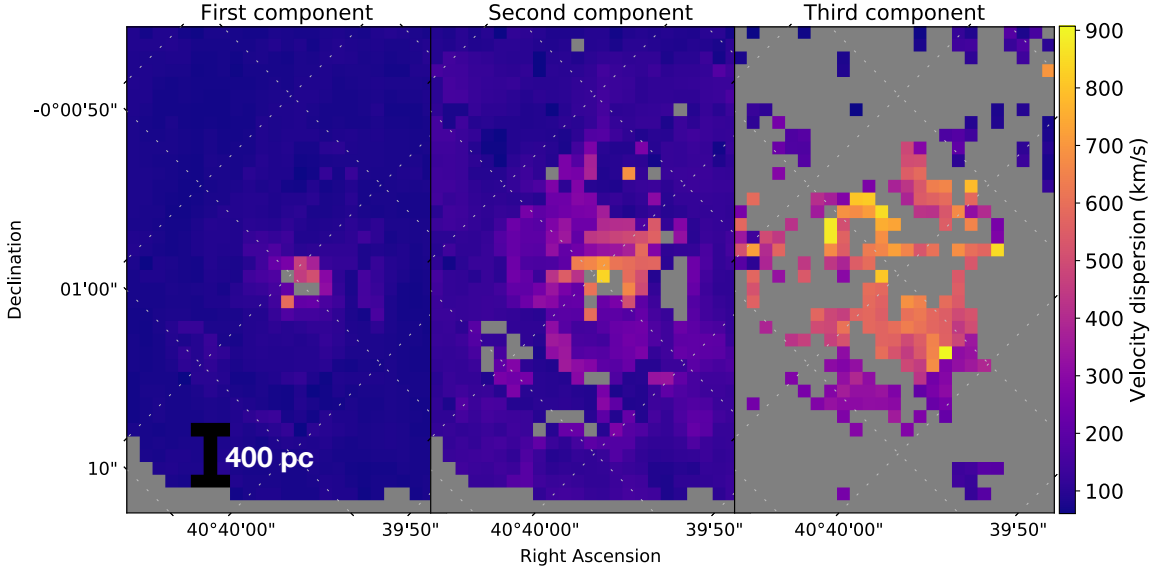


Figure 5.1 Maps of NGC 1068 showing the distribution and amplitude of each individual velocity component in the data. Dashed lines represent grid lines of constant right ascension and declination.

is detected in the $[\text{O III}]/\text{H}\beta$ map, the peak is treated as the centre of the galaxy, and the distance measurement defaults to the deprojected galactocentric radius. A map showing the distribution of distance values across NGC 1068 is shown in Figure 5.4b. Hereafter, the distance measurement may simply be referred to as ‘distance’.

5.5.3. Defining the Star Formation, Shock, and AGN Extrema

The 100% regions in the 3D diagram indicate where emission is expected to be solely from one ionising source. Each of the 100% star formation, shock, and AGN regions of the 3D diagram are defined by a value of the ELR function, similarly to the spaxels on the BPT diagram. We calculate the 100% star formation, shock, and AGN ELR function values through photoionisation modelling using MAPPINGS v.1.

The 100% star formation and AGN emission line ratios for NGC 1068 are obtained by using the BPT diagram directly. We first construct new grid lines of constant metallicity on the H II region and NLR grids, after calculating the metallicity gradient of the galaxy using the Kewley & Dopita (2002) (hereafter KD02) metallicity diagnostic. The $[\text{N II}]/[\text{O II}]$ diagnostic described by KD02 is a good choice when attempting to calculate the metallicity gradient of galaxies which contain an AGN. Kewley & Ellison (2008) show that the relative contribution from an AGN has a very minor effect (≤ 0.04 dex at $\sim 15\%$ AGN contribution) on the $[\text{N II}]/[\text{O II}]$ ratio, in spaxels below the Kewley et al. (2001) theoretical maximum starburst line. The central and outer metallicities for NGC 1068 are shown in Table 5.1. The newly-constructed line of constant metallicity in the H II region grid uses the outer metallicity of the galaxy, whilst the line constructed on the NLR grid uses the central metallicity. This is because the mixing sequence of the galaxy traces increasing AGN contribution from H II regions outside of the AGN extended narrow-line region (ENLR) towards the AGN at the centre of the galaxy (see Kewley et al. 2001, 2013a; Davies et al. 2014a; D’Agostino et al. 2018).

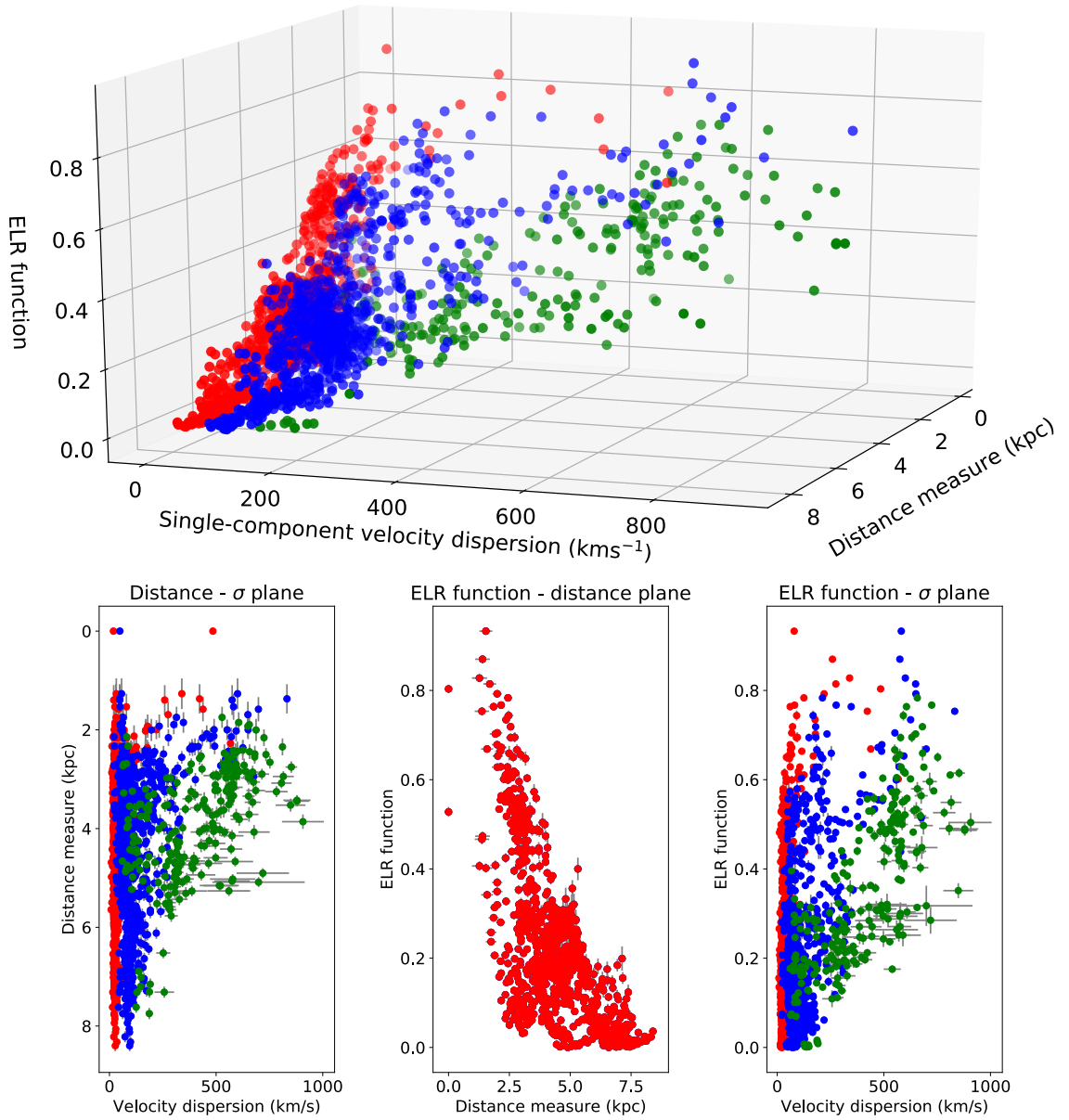


Figure 5.2 3D diagnostic diagram showing data from NGC 1068. Red spaxels are spaxels using the first-component fits to the velocity dispersion, blue spaxels are the second-component fits, and green spaxels are the third-component fits. First-, second-, and third-component velocity components in each spaxel, if present, all use the total flux ('zeroth' component) and the distance measurement for the individual spaxel. The ELR function is given in Equation 5.1. Bottom panels show the 2D projections in the distance- σ , ELR function-distance, and ELR function- σ planes. Grey lines in each of the three panels represent the errors associated with each dimension. Errors are omitted from the 3D diagram for clarity.

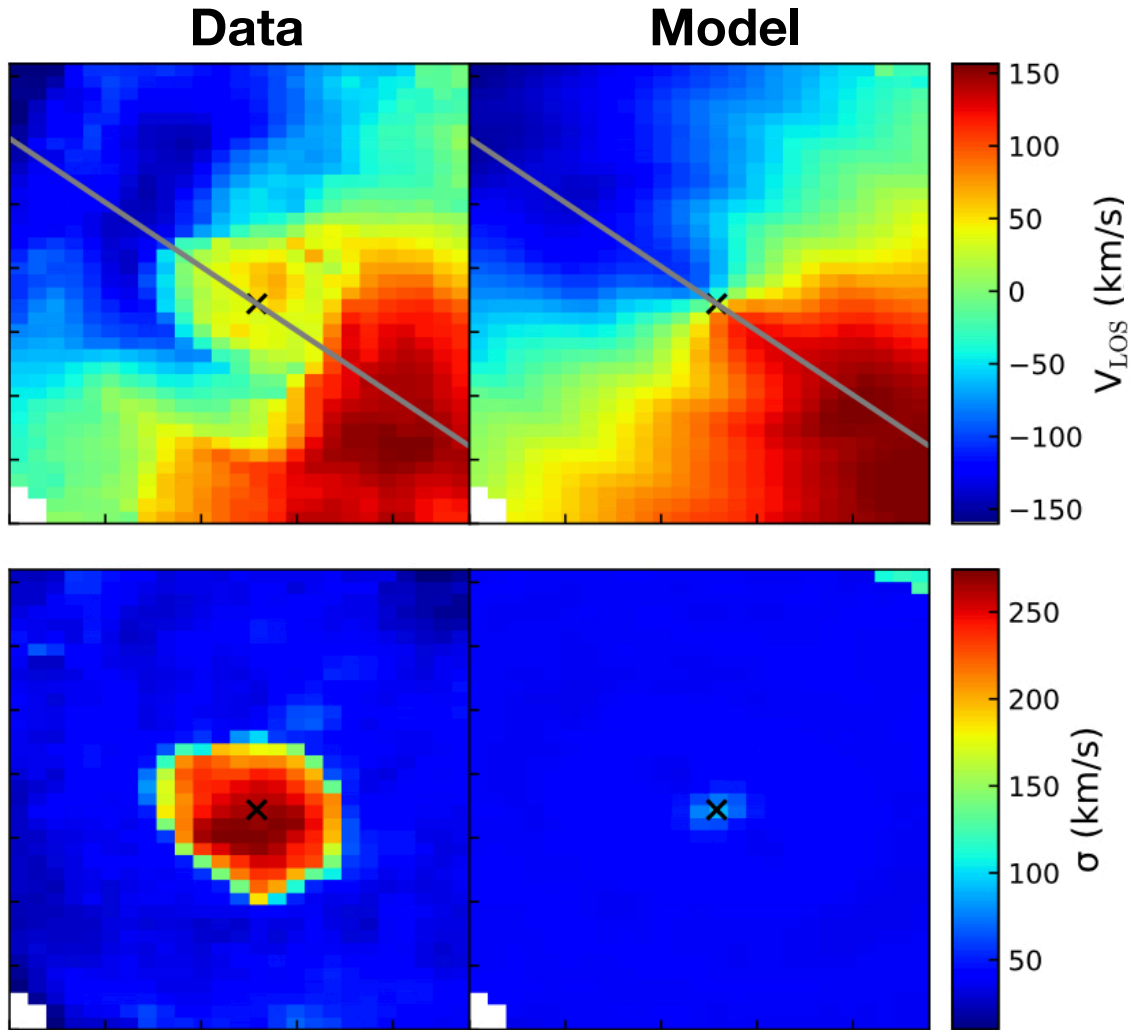


Figure 5.3 Maps of the line-of-sight velocity (v_{LOS}) and the velocity dispersion (σ) for NGC 1068 in the S7 field-of-view (38×25 arcsec 2). The left-hand panels show the maps obtained from the data directly. The right-hand panels show the maps of the model produced using $3\text{D}_{\text{BAROLO}}$. The centre of the galaxy is marked with an 'X' in all panels.

We select two basis points each on both the new H II region and NLR grid lines, to account for the spread in ionisation parameter in the mixing sequence on the BPT diagram. The basis points are intended to signify the regions of 100% star formation and 100% AGN on the H II region and NLR grids respectively. These basis points are located along the new lines of constant metallicity, and are shown in light blue on Figure 5.5. The mean value of the pair of basis points then determines the 100% ELR function value for the star-forming and AGN regions. The point representing the mean value for each pair is shown in light green on Figure 5.5. We use the 100% AGN ELR function value for the 100% shock ELR function value also. This is because shocks may be prevalent in the NLR of galaxies, produced from sources such as the radiation pressure from accretion disk emission, and the pressure from the radio jets (e.g. Dopita 1995; Wilson & Raymond 1999; Dopita et al. 2015b, and references therein). The values of the ELR function used to represent 100% star formation, AGN, and shock emission are given in Table 5.1.

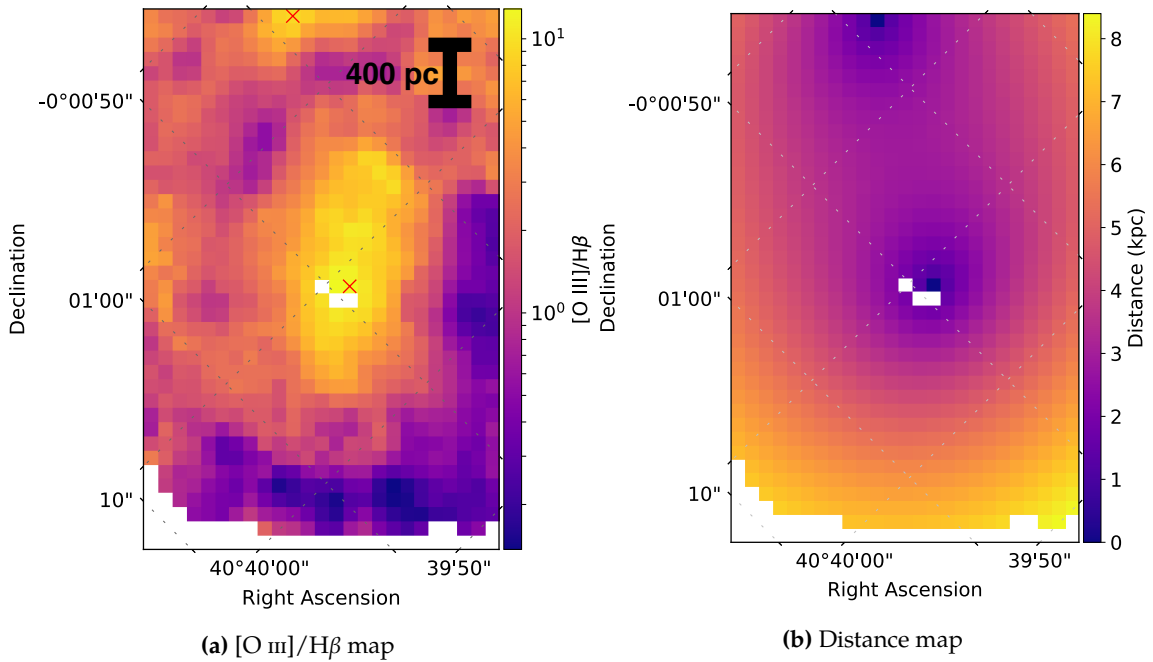


Figure 5.4 $[\text{O III}]/\text{H}\beta$ map in (a) and distance map in (b) for NGC 1068. The distance in each spaxel is calculated by first identifying peaks in the $[\text{O III}]/\text{H}\beta$ distribution. Peaks are identified in (a) by red crosses. Dashed lines represent grid lines of constant right ascension and declination.

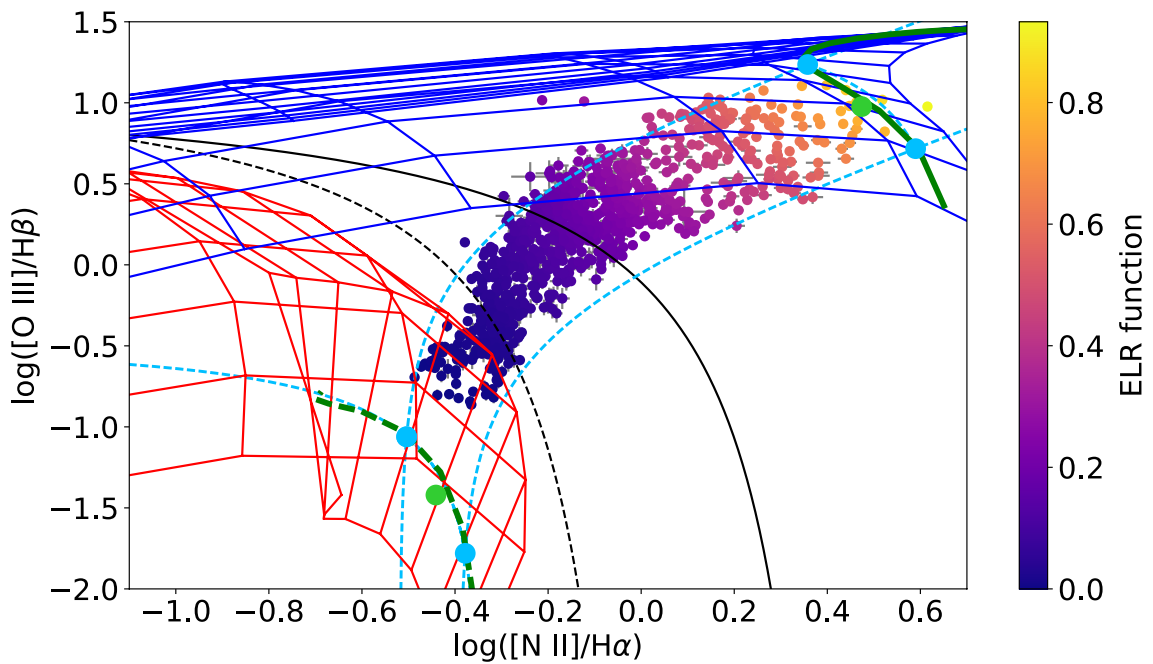


Figure 5.5 BPT diagram of NGC 1068 with spaxels coloured to the ELR function in Equation 5.1. The red grid is the H II region model grid, and the blue grid is the NLR model grid, both described in Section 5.4. The green dashed line on the H II region grid is a constructed line of constant metallicity for the outer regions of the galaxy, within the S7 field-of-view. The solid green line on the NLR model is the constructed line of constant metallicity for the centre of the galaxy. Both metallicity values are found in Table 5.1. The light blue points are the basis points used to calculate the star formation and AGN/shock extrema for the 3D diagnostic diagram. Light green points represent the mean value of each pair of light blue basis points, and define the 100% star formation and AGN/shock ELR function values, also found in Table 5.1. The dashed black line is the [Kauffmann et al. \(2003\)](#) demarcation line, and the solid black line is the [Kewley et al. \(2001\)](#) demarcation line.

Outer metallicity (Z_{\odot})	1.48
Central metallicity (Z_{\odot})	2.20
100% star formation ELR function value	-0.01
100% shock/AGN ELR function value	0.81

Table 5.1 Metallicity gradient and 100% emission line ratio values for NGC 1068. Solar metallicity (Z_{\odot}) is set to $12 + \log(\text{O}/\text{H}) = 8.93$ (Anders & Grevesse 1989).

5.5.4. Calculating the Star Formation-Shock-AGN Fraction

The positions of the spaxels on the 3D diagram are important in quantifying the contribution to emission from star formation, shocks, and AGN in each spaxel. Seen in Figure 5.2, the spread of spaxels on the 3D diagram shows two distinct and clear sequences. The first sequence contains spaxels at low velocity dispersions, and shows very little change in velocity dispersion with increasing values of the ELR function. The second sequence however displays a clear increase in velocity dispersion as the value of the ELR function increases in the spaxels. D’Agostino et al. (2019b) show that the first and second sequences represent the star formation-AGN and star formation-shock mixing respectively (see D’Agostino et al. 2019b for complete details on the diagram and its interpretation).

Each data point on the 3D diagnostic diagram is assigned a star formation-shock-AGN fraction. The star formation-shock-AGN fraction for each data point is calculated by considering its distance along the two sequences. Points containing high ELR function values, found towards the top of the first and second sequences, are assigned high AGN and shock fractions respectively. Conversely, points with low ELR function values will be assigned higher star formation fractions. The proximity of the data point to each sequence influences its final AGN and shock fractions. Depending on the position of the data points on the 3D diagnostic diagram, it is possible that any given data point will be assigned a fraction of 0% for one or more of the ionising sources.

Results

The results of calculating AGN, shock, and star formation fractions on the 3D diagnostic diagram for NGC 1068 are shown in Figures 5.6, 5.7, and 5.8, respectively. We also include 2D projections of the fractions in the distance- σ and ELR function- σ planes in Figures 5.6, 5.7, and 5.8. Unlike in Figure 5.2, we do not include the ELR function-distance plane projection, due to the obscuration of many spaxels preventing its usefulness. A line of best fit is applied to both the star formation-AGN and star formation-shock sequences of spaxels to show the direction of star formation-AGN and star formation-shock mixing respectively. The fractions are calculated for all spaxels on the 3D diagnostic diagram; some spaxels may at this point have multiple values for their star formation-shock-AGN fractions, depending on the number of velocity components present in the spaxel. As a result, for a spaxel with multiple velocity components, the final fractions are calculated as the weighted average of the fractions in the individual components, weighted by the contribution of each component to the total $[\text{O III}]\lambda 5007$ flux. Maps of the final star formation, shock, and AGN fractions across the galaxy in the S7 field-of-view are shown in Figure 5.9. BPT diagrams of NGC

NGC 1068					
	New method			Old method	
Emission line	Star formation	Shocks	AGN	Star formation	AGN
H α	$59.7 \pm 8.0\%$	$26.1 \pm 7.4\%$	$14.2 \pm 4.5\%$	$64.4 \pm 7.1\%$	$35.6 \pm 7.1\%$
H β	$60.0 \pm 8.1\%$	$26.0 \pm 7.4\%$	$14.1 \pm 4.5\%$	$64.6 \pm 7.1\%$	$35.4 \pm 7.1\%$
[O II] $\lambda\lambda 3726, 3729$	$35.4 \pm 10.0\%$	$41.2 \pm 12.1\%$	$23.3 \pm 8.8\%$	$38.3 \pm 12.0\%$	$61.7 \pm 12.0\%$
[O III] $\lambda 5007$	$36.1 \pm 10.8\%$	$46.1 \pm 11.5\%$	$17.8 \pm 6.5\%$	$39.6 \pm 12.8\%$	$60.4 \pm 12.8\%$
[S II] $\lambda\lambda 6716, 6731$	$39.4 \pm 9.5\%$	$39.1 \pm 11.3\%$	$21.5 \pm 8.0\%$	$42.5 \pm 11.1\%$	$57.5 \pm 11.1\%$
[N II] $\lambda 6584$	$43.9 \pm 9.5\%$	$37.6 \pm 10.3\%$	$18.5 \pm 6.7\%$	$48.0 \pm 10.4\%$	$52.0 \pm 10.4\%$

Table 5.2 Star formation, shock, and AGN fractions for various strong emission lines in NGC 1068 within the S7 field-of-view. Errors on the star formation, shock, and AGN fractions account for differences in final emission line weighting, uncertainties in photoionisation models, and uncertainties in the fits from LZIFU. Displayed also are the star formation and AGN fractions using the method from D’Agostino et al. (2018), assuming only star formation-AGN mixing. The errors associated with the star formation-AGN mixing fractions are the result of a 0.1 dex uncertainty in the photoionisation models, and the errors from LZIFU.

1068, with each spaxel colour-coded to the final star formation, shock, and AGN fractions, are shown in Figure 5.10. We have chosen [O III] $\lambda 5007$ as the line by which we calculate the relative weight of each component, because it is a strong emission line associated with the presence of an AGN and shocks. Hence, it is a reliable emission line to use for the analysis in this work. However, other strong lines are present in the data, such as H α and [N II] $\lambda 6584$. We calculate that the choice of which emission line is used to calculate the weighting can impact the final fractions by up to $\sim 8\%$. It is important to note that if two galaxies are to be compared equally, the emission line by which the final fractions are weighted must be identical. When calculating the relative contribution of each ionising source to the flux of strong emission lines in Table 5.2 (described below), the errors on the fractions account for the possible differences in value as a result of weighting by a different emission line.

The star-forming ring in NGC 1068 can be seen surrounding the nucleus in the star formation ratio map from Figure 5.9. The star formation ratio map also shows that ionisation in the nucleus is dominated by non-stellar sources. In particular, the biconical outflow most prominently seen in the [O III] $\lambda 5007$ is largely visible in the AGN ratio map. This agrees with previous work, claiming that the bicone is the result of material radiatively accelerated by the AGN (e.g. Pogge 1988; Cecil et al. 2002; Dopita et al. 2002a; D’Agostino et al. 2018). The shock ratio map shows that shocks are seen to dominate the central few arcseconds of NGC 1068, however, due to the location of the high shock fractions, these shocks are likely from the AGN. An accreting supermassive black hole will produce thermal X-rays which provide a radiation pressure on nearby gas, causing expulsion of the gas in the form of a wind. This high-velocity wind will cause shocked material upon interaction with the ISM (Zubovas & King 2012). Hence, the shocked structure seen in the nucleus of NGC 1068 is likely the result of the AGN.

The star formation, shock, and AGN contributions to the flux of several strong lines are shown in Table 5.2. For comparison, also in Table 5.2, we show the star formation and AGN contributions to the same strong emission lines, calculated using the star formation-

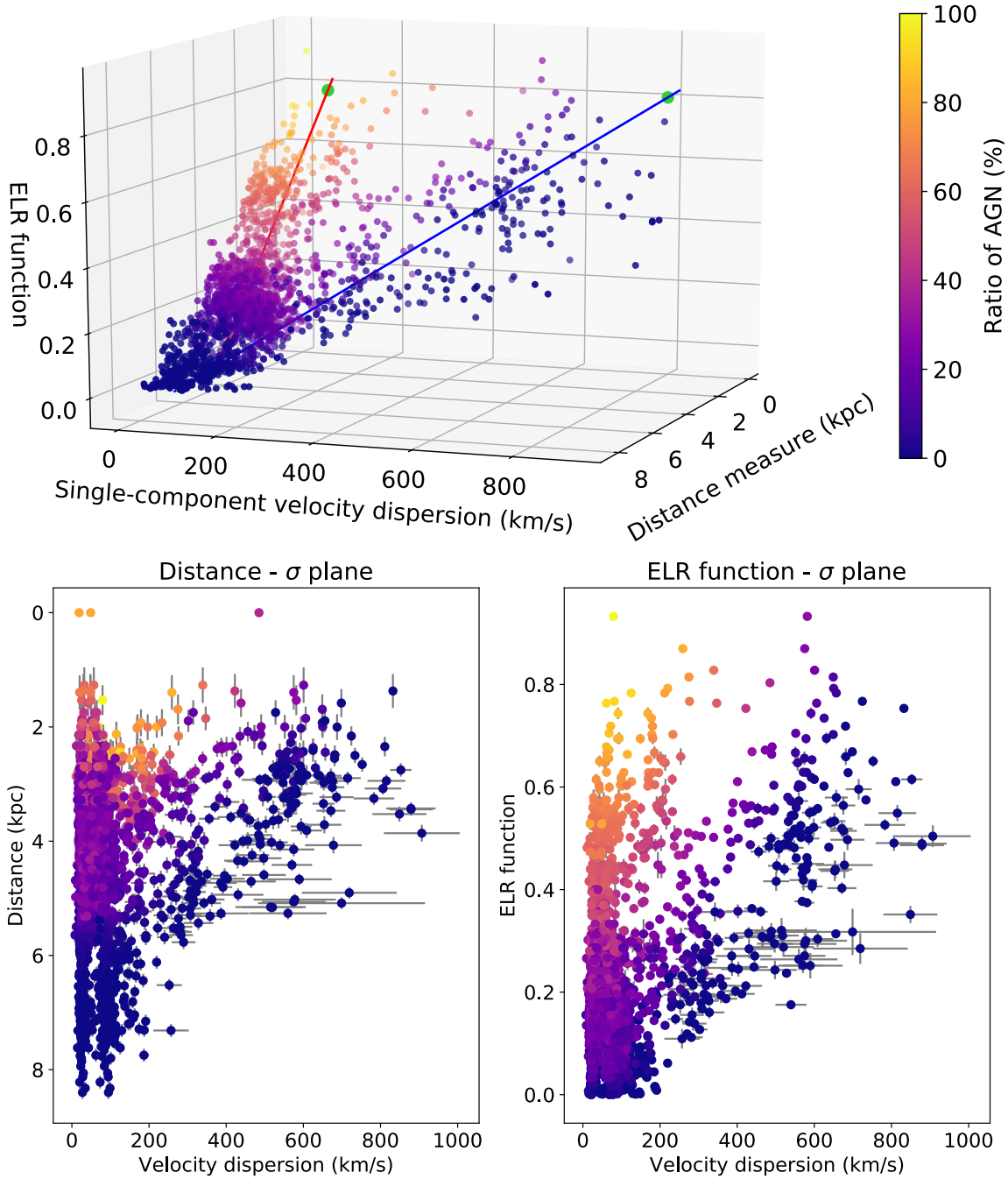


Figure 5.6 3D diagnostic diagram, showing the ratio of AGN in each spaxel of NGC 1068. Light green points represent the basis points for the ELR function. Bottom panels show the 2D projections in the distance- σ and ELR function- σ planes. Grey lines in the two panels represent the errors associated with each dimension. Errors are omitted from the 3D diagram for clarity.

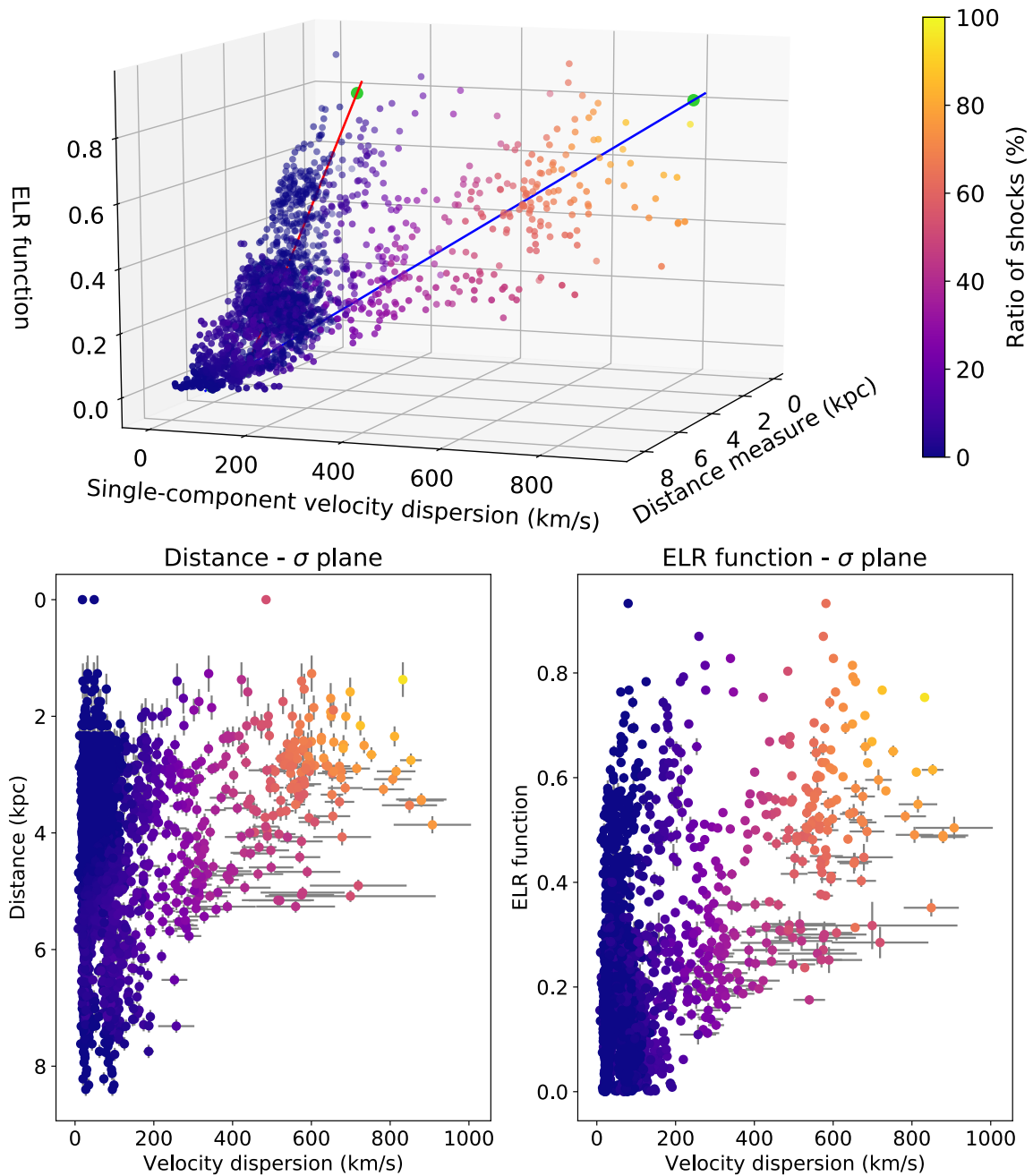


Figure 5.7 3D diagnostic diagram, showing the ratio of shocks in each spaxel of NGC 1068. Light green points represent the basis points for the ELR function. Bottom panels show the 2D projections in the distance- σ and ELR function- σ planes. Grey lines in the two panels represent the errors associated with each dimension. Errors are omitted from the 3D diagram for clarity.

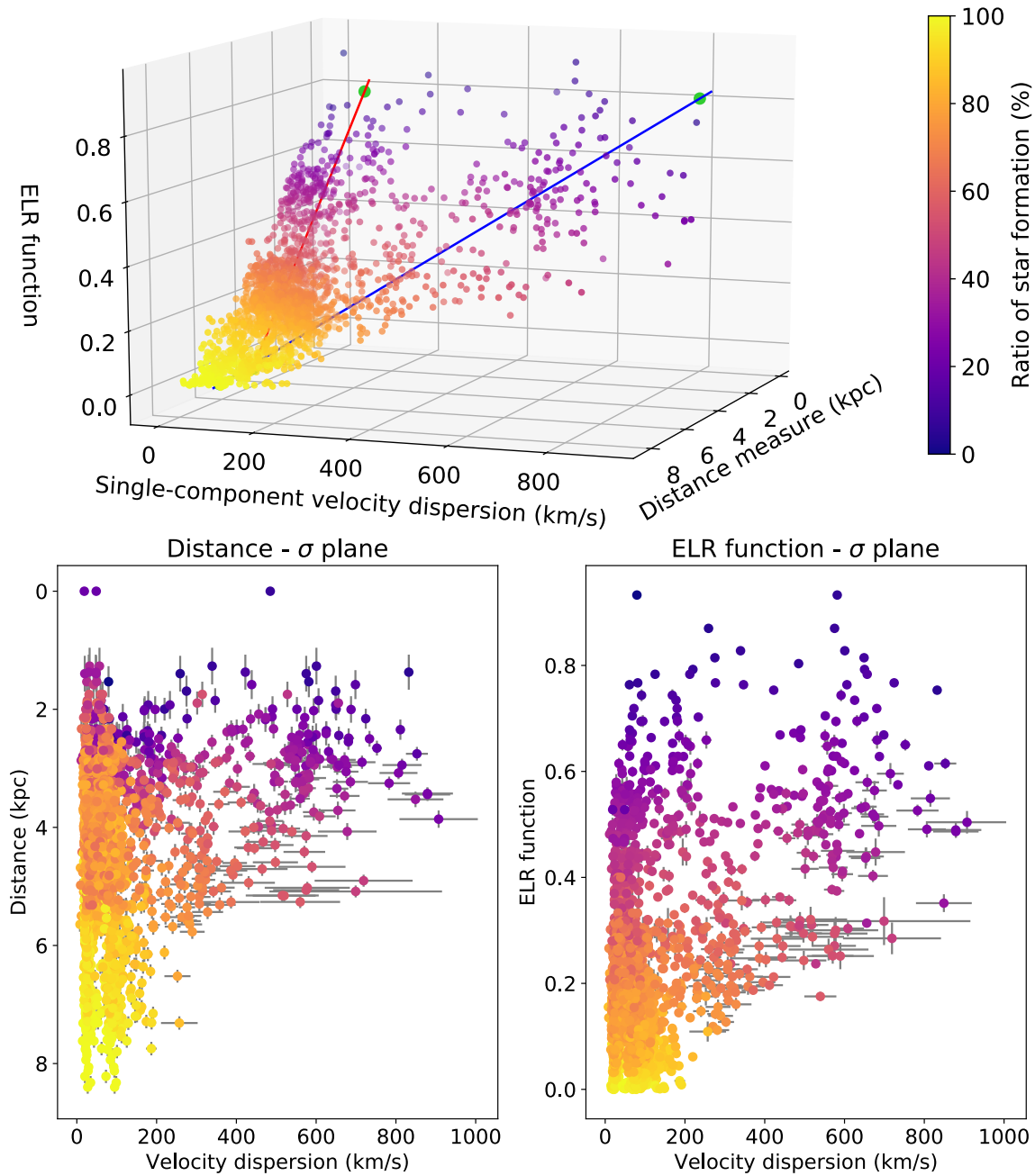


Figure 5.8 3D diagnostic diagram, showing the ratio of star formation in each spaxel of NGC 1068. Light green points represent the basis points for the ELR function. Bottom panels show the 2D projections in the distance- σ and ELR function- σ planes. Grey lines in the two panels represent the errors associated with each dimension. Errors are omitted from the 3D diagram for clarity.

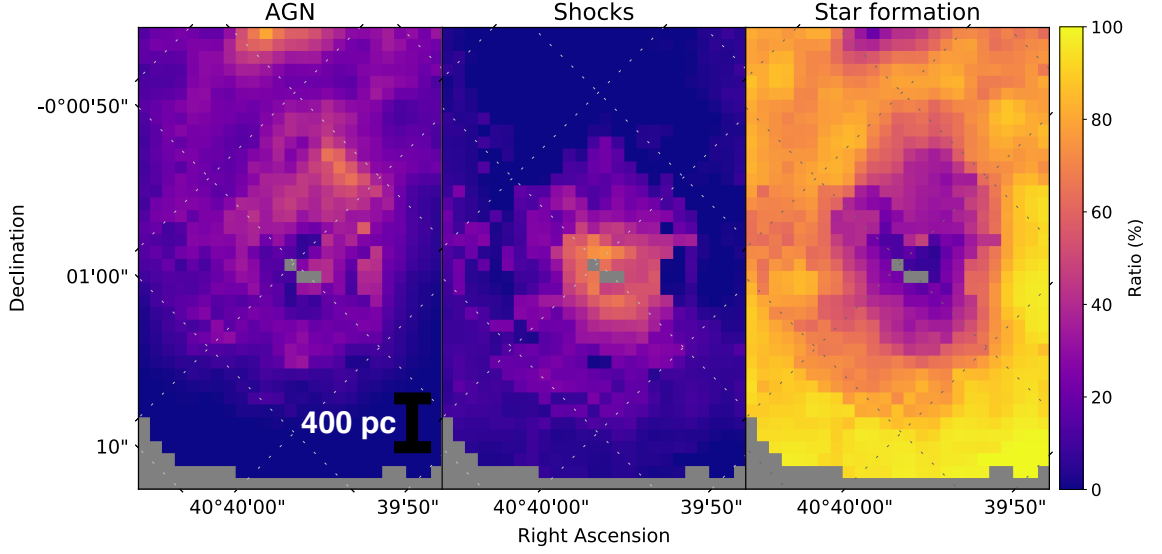


Figure 5.9 Maps of NGC 1068 showing the distribution of the AGN, shock, and star formation fractions seen in Figures 5.6, 5.7, and 5.8, respectively. In the event that a spaxel contains more than one velocity component, the final ratio is weighted by the contribution of each component to the total $[\text{O III}]\lambda 5007$ flux. Dashed lines represent grid lines of constant right ascension and declination.

AGN mixing method from D’Agostino et al. (2018). The method used to calculate the star formation, shock, and AGN contributions to each emission line listed in Table 5.2 is identical to the method described in Davies et al. (2014a) and D’Agostino et al. (2018):

The total luminosity of any emission line in an IFU field-of-view is given by:

$$L_{\text{Tot}} = \sum_{i=1}^n L_i$$

where L_i is the luminosity of the emission line in spaxel i . The total luminosity of the emission line attributable to any source (star formation, shocks, or AGN) can be calculated by

$$L_{\text{source}} = \sum_{i=1}^n f_i^{\text{source}} L_i$$

where f_i^{source} is the source fraction in spaxel i . It follows that the relative fraction of emission attributable to each source for the given emission line is provided by

$$f_{\text{Tot}}^{\text{source}} = \frac{L_{\text{source}}}{L_{\text{Tot}}}$$

In addition to accounting for the choice of emission line used for the final weightings, the errors associated with each fraction given in Table 5.2 also consider the error in the photoionisation models described in Section 5.4. Assuming an error of ~ 0.1 dex in both the $[\text{O III}]/\text{H}\beta$ and $[\text{N II}]/\text{H}\alpha$ ratios (e.g. Kewley et al. 2001; D’Agostino et al. 2019a), the resulting change in the position of the basis points on the 3D diagram can alter the final fractions by up to $\sim 10\%$. Finally, the errors on the fractions in Table 5.2 also consider the uncertainties in the emission line fits from LZIFU. The error analysis performed on the star formation-AGN mixing fractions also in Table 5.2 is updated from that in D’Agostino et al. (2018), considering the 0.1 dex uncertainty in the photoionisation models.

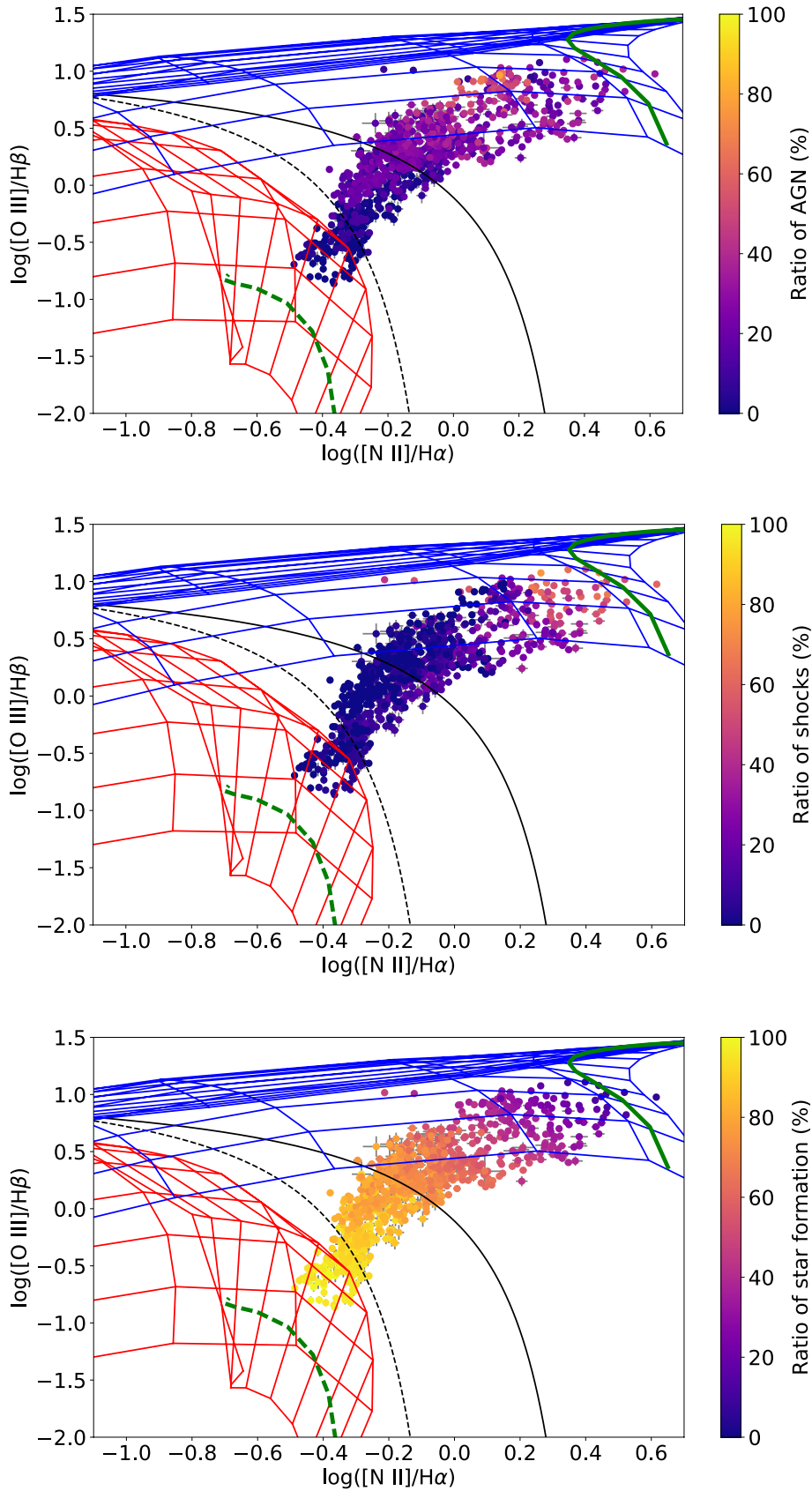


Figure 5.10 BPT diagrams showing data from NGC 1068, colour-coded to the AGN, shock, and star formation fractions in each spaxel. The red grid is the H II region model grid, and the blue grid is the NLR model grid, both described in Section 5.4. The green dashed line on the H II region grid is a constructed line of constant metallicity for the outer regions of the galaxy, within the S7 field-of-view. The solid green line on the NLR model is the constructed line of constant metallicity for the centre of the galaxy. Both metallicity values are found in Table 5.1. The dashed black line is the [Kauffmann et al. \(2003\)](#) demarcation line, and the solid black line is the [Kewley et al. \(2001\)](#) demarcation line.

The method from [D’Agostino et al. \(2018\)](#) assumes the emission in each spaxel can be expressed as a combination of star formation and AGN activity, without accounting for shock emission. The fractions in [Table 5.2](#) show that if shocks are not considered as a possible source of ionisation, then the contribution to photoionisation from an AGN may be severely overestimated. The star formation fractions in each of the strong lines listed are similar between the two methods, implying that the majority of shock emission mixes with the emission from AGN photoionisation. This is further illustrated in [Figure 5.11](#). We show a BPT diagram and map of NGC 1068 coloured by AGN fraction, assuming only a star formation-AGN mixing regime, against a BPT diagram and map coloured by the shock + AGN fraction, calculated by adding the fractions seen in [Figures 5.9](#) and [5.10](#). The results are very similar. This is unsurprising, given that shocks can produce emission line ratios similar to that of AGN. This is particularly true on the BPT diagram, where emission from shocks and AGN can be found within the same region of the diagram. Hence, using the BPT diagram to calculate star formation and AGN fractions, and only assuming a star formation-AGN mixing regime as in [Davies et al. \(2014a,b\)](#), [Davies et al. \(2016\)](#), and [D’Agostino et al. \(2018\)](#), will likely overestimate the true contribution from the AGN to emission line fluxes.

[Davies et al. \(2014a,b\)](#), [Davies et al. \(2016\)](#), and [D’Agostino et al. \(2018\)](#) all show that using $H\alpha$ as a SFR indicator in an AGN galaxy may lead to an overestimate of the true SFR, as the AGN is responsible for a fraction of the total $H\alpha$ luminosity. This is also seen in [Table 5.2](#), as the AGN contribution to the $H\alpha$ flux in NGC 1068 is non-zero, irrespective of the inclusion of shocks to the decomposition. However, once shocks are accounted for in the decomposition, the star formation fractions of each of the strong lines, while similar, are systematically lower. Therefore, it is evident that emission from star formation does not solely mix with AGN, but rather multiple sources of ionisation and excitation. In order to calculate a SFR as accurately as possible using the $H\alpha$ flux, as many sources of ionisation and excitation as possible must be simultaneously separated. Failure to do so will result in the SFR consistently being overestimated. Using the $SFR(H\alpha)$ relation given by [Kennicutt et al. \(1994\)](#), we calculate a SFR of $3.1 M_{\odot} \text{ yr}^{-1}$ in the S7 field-of-view (radius ~ 1 kpc), after calculating the $H\alpha$ luminosity from star formation to be $3.9 \times 10^{41} \text{ erg s}^{-1}$.

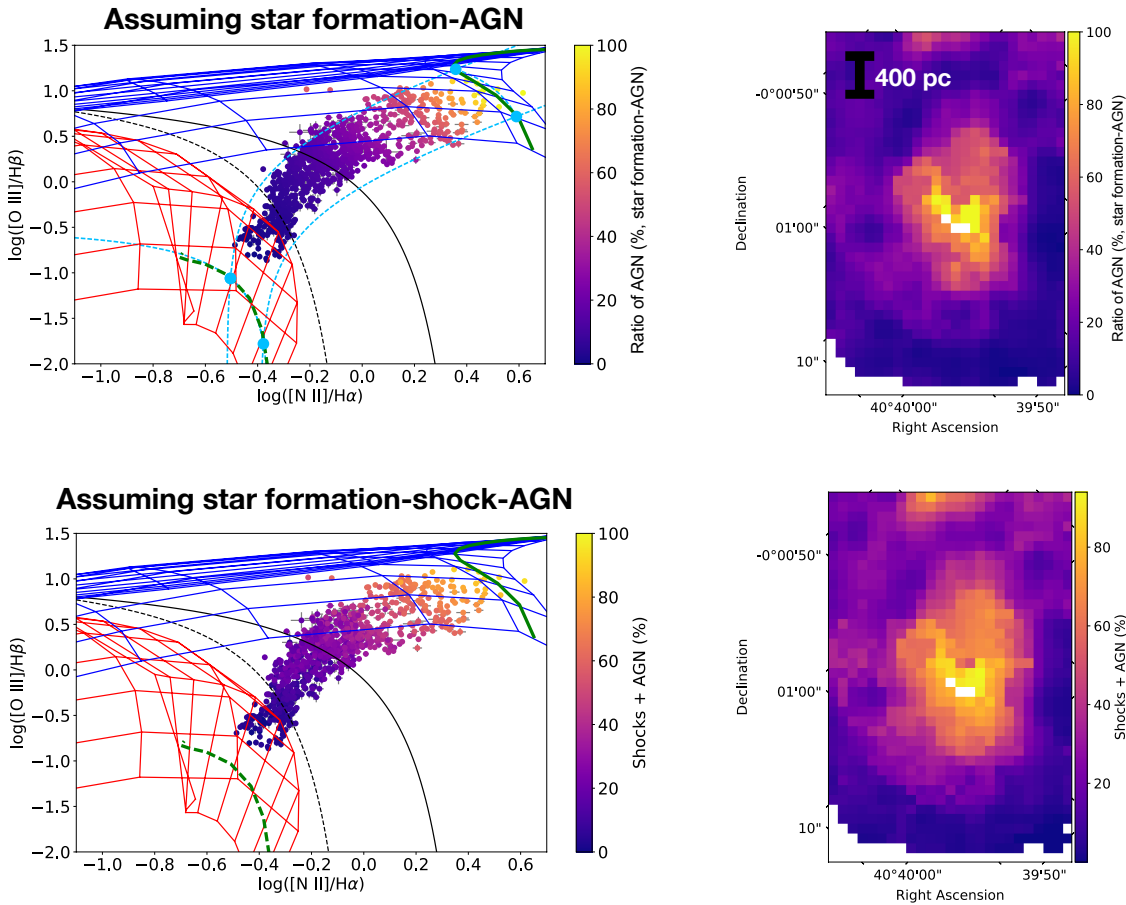


Figure 5.11 Maps and BPT diagrams of NGC 1068, assuming a star formation-AGN mixing regime on top, and our new star formation-shock-AGN regime below. The spaxels in the bottom BPT diagram and map are coloured by shock + AGN fraction, seen separately in Figures 5.9 and 5.10. The red grid on the BPT diagrams is the H II region model grid, and the blue grid is the NLR model grid, both described in Section 5.4. The green dashed line on the H II region grid is a constructed line of constant metallicity for the outer regions of the galaxy, within the S7 field-of-view. The solid green line on the NLR model is the constructed line of constant metallicity for the centre of the galaxy. Both metallicity values are found in Table 5.1. The light blue points are the basis points used to calculate the AGN fraction in each spaxel (see D’Agostino et al. 2018). The dashed black line is the Kauffmann et al. (2003) demarcation line, and the solid black line is the Kewley et al. (2001) demarcation line.

5.6. Comparison with Other Data

To verify our star formation, shock, and AGN fractions in NGC 1068, we use the structure seen in other wavelengths. X-ray emission is known to be ubiquitous in AGN (e.g. Gandhi 2005), and nuclear shocks may be caused by the relativistic jets from the SMBH, which are very visible in the radio part of the spectrum (Blandford & Königl 1979). We also study the CO(3-2) distribution in the nucleus of NGC 1068 to verify our star formation results. García-Burillo et al. (2014) show that the majority of CO(3-2) flux measured by ALMA (~63% of the total) is detected in the star-forming ring surrounding the nucleus.

Shown in Figure 5.12 are maps of the [O III] λ 5007 luminosity from the AGN, and the 0.25-7.5 keV *Chandra* X-ray distribution from Young et al. (2001). Contours of each map are shown on the other. The X-ray contours accurately trace the regions of high luminosity in the AGN map. Similarly, we find large agreement with the distribution of the [O III] λ 5007

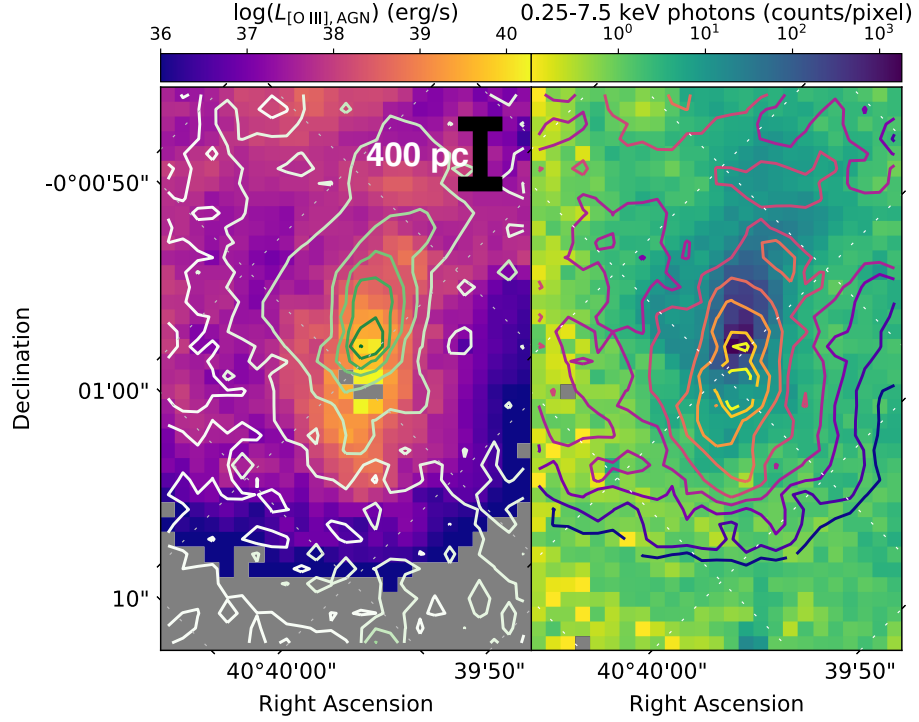


Figure 5.12 Maps of NGC 1068 showing the [O III] λ 5007 luminosity attributable to AGN in the left panel, and the 0.25-7.5 keV X-ray photon map from [Young et al. \(2001\)](#) on the right. Contours of each map are shown in the adjacent panel. Dashed lines represent grid lines of constant right ascension and declination.

shock luminosity, and the 3mm radio continuum contours from [García-Burillo et al. \(2017\)](#) in Figure 5.13. The 3mm radio continuum data from [García-Burillo et al. \(2017\)](#) clearly shows the distribution and position of the radio jets. Finally, in Figure 5.14 we show the CO(3-2) contours from [García-Burillo et al. \(2014\)](#) over the $H\alpha$ luminosity distribution from star formation, and the star formation ratio map from Figure 5.9. The CO(3-2) contours accurately trace regions of high star formation surrounding the nucleus, in agreement with the findings of [García-Burillo et al. \(2014\)](#).

We also use of the He II λ 4686/ $H\beta$ distribution map to verify our results. He II is a high-ionisation line (ionisation potential of ~ 54 eV), thus requiring a hard radiation field (the kind associated with AGN) for ionisation. The line ratio He II/ $H\beta$ is not contained in our emission line ratio function shown in Equation 5.1, and so provides an independent test of our results. The He II/ $H\beta$ map from the S7 data is shown in Figure 5.15, normalised to the maximum value. Regions of high He II/ $H\beta$ can be seen to align with regions of high AGN fraction in Figure 5.9, as expected.

To further verify our shock results, we consider the distribution of the [O III] λ 4363/[O III] λ 5007 ratio across the galaxy. The [O III] ratio is a temperature-sensitive line ratio, and increases in the line ratio indicate an increase in the electron temperature. Shocked gas can reach temperatures on the order of 10^6 K (for a fully-ionised plasma; e.g. [Dopita & Sutherland 2003](#)), compared to the NLR [O III] temperatures of $\sim 20,000$ K discussed in Section 5.4. Hence, an increase in the [O III] line ratio is expected to coincide with regions of high shock fractions in Figure 5.9.

The [O III] line ratio map is shown in Figure 5.16. Only spaxels which contain significant

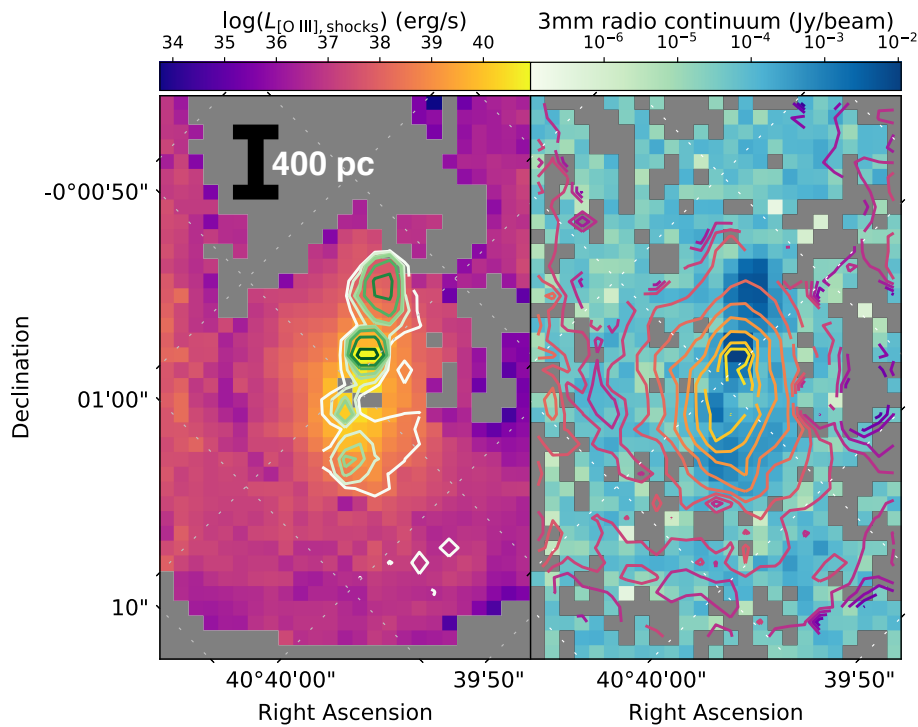


Figure 5.13 Maps of NGC 1068 showing the $[\text{O III}]\lambda 5007$ luminosity attributable to shocks in the left panel, and the 3mm radio continuum map from [García-Burillo et al. \(2017\)](#) on the right. Contours of each map are shown in the adjacent panel. Dashed lines represent grid lines of constant right ascension and declination.

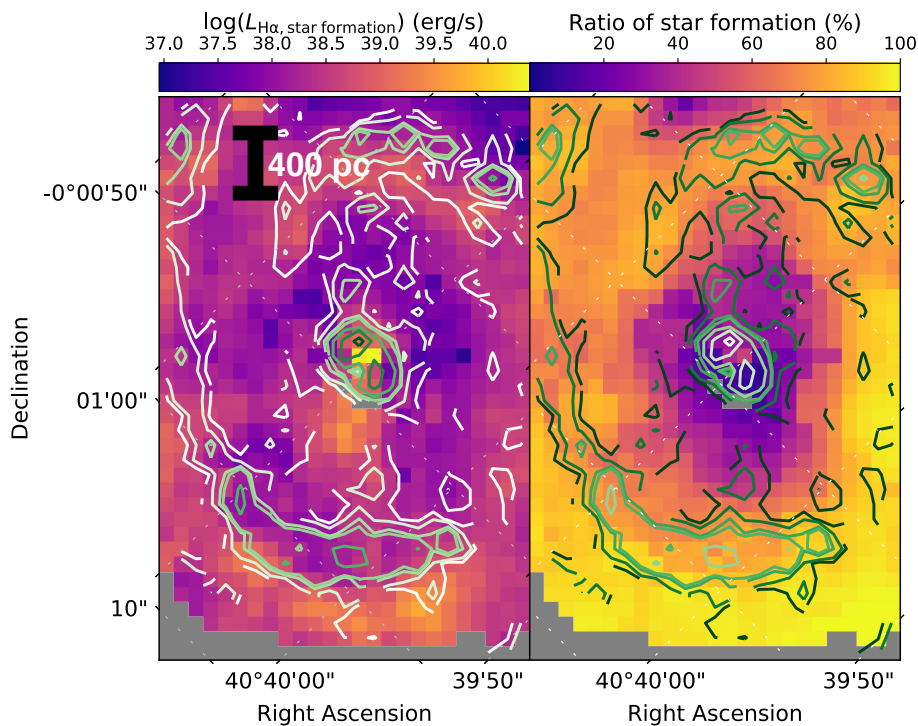


Figure 5.14 Maps of NGC 1068 showing the $\text{H}\alpha$ luminosity attributable to star formation in the left panel, and the star formation ratio map from [Figure 5.9](#) on the right. Identical contours of the $\text{CO}(3-2)$ flux from [García-Burillo et al. \(2014\)](#) are shown on both maps. Dashed lines represent grid lines of constant right ascension and declination.

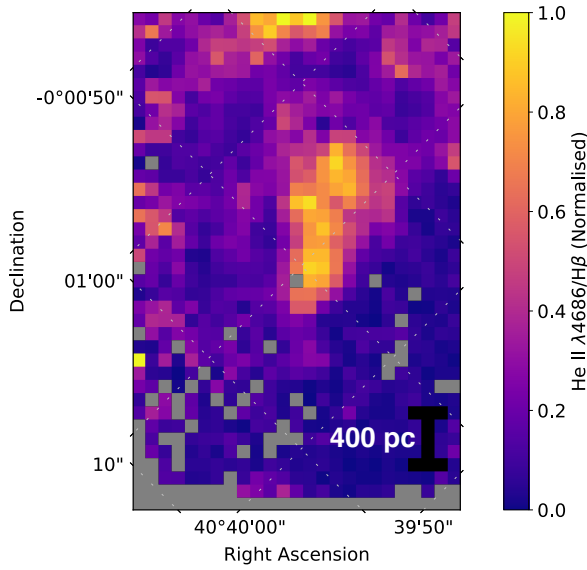


Figure 5.15 $\text{He II}/\text{H}\beta$ distribution map for NGC 1068. The $\text{He II}/\text{H}\beta$ ratio in each spaxel has been normalised to the maximum value ($\text{He II}/\text{H}\beta_{\text{max}} \sim 0.49$). The $\text{He II}/\text{H}\beta$ emission is seen to form a clean one-sided cone. Dashed lines represent grid lines of constant right ascension and declination.

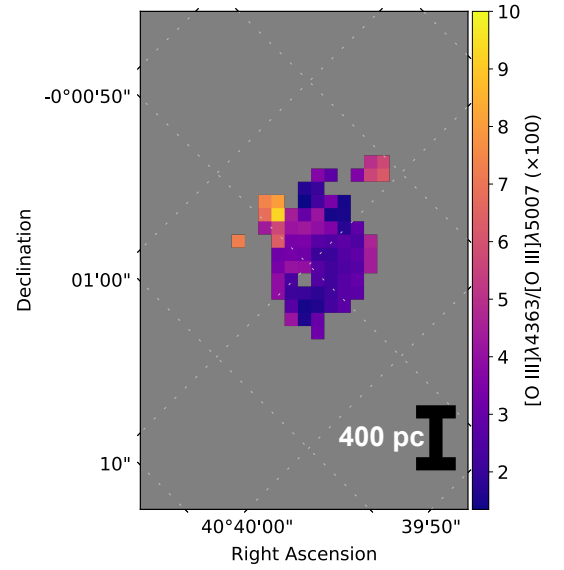


Figure 5.16 Distribution of the temperature-sensitive $[\text{O III}]\lambda 4363/[\text{O III}]\lambda 5007$ line ratio in NGC 1068. Only spaxels with significant detection of both the $[\text{O III}]\lambda 4363$ and $[\text{O III}]\lambda 5007$ emission lines are shown (signal-to-noise > 3). Significant spaxels are seen to align with spaxels containing high shock + AGN fractions in Figure 5.9. Dashed lines represent grid lines of constant right ascension and declination.

detection of both the $[\text{O III}]\lambda 4363$ and $[\text{O III}]\lambda 5007$ emission lines are shown in Figure 5.16, corresponding to a signal-to-noise greater than 3. Such spaxels are concentrated towards the centre, where the $[\text{O III}]$ luminosity is high, seen for example in Figures 5.12 and 5.13. The variation in the $[\text{O III}]$ ratio amongst included spaxels is low, and hence the values in Figure 5.16 have been enhanced $\times 100$ to better highlight the variation. Clearly, an increase in the $[\text{O III}]$ ratio is seen towards the top-left of the included spaxels. Similarly, the shock fraction map in Figure 5.9 also shows a slight increase in the shock fractions in spaxels towards the top-left of centre. Although, it should be noted that in this region, the AGN fractions of the spaxels also seen in Figure 5.9 are considerably high ($\sim 40\%$). Furthermore, photoionisation modelling with MAPPINGS shows that AGN photoionisation can lead to an increase in the $[\text{O III}]$ ratio, in the range from that expected from fast shocks of $\sim 0.1 - 0.01$ (e.g. Dopita et al. 2002b; Allen et al. 2008). The variation seen in the $[\text{O III}]$ ratio map is better aligned with the features in the shock + AGN map in Figure 5.11. Thus, we conclude that the distribution of the $[\text{O III}]$ ratio does not show sufficient variation to make confident assumptions about the shock-to-AGN ratio.

The shock-dominated regions are primarily located close to the nucleus of NGC 1068. Thus, possible mechanisms for their creation include NLR outflows, or the associated radio structures. We suggest that the shocks are the result of NLR outflows. The radio jet structure seen in *HST* imaging from Cecil et al. (2002) shows a radio structure at the nucleus of NGC 1068 with an extent of $\sim 1 - 2$ arcseconds. This is far smaller than the extent of the shock-dominated spaxels, which can extend beyond 10 arcseconds, seen in Figure 5.9. In addition, our Figure 5.1, and Figure 4 from D’Agostino et al. (2019b) show the extent of

the high- σ spaxels to be far beyond $\sim 1-2$ arcseconds. Hence, the small-scale radio jet must not be the dominant shock-production mechanism.

5.7. Conclusions and Future Work

We have demonstrated a new method to simultaneously separate line emission from gas ionised by star formation, shocks, and AGN in IFU data. Our 3D diagnostic diagram shows two clear mixing sequences, indicating star formation-AGN and star formation-shock mixing within a single galaxy. Using the information in these two clear mixing sequences, we have quantified the ratio of star formation-, shock-, and AGN-ionised line emission in each spaxel of the Seyfert galaxy NGC 1068.

We have shown that if shocks are not considered as an ionising source, then the relative contribution from an AGN to emission line fluxes may be greatly overestimated. The shock + AGN fractions for each emission line are very similar to the AGN fractions calculated assuming only a star formation-AGN mixing regime, using the method from [D’Agostino et al. \(2018\)](#). This indicates that shocked line emission mixes heavily with the AGN-ionised line emission. Including shocks as a possible ionising source also systematically lowers the star-forming fractions calculated in each emission line. If the flux of $H\alpha$ is to be used as a SFR indicator, it is recommended to separate as many ionising sources as possible.

We have compared our results to data in various wavelengths. These comparisons are summarised:

- (i) The luminosity distribution of AGN-ionised line emission closely resembles the 0.25-7.5 keV X-ray photon map from [Young et al. \(2001\)](#).
- (ii) The luminosity distribution of shock-ionised line emission is accurately aligned with the radio jets in NGC 1068, seen in the 3mm radio continuum map from [García-Burillo et al. \(2017\)](#).
- (iii) The luminosity distribution of star formation-ionised line emission closely traces the CO(3-2) molecular line flux from [García-Burillo et al. \(2014\)](#). The star-forming ring in NGC 1068 is host to the majority ($\sim 63\%$) of the CO(3-2) flux in the ALMA field-of-view ([García-Burillo et al. 2014](#)).
- (iv) Regions of AGN-dominated line emission correlate very accurately with regions of high $He\ II/H\beta$ ratios. $He\ II\lambda 4686$ is a high-ionisation line, and thus requires a hard radiation field (such as that from an AGN) to produce large emission line fluxes.
- (v) Regions of shock-dominated line emission show a slight correlation with regions of increased $[O\ III]\lambda 4363/[O\ III]\lambda 5007$, although the AGN contribution in these regions is also considerable. This indicates that the shock and AGN separation may need further advancements.

In a future publication, we aim to use our star formation-shock-AGN separation method to quantify the star formation, shock, and AGN fractions of merging galaxies, at various merger stages.

Acknowledgements

Parts of this research were conducted by the Australian Research Council Centre of Excellence for All Sky Astrophysics in 3 Dimensions (ASTRO 3D), through project number CE170100013.

Support for AMM is provided by NASA through Hubble Fellowship grant #HST-HF2-51377 awarded by the Space Telescope Science Institute, which is operated by the Association of Universities for Research in Astronomy, Inc., for NASA, under contract NAS5-26555.

The authors wish to also acknowledge the contribution from the reviewer, who facilitated great discussion amongst the co-authors and thus greatly improved the paper.

CHAPTER 6

Future Work

Surrender is an outcome far worse than defeat.

– Vegeta

This chapter presents an extension to the work described in Chapter 5. It should be noted that all results shown in this chapter are preliminary, and have not been previously published. In addition to showing the beginnings of future work in the field, this chapter also describes possible future directions of the content of this thesis. All new datacubes at varying spectral and spatial resolutions presented in this chapter were reduced from the raw data by the candidate.

6.1. The Effect of Resolution on the Star Formation-Shock-AGN Fraction

During Chapters 4 and 5, when introducing and describing the 3D diagnostic diagram, we used data from the S7. The S7 has high spatial resolution (pixel size ~ 81 pc in the case of NGC 1068) and spectral resolution ($R \sim 7000$ at $H\alpha$), and so was the perfect test case for the 3D diagram. The high spatial resolution provided accurate separation between multiple ionisation sources in the line emission, and the high spectral resolution allowed the observation of multiple velocity components in the emission lines. The combined high spatial and spectral resolution of the S7 resulted in a straightforward separation of line emission between star formation, shocks, and AGN on the 3D diagram.

However, many IFU surveys do not have spatial and/or spectral resolution as high as those of the S7. In the following sections, we show some early results on how changes in the spatial and spectral resolution of a datacube impacts the final star formation-shock-AGN fractions calculated using the 3D diagnostic diagram.

6.1.1. Spatial Resolution

To test the effect of changes in spatial resolution on the final star formation-shock-AGN fractions, we use the NGC 1068 datacube from the S7. The spaxels in the datacube are $1'' \times 1''$, corresponding to a spatial scale of ~ 81 pc. To simulate changes in spatial resolution, we also degrade the sampling in this datacube to pixel sizes of $2''$ and $3''$, corresponding to scales of ~ 159 and ~ 245 pc, respectively. We perform the same analysis as shown for the $1''$ datacube in Chapter 5 on both the $2''$ and $3''$ datacubes. The emission-line ratio values representing 100% star formation and 100% shock/AGN emission are kept constant for all datacubes. This is because lowering the spatial resolution leads to mixing of line emission from different sources in each spaxel (see Section 3.6 of this thesis). Hence, recalculating the extrema using the method described in Section 5.5.3 for each datacube at coarser resolutions will lead to basis points which do not truly represent 100% ionisation from star formation and shocks/AGN. The basis points calculated using the native $1''$ S7 datacube may also not truly represent emission 100% from star formation and shocks/AGN, because Section 3.6 of this thesis also shows that continually increasing the spatial resolution of the data will further separate out the various ionising sources. However, for the purposes of this work, $1''$ is the best resolution available. Hence, similarly to Chapter 5, we define the basis points calculated in Chapter 5 to be representative of 100% star formation and shock/AGN emission.

3D diagrams, colour-coded to the AGN, shock, and star formation fractions in each spaxel for the $2''$ (159 pc) datacube are shown in Figures 6.1, 6.2, and 6.3, respectively. Congruous 3D diagrams for the $3''$ (245 pc) datacube are shown in Figures 6.4, 6.5, and 6.6, respectively. From these diagrams, we calculate the final star formation, shock, and AGN fractions in each spaxel. Similarly to the analysis performed on the native $1''$ datacube in Chapter 5, each velocity component present in every spaxel contributes to the star formation-shock-AGN fraction in that given spaxel, weighted by the velocity component's total contribution to the $[\text{O III}]\lambda 5007$ flux. Maps of the galaxy showing the distribution of AGN, shock, and star formation fractions are shown in Figure 6.7. Maps for all three resolutions ($1''$, $2''$, and $3''$, corresponding to ~ 81 , 159, and 245 pc) are shown together in Figure 6.7 for comparison.

Table 6.1 shows the star formation, shock, and AGN contributions to the flux of several strong emission lines for all three tested spatial resolutions. Errors of roughly 10% should be assumed on the fractions in Table 6.1, as in the fractions presented in Table 5.2 in Chapter 5. Importantly, when the datacube is rebinned firstly to $2''$ resolution spaxels, the shock fractions of the strong emission lines increase sharply. This is a result of the rebinning process, which increases the signal-to-noise of low surface brightness features when adjacent spaxels are binned together, akin to the findings of Section 3.6.2 of this thesis. Both the star formation and AGN fractions of the strong lines experience a decrease, to compensate for the higher shock fractions. Once rebinned further to $3''$ spaxels however, the shock fractions of the strong lines begin to lower, while the AGN fractions of the strong lines all increase. At such coarse resolutions, the ionised gas emission from all three processes mixes thoroughly. Thus, the relative calculated contribution from star formation, shocks, and AGN to the ionisation tends towards equilibrium. Similarly to Section 3.6.2, these results suggest there is a window of spatial resolution where contribution from shocks to the total ionising emission appears highest.

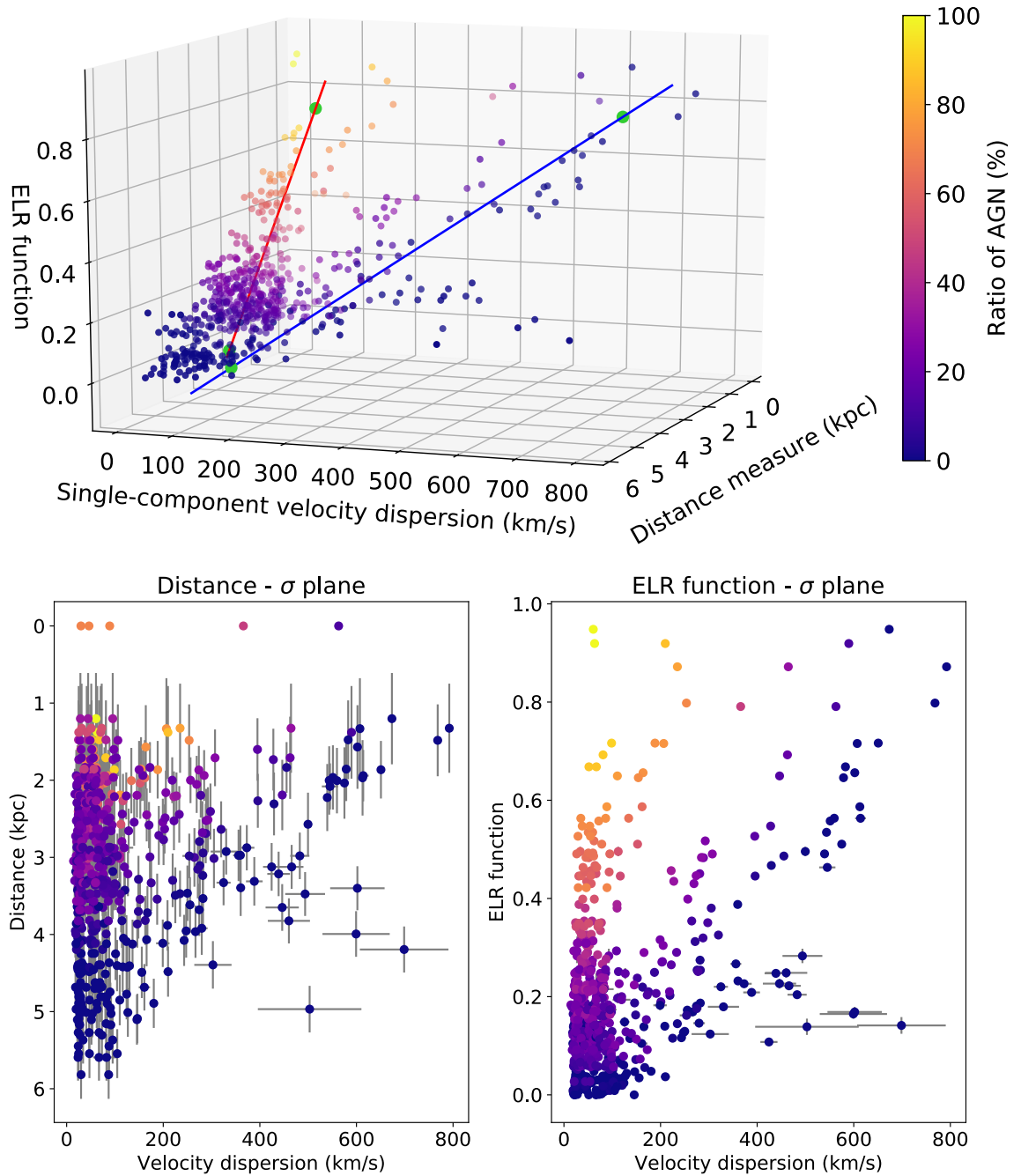


Figure 6.1 3D diagnostic diagram, showing the ratio of AGN in each spaxel of the $2''$ (~ 159 pc) resolution datacube for NGC 1068. Light green points represent the basis points for the ELR function. Bottom panels show the 2D projections in the distance- σ and ELR function- σ planes. Grey lines in the two panels represent the errors associated with each dimension. Errors are omitted from the 3D diagram for clarity.

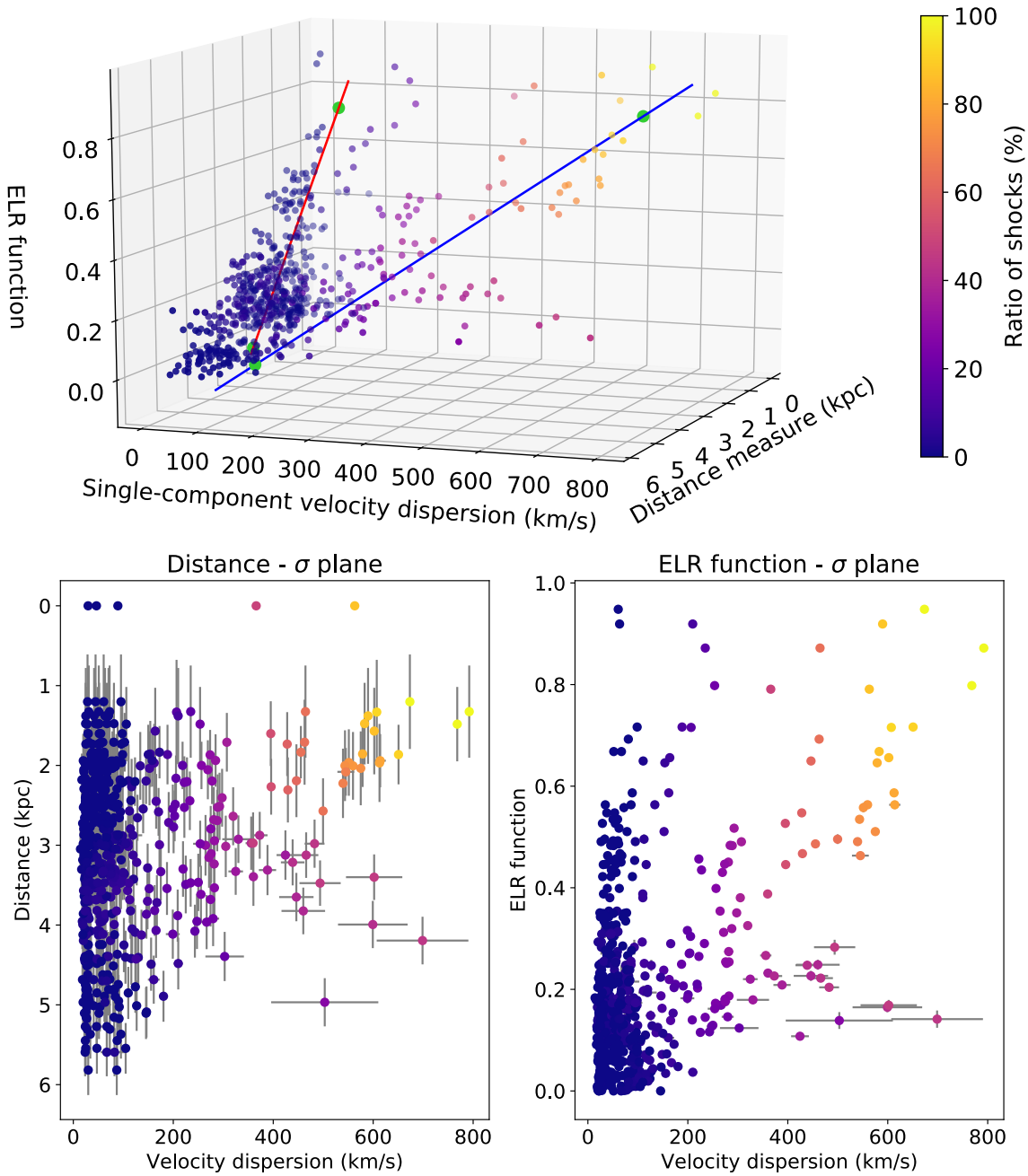


Figure 6.2 3D diagnostic diagram, showing the ratio of shocks in each spaxel of the 2'' (~159 pc) resolution datacube for NGC 1068. Light green points represent the basis points for the ELR function. Bottom panels show the 2D projections in the distance- σ and ELR function- σ planes. Grey lines in the two panels represent the errors associated with each dimension. Errors are omitted from the 3D diagram for clarity.

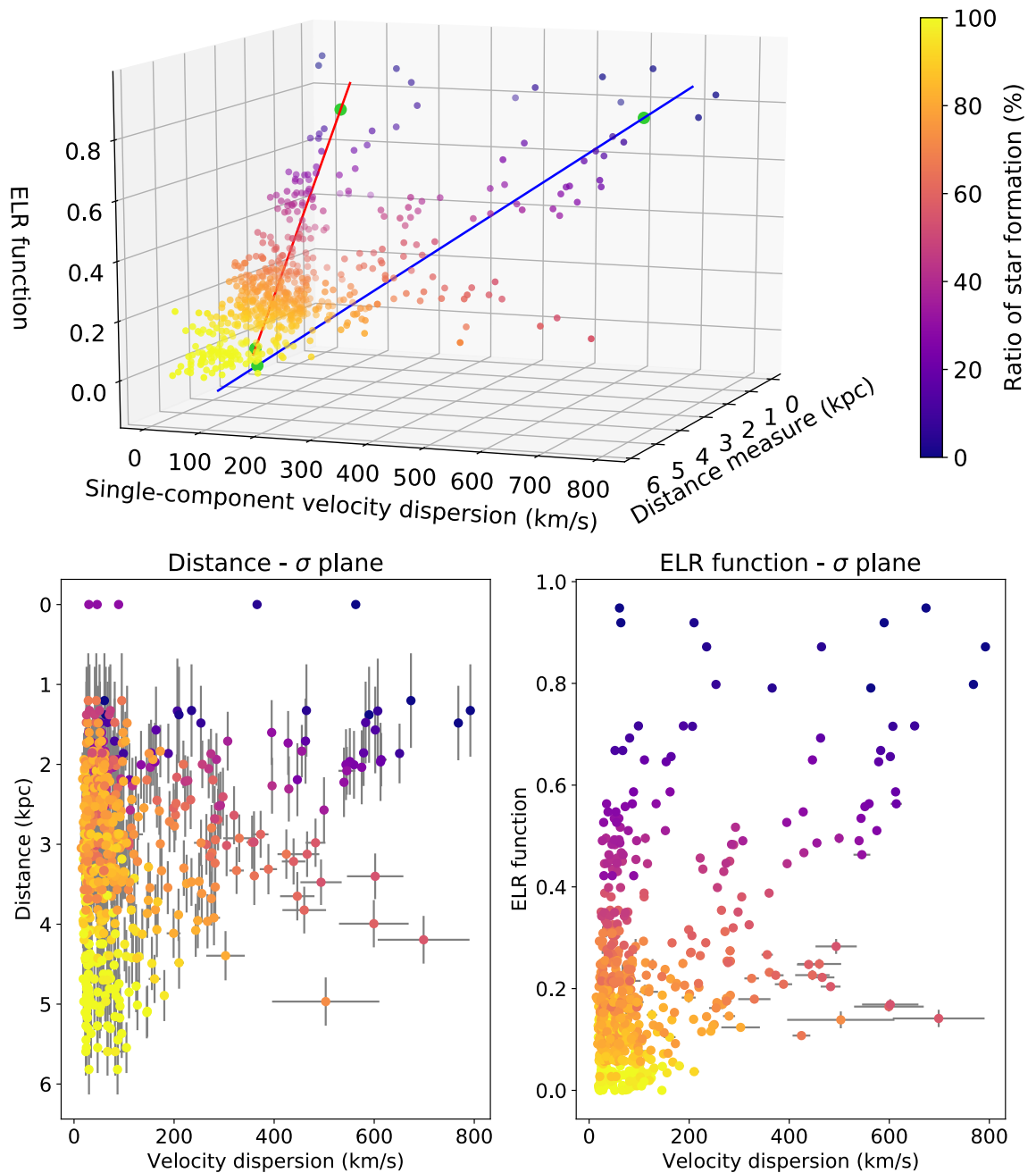


Figure 6.3 3D diagnostic diagram, showing the ratio of star formation in each spaxel of the 2'' (~ 159 pc) resolution datacube for NGC 1068. Light green points represent the basis points for the ELR function. Bottom panels show the 2D projections in the distance- σ and ELR function- σ planes. Grey lines in the two panels represent the errors associated with each dimension. Errors are omitted from the 3D diagram for clarity.

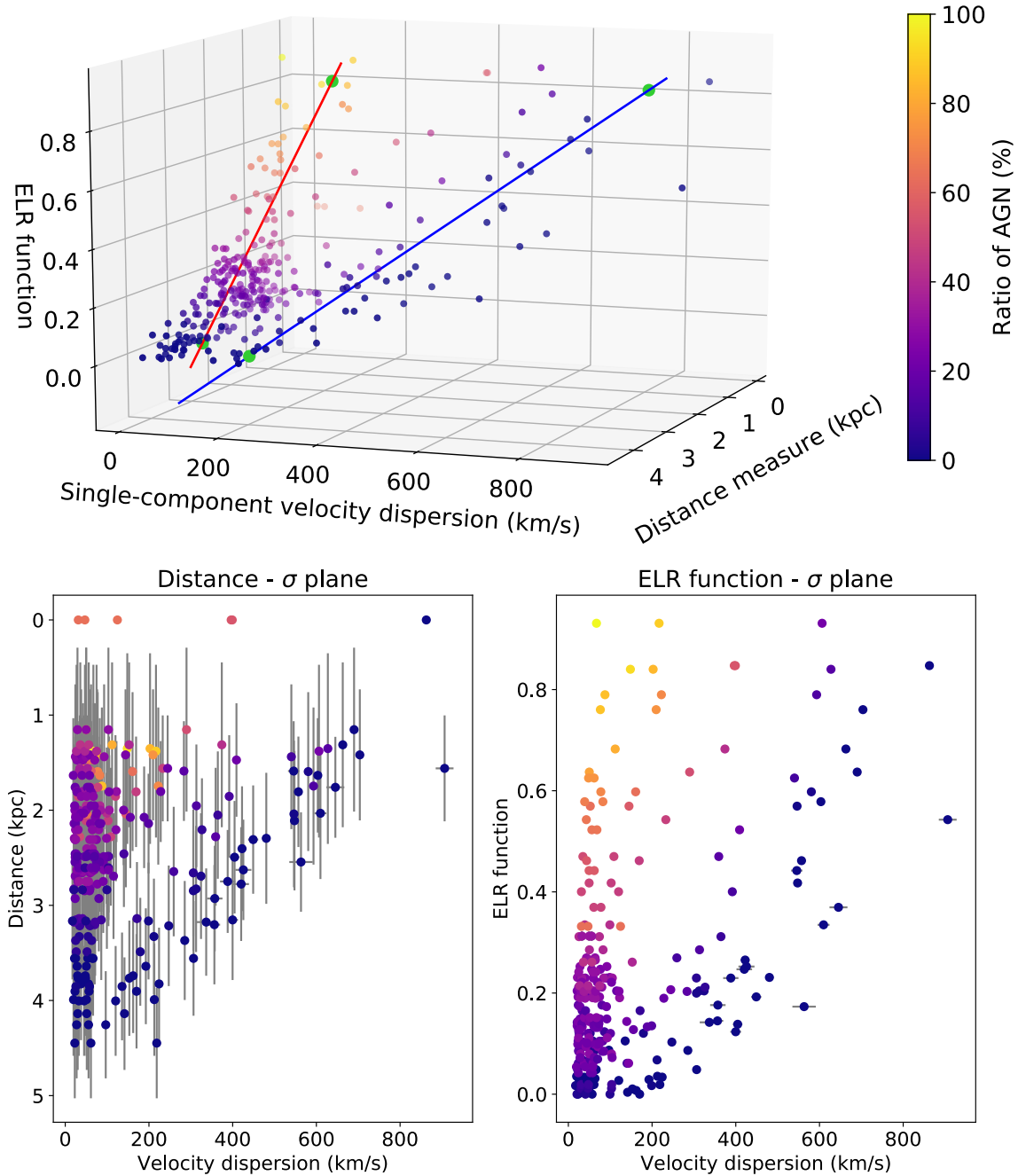


Figure 6.4 3D diagnostic diagram, showing the ratio of AGN in each spaxel of the 3'' (~ 245 pc) resolution database for NGC 1068. Light green points represent the basis points for the ELR function. Bottom panels show the 2D projections in the distance- σ and ELR function- σ planes. Grey lines in the two panels represent the errors associated with each dimension. Errors are omitted from the 3D diagram for clarity.

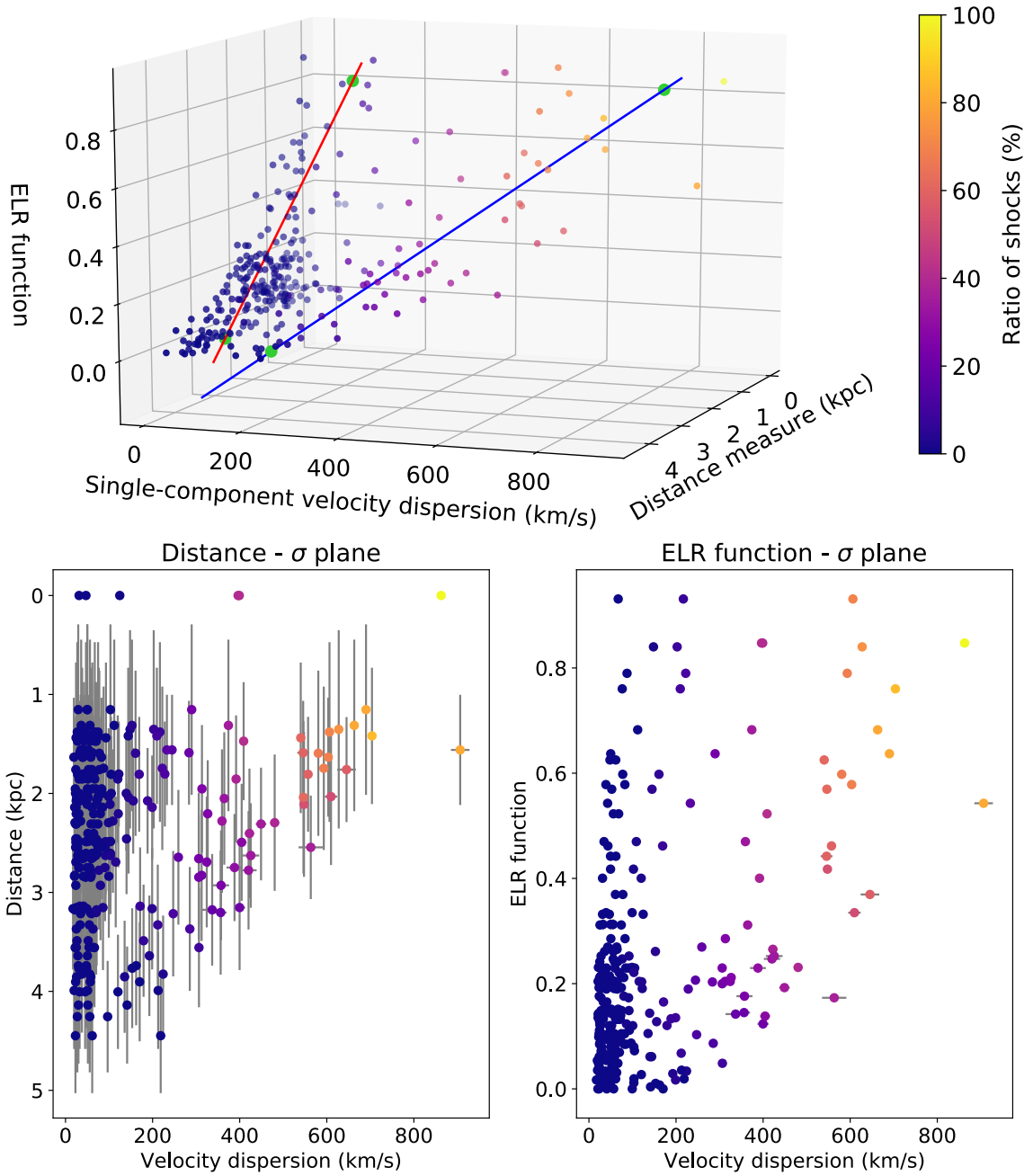


Figure 6.5 3D diagnostic diagram, showing the ratio of shocks in each spaxel of the 3'' (~ 245 pc) resolution datacube for NGC 1068. Light green points represent the basis points for the ELR function. Bottom panels show the 2D projections in the distance- σ and ELR function- σ planes. Grey lines in the two panels represent the errors associated with each dimension. Errors are omitted from the 3D diagram for clarity.

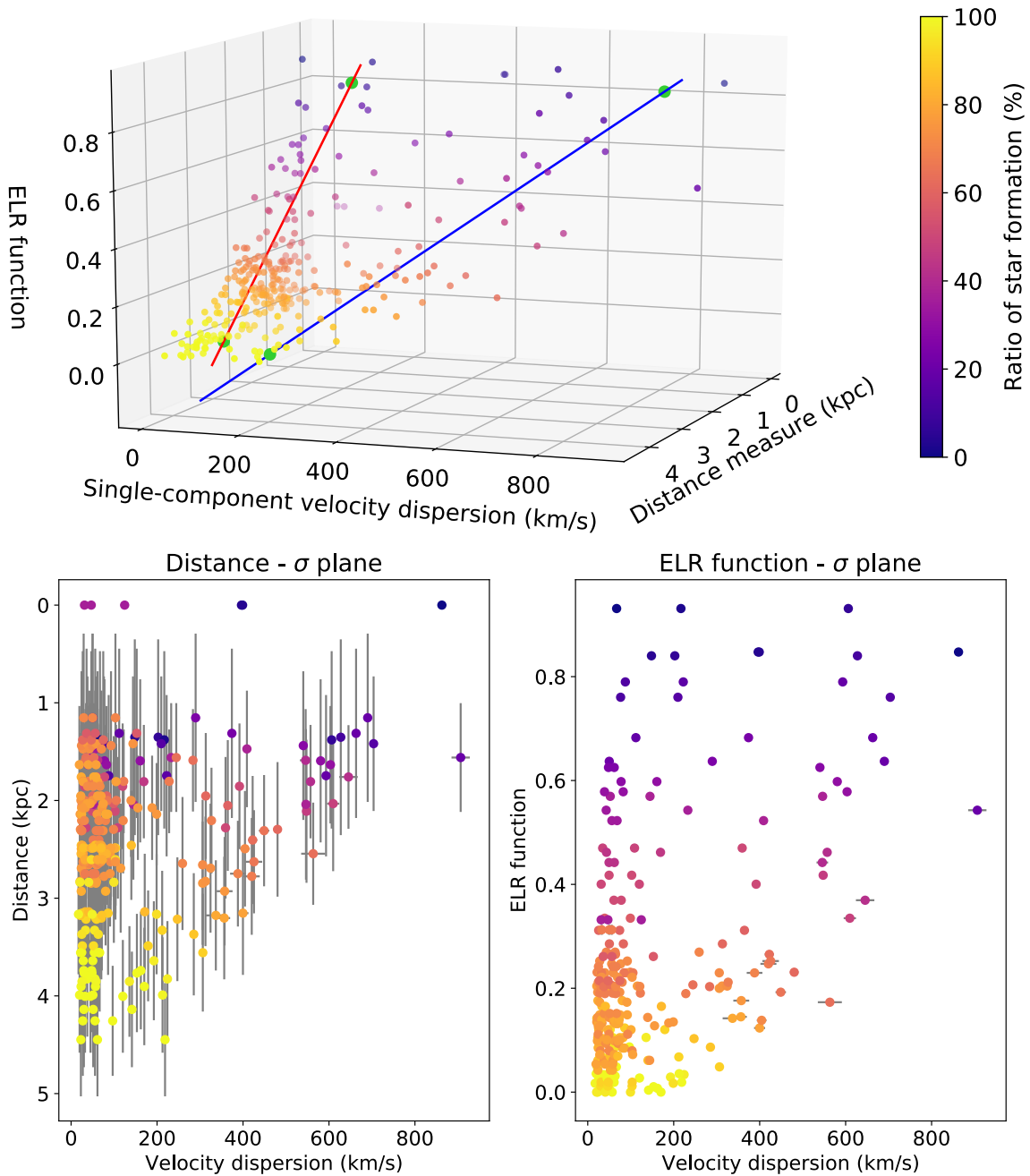


Figure 6.6 3D diagnostic diagram, showing the ratio of star formation in each spaxel of the 3'' (~245 pc) resolution datacube for NGC 1068. Light green points represent the basis points for the ELR function. Bottom panels show the 2D projections in the distance- σ and ELR function- σ planes. Grey lines in the two panels represent the errors associated with each dimension. Errors are omitted from the 3D diagram for clarity.

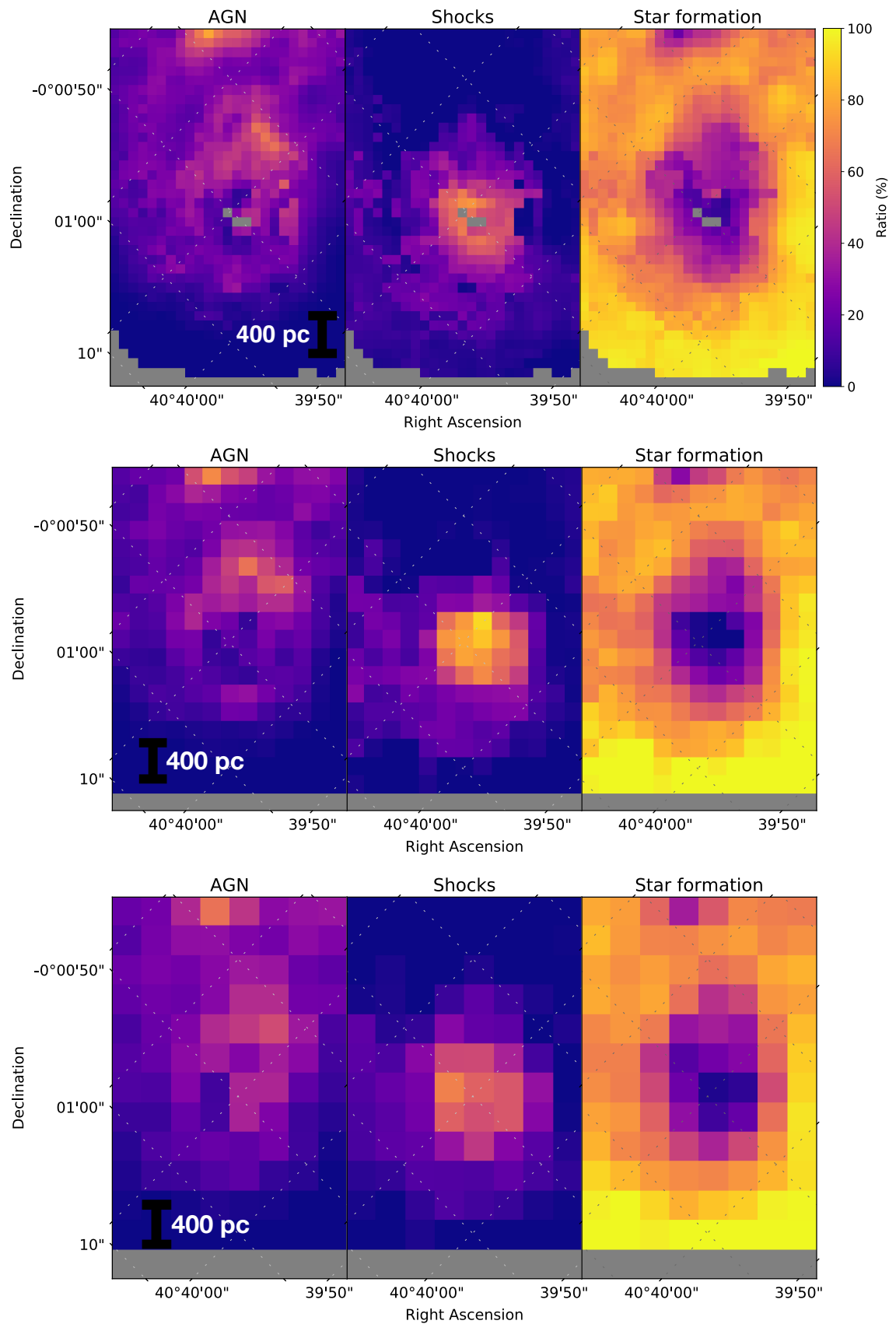


Figure 6.7 Maps of NGC 1068 showing the distribution of AGN, shock, and star formation fractions. Top row shows the native resolution (1'', ~81 pc) maps, middle row shows the 2'' (~159 pc) resolution maps, and bottom row shows the 3'' (~245 pc) resolution maps. Dashed lines represent grid lines of constant right ascension and declination.

NGC 1068, 1" (81 pc)			
Emission line	Star formation (%)	Shocks (%)	AGN (%)
H α	59.7	26.1	14.2
H β	60.0	26.0	14.1
[O II] $\lambda\lambda$ 3726,3729	35.4	41.2	23.3
[O III] λ 5007	36.1	46.1	17.8
[S II] $\lambda\lambda$ 6716,6731	39.4	39.1	21.5
[N II] λ 6584	43.9	37.6	18.5
2" (159 pc)			
H α	59.3	29.1	11.7
H β	59.6	28.8	11.6
[O II] $\lambda\lambda$ 3726,3729	25.6	57.8	16.6
[O III] λ 5007	24.6	60.4	15.0
[S II] $\lambda\lambda$ 6716,6731	29.1	55.8	15.1
[N II] λ 6584	35.9	50.2	13.9
3" (245 pc)			
H α	57.5	24.2	18.3
H β	57.8	24.0	18.2
[O II] $\lambda\lambda$ 3726,3729	27.4	44.1	28.5
[O III] λ 5007	25.7	46.9	27.5
[S II] $\lambda\lambda$ 6716,6731	29.9	42.7	27.4
[N II] λ 6584	35.5	40.0	24.5

Table 6.1 Star formation, shock, and AGN fractions for various strong emission lines in NGC 1068 within the S7 field-of-view, for various spatial resolutions. Errors on the star formation, shock, and AGN fractions is assumed to be $\sim 10\%$, similar to the fractions shown in Table 5.2.

6.1.2. Spectral Resolution

Similarly to testing the effects of spatial resolution, we use the S7 NGC 1068 datacube to test the effect spectral resolution has on the star formation-shock-AGN fraction. The native spectral resolution for S7, having been performed on the WiFeS (Dopita et al. 2007, 2010), is $R \sim 7000$ in the red. We construct two new datacubes for NGC 1068, by Gaussian smoothing the wavelength axis to lower spectral resolutions. The resolutions chosen were $R = 2000$, and $R = 800$, at H α . These spectral resolutions were chosen to closely resemble IFU data from other large-scale surveys, such as MaNGA (Bundy et al. 2015) at $R = 2000$, and TYPHOON (Seibert et al. in prep.) and CALIFA (particularly in the red; Sánchez et al. 2012a; Husemann et al. 2013a) at $R = 800$.

To construct the $R = 2000$ and $R = 800$ datacubes from the native $R \sim 7000$ datacube, we smooth the native datacube with a Gaussian kernel in the wavelength dimension. Considering that the convolution of two Gaussians is also a Gaussian, we convolve the native wavelength dimension with a Gaussian of standard deviation σ_c , such that

Target R	Corresponding σ_f (Å)	σ_c (Å)
2000	1.39	1.33
800	3.5	3.48

Table 6.2 Target spectral resolutions R , corresponding standard deviations at the target resolution σ_f , and standard deviations used for the convolution with the native S7 datacube σ_c for the new smoothed datacubes.

$$\sigma_i^2 + \sigma_c^2 = \sigma_f^2 \quad (6.1)$$

where σ_i is the initial standard deviation (the standard deviation of the native datacube in the wavelength dimension), σ_c is the standard deviation for the convolution, and σ_f is the final standard deviation.

Assuming a native resolution of $R = 7000$ at H α ($\lambda = 6563$), the spectral resolution at FWHM $\Delta\lambda$ of the S7 cube is

$$\begin{aligned} R &= \frac{\lambda}{\Delta\lambda} \\ \Rightarrow \Delta\lambda &= \frac{6563}{7000} \\ \therefore \Delta\lambda &\sim 0.95\text{Å at FWHM} \end{aligned}$$

Given there exist ~ 2.35 standard deviations per FWHM, it follows that the standard deviation of the native S7 datacube is $\sigma_i \sim 0.4\text{Å}$. Using this value of σ_i , and Equation 6.1, we calculate the necessary values of σ_c needed to smooth to lower spectral resolutions. We calculate σ_f in an identical way to the above calculation of σ_i , substituting R for our target resolutions. All values of R , σ_f , and σ_c are provided in Table 6.2.

3D diagrams showing the AGN, shock, and star formation fractions in each spaxel are shown in Figures 6.8, 6.9, and 6.10 for the $R = 2000$ datacube, and in Figures 6.11, 6.12, and 6.13 for the $R = 800$ datacube. Maps of the galaxy, showing the distribution of AGN, shock, and star formation fractions are shown in Figure 6.14. Maps for all resolutions ($R = 7000, 2000, 800$) are shown in Figure 6.14 for comparison. We also include 3D diagrams for both the $R = 2000$ and $R = 800$ datacubes with each spaxel colour-coded according to its component number in Figures 6.15 and 6.16, respectively. The 3D diagrams in Figures 6.15 and 6.16 show how the number of observed velocity components in each spaxel tends to decrease as the spectral resolution worsens.

Star formation, shock, and AGN fractions for various strong emission lines are shown in Table 6.3 for the three spectral resolutions studied. While the shock fractions are all systematically higher, and the AGN fractions are systematically lower between spectral resolutions of $R = 7000$ and $R = 2000$, the difference is too small to be significant. However, such differences are significant at a resolution of $R = 800$. At this resolution, the shock and AGN fractions differ from those at $R = 2000$ by 10 – 20%. Star formation fractions display no significant difference across all spectral resolutions. The large increase and decrease in shock and AGN fractions at lower spectral resolutions, respectively, coincides with the diminishing detection of multiple velocity components in the data. At a spectral resolution

NGC 1068, $R \sim 7000$			
Emission line	Star formation (%)	Shocks (%)	AGN (%)
H α	59.7	26.1	14.2
H β	60.0	26.0	14.1
[O II] $\lambda\lambda 3726, 3729$	35.4	41.2	23.3
[O III] $\lambda 5007$	36.1	46.1	17.8
[S II] $\lambda\lambda 6716, 6731$	39.4	39.1	21.5
[N II] $\lambda 6584$	43.9	37.6	18.5
$R \sim 2000$			
H α	56.4	29.5	14.1
H β	56.6	29.4	14.0
[O II] $\lambda\lambda 3726, 3729$	32.9	45.7	21.5
[O III] $\lambda 5007$	28.3	55.3	16.4
[S II] $\lambda\lambda 6716, 6731$	35.4	45.5	19.1
[N II] $\lambda 6584$	38.1	44.5	17.4
$R \sim 800$			
H α	51.8	40.6	7.6
H β	52.0	40.5	7.6
[O II] $\lambda\lambda 3726, 3729$	37.4	53.5	9.0
[O III] $\lambda 5007$	25.7	71.6	5.2
[S II] $\lambda\lambda 6716, 6731$	37.7	54.8	7.4
[N II] $\lambda 6584$	35.1	58.7	6.2

Table 6.3 Star formation, shock, and AGN fractions for various strong emission lines in NGC 1068 within the S7 field-of-view, for various spectral resolutions. Errors on the star formation, shock, and AGN fractions is assumed to be $\sim 10\%$, similar to the fractions shown in Table 5.2.

of $R = 800$, the amount of observed second components in the data is very low, and third components are non-existent. This is because if the spectral resolution is sufficiently low to not detect multiple components in the emission lines, the emission line profile will be fit with just a single component Gaussian. The result of this is that the single, first component is far broader than the first component of an emission line detected at a higher spectral resolution, and hence has a larger measurable velocity dispersion. It follows then that the first component, with a high velocity dispersion, is found along the star formation-shock sequence, and the star formation-AGN sequence is increasingly vacated. This will inevitably lead to shocks appearing to contribute more to the total ionisation in a given spaxel.

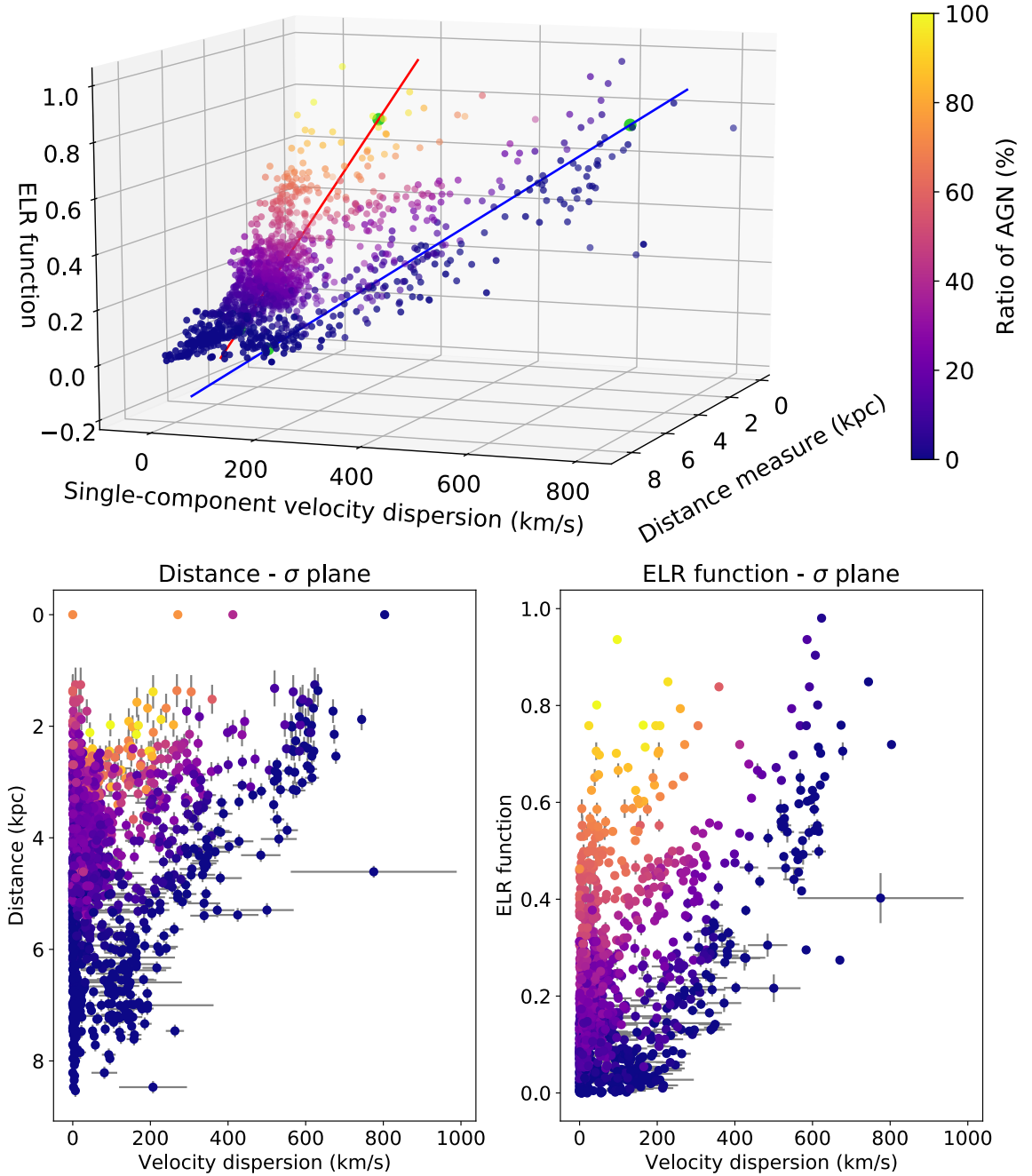


Figure 6.8 3D diagnostic diagram, showing the ratio of AGN in each spaxel of the $R \sim 2000$ resolution datacube for NGC 1068. Light green points represent the basis points for the ELR function. Bottom panels show the 2D projections in the distance- σ and ELR function- σ planes. Grey lines in the two panels represent the errors associated with each dimension. Errors are omitted from the 3D diagram for clarity.

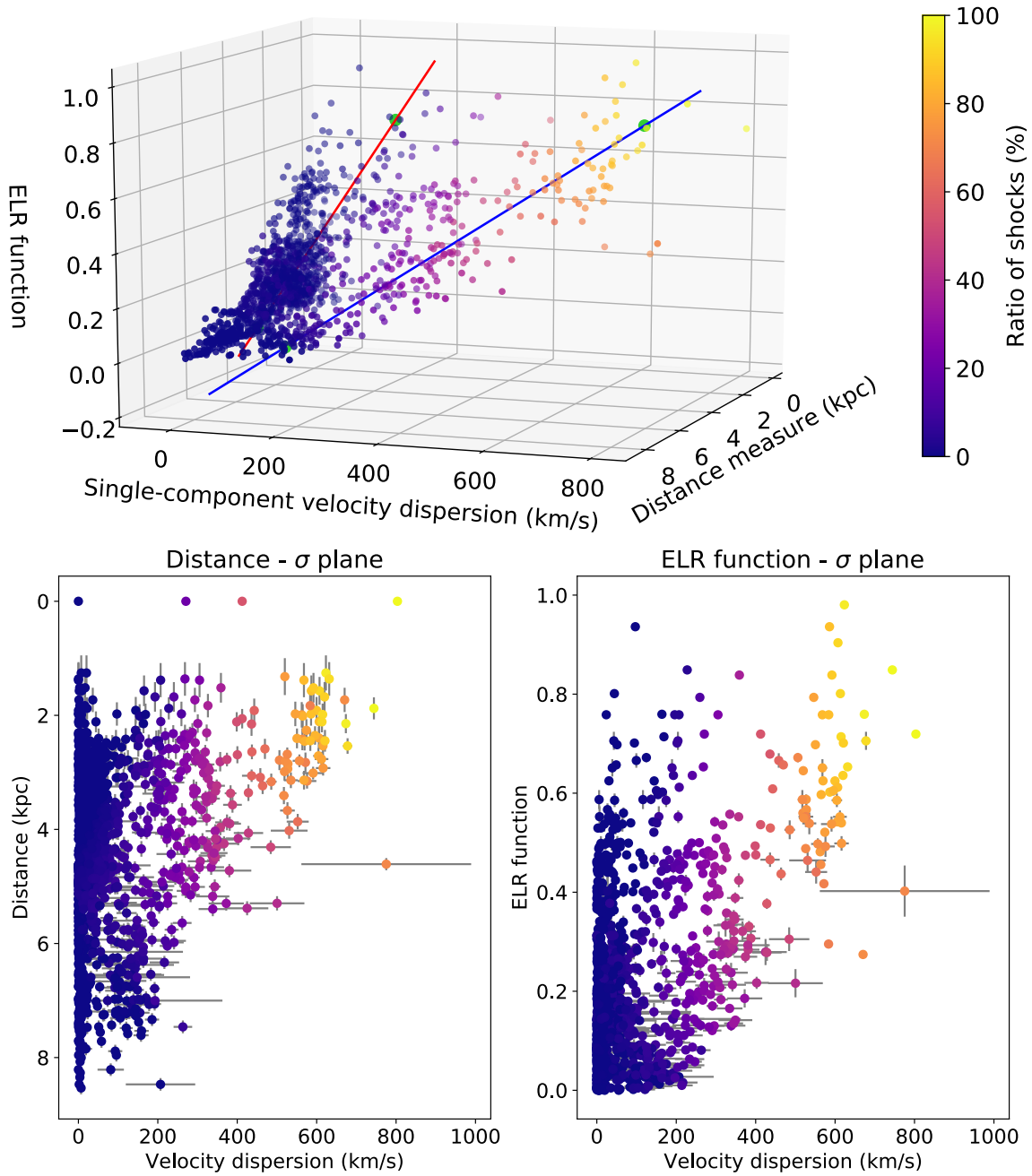


Figure 6.9 3D diagnostic diagram, showing the ratio of shocks in each spaxel of the $R \sim 2000$ resolution datacube for NGC 1068. Light green points represent the basis points for the ELR function. Bottom panels show the 2D projections in the distance- σ and ELR function- σ planes. Grey lines in the two panels represent the errors associated with each dimension. Errors are omitted from the 3D diagram for clarity.

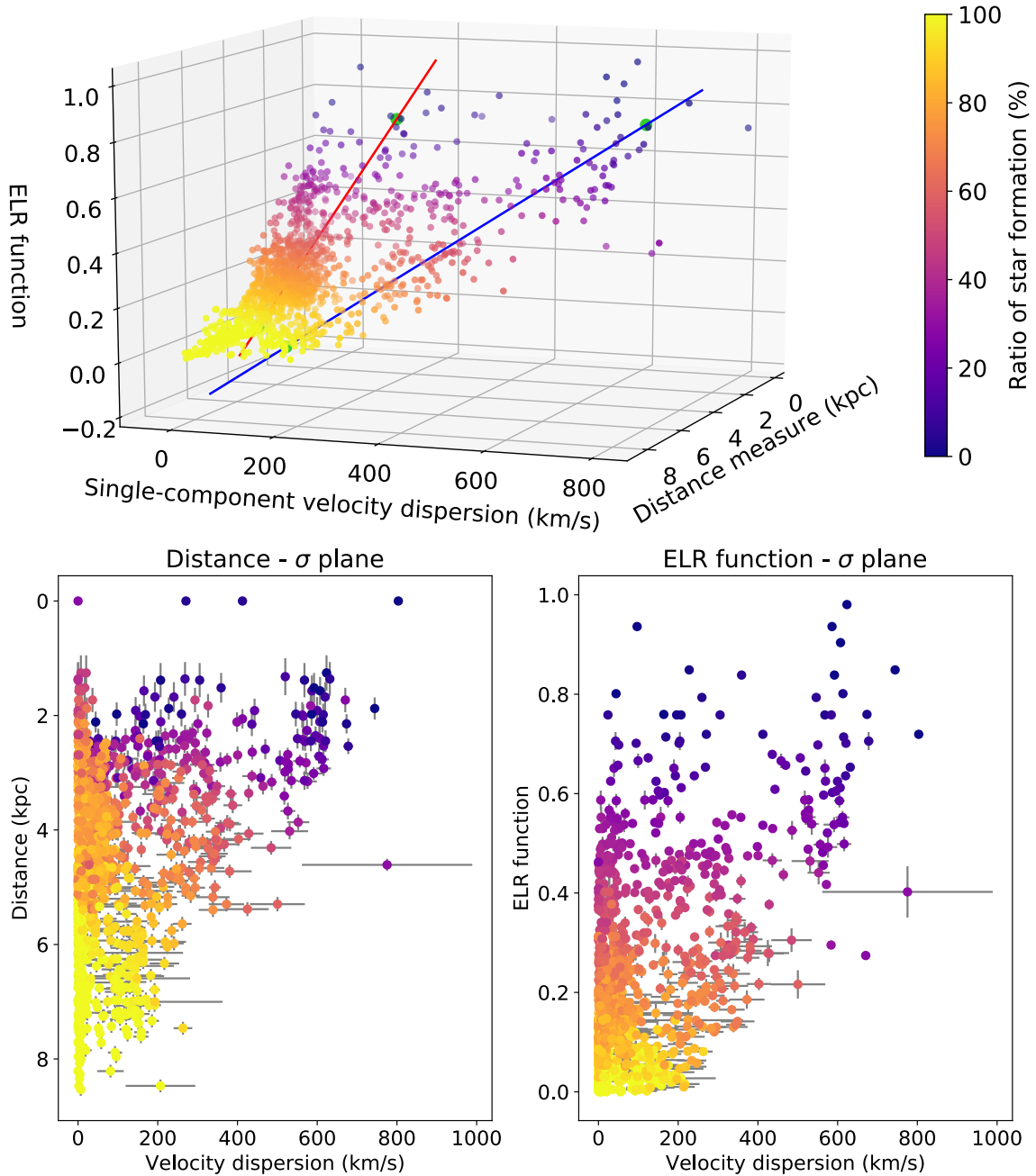


Figure 6.10 3D diagnostic diagram, showing the ratio of star formation in each spaxel of the $R \sim 2000$ resolution datacube for NGC 1068. Light green points represent the basis points for the ELR function. Bottom panels show the 2D projections in the distance- σ and ELR function- σ planes. Grey lines in the two panels represent the errors associated with each dimension. Errors are omitted from the 3D diagram for clarity.

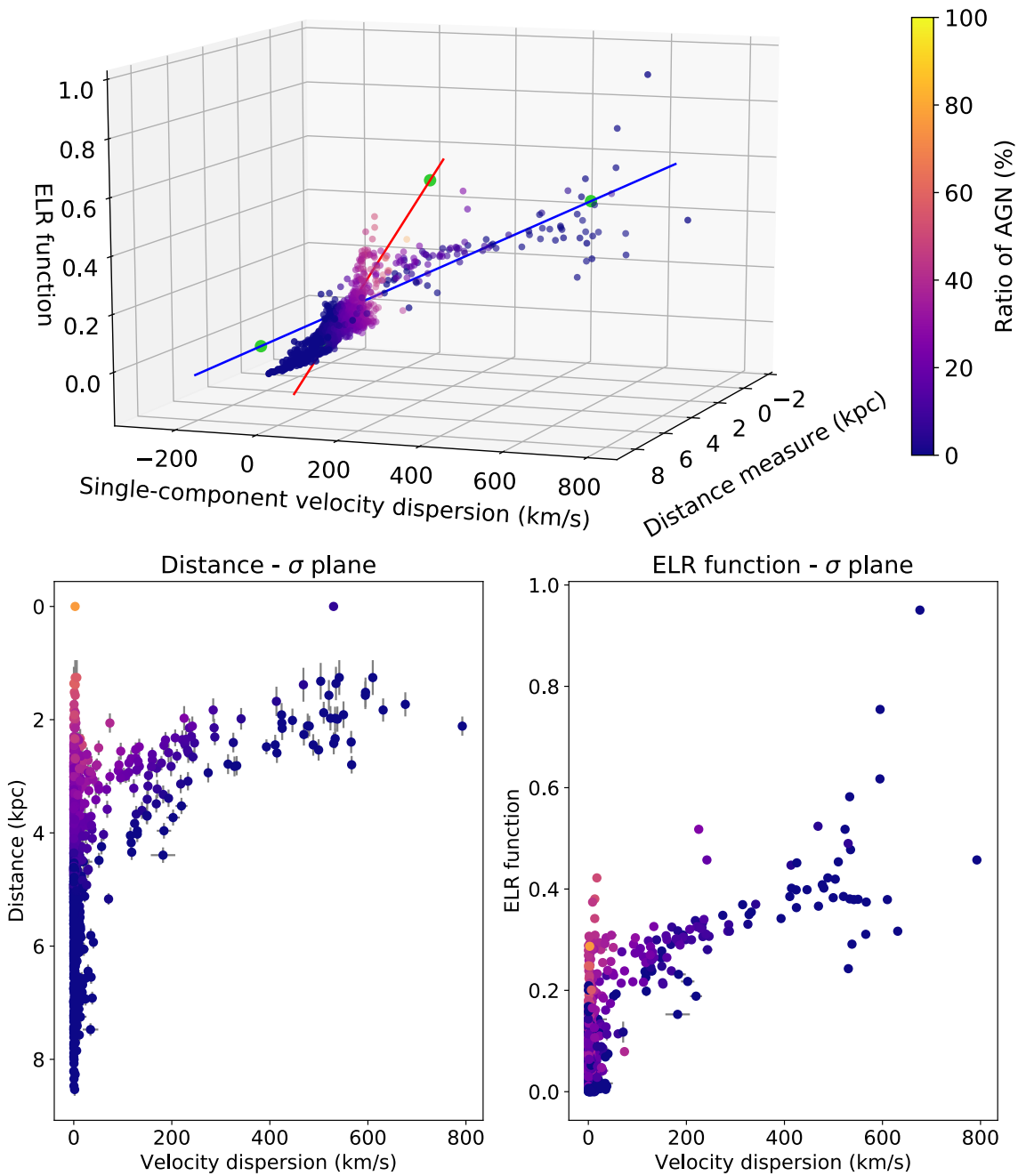


Figure 6.11 3D diagnostic diagram, showing the ratio of AGN in each spaxel of the $R \sim 800$ resolution datacube for NGC 1068. Light green points represent the basis points for the ELR function. Bottom panels show the 2D projections in the distance- σ and ELR function- σ planes. Grey lines in the two panels represent the errors associated with each dimension. Errors are omitted from the 3D diagram for clarity.

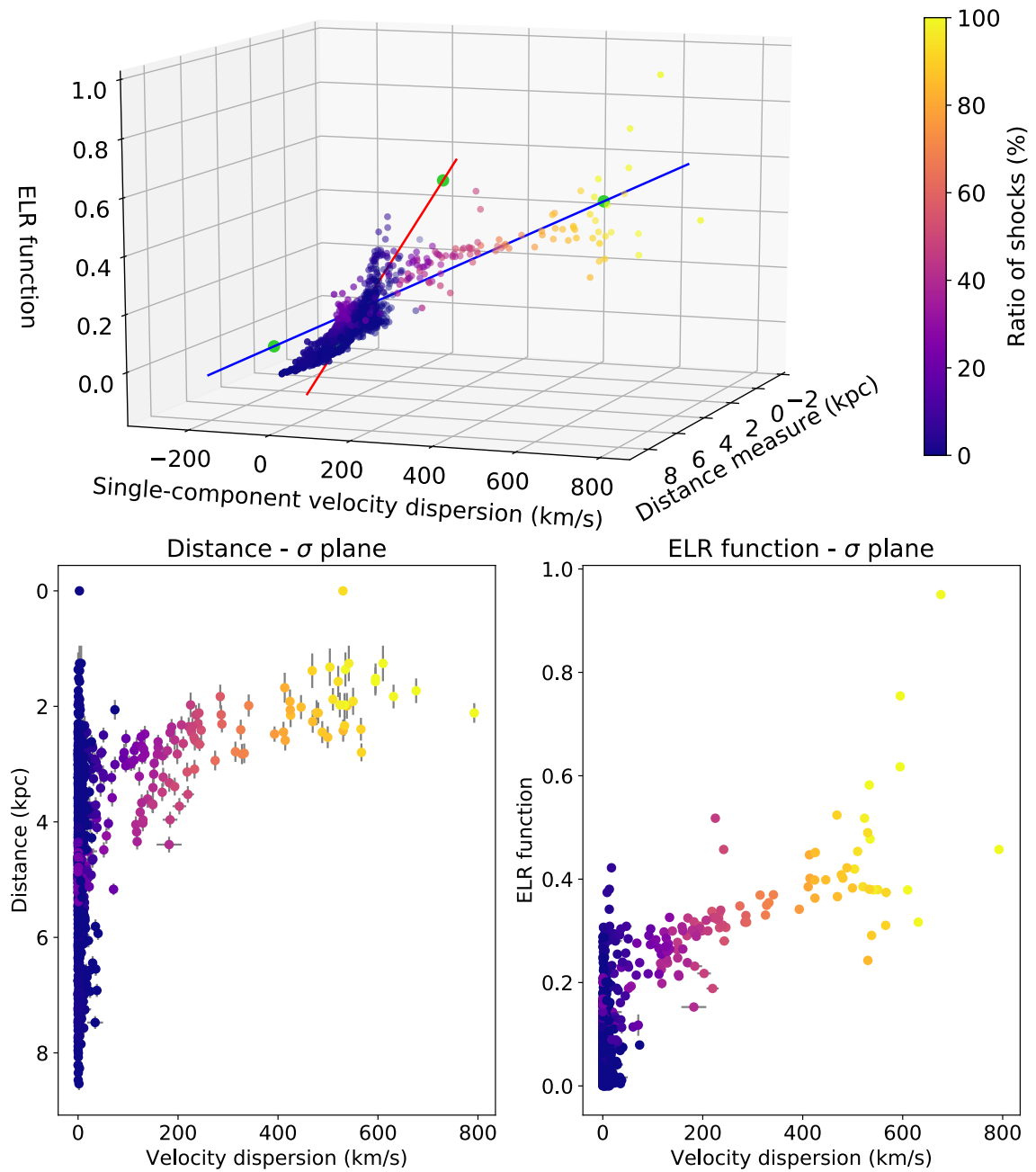


Figure 6.12 3D diagnostic diagram, showing the ratio of shocks in each spaxel of the $R \sim 800$ resolution datacube for NGC 1068. Light green points represent the basis points for the ELR function. Bottom panels show the 2D projections in the distance- σ and ELR function- σ planes. Grey lines in the two panels represent the errors associated with each dimension. Errors are omitted from the 3D diagram for clarity.

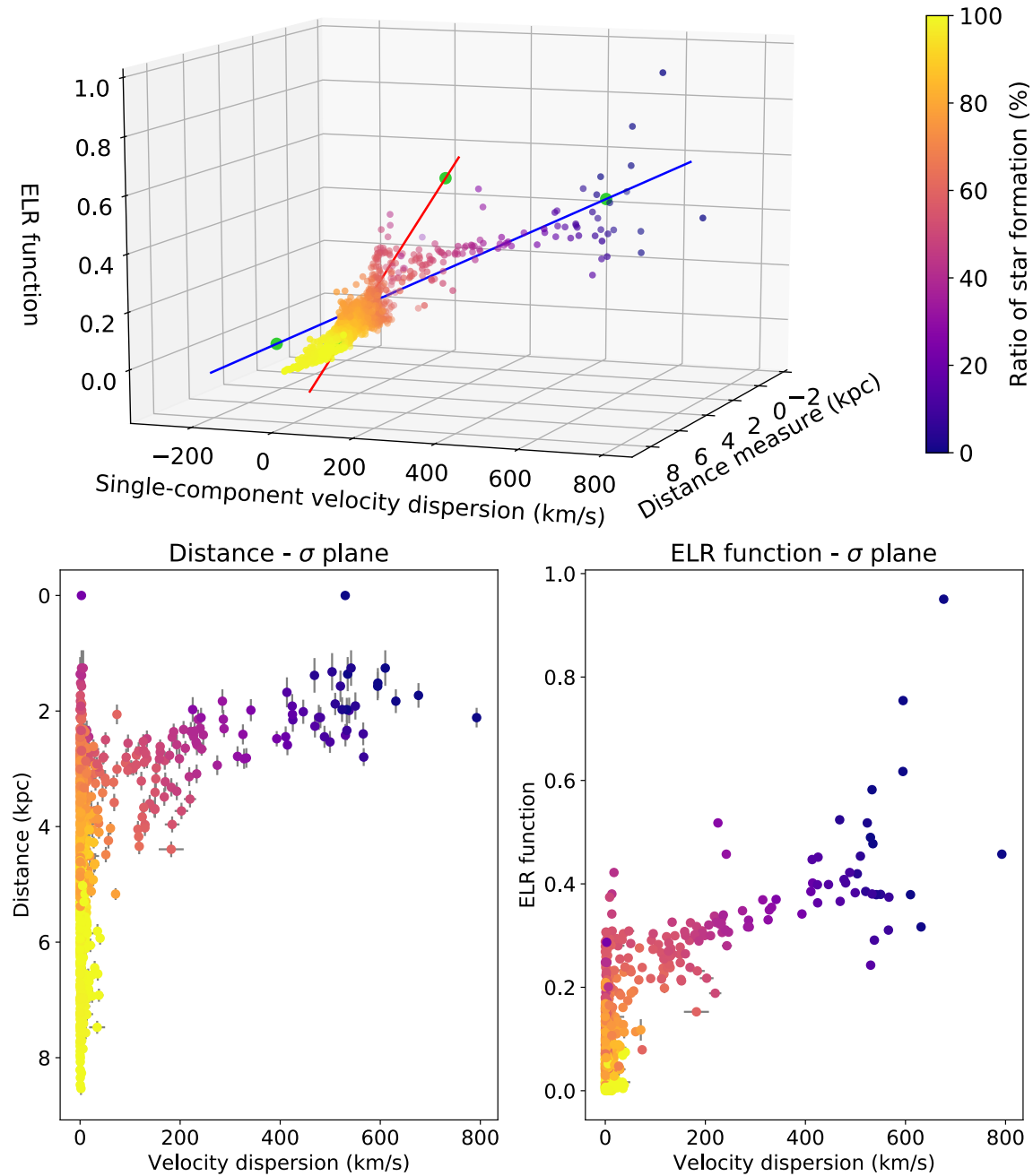


Figure 6.13 3D diagnostic diagram, showing the ratio of star formation in each spaxel of the $R \sim 800$ resolution datacube for NGC 1068. Light green points represent the basis points for the ELR function. Bottom panels show the 2D projections in the distance- σ and ELR function- σ planes. Grey lines in the two panels represent the errors associated with each dimension. Errors are omitted from the 3D diagram for clarity.

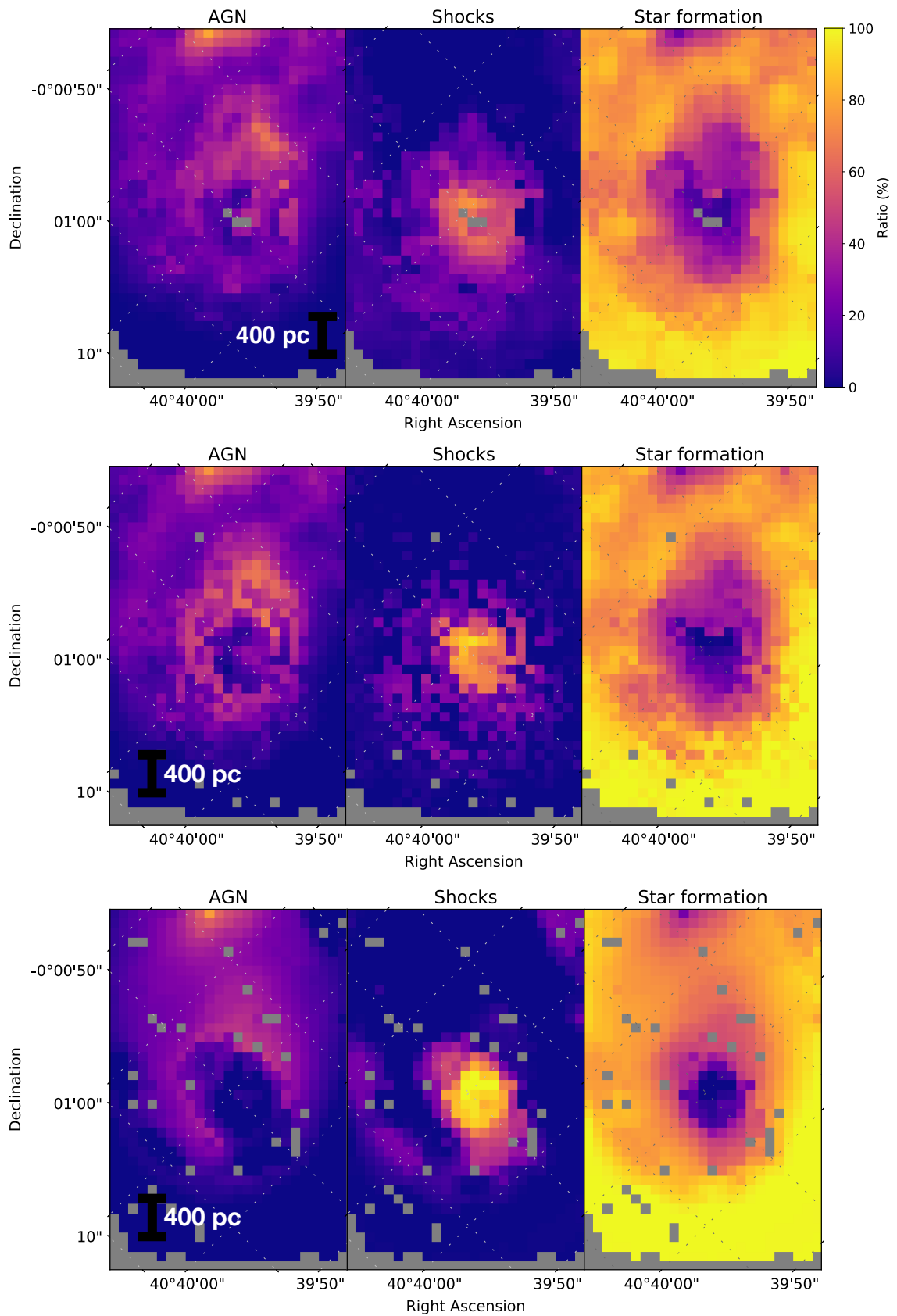


Figure 6.14 Maps of NGC 1068 showing the distribution of AGN, shock, and star formation fractions. Top row shows the native resolution ($R \sim 7000$) maps, middle row shows the $R \sim 2000$ resolution maps, and bottom row shows the $R \sim 800$ resolution maps. Dashed lines represent grid lines of constant right ascension and declination.

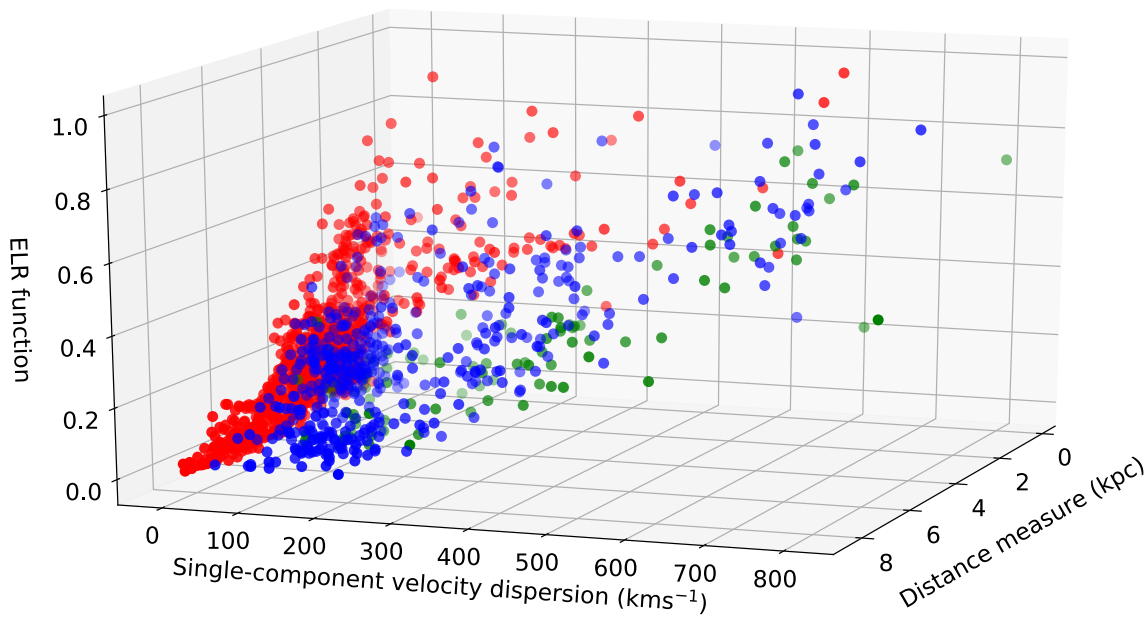


Figure 6.15 3D diagram of the $R = 2000$ datacube for NGC 1068. The colour of each spaxel is defined by its component number. Red spaxels are first components, blue spaxels are second components, and green spaxels are third components.

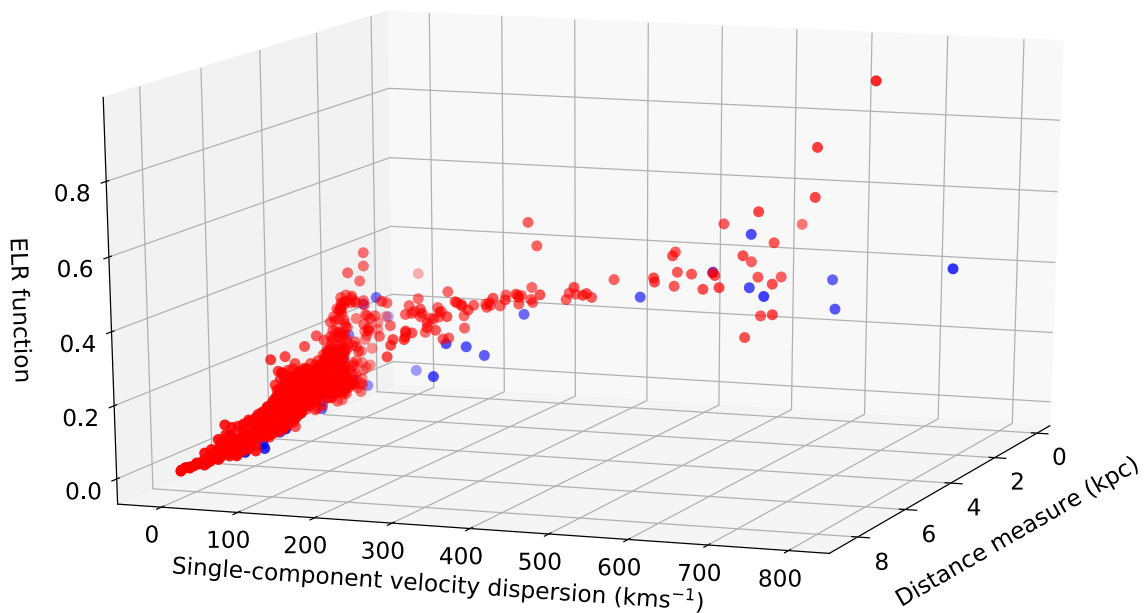


Figure 6.16 3D diagram of the $R = 800$ datacube for NGC 1068. The colour of each spaxel is defined by its component number. Red spaxels are first components, blue spaxels are second components, and green spaxels are third components.

6.2. Future Directions

There are several avenues of further exploration for the work presented in this thesis. Firstly, the previous section of the effect of spatial and spectral resolution on the star formation-shock-AGN fraction is unfinished. In particular, the results of the previous section show an increase in shock contribution at a spatial resolution of $2''$, when compared to the results at resolutions of $1''$ and $3''$. A logical extension of this result would be to determine the exact cause and nature of this increase in shocks at intermediate spatial resolutions. Furthermore, it would be interesting to determine whether or not there exists a spatial resolution beyond $3''$ spaxels, where the mixing between all ionising sources is such that the relative contribution from each source becomes equal. Such a resolution could be deemed a limit on the spatial resolution required to perform science of mixing between ionising sources.

Secondly, the three-dimensional diagram presented and used in this thesis is not necessarily optimal. We developed a diagnostic that was suitable for the work we undertook, however improvements to the diagram are possible. The ELR function, for example, only uses information from the BPT emission-line ratios. [Veilleux & Osterbrock \(1987\)](#) however, popularised several emission-line ratio diagnostic diagrams, all of which are commonly used when attempting to separate emission from various ionising sources. Substituting a different line ratio into the ELR function (e.g. $[\text{S II}]/\text{H}\alpha$ for $[\text{N II}]/\text{H}\alpha$), or combining more than just two emission line ratios (e.g. some combination of $[\text{O III}]/\text{H}\beta$, $[\text{N II}]/\text{H}\alpha$, $[\text{S II}]/\text{H}\alpha$, and $[\text{O I}]/\text{H}\alpha$) could produce interesting results. A slight issue with the diagnostic diagram shown in Chapter 4 and used in Chapter 5 was in the separation of shocked emission and emission from an AGN. The results of Chapter 5 provide a great advancement to the problem, yet there is still room for improvement. More information in the ELR function could potentially produce better results.

Lastly, the 3D diagram is ready to be applied to a large-scale survey. In particular, the GOALS/S7 sample used by [Rich et al. \(2014\)](#) is an ideal dataset, because using the 3D diagram could be considered an extension of the work performed by [Rich et al. \(2014\)](#). The work done by [Rich et al. \(2014\)](#) shows the calculation of shock fractions as a function of galaxy merger stage, however the contribution from AGNs was considerable. Using the 3D diagram, contributions to the line emission from star formation, shocks, and AGN can be calculated as a function of galaxy merger stage.

CHAPTER 7

Conclusions

My family is my life, and everything else comes second as far as what's important to me.

– Michael Imperioli

This chapter contains summarised conclusions of preceding chapters, as well as a discussion on the possible directions of future work in the field.

7.1. H II Region Modelling

In the photoionisation modelling of H II regions, many different versions of input parameters and models exist. Such variations in the models or parameter values will impact the final spectrum produced from the H II region. In Chapter 2 (published by [D'Agostino et al. 2019a](#)), we study and compare the effect of various model parameters on the resultant emission-line ratios on the BPT diagram.

We first consider the parameters that constitute the ionising spectrum from the stellar cluster. In particular, we study various models and values for the stellar atmospheres, stellar evolutionary tracks, the star-formation history, cluster age, and stellar population type (single-star or binary). Furthermore, we perform the same analysis using different photoionisation modelling codes. The results show that differences between the models that create the stellar ionising spectrum result in an average error of ~ 0.1 dex in the $[\text{O III}]/\text{H}\beta$ and $[\text{N II}]/\text{H}\alpha$ ratios.

Similarly, we study the systematic effects of varying the values intrinsic to the H II region. Namely, we vary the value of the H II region pressure, and the H II region boundedness (radiation-bounded or density-bounded). Our results show that galaxies at high redshift, which have systematically-higher BPT line ratios, are better explained by H II region models with higher pressure values. Additionally, density-bounded H II region models provide a better fit for low-mass galaxies, due to the higher fraction of escaping photons from the low-mass nebulae.

7.2. Star Formation-AGN Mixing with TYPHOON/PrISM

Previous work on quantifying the ratio between line emission resulting from star formation and AGN was calculated on an empirical basis (e.g. [Davies et al. 2014a,b](#)). In Chapter 3 (published by [D’Agostino et al. 2018](#)), we present a new method of performing star formation-AGN mixing calculations on the BPT diagram, with the aid of theoretical photoionisation models. The models remove a large ambiguity in the position of the basis points (representing 100% star formation and AGN), by defining the position of the basis points by metallicity on both the H II region and NLR models.

Data from the TYPHOON/PrISM survey is used in this work: specifically the AGN systems NGC 1365 and NGC 1068. These data are optimal, because the very large field-of-view allows the observation of the extended star-forming sequence towards the edge of the galaxy, particularly in NGC 1365. The large field-of-view is also beneficial for NGC 1068, because the extended [O III] λ 5007 outflow is also visible in its entirety.

In addition to demonstrating a new theoretical calculation of the AGN fraction in each spaxel, we also study the effect of spatial resolution on the AGN fraction. The TYPHOON/PrISM datacubes are rebinned to coarser spatial resolutions, and the same AGN fraction calculations performed on each new datacube. The results show that lower spatial resolutions will lead to an overestimate of the contribution to line emission from the AGN. Furthermore, AGN contribution is shown to increase in radius with lower resolutions. These findings suggest that data with a spatial resolution as high as possible should be obtained in order to study the effects of AGN activity accurately. Finally, we find an increased detection of low-surface-brightness features (such as shocks or diffuse ionised gas) at lower resolutions.

7.3. The Three-Dimensional Diagnostic Diagram

The results of Chapter 3 suggest that shocks are prevalent in the line emission observed from an AGN system. However, conventional methods used to study star formation-AGN mixing (such as the BPT diagram, and other diagnostic diagrams presented by [Veilleux & Osterbrock 1987](#)) fail to distinguish between emission from shocks and AGN. In Chapter 4 (published by [D’Agostino et al. 2019b](#)), we present a new three-dimensional diagnostic diagram, which aids in the simultaneous separation of line emission from star formation, shocks, and AGN.

The 3D diagram retains the emission-line ratio information from the BPT diagram on one axis, in the form of our emission-line ratio (ELR) function. Further axes of spaxel distance and velocity dispersion complete the diagram. To test the diagram, we use data from the Siding Spring Southern Seyfert Spectroscopic Snapshot Survey (S7), specifically the Seyfert galaxy NGC 1068. The high spectral resolution of the S7 allows the study of individual velocity components in emission lines, which provides more information on shocks in the data.

Spaxels on the 3D diagram display two clear sequences. We show that these two sequences represent the mixing between star formation and AGN, and star formation and shocks, respectively. Large scatter is seen between the AGN and shock regions of their respective

sequences, indicating mixing also between the two ionising sources. We verify our star formation-AGN sequence by showing alignment between the distribution of spaxels within the sequence, and the distribution of 0.25-7.5 keV X-rays from Young et al. (2001). Furthermore, the distribution of spaxels in the star formation-shock sequence correlates strongly with regions of high velocity dispersion in the galaxy.

7.4. Separating Line Emission from Star Formation, Shocks, and AGN Ionisation

Using the three-dimensional diagnostic diagram shown in Chapter 4, we calculate the relative contribution to line emission from the ionising sources of star formation, shocks, and AGN in each spaxel of NGC 1068 from the S7. To do so, we use MAPPINGS photoionisation models as in Chapter 3 to predict line ratios where 100% of the observed emission is expected to be from star formation, and shocks/AGN. We fit lines in three-dimensional space to the star formation-AGN and star formation-shock sequences defined in Chapter 4, and calculate each spaxel's projected distance along these lines to define their star formation-shock-AGN fractions.

The results give credence to the method, as the star formation, shock, and AGN luminosity distributions across the galaxy correlate well with the observed CO(3-2) molecular line flux, radio jets, and 0.25-7.5 keV X-ray photon flux, respectively. Furthermore, we compare our results to the He II/H β line ratio map from the S7 data. Because this line ratio is not included in our ELR function, such a comparison provides an independent test of the results. We find that the AGN fraction distribution across the galaxy correlates well with the He II/H β map. This finding supports our results, because He II λ 4686 is a high-ionisation line which requires a hard radiation field to produce high emission line fluxes, such as that from an AGN.

We also use the [O III] λ 4363/5007 ratio to verify the shock results. Shocks can produce temperatures of up to a factor of 10^4 K higher than temperatures from a NLR, hence regions of high [O III] ratio should correlate with regions of high shock fractions. We find a slight correlation between high shock fractions and increased [O III] ratio. However, such regions also contain considerable AGN fractions. This suggests that while an improvement, the separation between shocked and AGN emission may require further future advancements.

7.5. The Effect of Resolution on the Star Formation-Shock-AGN Fraction, and Future Directions

The high spatial and spectral resolution of the S7 data provided a great test case for the 3D diagnostic diagram. However, the spatial and spectral resolutions of many IFU surveys is not necessarily as high as the S7. We rebin the S7 data to lower spatial resolutions, and Gaussian smooth the wavelength axis to lower spectral resolutions, to study the effect of resolution on the final star formation-shock-AGN fractions calculated using the 3D diagram. Similarly to the results of Chapter 3, we find that there exists a window of spatial resolution where the contribution from low surface brightness features is at a maximum. This corres-

ponds to an increase in the calculated shock fractions at such spatial resolutions. Lowering the spatial resolution further however, begins to blend the emission from all three ionising sources in a given spaxel. As a result, the star formation, shock, and AGN fractions all begin to tend towards equilibrium.

Lowering the spectral resolution through Gaussian smoothing severely impacts the number of observed velocity components in the emission line profiles. Hence, higher-order components in each spaxel are increasingly absent with lower spectral resolutions. This impacts the star formation-AGN sequence of the 3D diagram, because the first components in the data become broader, corresponding to a higher velocity dispersion which places them along the star formation-shock sequence. The result is that the calculated shock contribution in each spaxel increases, while the AGN contribution decreases.

Future directions of the work in this thesis include completing the unfinished aforementioned resolution work, exploring possible improvements to the ELR function of the 3D diagram, and applying the 3D diagram to a large-scale survey. These future directions will complement the work presented in this thesis, which has truly progressed the understanding of heating and ionisation processes in galaxies.

Bibliography

- Abazajian, K., et al. 2003, *AJ*, 126, 2081 ([ADS entry](#))
- Abazajian, K. N., et al. 2009, *ApJS*, 182, 543 ([ADS entry](#))
- Abdullah, A., et al. 2017, *ApJ*, 842, 4 ([ADS entry](#))
- Ackermann, M., et al. 2011, *ApJ*, 743, 171 ([ADS entry](#))
- Adelman-McCarthy, J. K., et al. 2006, *ApJS*, 162, 38 ([ADS entry](#))
- Akima, H. 1970, *J. ACM*, 17, 589 ([Link](#))
- Alexander, D. M., & Hickox, R. C. 2012, *New Astron. Rev.*, 56, 93 ([ADS entry](#))
- Allen, M. G., Groves, B. A., Dopita, M. A., Sutherland, R. S., & Kewley, L. J. 2008, *ApJS*, 178, 20 ([ADS entry](#))
- Alloin, D., Edmunds, M. G., Lindblad, P. O., & Pagel, B. E. J. 1981, *A&A*, 101, 377 ([ADS entry](#))
- Alonso-Herrero, A., et al. 2012, *MNRAS*, 425, 311 ([ADS entry](#))
- Anders, E., & Grevesse, N. 1989, *Geochim. Cosmochim. Acta*, 53, 197 ([ADS entry](#))
- Anderson, L. D., Bania, T. M., Jackson, J. M., Clemens, D. P., Heyer, M., Simon, R., Shah, R. Y., & Rathborne, J. M. 2009, *The Astrophysical Journal Supplement Series*, 181, 255 ([ADS entry](#))
- Antonucci, R. 1993, *ARA&A*, 31, 473 ([ADS entry](#))
- Antonucci, R. R. J., & Miller, J. S. 1985, *ApJ*, 297, 621 ([ADS entry](#))
- Armus, L., et al. 2009, *PASP*, 121, 559 ([ADS entry](#))
- Arribas, S., Mediavilla, E., & Garcia-Lorenzo, B. 1996, *ApJ*, 463, 509 ([ADS entry](#))
- Baldwin, J. A., Phillips, M. M., & Terlevich, R. 1981, *PASP*, 93, 5 ([ADS entry](#))

- Balmer, J. J. 1885, *Annalen der Physik*, 261, 80 ([ADS entry](#))
- Beckmann, V., & Shrader, C. 2012, in Proceedings of “An INTEGRAL view of the high-energy sky (the first 10 years)” - 9th INTEGRAL Workshop and celebration of the 10th anniversary of the launch (INTEGRAL 2012). 15-19 October 2012. Bibliothèque Nationale de France, Paris, France. Published online at “<http://pos.sissa.it/cgi-bin/reader/conf.cgi?confid=176>”, id.69, 69 ([ADS entry](#))
- Begeman, K. G. 1987, PhD thesis, , Kapteyn Institute, (1987) ([ADS entry](#))
- Belsole, E., Worrall, D. M., & Hardcastle, M. J. 2006, *MNRAS*, 366, 339 ([ADS entry](#))
- Bennert, V. N., Auger, M. W., Treu, T., Woo, J.-H., & Malkan, M. A. 2011, *ApJ*, 742, 107 ([ADS entry](#))
- Binette, L., Magris, C. G., Stasińska, G., & Bruzual, A. G. 1994, *A&A*, 292, 13 ([ADS entry](#))
- Binney, J., & Merrifield, M. 1998, *Galactic Astronomy* ([ADS entry](#))
- Biretta, J. A., Sparks, W. B., & Macchetto, F. 1999, *ApJ*, 520, 621 ([ADS entry](#))
- Blandford, R. D., & Königl, A. 1979, *ApJ*, 232, 34 ([ADS entry](#))
- Bordoloi, R., Heckman, T. M., & Norman, C. A. 2016, ArXiv e-prints ([ADS entry](#))
- Bosma, A. 1978, PhD thesis, PhD Thesis, Groningen Univ., (1978) ([ADS entry](#))
- Bressan, A., Fagotto, F., Bertelli, G., & Chiosi, C. 1993, *A&AS*, 100, 647 ([ADS entry](#))
- Brown, W. R., Kewley, L. J., & Geller, M. J. 2008, *AJ*, 135, 92 ([ADS entry](#))
- Bryant, J. J., et al. 2015, *MNRAS*, 447, 2857 ([ADS entry](#))
- Bundy, K., et al. 2015, *ApJ*, 798, 7 ([ADS entry](#))
- Byler, N., Dalcanton, J. J., Conroy, C., & Johnson, B. D. 2017, *ApJ*, 840, 44 ([ADS entry](#))
- Camenzind, M., & Courvoisier, T. J.-L. 1983, *ApJ*, 266, L83 ([ADS entry](#))
- Cao, X. 2009, *MNRAS*, 394, 207 ([ADS entry](#))
- Cardelli, J. A., Clayton, G. C., & Mathis, J. S. 1989, *ApJ*, 345, 245 ([ADS entry](#))
- Cattaneo, A., Haehnelt, M. G., & Rees, M. J. 1999, *MNRAS*, 308, 77 ([ADS entry](#))
- Caughlan, G. R., & Fowler, W. A. 1988, *Atomic Data and Nuclear Data Tables*, 40, 283 ([ADS entry](#))
- Caughlan, G. R., Fowler, W. A., Harris, M. J., & Zimmerman, B. A. 1985, *Atomic Data and Nuclear Data Tables*, 32, 197 ([ADS entry](#))
- Cecil, G., Bland, J., & Tully, R. B. 1990, *ApJ*, 355, 70 ([ADS entry](#))
- Cecil, G., Dopita, M. A., Groves, B., Wilson, A. S., Ferruit, P., Pécontal, E., & Binette, L. 2002, *ApJ*, 568, 627 ([ADS entry](#))

- Cerviño, M., Román-Zúñiga, C., Luridiana, V., Bayo, A., Sánchez, N., & Pérez, E. 2013, *A&A*, 553, A31 ([ADS entry](#))
- Charlot, S., & Bruzual, A. G. 1991, *ApJ*, 367, 126 ([ADS entry](#))
- Charlot, S., & Longhetti, M. 2001, *MNRAS*, 323, 887 ([ADS entry](#))
- Cid Fernandes, R., Heckman, T., Schmitt, H., González Delgado, R. M., & Storchi-Bergmann, T. 2001, *ApJ*, 558, 81 ([ADS entry](#))
- Cid Fernandes, R., Stasińska, G., Schlickmann, M. S., Mateus, A., Vale Asari, N., Schoenell, W., & Sodré, L. 2010, *MNRAS*, 403, 1036 ([ADS entry](#))
- Clegg, R. E. S., & Middlemass, D. 1987, *MNRAS*, 228, 759 ([ADS entry](#))
- Cody, W. J., & Thacher, H. C. 1968, *Mathematics of Computation*, 22, 641 ([Link](#))
- . 1969, *Mathematics of Computation*, 23, 289 ([Link](#))
- Conroy, C., Gunn, J. E., & White, M. 2009, *ApJ*, 699, 486 ([ADS entry](#))
- Conti, P. S. 1976, *Memoires of the Societe Royaledes Sciences de Liege*, 9, 193
- Crenshaw, D. M., & Kraemer, S. B. 2000, *ApJ*, 532, L101 ([ADS entry](#))
- Crowther, P. A. 2007, *ARA&A*, 45, 177 ([ADS entry](#))
- Crowther, P. A., Hadfield, L. J., Clark, J. S., Negueruela, I., & Vacca, W. D. 2006, *MNRAS*, 372, 1407 ([ADS entry](#))
- da Silva, R. L., Fumagalli, M., & Krumholz, M. 2012, *ApJ*, 745, 145 ([ADS entry](#))
- D’Agostino, J. J., Kewley, L. J., Groves, B., Byler, N., Sutherland, R. S., Nicholls, D., Leitherer, C., & Stanway, E. R. 2019a, *ApJ*, 878, 2 ([ADS entry](#))
- D’Agostino, J. J., Kewley, L. J., Groves, B. A., Medling, A., Dopita, M. A., & Thomas, A. D. 2019b, *MNRAS*, 485, L38 ([ADS entry](#))
- D’Agostino, J. J., Poetrodjojo, H., Ho, I. T., Groves, B., Kewley, L., Madore, B. F., Rich, J., & Seibert, M. 2018, *MNRAS*, 479, 4907 ([ADS entry](#))
- Das, V., Crenshaw, D. M., Kraemer, S. B., & Deo, R. P. 2006, *AJ*, 132, 620 ([ADS entry](#))
- Davies, R. I., Müller Sánchez, F., Genzel, R., Tacconi, L. J., Hicks, E. K. S., Friedrich, S., & Sternberg, A. 2007, *ApJ*, 671, 1388 ([ADS entry](#))
- Davies, R. L., Kewley, L. J., Ho, I.-T., & Dopita, M. A. 2014a, *MNRAS*, 444, 3961 ([ADS entry](#))
- Davies, R. L., Rich, J. A., Kewley, L. J., & Dopita, M. A. 2014b, *MNRAS*, 439, 3835 ([ADS entry](#))
- Davies, R. L., et al. 2016, *ApJ*, 824, 50 ([ADS entry](#))
- . 2017, *MNRAS*, 470, 4974 ([ADS entry](#))

- de Jager, C., Nieuwenhuijzen, H., & van der Hucht, K. A. 1988, *A&AS*, 72, 259 ([ADS entry](#))
- de Vaucouleurs, G., de Vaucouleurs, A., Corwin, Jr., H. G., Buta, R. J., Paturel, G., & Fouqué, P. 1991, Third Reference Catalogue of Bright Galaxies. Volume I: Explanations and references. Volume II: Data for galaxies between 0^h and 12^h . Volume III: Data for galaxies between 12^h and 24^h . ([ADS entry](#))
- Del Zanna, G., Dere, K. P., Young, P. R., Landi, E., & Mason, H. E. 2015, *A&A*, 582, A56 ([ADS entry](#))
- Dennett-Thorpe, J., Bridle, A. H., Laing, R. A., & Scheuer, P. A. G. 1999, *MNRAS*, 304, 271 ([ADS entry](#))
- Dere, K. P., Landi, E., Mason, H. E., Monsignori Fossi, B. C., & Young, P. R. 1997, *A&AS*, 125, 149 ([ADS entry](#))
- Di Teodoro, E. M., & Fraternali, F. 2015, *MNRAS*, 451, 3021 ([ADS entry](#))
- Dopita, M., Hart, J., McGregor, P., Oates, P., Bloxham, G., & Jones, D. 2007, *Ap&SS*, 310, 255 ([ADS entry](#))
- Dopita, M., et al. 2010, *Ap&SS*, 327, 245 ([ADS entry](#))
- Dopita, M. A. 1995, *Ap&SS*, 233, 215 ([ADS entry](#))
- Dopita, M. A., Groves, B. A., Sutherland, R. S., Binette, L., & Cecil, G. 2002a, *ApJ*, 572, 753 ([ADS entry](#))
- . 2002b, *ApJ*, 572, 753 ([ADS entry](#))
- Dopita, M. A., Pereira, M., Kewley, L. J., & Capaccioli, M. 2002c, *ApJS*, 143, 47 ([ADS entry](#))
- Dopita, M. A., & Sutherland, R. S. 1995, *ApJ*, 455, 468 ([ADS entry](#))
- . 2003, *Astrophysics of the diffuse universe* ([ADS entry](#))
- Dopita, M. A., Sutherland, R. S., Nicholls, D. C., Kewley, L. J., & Vogt, F. P. A. 2013, *ApJS*, 208, 10 ([ADS entry](#))
- Dopita, M. A., et al. 2006, *ApJS*, 167, 177 ([ADS entry](#))
- . 2015a, *ApJS*, 217, 12 ([ADS entry](#))
- . 2015b, *ApJ*, 801, 42 ([ADS entry](#))
- Dray, L. M., & Tout, C. A. 2007, *MNRAS*, 376, 61 ([ADS entry](#))
- Eddington, A. S. 1924, *MNRAS*, 84, 308 ([ADS entry](#))
- Eggleton, P. P. 1971, *MNRAS*, 151, 351 ([ADS entry](#))
- Eldridge, J. J., Izzard, R. G., & Tout, C. A. 2008, *MNRAS*, 384, 1109 ([ADS entry](#))
- Eldridge, J. J., & Stanway, E. R. 2009, *MNRAS*, 400, 1019 ([ADS entry](#))

- . 2012, *MNRAS*, 419, 479 ([ADS entry](#))
- Esquej, P., et al. 2014, *ApJ*, 780, 86 ([ADS entry](#))
- Evans, I. N., Ford, H. C., Kinney, A. L., Antonucci, R. R. J., Armus, L., & Caganoff, S. 1991, *ApJ*, 369, L27 ([ADS entry](#))
- Fagotto, F., Bressan, A., Bertelli, G., & Chiosi, C. 1994a, *A&AS*, 104, 365 ([ADS entry](#))
- . 1994b, *A&AS*, 105, 29 ([ADS entry](#))
- . 1994c, *A&AS*, 105, 39 ([ADS entry](#))
- Feltre, A., Charlot, S., & Gutkin, J. 2016, *MNRAS*, 456, 3354 ([ADS entry](#))
- Ferguson, A. M. N., Wyse, R. F. G., Gallagher, III, J. S., & Hunter, D. A. 1996, *AJ*, 111, 2265 ([ADS entry](#))
- Ferland, G. J. 1996, *Hazy, A Brief Introduction to Cloudy 90* ([ADS entry](#))
- Ferland, G. J., & Mushotzky, R. F. 1982, *ApJ*, 262, 564 ([ADS entry](#))
- Ferland, G. J., et al. 2013, *RMxAA*, 49, 137 ([ADS entry](#))
- Ferrarese, L., & Merritt, D. 2000, *ApJ*, 539, L9 ([ADS entry](#))
- Ferrière, K. M. 2001, *Reviews of Modern Physics*, 73, 1031 ([ADS entry](#))
- Fioc, M., & Rocca-Volmerange, B. 1997, *A&A*, 326, 950 ([ADS entry](#))
- Forbes, D. A., & Norris, R. P. 1998, *MNRAS*, 300, 757 ([ADS entry](#))
- Freitas, I. C., et al. 2018, *MNRAS*, 476, 2760 ([ADS entry](#))
- Frieman, J. A., et al. 2008, *AJ*, 135, 338 ([ADS entry](#))
- Galliano, E., Alloin, D., Pantin, E., Granato, G. L., Delva, P., Silva, L., Lagage, P. O., & Panuzzo, P. 2008, *A&A*, 492, 3 ([ADS entry](#))
- Galliano, E., Alloin, D., Pantin, E., Lagage, P. O., & Marco, O. 2005, *A&A*, 438, 803 ([ADS entry](#))
- Gallimore, J. F., Baum, S. A., O’Dea, C. P., & Pedlar, A. 1996, *ApJ*, 458, 136 ([ADS entry](#))
- Gandhi, P. 2005, *Asian Journal of Physics*, 13, 90 ([ADS entry](#))
- García-Burillo, S., et al. 2014, *A&A*, 567, A125 ([ADS entry](#))
- . 2016, *ApJ*, 823, L12 ([ADS entry](#))
- . 2017, *A&A*, 608, A56 ([ADS entry](#))
- Gebhardt, K., et al. 2000, *ApJ*, 539, L13 ([ADS entry](#))
- Georganopoulos, M., Kazanas, D., Perlman, E., & Stecker, F. W. 2005, *ApJ*, 625, 656 ([ADS entry](#))

- Geogy, C., Ekström, S., Hirschi, R., Meynet, G., Groh, J. H., & Eggenberger, P. 2015, in *Wolf-Rayet Stars: Proceedings of an International Workshop held in Potsdam, Germany, 1-5 June 2015*. Edited by Wolf-Rainer Hamann, Andreas Sander, Helge Todt. Universitätsverlag Potsdam, 2015., p.229-232, ed. W.-R. Hamann, A. Sander, & H. Todt, 229–232 ([ADS entry](#))
- Girardi, L., Bressan, A., Bertelli, G., & Chiosi, C. 2000, *A&AS*, 141, 371 ([ADS entry](#))
- Girardi, L., Bressan, A., Chiosi, C., Bertelli, G., & Nasi, E. 1996, *A&AS*, 117, 113 ([ADS entry](#))
- Goosmann, R. W., & Matt, G. 2011, *MNRAS*, 415, 3119 ([ADS entry](#))
- Granato, G. L., De Zotti, G., Silva, L., Bressan, A., & Danese, L. 2004, *ApJ*, 600, 580 ([ADS entry](#))
- Gray, W. J., & Scannapieco, E. 2017, *ApJ*, 849, 132 ([ADS entry](#))
- Groh, J. H., Meynet, G., & Ekström, S. 2013, *A&A*, 550, L7 ([ADS entry](#))
- Groves, B. A., Dopita, M. A., & Sutherland, R. S. 2004, *ApJS*, 153, 9 ([ADS entry](#))
- Groves, B. A., Heckman, T. M., & Kauffmann, G. 2006, *MNRAS*, 371, 1559 ([ADS entry](#))
- Gültekin, K., et al. 2009, *ApJ*, 698, 198 ([ADS entry](#))
- Haehnelt, M. G., & Kauffmann, G. 2000, *MNRAS*, 318, L35 ([ADS entry](#))
- Hamann, W.-R., Gräfener, G., & Liermann, A. 2006, *A&A*, 457, 1015 ([ADS entry](#))
- Hampton, E. J., et al. 2017, *MNRAS*, 470, 3395 ([ADS entry](#))
- Heckman, T. M. 1980, *A&A*, 87, 152 ([ADS entry](#))
- Heckman, T. M., Armus, L., & Miley, G. K. 1987, *AJ*, 93, 276 ([ADS entry](#))
- Hillier, D. J., & Miller, D. L. 1998, *ApJ*, 496, 407 ([ADS entry](#))
- Hirota, K., Iguchi, S., Kimura, M., & Wajima, K. 2000, *ApJ*, 545, 100 ([ADS entry](#))
- Hjelm, M., & Lindblad, P. O. 1996, *A&A*, 305, 727 ([ADS entry](#))
- Ho, I.-T. 2016, *LZIFU: IDL emission line fitting pipeline for integral field spectroscopy data*, *Astrophysics Source Code Library* ([ADS entry](#))
- Ho, I.-T., et al. 2014, *MNRAS*, 444, 3894 ([ADS entry](#))
- . 2016, *Ap&SS*, 361, 280 ([ADS entry](#))
- Ho, I. T., et al. 2017, *ApJ*, 846, 39 ([ADS entry](#))
- Ho, L. C. 2008, *ARA&A*, 46, 475 ([ADS entry](#))
- Hoffmann, T. L., Lieb, S., Pauldrach, A. W. A., Lesch, H., Hultsch, P. J. N., & Birk, G. T. 2012, *A&A*, 544, A57 ([ADS entry](#))

- Husemann, B., et al. 2013a, *A&A*, 549, A87 ([ADS entry](#))
- . 2013b, *A&A*, 549, A87 ([ADS entry](#))
- Inoue, A. K., Iwata, I., & Deharveng, J.-M. 2006, *MNRAS*, 371, L1 ([ADS entry](#))
- Izotov, Y. I., Stasińska, G., Meynet, G., Guseva, N. G., & Thuan, T. X. 2006, *A&A*, 448, 955 ([ADS entry](#))
- Izotov, Y. I., Thuan, T. X., & Guseva, N. G. 2012, *A&A*, 546, A122 ([ADS entry](#))
- Jansen, R. A. 2000, PhD thesis, Kapteyn Astronomical Institute, Groningen, The Netherlands, and Harvard-Smithsonian Center for Astrophysics, Cambridge, MA ([ADS entry](#))
- Jenkins, E. B. 2014, ArXiv e-prints ([ADS entry](#))
- Kaasinen, M., Bian, F., Groves, B., Kewley, L. J., & Gupta, A. 2017, *MNRAS*, 465, 3220 ([ADS entry](#))
- Kashino, D., et al. 2017, *ApJ*, 835, 88 ([ADS entry](#))
- Kauffmann, G., et al. 2003, *MNRAS*, 346, 1055 ([ADS entry](#))
- Kennicutt, Jr., R. C., Tamblyn, P., & Congdon, C. E. 1994, *ApJ*, 435, 22 ([ADS entry](#))
- Kewley, L. J., & Dopita, M. A. 2002, *ApJS*, 142, 35 ([ADS entry](#))
- Kewley, L. J., Dopita, M. A., Leitherer, C., Davé, R., Yuan, T., Allen, M., Groves, B., & Sutherland, R. 2013a, *ApJ*, 774, 100 ([ADS entry](#))
- Kewley, L. J., Dopita, M. A., Sutherland, R. S., Heisler, C. A., & Trevena, J. 2001, *ApJ*, 556, 121 ([ADS entry](#))
- Kewley, L. J., & Ellison, S. L. 2008, *ApJ*, 681, 1183 ([ADS entry](#))
- Kewley, L. J., Groves, B., Kauffmann, G., & Heckman, T. 2006, *MNRAS*, 372, 961 ([ADS entry](#))
- Kewley, L. J., Heisler, C. A., Dopita, M. A., Sutherland, R., Norris, R. P., Reynolds, J., & Lumsden, S. 2000, *ApJ*, 530, 704 ([ADS entry](#))
- Kewley, L. J., Maier, C., Yabe, K., Ohta, K., Akiyama, M., Dopita, M. A., & Yuan, T. 2013b, *ApJ*, 774, L10 ([ADS entry](#))
- Kobulnicky, H. A., & Kewley, L. J. 2004, *ApJ*, 617, 240 ([ADS entry](#))
- Kong, X., & Cheng, F. Z. 2002, *A&A*, 389, 845 ([ADS entry](#))
- Kong, X., Cheng, F. Z., Weiss, A., & Charlot, S. 2002, *A&A*, 396, 503 ([ADS entry](#))
- Kraemer, S. B., Trippe, M. L., Crenshaw, D. M., Meléndez, M., Schmitt, H. R., & Fischer, T. C. 2009, *ApJ*, 698, 106 ([ADS entry](#))
- Kristen, H., Jorsater, S., Lindblad, P. O., & Boksenberg, A. 1997, *A&A*, 328, 483 ([ADS entry](#))

- Kroupa, P. 2002, *Science*, 295, 82 ([ADS entry](#))
- Krumholz, M. R., Fumagalli, M., da Silva, R. L., Rendaahl, T., & Parra, J. 2015, *MNRAS*, 452, 1447 ([ADS entry](#))
- Kundt, W. 2014, in Proceedings of Frontier Research in Astrophysics (FRAPWS2014) held 26-31 May, 2014 in Mondello (Palermo), Italy. Online at “<http://pos.sissa.it/cgi-bin/reader/conf.cgi?confid=237>”, id.25, 25 ([ADS entry](#))
- LaMassa, S. M., Heckman, T. M., Ptak, A., Schiminovich, D., O’Dowd, M., & Bertincourt, B. 2012, *ApJ*, 758, 1 ([ADS entry](#))
- Lamers, H. J. G. L. M., Maeder, A., Schmutz, W., & Cassinelli, J. P. 1991, *ApJ*, 368, 538 ([ADS entry](#))
- Langer, N. 1989, *A&A*, 220, 135 ([ADS entry](#))
- Leitherer, C., Ekström, S., Meynet, G., Schaerer, D., Agienko, K. B., & Levesque, E. M. 2014, *ApJS*, 212, 14 ([ADS entry](#))
- Leitherer, C., et al. 1999, *ApJS*, 123, 3 ([ADS entry](#))
- Lejeune, T., Cuisinier, F., & Buser, R. 1997, *A&AS*, 125 ([ADS entry](#))
- Levesque, E. M., Kewley, L. J., & Larson, K. L. 2010, *AJ*, 139, 712 ([ADS entry](#))
- MacAlpine, G. M. 1986, *PASP*, 98, 134 ([ADS entry](#))
- Machida, M. N. 2017, arXiv e-prints, arXiv:1711.00384 ([ADS entry](#))
- Madau, P., & Dickinson, M. 2014, *ARA&A*, 52, 415 ([ADS entry](#))
- Magorrian, J., et al. 1998, *AJ*, 115, 2285 ([ADS entry](#))
- Marconi, A., & Hunt, L. K. 2003, *ApJ*, 589, L21 ([ADS entry](#))
- Marinucci, A., et al. 2016, *MNRAS*, 456, L94 ([ADS entry](#))
- Martins, F., Schaerer, D., & Hillier, D. J. 2005, *A&A*, 436, 1049 ([ADS entry](#))
- Mathis, J. S., Ruml, W., & Nordsieck, K. H. 1977, *ApJ*, 217, 425 ([ADS entry](#))
- McConnell, N. J., & Ma, C.-P. 2013, *ApJ*, 764, 184 ([ADS entry](#))
- Meynet, G. 1993, in *The Feedback of Chemical Evolution on the Stellar Content of Galaxies*, ed. D. Alloin & G. Stasińska, 40 ([ADS entry](#))
- Meynet, G., & Maeder, A. 2005, *A&A*, 429, 581 ([ADS entry](#))
- Meynet, G., Maeder, A., Schaller, G., Schaerer, D., & Charbonnel, C. 1994, *A&AS*, 103 ([ADS entry](#))
- Miller, J. S., & Antonucci, R. R. J. 1983, *ApJ*, 271, L7 ([ADS entry](#))
- Miller, J. S., & Goodrich, R. W. 1990, *ApJ*, 355, 456 ([ADS entry](#))

- Miller, J. S., Goodrich, R. W., & Mathews, W. G. 1991a, *ApJ*, 378, 47 ([ADS entry](#))
- . 1991b, *ApJ*, 378, 47 ([ADS entry](#))
- Mokiem, M. R., et al. 2007, *A&A*, 473, 603 ([ADS entry](#))
- Molteni, D., Lanzafame, G., & Chakrabarti, S. K. 1994, *ApJ*, 425, 161 ([ADS entry](#))
- Morganti, R., Tsvetanov, Z. I., Gallimore, J., & Allen, M. G. 1999, *A&AS*, 137, 457 ([ADS entry](#))
- Morisset, C., et al. 2016, *A&A*, 594, A37 ([ADS entry](#))
- Mortlock, D. J., et al. 2011, *Nature*, 474, 616 ([ADS entry](#))
- Netzer, H. 1990, in *Active Galactic Nuclei*, ed. R. D. Blandford, H. Netzer, L. Woltjer, T. J.-L. Courvoisier, & M. Mayor, 57–160 ([ADS entry](#))
- Netzer, H. 2015, *ARA&A*, 53, 365 ([ADS entry](#))
- Neustroev, V. V., & Borisov, N. V. 1998, *A&A*, 336, L73 ([ADS entry](#))
- Nicholls, D. C., Dopita, M. A., Jerjen, H., & Meurer, G. R. 2011, *AJ*, 142, 83 ([ADS entry](#))
- Nicholls, D. C., Dopita, M. A., Sutherland, R. S., Jerjen, H., & Kewley, L. J. 2014, *ApJ*, 790, 75 ([ADS entry](#))
- Nicholls, D. C., Sutherland, R. S., Dopita, M. A., Kewley, L. J., & Groves, B. A. 2017, *MNRAS*, 466, 4403 ([ADS entry](#))
- Oey, M. S., & Kennicutt, Jr., R. C. 1997, *MNRAS*, 291, 827 ([ADS entry](#))
- Onodera, M., et al. 2016, *ApJ*, 822, 42 ([ADS entry](#))
- Osterbrock, D. E. 1981, *ApJ*, 249, 462 ([ADS entry](#))
- Osterbrock, D. E., & Ferland, G. J. 2006, *Astrophysics of gaseous nebulae and active galactic nuclei* ([ADS entry](#))
- Osterbrock, D. E., & Martel, A. 1993, *ApJ*, 414, 552 ([ADS entry](#))
- Pauldrach, A. W. A., Hoffmann, T. L., & Lennon, M. 2001, *A&A*, 375, 161 ([ADS entry](#))
- Pellegrini, E. W., Oey, M. S., Winkler, P. F., Points, S. D., Smith, R. C., Jaskot, A. E., & Zastrow, J. 2012, *ApJ*, 755, 40 ([ADS entry](#))
- Peterson, B. 2006, *The Broad-Line Region in Active Galactic Nuclei*, ed. D. Alloin, R. Johnson, & P. Lira (Berlin, Heidelberg: Springer Berlin Heidelberg), 77–100 ([Link](#))
- Phillips, M. M., Edmunds, M. G., Pagel, B. E. J., & Turtle, A. J. 1983, *MNRAS*, 203, 759 ([ADS entry](#))
- Poetrodjojo, H., D’Agostino, J. J., Groves, B., Kewley, L., Ho, I. T., Rich, J., Madore, B. F., & Seibert, M. 2019, *MNRAS*, 487, 79 ([ADS entry](#))

- Pogge, R. W. 1988, *ApJ*, 328, 519 ([ADS entry](#))
- Poncelet, A., Sol, H., & Perrin, G. 2008, *A&A*, 481, 305 ([ADS entry](#))
- Rafferty, D. A., Brandt, W. N., Alexander, D. M., Xue, Y. Q., Bauer, F. E., Lehmer, B. D., Luo, B., & Papovich, C. 2011, *ApJ*, 742, 3 ([ADS entry](#))
- Reynolds, C. S. 2013, *Nature*, 494, 432 ([ADS entry](#))
- Rich, J. A., Dopita, M. A., Kewley, L. J., & Rupke, D. S. N. 2010, *ApJ*, 721, 505 ([ADS entry](#))
- Rich, J. A., Kewley, L. J., & Dopita, M. A. 2011, *ApJ*, 734, 87 ([ADS entry](#))
- . 2014, *ApJ*, 781, L12 ([ADS entry](#))
- Rigby, J. R. 2006, PhD thesis, The University of Arizona ([ADS entry](#))
- Rigby, J. R., & Rieke, G. H. 2004, *ApJ*, 606, 237 ([ADS entry](#))
- Risaliti, G., Elvis, M., Fabbiano, G., Baldi, A., Zezas, A., & Salvati, M. 2007, *ApJ*, 659, L111 ([ADS entry](#))
- Risaliti, G., et al. 2013, *Nature*, 494, 449 ([ADS entry](#))
- Rupke, D. S., Veilleux, S., & Sanders, D. B. 2005, *ApJS*, 160, 115 ([ADS entry](#))
- Rupke, D. S. N., & Veilleux, S. 2011, *ApJ*, 729, L27 ([ADS entry](#))
- . 2013, *ApJ*, 768, 75 ([ADS entry](#))
- Sánchez, S. F., et al. 2012a, *A&A*, 538, A8 ([ADS entry](#))
- . 2012b, *A&A*, 538, A8 ([ADS entry](#))
- Sanders, R. L., et al. 2016, *ApJ*, 816, 23 ([ADS entry](#))
- Sandqvist, A., Joersaeter, S., & Lindblad, P. O. 1995, *A&A*, 295, 585 ([ADS entry](#))
- Sandqvist, A., Jorsater, S., & Lindblad, P. O. 1982, *A&A*, 110, 336 ([ADS entry](#))
- Schaller, G., Schaerer, D., Meynet, G., & Maeder, A. 1992, *A&AS*, 96, 269 ([ADS entry](#))
- Schneider, F. R. N., Podsiadlowski, P., Langer, N., Castro, N., & Fossati, L. 2016, *MNRAS*, 457, 2355 ([ADS entry](#))
- Schoniger, F., & Sofue, Y. 1994, *A&A*, 283, 21 ([ADS entry](#))
- Seyfert, C. K. 1943, *ApJ*, 97, 28 ([ADS entry](#))
- Shakura, N. I., & Sunyaev, R. A. 1973, *A&A*, 24, 337 ([ADS entry](#))
- Sharp, R. G., & Bland-Hawthorn, J. 2010, *ApJ*, 711, 818 ([ADS entry](#))
- Shimakawa, R., et al. 2015, *MNRAS*, 451, 1284 ([ADS entry](#))
- Smith, L. J., Norris, R. P. F., & Crowther, P. A. 2002, *MNRAS*, 337, 1309 ([ADS entry](#))

- Smith, N. 2014, *ARA&A*, 52, 487 ([ADS entry](#))
- Snijders, L., Kewley, L. J., & van der Werf, P. P. 2007, *ApJ*, 669, 269 ([ADS entry](#))
- Sponholz, H., & Molteni, D. 1994, *MNRAS*, 271 ([ADS entry](#))
- Spruit, H. C. 1987, *A&A*, 184, 173 ([ADS entry](#))
- Stanway, E. R., Eldridge, J. J., & Becker, G. D. 2016, *MNRAS*, 456, 485 ([ADS entry](#))
- Stasińska, G., Cid Fernandes, R., Mateus, A., Sodré, L., & Asari, N. V. 2006, *MNRAS*, 371, 972 ([ADS entry](#))
- Stasińska, G., et al. 2008, *MNRAS*, 391, L29 ([ADS entry](#))
- Steidel, C. C., et al. 2014, *ApJ*, 795, 165 ([ADS entry](#))
- Storchi Bergmann, T. 2015, in *IAU Symposium*, Vol. 309, *Galaxies in 3D across the Universe*, ed. B. L. Ziegler, F. Combes, H. Dannerbauer, & M. Verdugo, 190–195 ([ADS entry](#))
- Storchi-Bergmann, T., Riffel, R. A., Riffel, R., Diniz, M. R., Borges Vale, T., & McGregor, P. J. 2012, *ApJ*, 755, 87 ([ADS entry](#))
- Stoughton, C., et al. 2002, *AJ*, 123, 485 ([ADS entry](#))
- Sturch, L. K., & Madore, B. F. 2012, in *IAU Symposium*, Vol. 284, *The Spectral Energy Distribution of Galaxies - SED 2011*, ed. R. J. Tuffs & C. C. Popescu, 180–182 ([ADS entry](#))
- Sutherland, R., Dopita, M., Binette, L., & Groves, B. 2018, *MAPPINGS V: Astrophysical plasma modeling code*, *Astrophysics Source Code Library* ([ADS entry](#))
- Sutherland, R. S., & Dopita, M. A. 1993, *ApJS*, 88, 253 ([ADS entry](#))
- Tacconi, L. J., Genzel, R., Blietz, M., Cameron, M., Harris, A. I., & Madden, S. 1994, *ApJ*, 426, 77 ([ADS entry](#))
- Taylor, M. D., Tadhunter, C. N., & Robinson, T. G. 2003, *MNRAS*, 342, 995 ([ADS entry](#))
- Thilker, D. A., Braun, R., & Walterbos, R. A. M. 2000, *AJ*, 120, 3070 ([ADS entry](#))
- Thomas, A. D., Groves, B. A., Sutherland, R. S., Dopita, M. A., Kewley, L. J., & Jin, C. 2016, *ApJ*, 833, 266 ([ADS entry](#))
- Thomas, A. D., et al. 2017, *ApJS*, 232, 11 ([ADS entry](#))
- Thronson, Jr., H. A., et al. 1989, *ApJ*, 343, 158 ([ADS entry](#))
- Trani, A. A., Mapelli, M., & Bressan, A. 2014, *MNRAS*, 445, 1967 ([ADS entry](#))
- Trebitsch, M., Blaizot, J., Rosdahl, J., Devriendt, J., & Slyz, A. 2017, *MNRAS*, 470, 224 ([ADS entry](#))
- Tremaine, S., et al. 2002, *ApJ*, 574, 740 ([ADS entry](#))

- Tremonti, C. A., et al. 2004, *ApJ*, 613, 898 ([ADS entry](#))
- Urry, C. M., & Padovani, P. 1995, *PASP*, 107, 803 ([ADS entry](#))
- Vacca, W. D., Garmany, C. D., & Shull, J. M. 1996, *ApJ*, 460, 914 ([ADS entry](#))
- Vaona, L., Ciroi, S., Di Mille, F., Cracco, V., La Mura, G., & Rafanelli, P. 2012, *MNRAS*, 427, 1266 ([ADS entry](#))
- Vassiliadis, E., & Wood, P. R. 1993, *ApJ*, 413, 641 ([ADS entry](#))
- Vázquez, G. A., & Leitherer, C. 2005, *ApJ*, 621, 695 ([ADS entry](#))
- Veilleux, S., & Osterbrock, D. E. 1987, *ApJS*, 63, 295 ([ADS entry](#))
- Veilleux, S., Shopbell, P. L., Rupke, D. S., Bland-Hawthorn, J., & Cecil, G. 2003, *AJ*, 126, 2185 ([ADS entry](#))
- Véron-Cetty, M.-P., & Véron, P. 2006, *A&A*, 455, 773 ([ADS entry](#))
- Westera, P., Lejeune, T., Buser, R., Cuisinier, F., & Bruzual, G. 2002, *A&A*, 381, 524 ([ADS entry](#))
- Wilson, A. S., Helfer, T. T., Haniff, C. A., & Ward, M. J. 1991, *ApJ*, 381, 79 ([ADS entry](#))
- Wilson, A. S., & Raymond, J. C. 1999, *ApJ*, 513, L115 ([ADS entry](#))
- Wilson, A. S., & Ulvestad, J. S. 1983, *ApJ*, 275, 8 ([ADS entry](#))
- . 1987, *ApJ*, 319, 105 ([ADS entry](#))
- Wofford, A., et al. 2016, *MNRAS*, 457, 4296 ([ADS entry](#))
- Woltjer, L. 1959, *ApJ*, 130, 38 ([ADS entry](#))
- Yanny, B., et al. 2009, *AJ*, 137, 4377 ([ADS entry](#))
- York, D. G., et al. 2000, *AJ*, 120, 1579 ([ADS entry](#))
- Young, A. J., Wilson, A. S., & Shopbell, P. L. 2001, *ApJ*, 556, 6 ([ADS entry](#))
- Yuan, T.-T., Kewley, L. J., & Sanders, D. B. 2010, *ApJ*, 709, 884 ([ADS entry](#))
- Zastrow, J., Oey, M. S., Veilleux, S., & McDonald, M. 2013, *ApJ*, 779, 76 ([ADS entry](#))
- Zubovas, K., & King, A. R. 2012, in *Astronomical Society of the Pacific Conference Series*, Vol. 460, *AGN Winds in Charleston*, ed. G. Chartas, F. Hamann, & K. M. Leighly, 235 ([ADS entry](#))
- Zurita, A., Beckman, J. E., Rozas, M., & Ryder, S. 2002, *A&A*, 386, 801 ([ADS entry](#))